Wall-bounded turbulence at high Reynolds numbers

Margit Vallikivi

A Dissertation

Presented to the Faculty

of Princeton University

in Candidacy for the Degree

of Doctor of Philosophy

Recommended for Acceptance

by the Department of

Mechanical and Aerospace Engineering

Adviser: Alexander J. Smits

June 2014

Abstract

Measurements are reported that give new insight into the behavior of turbulent wall-bounded flows at high Reynolds number. Turbulent pipe and boundary layer flows are examined experimentally over a wide range of Reynolds numbers – up to $Re_\tau = 100,000$ ($Re_D = 6 \times 10^6$) in pipe flow, and up to $Re_\tau = 73,000$ ($Re_\theta = 235 \times 10^3$) in a flat plate zero pressure gradient boundary layer. A Nano-Scale Thermal Anemometry Probe (NSTAP) was developed for very high spatial and temporal resolution measurements. Sensors with wire lengths 30 and 60 μm were fabricated, tested and validated in known flows, and then used to obtain single-point measurements at high Reynolds numbers in pipe and boundary layers.

The mean velocity data together with data from previous studies and extensive error analysis showed that the von Kármán's constant in the log-law is $\kappa = 0.40 \pm 0.02$. It was shown that the streamwise Reynolds stress exhibits a logarithmic behavior in the inertial sublayer for $Re_\tau \geq 20,000$, in both pipes and boundary layers. Variances as well as higher order even moments were compared for pipes and boundary layers and it was shown that all even moments have a logarithmic behavior in the inertial sublayer, suggesting a true scale separation.

Streamwise turbulent spectra showed a clear $k^{-5/3}$ region for up to two decades in wavenumber. No k^{-1} region was found to be present in any of the cases in the pipe or the boundary layer. The location of the outer spectral peak, associated with very large scale motions, was found to have only a weak dependence on Reynolds number. The loci of these peak occur at the same wall-normal distance where the streamwise stresses establish a logarithmic behavior and where the amplitude modulation coefficient has a zero value. This suggests that with Reynolds number increasing to infinity most of the energy is contained within a diminishing wall-layer in physical coordinates.

Acknowledgements

Successful PhD research requires both passion for a subject and outstanding guidance, and I have been fortunate enough to have both. First and foremost, I would like to thank my advisor Lex Smits, whose mentorship has been a privilege these past five years. Lex gave me the freedom to explore and pursue my own interests, while at the same time offering unparalleled support and advice. His encouragement, guidance, and friendship have made my time at Princeton unforgettable and invaluable.

Many thanks to Marcus Hultmark, for being an enthusiastic research partner and trusted companion during endless nights and days next to the wind tunnel, as well as throughout my time at Princeton. Thank you to everyone I have had the honor of collaborating with; to Bill George, for introducing me to the exciting world of turbulence; to Sean Bailey, for encouraging me during the first stages of my research career and for our continued collaborations; and to Bharath Ganapathisubramani for providing exceptional feedback during the writing of this dissertation. I would also like to thank committee members Elie Bou-Zeid, Gigi Martinelli and Michael Mueller for their advice and guidance during my PhD research.

Thanks to Pat Watson and all the MNFL staff for sharing their extensive clean-room knowledge, and to Dan Hoffman for his substantial technical assistance at Forrestal. I am grateful to Dan Quinn, who made preparing for generals and nights around the campfire equally fun. Thank you Leo, Yuyang, Owen, Anand, Katie, Brian, Jessica, Joshue, Keith, Gilad, Tristen and Peter for making D100 a great place to work, as well as everyone else in the department for making EQuad a thriving environment. And to all my volleyball buddies – thank you for all the fun times on the court and in the sand!

To my family I am forever grateful. My mother: your unconditional love, generosity and selflessness made me the person I am today. I thank my father Ako, little sister Laura, as well as Astra, Asse, Tanja and Ahto for love and support during my

years on the other side of Atlantic. Thank you Hanna for your genuine friendship and support. Finally, I would like to thank all my close friends in Princeton, Estonia, and all over the world for always being there for me – I couldn't have done it without you!

This work was supported by the Office of Naval Research Grant No. N00014-13-1-0174 and the National Science Foundation Grant No. CBET-1064257. I am also thankful for additional financial support from Estonian Students Fund, Zonta International, as well as several Princeton alumni fellowships.

This dissertation carries the number T-3283T in the records of the Department of Mechanical and Aerospace Engineering.

Contents

List of Tables

List of Figures

Chapter 1

Introduction

1.1 Motivation and Goals

Turbulence is an important phenomenon that is present in most fluid flows in nature as well as in practical applications. In industrial or environmental applications, the Reynolds number, describing the ratio of inertial to viscous forces, is usually very high and turbulence introduces large energy losses due to dissipation. Nowadays transportation consumes about 38% and industry 34% of the total energy production in the USA (as reported in U.S. Energy Information Administration [2013]), so together these sectors are responsible for about three quarters of total energy consumption. For aircraft or other high-speed vehicles (where Reynolds number is $\mathcal{O}\left(10^5 - 10^6\right)$) the viscous drag accounts for about half of total drag and any transport of fluids in pipelines (i.e. gas, oil, cooling water) introduces significant pressure losses, so that approximately half of energy used in the transportation of people or fluids is spent in turbulent dissipation. Therefore, being able to correctly estimate the losses due to turbulence, together with designing and developing more efficient systems to reduce these losses will play an important role in the world energy consumption.

In addition to industrial applications, high Reynolds number turbulence is also an

important part of atmospheric and ocean studies. There Reynolds numbers are often $\mathcal{O}\left(10^7 - 10^8\right)$, making it difficult to develop reliable meteorological tools, climate models and global warming predictions. Turbulence has been a topic of research for more than a century but there is still little understanding of the underlying physics and no general model for describing turbulence at high Reynolds numbers.

Turbulence is often considered to be the most complicated and challenging form of fluid motion, and by quote from Richard Feynman (or sometimes ascribed to Albert Einstein or Arnold Sommerfeld) *'Turbulence is the last great unsolved problem in classical physics'*. There is no standard way to define turbulence, but maybe one of the most comprehensive descriptions is given by Tennekes and Lumley [1972] who, instead of giving a precise definition, list the most important characteristics of turbulent flow: a) Irregularity; b) Diffusivity; c) Large Reynolds numbers; d) Three-dimensional vorticity fluctuations; e) Dissipation at small scales; f) Continuum; and finally g) Turbulence is a feature of flow, not the fluid. These characteristics describe well the complexity of turbulence and in order to make any advancements in understanding of turbulent flows, all of them need to be kept in mind simultaneously.

Turbulent fluid motion, described by the instantaneous Navier-Stokes equations, is inherently a multi-scale phenomenon where energy is extracted through velocity gradients at the largest scales of the flow. The energy is then transported down to smaller and smaller scales until dissipated at the smallest viscous scales (concept of this forward energy cascade was first introduced by Richardson [1922]). This cascade process is also highly time-dependent, so in order to study and understand turbulence, one needs to resolve all these spatial and time scales simultaneously, down to the very small dissipative scales. As the Reynolds number increases, the separation in scales increases and resolving all the flow features becomes increasingly more complicated.

In order to directly solve the instantaneous Navier-Stokes equations using Direct Numerical Simulations (DNS) [Moin and Mahesh, 1998], one needs to have the

computational grid large enough to capture all the large scales and fine enough so that grid size is smaller than the smallest dissipation scales in the flow. This is increasingly more computationally expensive with Reynolds number, as increasing one decade in Reynolds number requires increase in number of gridpoints as $\sim Re^3$ [Piomelli and Balaras, 2002] and another order of magnitude better temporal resolution, so the total computational cost increases as $\sim Re^4$ for wall-bounded flows. Even with the technological and computational advancements of the last decade, the highest DNS currenly available are at $Re \approx 2,000$ (in a boundary layer by Sillero et al. [2011] and Pirozzoli and Bernardini [2013], and in a channel by del Álamo et al. [2004] and Hoyas and Jiménez [2006]), which is still many orders of magnitude lower than most industrial and environmental applications.

Because directly solving the Navier-Stokes equations is not feasible at even moderate Reynolds numbers, alternative numerical approaches use Reynolds-Averaged Navier Stokes (RANS) models [Mellor and Herring, 1973] and Large-Eddy Simulations (LES) Lesieur and Métais [1996]. RANS models are based on averaged equations describing the mean flow, and the turbulent stresses are modeled using some type of eddy-viscosity or Reynolds stress model. RANS modeling is fast and reliable for many industrial applications for standard flows, but RANS performs poorly in flows and Reynolds numbers where the model coefficients have not been calibrated, as there is little connection between the models and the underlying physics of the flow. Bridging the gap between DNS and RANS models, LES has become the preferred approach in turbulence computations, being less computationally expensive than DNS but still capturing large scale instantaneous phenomena. In LES-type models, the large scale turbulent motions are fully resolved and only the small scale turbulence is modeled using a sub-grid scale (SGS) model for motions smaller than the grid size [Meneveau and Katz, 2000](assuming that at small scales the turbulence behavior is universal and independent of the flow geometry). The study and continued develop-

ment of SGS models requires accurate high-Reynolds-number data, and therefore a greater integration of experimental with numerical and theoretical research in turbulence is needed. Sub-grid model approach works relatively well in free shear flows, but near solid boundaries the grid size needs to be decreased substantially and the cost of LES becomes comparable to DNS. Alternatively, one could compute most of the flow using LES and try modeling the near-wall behavior, and so in recent years developing these wall-models has been an important area of research ([Marusic et al., 2010b, Piomelli and Balaras, 2002]). In developing near-wall models which represent correctly high Reynolds number flows, a fundamental knowledge of the turbulence behavior near walls at high Reynolds numbers is needed.

Numerous reviews on wall-bounded turbulence have been written over the years, discussing the understanding and advances in the field, notably Cantwell [1981], Robinson [1991], Marusic et al. [2010c], Smits et al. [2011a], Smits and Marusic [2013]. Some significant progress has been made over the years to understand the behavior of wall-bounded flows, but these reviews all agree that high Reynolds number experimental data is needed to validate any of the proposed models, to gain a better understanding of the dynamics of turbulence and to be able to predict high Reynolds number flows.

Therefore experimental studies of turbulence are crucial. The advantage of experiments is that all flow phenomena exist in the flow, without approximations. The main challenges are to actually measure what is of interest to the researcher, and setting up experiment so that it resembles the flow of interest. Conducting experiments at high Reynolds numbers typically requires very large and expensive facilities together with high precision spatially and temporally resolving measurement techniques. To achieve very high Reynolds numbers, the experimental facilities need to either be scaled up or, alternatively, the Reynolds number can be increased by changing viscosity. At the Princeton University Gas Dynamics Laboratory the second approach has been

chosen and two high Reynolds number facilities have been built, using pressurized air to increase the Reynolds number. This allows the facilities to be of reasonable size, but introduces problems in resolving the small-scale turbulence, because the dissipative scales in these facilities can be very small. Therefore, conventional measurement techniques cannot be used to resolve these flows.

The main goals of the current dissertation are to:

- to develop and validate a small-scale sensor that provides high spatial and temporal resolution for turbulence measurements;
- to conduct experiments with high spatial and temporal resolution at very high Reynolds numbers in two representative wall-bounded flows:
  - Turbulent pipe flow;
  - Turbulent boundary layer flow;
- to analyze the statistics of these wall-bounded flows and determine the trends in scaling and asymptotic behavior over a large range of Reynolds numbers;
- to study the dynamics of turbulence of these wall-bounded flows using spectral analysis and determine any asymptotic behavior and scaling of the energy content;
- to compare the behavior of turbulent pipe and boundary layer flows at very high Reynolds numbers and examine the similarities and differences between them.

1.2 Wall-bounded flows

Turbulence can broadly be divided into two categories of flows based on the generation mechanism: *wall-bounded flows*, where turbulence is generated through the no-slip

condition at the wall and viscous effects in the region very close to the wall (that is, boundary layers, pipes and channels); and *free shear flows*, occurring when fluids with different momentum interact (i.e. jets, wakes, plumes). In this dissertation, we concentrate on the behavior of canonical wall-bounded flows only, namely the zero pressure gradient turbulent boundary layer and fully developed turbulent pipe flow.

In this study, only single-point statistics are studied of the instantaneous velocity $\tilde{u}(y,t)$, where u is the streamwise component of the velocity, y is the wall-normal location, and t is time. Using Reynolds decomposition, $\tilde{u}$ is separated into a time averaged mean value $U = U(y) = \overline{\tilde{u}(y,t)}$ and a fluctuating value $u(y,t) = \tilde{u}(y,t) - U(y)$, where time averaging is denoted with over-bar $\overline{(\ )}$. For the purpose of studying the statistics of the flow, the streamwise Reynolds stress is found as the variance of the instantaneous velocity $u^2 = u^2(y) = \overline{u^2(y,t)}$, which depends only on the wall-normal location y for fully developed pipe flow, but depends on both y and x (or a local Reynolds number) in a boundary layer.

Turbulence is generated when inertial forces cause flow instabilities to grow larger than the viscous forces which tend to dampen them, so the instabilities grow until the full flow-field becomes unstable. The ratio between inertial and viscous forces is defined as the Reynolds number $Re = U_c L_c/\nu$, where U_c and L_c are some velocity and length scales and ν is the kinematic viscosity of the fluid. The conventional Reynolds number in pipe flow is defined as $Re_D = \frac{\langle U \rangle D}{\nu}$, where D is the diameter of the pipe and $\langle U \rangle$ is the bulk velocity (defined as $\langle U \rangle = \frac{1}{\pi R^2}\int_0^R U(r) 2\pi r \, \mathrm{d}r$, where r is the radial coordinate and $R = D/2$ is the pipe radius). In boundary layers, the usual velocity for defining Reynolds number is the free stream velocity U_∞ and usual length is the momentum thickness $\theta = \int_0^\infty \frac{U(y)}{U_\infty}\left(1 - \frac{U(y)}{U_\infty}\right)\mathrm{d}y$, so that $Re_\theta = \frac{U_\infty \theta}{\nu}$ is the conventional Reynolds number for boundary layers.

Near the wall the flow needs to satisfy the no-slip condition, so that $\tilde{u}(y=0) = 0$, and the total shear stress is equivalent to the viscous shear stress at the wall. This wall

shear stress $\tau_w = \rho\nu \left(\frac{\mathrm{d}U(y)}{\mathrm{d}y}\right)_{y=0}$ together with kinematic viscosity ν and density of the fluid ρ are evidently the important parameters close to the wall. From these quantities we can define appropriate *viscous* or *inner scales* near the wall. The velocity scale is defined as the friction velocity $u_\tau = \sqrt{\tau_w/\rho}$ and the length scale is the viscous length $\eta = \nu/u_\tau$. Using these inner scales, a friction Reynolds number can be defined as $Re_\tau = \frac{\delta u_\tau}{\nu}$, where δ is the boundary layer thickness, or in pipe flow the pipe radius. For boundary layers we define $\delta = \delta_{99}$, distance from the wall y at which the mean velocity equals 99% of the free-stream velocity U_∞. This friction Reynolds number expresses the ratio between the large energetic scales to the small viscous scales in wall shear flows and can be used for comparing pipe flows and boundary layers, as well as any other wall-bounded flows.

1.2.1 Scaling of wall-bounded flows

Classically, in turbulent wall-bounded flow, two different scaling parameters are used. Very close to the wall, the viscous or *inner scaling* is relevant, where the important parameters are the viscosity ν and the friction velocity u_τ. By scaling with these parameters, at high enough Reynolds number, self-similarities in velocity profiles are expected independent of the Reynolds number. Properties scaled with inner variables are from here on denoted with a superscript $(\,)^+$: wall-normal distance $y^+ = y/\eta$ and mean velocity $U^+ = U/u_\tau$ and streamwise Reynolds stress $u^{2+} = u^2/u_\tau^2$.

In the outer region of the flow, the behavior is expected to be governed by the large energy containing scales. The length scale in this region would be the scale of the largest motions, that is boundary layer thickness δ in external flows and pipe radius R in internal flows. The velocity scale for outer region is not as well agreed on. The most conventional is to use u_τ again as the velocity scale for both internal and external flows, where instead of mean velocity U, the deficit velocity $U_\infty - U$ or $U_{cl} - U$ are described (U_∞ denoting the free-stream velocity in boundary layers and

U_{cl} the center-line velocity in pipes and channels).

Conventionally, wall-bounded flows are described as consisting of four wall-normal layers [Pope, 2000]. Very close to the wall is the *viscous sublayer*, divided into *linear sublayer* and *buffer layer*. In the linear sublayer the viscosity dominates the flow and the velocity profile can be shown to be linear so that $U^+ = y^+$. This region extends up to $y^+ \approx 3$. At about $y^+ > 3$ there is a buffer layer where the turbulent shear stress $-\rho\overline{uv}$ becomes increasingly important compared to the viscous shear stress $\rho\nu\frac{\mathrm{d}U}{\mathrm{d}y}$, and the total shear stress is a sum of these two. For $y^+ > 30$ the total shear stress consists mainly of turbulent shear stress, and from here on the outer scaling is expected to be relevant. This is the usual expectation, however resent results, including results presented in this dissertation, indicate that the viscous effects stay important even up to $y^+ = \mathcal{O}(10^3)$. The inner scaling is expected to be valid from the wall until $y/\delta \approx 0.1$. The region where both of the scalings are simultaneously valid is called an *overlap region*, or turbulent wall region, and as the Reynolds number increases this region is also increasing (in terms of y^+). Conventionally this overlap region is considered to be equivalent to an *inertial sublayer*, indicating that neither viscous nor energetic scales are relevant. The region far away from the wall, where $y/\delta \gtrsim 0.1$, is called the *outer boundary layer* or *wake region* and here the flow is fully governed by the outer scales. It is important to note that this distinction of regions is only true if the Reynolds number is high enough.

Compared to this conventional approach, where only linear sublayer, buffer layer, inertial sublayer and the outer layer are identified, George and Castillo [1997] introduced another region for turbulent boundary layers, the so-called *mesolayer*. This region, first described by Long and Chen [1981], is the inner part of the overlap region at $30 \lesssim y^+ \lesssim 300$ and describes the region where the viscous stresses are negligible, but in which viscosity acts directly on the turbulence scales producing the Reynolds stresses. According to this description, the overlap region is divided into a mesolayer

and an inertial sublayer, where the latter only starts at $y^+ \approx 300$ and extends until the outer edge of the overlap region. The mesolayer was also introduced later in pipe flows by Wosnik et al. [2000]. Figure 1.1 shows the different regions in turbulent boundary layer as described by George and Castillo [1997], where $\delta^+ = Re_\tau$. A similar picture can be drawn for pipe flow, with the difference that the wake region would also be denoted as the turbulent core. The limits of these regions (which could be different for pipes and boundary layers) mentioned above are approximate and are still up for debate. The existence and extents of these regions in boundary layers and pipes will be discussed in current work.

1.3 Hot-wire anemometry

There are many different techniques available for measuring instantaneous velocities in turbulent flows, but hot-wire anemometry has been the method of choice, primarily because it gives spatially and temporally well resolved data of velocity fluctuations [Bruun, 1995]. A conventional hot-wire sensor consists of a thin freestanding wire of length ℓ and diameter d mounted between two electrically conducting prongs, with typical length of 1 to 0.5 mm and a typical diameter of 5 to 2.5 μm. The probe assembly is inserted into the flow, the filament is electrically heated above the ambient temperature, and typically a feedback circuit is used to keep the sensor temperature (and resistance) constant (known as a Constant Temperature Anemometer, or CTA). As the fluid flows over the probe, the convective heat transfer from the wire to the fluid cools the wire, and so the current increases to keep the probe resistance constant. The output voltage can therefore be related to the fluid velocity through an empirical calibration function [Bruun, 1995, Perry and Morrison, 1971]. As a result an instantaneous velocity measurement at sampling frequency f_s at a single point in space can be obtained.

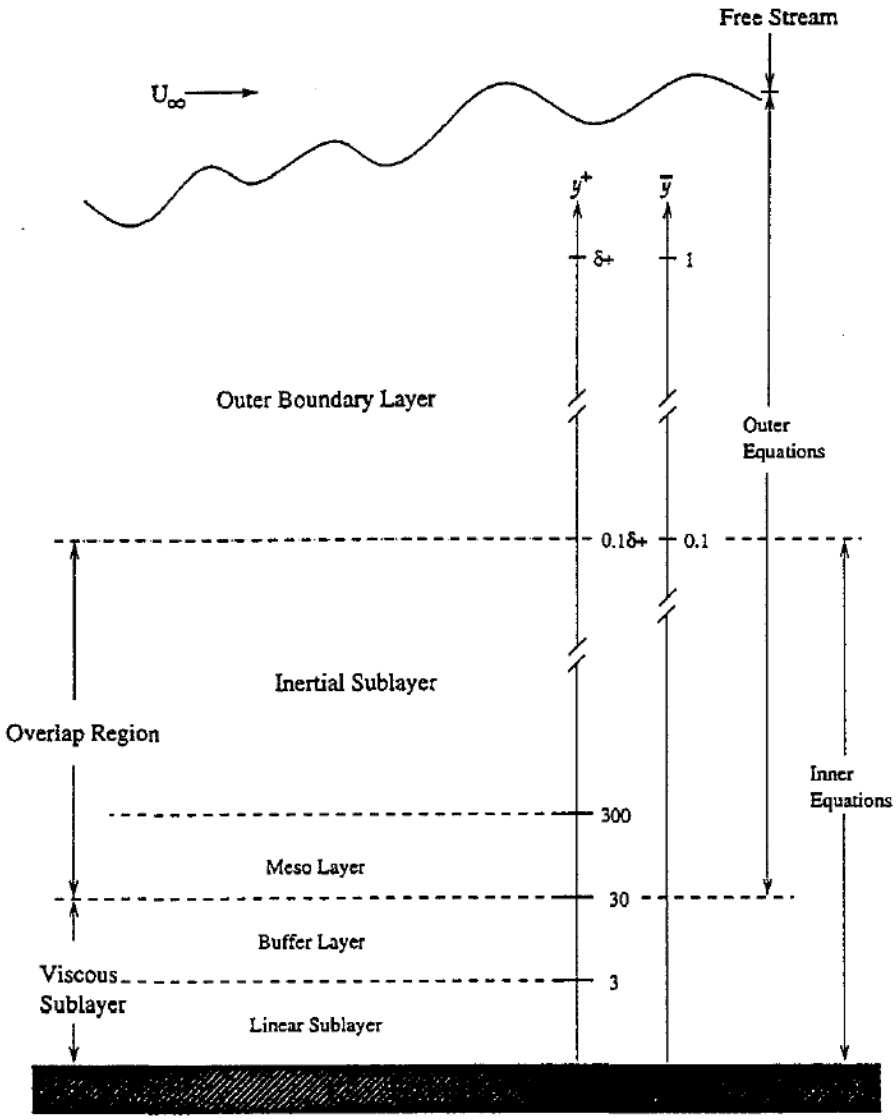

Figure 1.1: Schematic showing various regions and layers in boundary layer flow, adopted from George and Castillo [1997].

1.3.1 Spatial resolution

A major drawback of hot-wire anemometry, however, is the limited spatial resolution of the probe whereby eddies smaller than the wire length are masked in the signal. One of the first investigations of this phenomenon was performed by Wyngaard [1968], who studied the effects of spatial filtering in homogeneous isotropic turbulence by using a model spectrum to describe the high-wavenumber contributions to the signal. Later, Citriniti and George [1997] demonstrated experimentally and analytically that when spanwise wavelengths smaller than the wire length are filtered, the resulting measured one-dimensional spectrum will show filtering effects over the entire wavenumber range.

These studies give important insights into the effects of spatial filtering, but the effects are difficult to estimate quantitatively in the study of turbulent wall-bounded flows where the spectra are not known *a priori*. This problem is particularly evident at high Reynolds numbers, where in many cases the smallest scales of turbulence are much smaller than the wire length. Ligrani and Bradshaw [1987a] suggested that hot-wire probes will produce reliable turbulence statistics when the wire length in viscous units is $\ell^+ \leq 20$, where $\ell^+ = \ell u_\tau/\nu$. Hutchins et al. [2009] provide an empirical correlation to help estimate the filtering effects (at $y^+ = 15$) as a function of $Re_\tau = \delta u_\tau/\nu$, ℓ^+, and ℓ/δ.

Based on the attached eddy hypothesis combined with the near-wall peak correction, Smits et al. [2011b] developed a correction for streamwise turbulent stress u^{+2} in wall-bounded flows to account for spatial filtering effects at more distant wall-normal positions. Their analysis revealed that outside the near-wall region the spatial filtering effect scales inversely with the distance from the wall, in contrast to the commonly assumed scaling with the viscous length scale. Therefore the correction depends on both the wire length ℓ^+ as well as the wall-normal distance y^+, so that $\Delta u^{2+}/u_m^{2+} = M\left(\ell^+\right) f\left(y^+\right)$ where m denotes the measured value and Δ the difference between the true and measured values. They showed that this correction worked

equally well in various wall-bounded flows for at least up to $\ell^+ \approx 150$.

1.3.2 End-conduction effects

Any correction scheme must rely to some extent on known or predictable behavior, a bias that needs to be avoided when investigating new phenomena. There is a clear need for an instrument that has sufficient spatial and temporal resolution to measure turbulent fluctuations accurately over the entire spectrum, especially at high Reynolds numbers. The length of the sensor is the principal factor in setting its spatial resolution (that is, the smallest size eddy that can be resolved), and the mass of the sensor is the principal factor in determining its temporal resolution (how quickly can it respond to a change in velocity magnitude) [Smits et al., 2011b]. Therefore, to improve the sensor's spatial and temporal response, it is necessary to reduce its length and diameter. However, the length-to-diameter ratio ℓ/d must be kept large, of $\mathcal{O}(200)$, to minimize end-conduction effects [Hultmark et al., 2011, Klewicki and Falco, 1990, Ligrani and Bradshaw, 1987a, Perry et al., 1979]. End conduction is the process by which heat from the wire is conducted into the prongs that support the sensor, and it introduces frequency-dependent effects that are clearly undesirable in making accurate measurements. Therefore, it is not possible to reduce the probe size by simply reducing its length, since the diameter must be reduced proportionally, and there are limits on the smallest diameter that is achievable using conventional hot-wire manufacturing techniques.

One of the goals of this dissertation is to develop and implement a sensor of reduced size so that the sensor has significantly improved spatial and temporal resolution without introducing significant end-conduction effects. To achieve this goal, we turn to nano-fabrication in order to be able to decrease all dimensions of the sensing element at the same time. Development of these novel miniature hot-wire sensors is described in Chapter 2.

1.4 Contributions by the author

Chapter 2 describes the development, fabrication and validation of a Nano-Scale Thermal Anemometry Probe (NSTAP). Most of the chapter is based on a peer-reviewed article Vallikivi and Smits [2014], where all the writing, analysis and experiments were done by me. In addition, results from two previously published peer-reviewed articles were used in the validation section. Namely Section 2.5.3, which used data from Bailey et al. [2010], and Section 2.5.3 from Vallikivi et al. [2011], where data were taken collaboratively by Marcus Hultmark and myself.

Chapter 3 describes experiments in turbulent pipe flow obtained in the Princeton/ONR Superpipe facility. The NSTAP measurements were conducted by Marcus Hultmark and me collaboratively, and the Pitot measurements were taken by myself. This chapter consists of two peer-reviewed journal publications. Section 3.3 includes parts from Bailey et al. [2014], where all the data were taken by me and the analysis was done in parallel by myself and Sean Bailey. The writing of the paper, partially presented in this dissertation, was mostly done by Sean Bailey and me. Chapter 3.4 consists of material from Hultmark et al. [2012], where data was taken and analysis done in collaborative manner by me and M. Hultmark and writing was done by Marcus Hultmark, Sean Bailey and me.

Chapter 4 compares smooth and rough-wall turbulent pipe flow. It is based on Hultmark et al. [2013], where the measurements and analysis were done by me and Marcus Hultmark collaboratively, and the writing was done by Marcus Hultmark, Sean Bailey and me.

Chapter 5 describe experiments in a zero pressure gradient boundary layer obtained in the High Reynolds Number Test Facility (HRTF) at Princeton and

will be a basis of a paper. The experiment was set up by Marcus Hultmark, who also took the Pitot data and some preliminary NSTAP data. The NSTAP measurements, as well as all the analysis and writing were done by me.

Chapter 6 uses pipe and boundary layer data to analyze similarities and differences in higher order moments in both flows. All the analysis and writing was been done by me.

Chapter 7 describes the analysis of the spectral behavior of turbulent wall-bounded flows. Here all the analysis and writing were done by me. This Chapter will be the basis of a paper to be submitted to a peer-reviewed journal.

Chapter 2

A Nano-Scale Thermal Anemometry Probe

2.1 Introduction

There is a pressing need for probes that can measure velocity fluctuations with sufficiently small spatial resolution and sufficiently high frequency response, as was discussed in Chapter 1. Here, we describe a new sensor, manufactured using deep reactive ion etching (DRIE) together with other microelectromechanical systems (MEMS) fabrication techniques, to address the shortcomings of current sensing methods in measuring high Reynolds number flows.

A number of authors have tried to address the problem of spatial resolution (described in Chapter 1.3.1) by using conventional manufacturing techniques to create hot-wire probes with smaller sensing elements. Willmarth and Sharma [1984] constructed hot-wires as short as 25 μm but their results suffered from end-conduction effects because $\ell/d \ll 200$. Ligrani and Bradshaw [1987b] used the smallest of the available wires, with diameter of 0.625 μm, but with the restriction of $\ell/d > 200$ the smallest wire lengths were limited to 125 μm.

Integrated circuit fabrication and MEMS fabrication techniques have introduced new possibilities for developing anemometry sensors with considerably reduced physical sizes. Löfdahl et al. [1992] developed single and dual component velocity sensors, which gave results that compared well to conventional hot-wire probes, and Ebefors et al. [1998] introduced micro-joints for fabricating 3D poly-silicon hot-wires. Unfortunately, the largest dimensions of the sensing elements of these probes offered only a slight improvement in spatial resolution compared to conventional techniques. Jiang et al. [1994] used MEMS fabrication techniques to manufacture a poly-silicon thermal anemometry probe with a geometry similar to conventional hot-wires. These probes were a great improvement in terms of spatial dimensions, with the smallest having a length of 10 μm, but end-conduction was again an important limitation. This was also a problem for the multi-component hot-wire probes fabricated by Chen et al. [2003], with sensor dimensions $50 \times 6 \times 2.7$ μm. Moreover, these sensors were not suitable for conventional turbulence measurements, being fixed at one wall-normal location. Wang et al. [2007] had a different approach, using a micro-cantilever structure for measuring air flow, but these sensors were even larger than conventional hot-wire anemometers.

I have been working at Princeton University Gas Dynamics Laboratory to develop a Nano-Scale Thermal Anemometry Probe (NSTAP) that will have improved spatial and temporal resolution for small-scale turbulence measurements. NSTAP is a measurement device similar to conventional hot-wire anemometer, having an order of magnitude smaller sensing element compared to current commercial hot-wire anemometers, and it is manufactured using MEMS fabrication techniques.

2.2 History of the NSTAP

The development of a Nano-Scale Thermal Anemometry Probe (NSTAP) was originally started by Kunkel et al. [2006], proposing to develop a miniature sensor similar to hot-wire sensor but with smaller dimensions to improve spatial and temporal resolution. The proposed fabrication process was based on standard semiconductor processing techniques and they succeeded in fabricating a freestanding nano-scale platinum filament (with dimensions of $60 \times 2 \times 0.1 \mu$m) suspended between two current-carrying contacts. Kunkel et al. [2006] analyzed quantitatively the current-voltage characteristics and static response and showed that the performance of this new sensor was suitable for using in a similar configuration as hot-wires in order to conduct instantaneous velocity measurements.

Hot-wire anemometry is an intrusive method, therefore to avoid altering the flow behavior, the probes need to have an aerodynamic shape. The sensor developed by Kunkel et al. [2006] had significant amount of silicon protruding alongside of the filament and the probes were not suitable for quantitative analysis (Figure 2.1(A)). To address that problem, Hill [Senior Thesis,2007] developed a precise laser micromachining routine for ablating some of the protruding silicon (Figure 2.1(B)). Further improvements of the fabrication process were conducted by Bailey et al. [2008] and Meyer [Senior Thesis,2008], who manufactured a few sensors with freestanding filaments (Figure 2.1(C)), which were a great improvement compared to Kunkel et al. [2006]. However, the issue of aerodynamic interference of protruding silicon with the flow still remained, which affected proper turbulence measurements.

Our first successful effort to fabricate an NSTAP that could be used in turbulence measurements was reported by Bailey et al. [2010], shown in Figure 2.1(D). I improved the microfabrication process flow and laser ablation was used to shape the 3D silicon support structure. Although this design gave results that agreed well with conventional hot-wires in grid turbulence, the laser ablation method could only yield

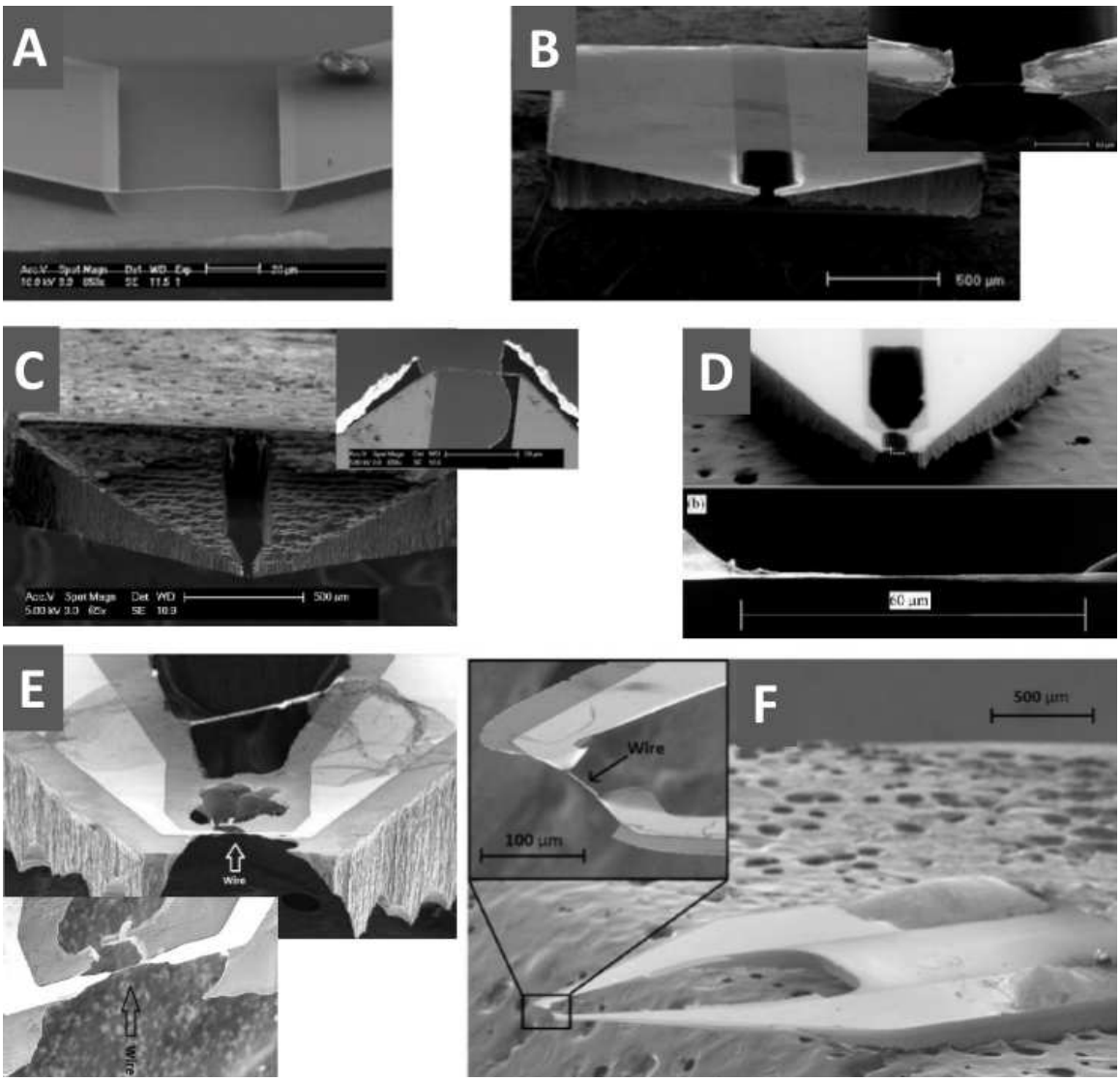

Figure 2.1: Scanning Electron Microscope images of development of NSTAPs over 8 years. (A) Kunkel et al. [2006]; (B) Hill [Senior Thesis,2007]; (C) Meyer [Senior Thesis,2008]; (D)Bailey et al. [2010]; (E) Vallikivi [2010]; (F) Vallikivi et al. [2011].

a bulky support structure of limited precision, and all the sensors suffered from significant aerodynamic interference due to the silicon support. In addition, the laser ablation was difficult to control, and consequently there was a very low yield of less than 5%. Similar problems persisted in the next attempt, described in Vallikivi [2010], where the sensor dimensions were decreased down to $30 \times 0.3 \times 0.1 \mu$m, but the silicon support was still disturbing the flow (as seen in Figure 2.1(E)).

To overcome these limitations, I developed a new approach using a deep reactive ion etching (DRIE) together with reactive ion etching lag (RIE lag) process and other improved fabrication steps to make possible high-yield, low-cost fabrication of durable small-scale thermal anemometry sensors. Additionally, the design of the sensors has been significantly changed to achieve an aerodynamic shape and minimize blockage effects behind the sensor. By modifying and improving the fabrication process, yields were increased from less than 5% to about 75%, and the fabrication time was at the same time decreased by at least 4 times. As an extra benefit, due to its small size, NSTAP can be positioned very close to the wall, down to 15 μm from the surface, to allow good velocity resolution in the near wall region (though the uncertainty of near-wall measurements increases due to calibration difficulties at lower velocities). First results using the DRIE were reported by Vallikivi et al. [2011] (Figure 2.1(F)), where 60μm sensors were compared with conventional hot wires (as described in Chapter 2.5.3). These NSTAP sensors have shown excellent agreement with conventional experimental techniques without any noticeable end-conduction effects, or aerodynamic interference.

2.3 Design and Fabrication Process

The conceptual shape of the NSTAP is shown in Figure 2.2. The sensor is designed to have a free-standing platinum sensor filament with two electrically conductive prongs

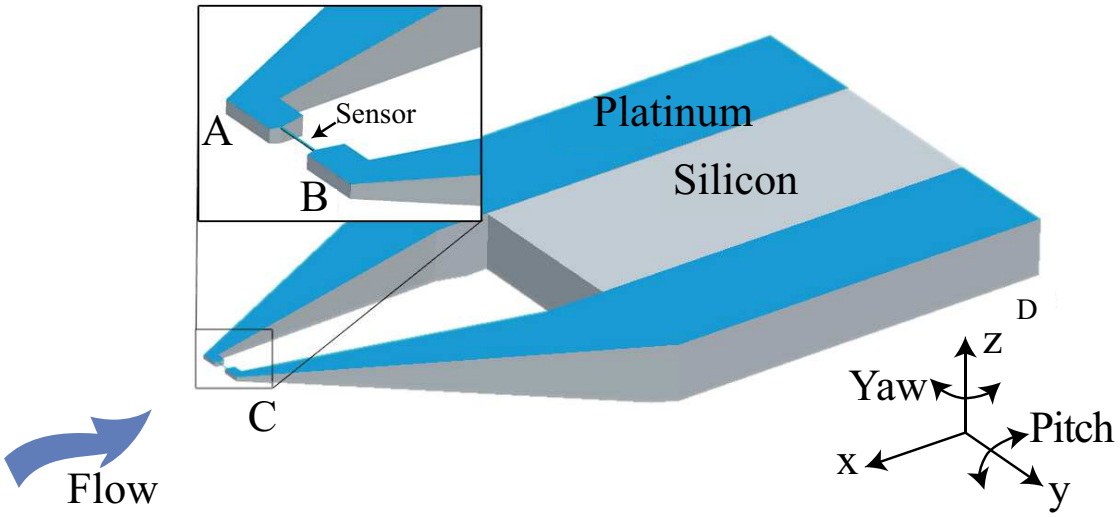

Figure 2.2: 3D model of the Nano-Scale Thermal Anemometry Probe.

and a supporting silicon structure. The supporting structure needs to be aerodynamically shaped, so that supports have a minimal size in front and a slow increase in size downstream. This requirement is crucial for making accurate measurements, and introduces a great challenge in microfabrication because most of the current fabrication techniques are designed for two-dimensional designs or layer stacking.

The fabrication of NSTAP sensors can be divided into three main stages: I) wafer fabrication; II) 3D shaping; III) wire release.

2.3.1 Stage I: Wafer fabrication

Integrated circuit fabrication techniques permit batch fabrication processes, which can optimize the fabrication flow as well as lower the cost per device. The fabrication starts with a 100 mm diameter 500–550 μm thick double-side polished prime grade silicon wafer, with low resistivity of 1-10 Ωcm.

The processing steps in Stage I are shown in Figure 2.3(a)-2.3(f), and they are:

a) Clean double side polished silicon wafer,

b) Silicon oxide deposition,

c) Photo-resist deposition,

d) Optical photo-lithography,

e) Metal deposition,

f) Metal lift-off.

First, a 500 nm thick layer of SiO_2 is deposited on the top side of the wafer using plasma-enhanced chemical vapor deposition (PECVD) (Figure 2.3(b)). The deposition is done in a Plasma-Therm 790 system using 2% SiH_4/N_2 at 35 sccm and N_2O at 69 sccm (with chamber temperature 250°C, pressure 400 mTorr, and power 25 W, resulting in a deposition rate of 20.6 nm/min). This oxide layer carries three main purposes: it provides an insulating layer between the silicon substrate and the metal film; it acts as an etch stop in Stage II; and it performs an important role in supporting the metal wire during the processing steps prior to the final wire release at the end of Stage III.

Optical photo-lithography is then used to define the pattern of the sensors. A Heidelberg DWL66 laser writer (with resolution down to 1 μm) is used for writing a customized mask on a soda lime chrome coated mask plate. This mask (Mask 1) with 12 $\times$ 17 patterns is fabricated in-house and can be used multiple times. A single pattern is shown in Figure 2.4(a). The overall size of the patterned sensor is 2 $\times$ 4 mm with a sensing element in front having dimensions 1 $\times$ 60 μm or 1 $\times$ 30 μm.

For optical lithography, the wafer is first spin-coated with a thin layer of hexa-methyl-di-silazane (HMDS) to improve adhesion and then spin-coated with a 500 nm

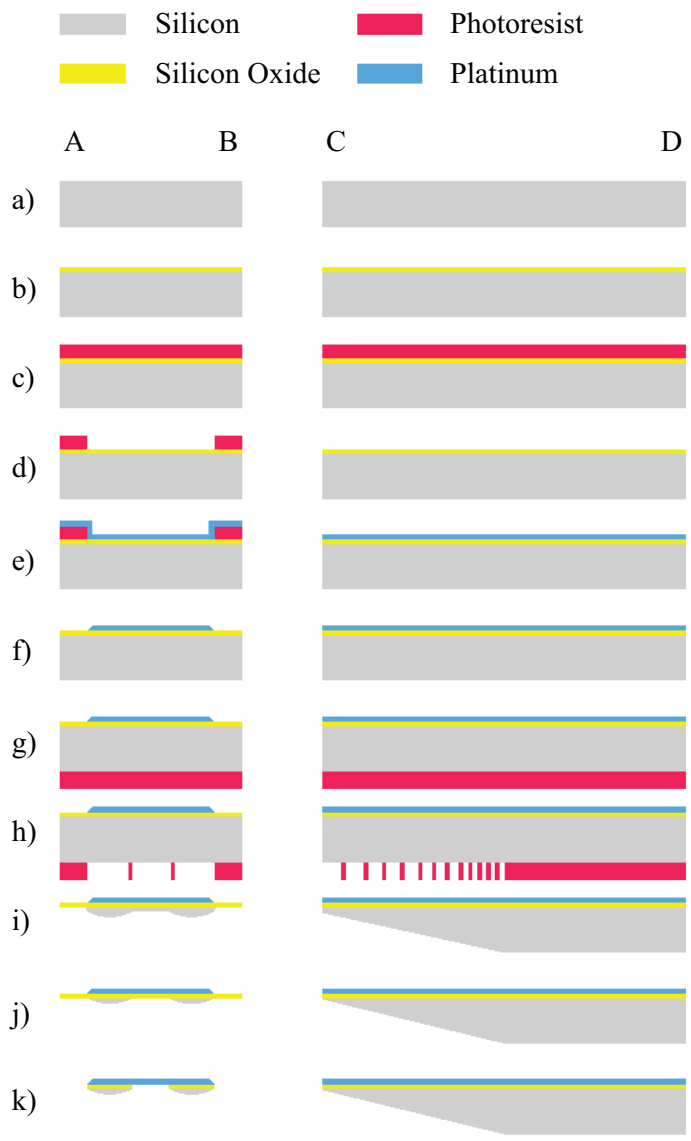

Figure 2.3: NSTAP fabrication process. Left: cross-section A-B; right: cross-section C-D with cross-sections shown in Figure 2.2. Steps: a) silicon wafer; b) silicon oxide deposition; c) photoresist; d) photo-lithography (Mask 1); e) metal deposition; f) metal lift-off; g) photoresist; h) photo-lithography (Mask 2); i) DRIE lag etching; j) RIE etching; k) wet BOE etching.

thick layer of AZ1505 photoresist (Figure 2.3(c)). The sample with resist is then soft-baked on a hot plate for one minute at 95°C. The wafer is exposed to UV light using Karl Suss MA6 optical aligner with vacuum contact to assure the highest precision. The exposed sample is then developed for 60 seconds and hard-baked on a hot plate for one minute at 95°C (Figure 2.3(d)).

Once the pattern is defined in the photoresist, we can proceed to metal deposition. To obtain high uniformity and low stress, a sputtering process is used to deposit the metal (employing Angstrom Sputterer system). First a 100 Ålayer of titanium is deposited as an adhesive layer between the oxide and the main metal. Then a 1000 Ålayer of platinum is deposited, and it is this layer that defines the final thickness of the sensing element (Figure 2.3(e)). Platinum is chosen as the sensor material due to its relatively low bulk thermal conductivity, and also because it has been extensively characterized and used in the conventional hot-wire industry. After the lift-off process, where the excess metal is removed, a wafer with ~200 NSTAP patterns is available, with a yield close to 100%.

2.3.2 Stage II: 3D shaping

To obtain measurements, the probe will be inserted into the flow, and therefore it is important to avoid aerodynamic interference, so that the supporting structure of the sensor does not affect the flow over the sensor. Here we describe a novel technique for three-dimensional etching of silicon, using DRIE together with the RIE lag effect, to achieve desired 3D structure.

DRIE is a powerful new MEMS fabrication technique for dry etching high aspect ratio trenches. One important aspect of this technique is known as RIE lag, that is, the fact that the etch rate depends on the size of the initial mask opening [Chung, 2004, Jansen et al., 1997]. RIE lag often introduces depth variations in the etched patterns and has proven to be a notorious problem in micro-machining community.

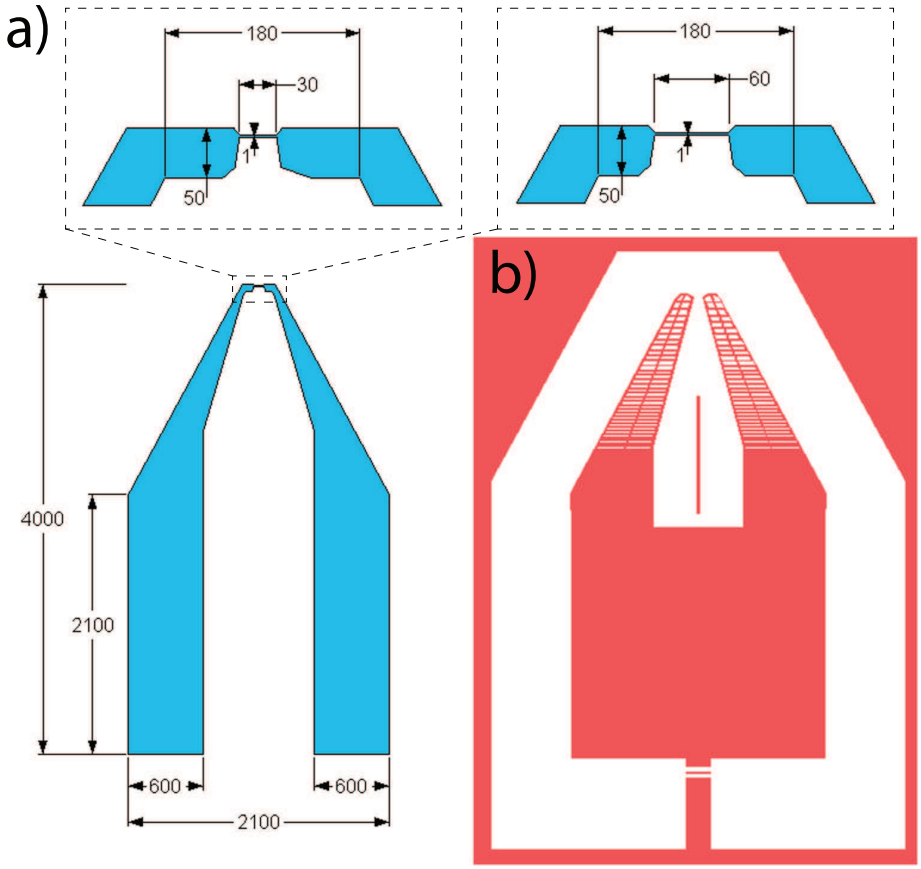

Figure 2.4: Photo-lithography mask patterns. a) Mask 1: Metal pattern for the standard 60 μm and 30 μm NSTAP, with a zoomed view of the front end. b) Mask 2: Mask design for the DRIE process. All dimensions are in μm.

However, RIE lag can be used constructively to achieve a 3D structure if the mask is designed accordingly. Here we use this RIE lag effect to construct an aerodynamically shaped support structure for NSTAP. The process flow is illustrated in Figure 2.5. First, regular optical lithography is used to define the pattern with varying size openings (Mask 2, Figure 2.5(a)). The sample is then etched using the anisotropic Bosch process, resulting in trenches of varying depth due to RIE lag (Figure 2.5(b)). Once the approximate desired depth is achieved, an isotropic plasma etch is used to remove the sidewalls between the trenches (Figure 2.5(c)). As a final step, more Bosch etching is performed to achieve the desired depth and to smooth out the steps between different height surfaces. The sample has now been formed into a three-dimensional structure defined by a two-dimensional mask (Figure 2.5(d)). Similar fabrication technique has been suggested by some authors [Chou and Najafi, 2002, Rao et al., 2004, Xiong et al., 2010], each having a slightly different approach based on the application.

To integrate this RIE lag etching into NSTAP fabrication, a customized mask is required. For the current application, a very deep etching is needed, as we also intend to cut individual sensors out of the 500 μm silicon substrate using DRIE while shaping the support structure using the same process. The variation of depth with trench size was determined experimentally, as shown in Figure 2.6, and a curve fit to the data was used for the mask design process. This simple power law fit, together with some iterative testing, produced a complex optical mask design (Mask 2), with a single pattern shown in Figure 2.4(b). The mask consists of several important elements. First, the gradual increase in width of the openings in the region where the sensor support was sloped. Next, in order to support the walls between the etched trenches, some bounding and extra supporting walls are added. Also, the area between the two protruding prongs is designed to be open to decrease blockage effects in the flow. Finally, a wide opening is left around the whole structure, which permitted the individual sensors to be cut out of the wafer.

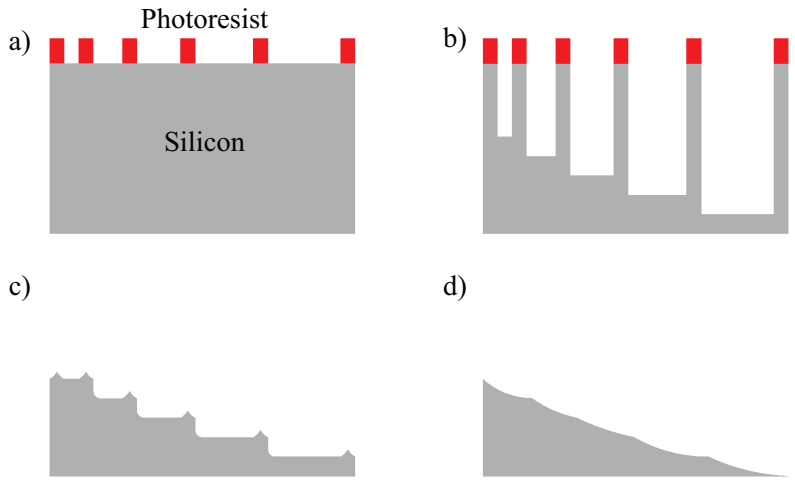

Figure 2.5: Slope formation using DRIE together with RIE lag. a) Mask design and photo-lithography; b) anisotropic etch, defining the surface; c) isotropic etch, sidewall removal d) anisotropic etch, smoothing the surface.

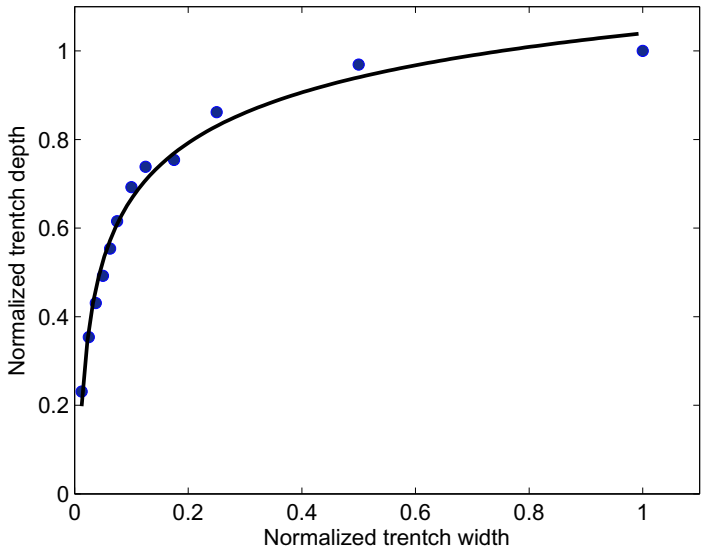

Figure 2.6: DRIE etch lag for high aspect ratio trenches: etch depth dependance on the mask opening width.

The process flow for 3D shaping is shown in Figure 2.3(g-i). The wafer fabricated in Stage I is first vapor primed by covering the surface with a monolayer of HMDS for promoting adhesion. The back side of the wafer (without metal) is then covered with a 4000 nm thick layer of AZ4330 photoresist followed by a soft bake at 110°C (Figure 2.3(g)). The wafer with the metal pattern is aligned with Mask 2 in Karl Suss MJB4 mask aligner system using infrared light for back side alignment, and then exposed in hard contact. The exposed substrate is developed for one minute, followed by one minute hard bake at 95°C (Figure 2.3(h)). Next, the sample is etched in a SAMCO RIE800iPB system using the described DRIE lag process. First, a 200 cycle Bosch process is used to etch through about half the full wafer thickness. Then the sample is mounted with high vacuum grease onto a carrier wafer. This carrier will allow us to etch through the full wafer, leaving all individual sensors on the carrier without damaging the chuck in the chamber. The remains of the photoresist are then removed with an oxygen clean to avoid overheating due to decreased thermal contact between the chuck and the substrate. Next, two series of 150 cycle Bosch processes are performed, with a relatively short 3 minute isotropic etch in between. Because the cooling of the substrate is extremely important to avoid surface impurities during the etching and provide smooth surface, a 20 second cooling step is added to each Bosch cycle. Finally, when all silicon has been etched from the wide open areas, the etch is automatically stopped on the oxide layer underneath the silicon. Individual sensors with the desired aerodynamic form can then be picked off the carrier (Figure 2.3(i)). The complete 3D shape of a fully fabricated sensor can be seen in the environmental scanning electron microscope (ESEM) images presented in Figure 2.7. The conductive platinum layer and the sensing element is shown in views B, E and F, while the sloped silicon surface can be clearly seen from the bottom views C and D. The zoomed-in views D and E show the diminishing thickness and smooth shape of the front end of the sensor, as well as a slightly more gradual thickness change in the back part.

2.3.3 Stage III: Probe release

For the support of the fragile metal sensor filament, in Stage II a thin silicon layer is left underneath the wire (Figure 2.3(i)). This silicon needs to be removed carefully from every sensor individually. First the sensor is fixed to a glass slide using some crystal-bond mounting adhesive, with metal side facing the glass. The glass slides with sensors can then be inserted into a RIE chamber for a short isotropic SF_6 dry etch, until the bridge of silicon is removed from underneath the wire. The sensors are then released from slides using acetone, and at this point only the silicon oxide layer is left as a support for the platinum wire (Figure 2.3(j)).

The design of the NSTAP sensors accommodates simple integration into regular hot-wire anemometry systems. For example, the prongs of conventional hot-wire probes can be used to connect the NSTAP to standard hot-wire anemometer electronics. The prongs are simply soldered onto the NSTAP under an inspection microscope, securing electrical and mechanical contact with a minimum amount of solder, as shown in Figure 2.7(A). This soldering step must be performed while the filament still has support from the SiO_2 layer, otherwise the mechanical stress and vibration during the soldering process can fracture the freestanding sensor element.

After NSTAP has been soldered onto prongs, a final short etch in buffered oxide etch (BOE) is performed, which removes the oxide layer as well as the thin layer of titanium from beneath the wire (Figure 2.3k). This final etch is followed by a deionized water rinse, immediately followed by an acetone soak. It is crucial to avoid the surface tension forces damaging the wire, and therefore BOE with surfactant must be used and the liquids cannot be allowed to dry between any of the steps. Due to the low surface tension of acetone, NSTAP with freestanding filament can be removed from the acetone and dried without damaging the wire. At this point, a functioning NSTAP sensor with a freestanding 60 or 30 $\times$ 1 $\times$ 0.1 μm platinum sensor filament, shown in Figure 2.7F, has been fabricated, mounted to conventional hot-wire prongs,

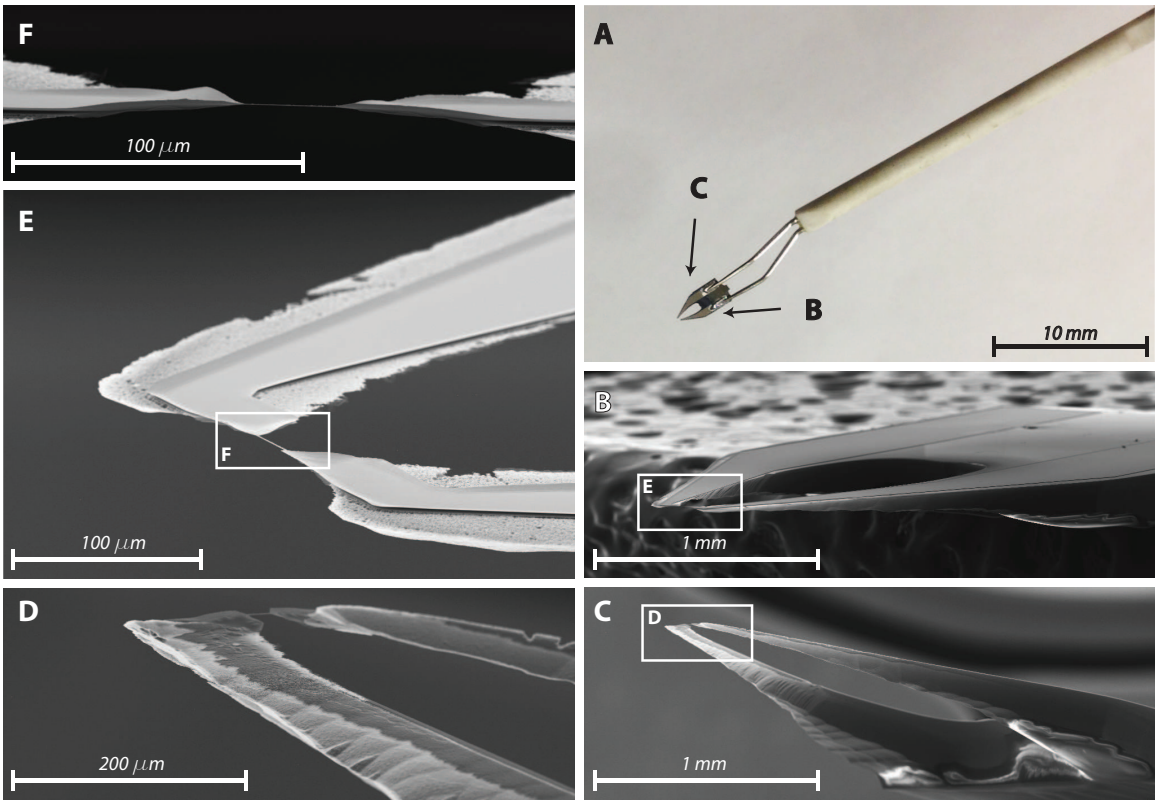

Figure 2.7: A photo and Environmental Scanning Electron Microscope images of a 30 μm NSTAP. A) Probe mounted onto prongs (photo). B) Full sensor from above; C) Full sensor from below; D) Close view of the sensor from below; E) Close view of the sensor from above; F) Zoom-in on the freestanding wire.

and is ready for characterization and testing. Once well calibrated and established, the full fabrication process can take from about two weeks to a month resulting a batch of about 100 sensors.

2.4 Characterization

2.4.1 Sensor resistance

The fabrication methods described above allow for considerable flexibility in the design of the sensors. The dimensions of the sensor filament can be easily changed by changing the design of one mask or by varying the metal layer thickness. Many sensors

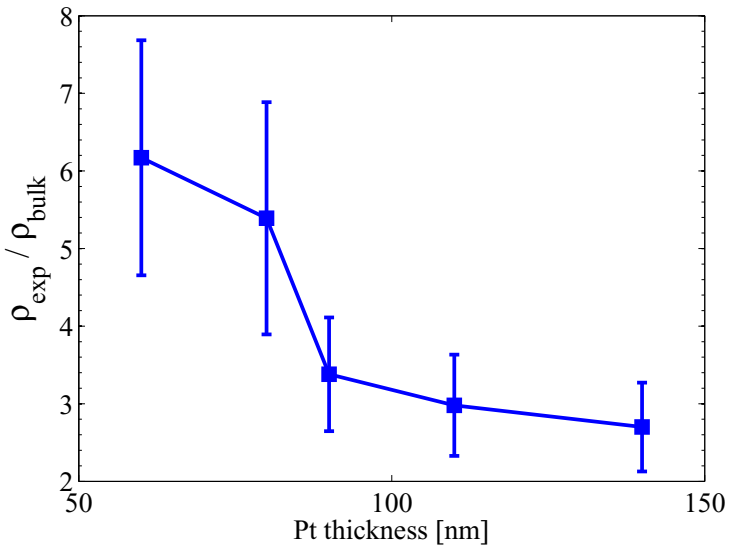

Figure 2.8: Measured resistivity over bulk resistivity for different platinum film thicknesses.

with lengths 60 and 30 μm and 100 nm thickness have been studied extensively and used here for characterization. Additionally sensors with thicknesses ranging from 50 to 140 nm were also made and investigated, as well as sensors with sensor lengths of 90, 120 and 150 μm.

The resistance of the sensor is one of the most important parameters in the operation of the probe, because it determines the operating conditions in the electrical circuit and the response of the sensor. Therefore it is crucial to know the value accurately and be able to predict it to some reasonable extent when designing new sensors. As the metal thickness gets smaller, the resistivity of a thin film, ρ_{exp}, begins to deviate from the bulk resistivity, which for platinum is $\rho_{bulk} = 1.06 \times 10^{-7}$ Ω·m. The resistivity of platinum wires of different thicknesses was determined by measuring the total resistance R_0, subtracting the resistance of the supports R_S, and using the relation $\rho = (R_0 - R_S)\frac{A}{\ell}$ where A is the cross-sectional area and ℓ the sensor length. The results are shown in Figure 2.8, with accompanying error estimates (based on statistical error together with approximately 20% uncertainty in ρ/ρ_{bulk}).

It can be seen that the resistivity increases with decreasing thickness, as expected, as the effects of varying grain size, deposition method and metal quality start playing an increasingly more important role. The resistances of fabricated sensors will always have some variation, due to slight non-uniformity in thicknesses and widths across the wafer. In the fabrication process described here, the thickness of the metal layer varied up to about 20%, and the sensor width varied about 25% across the wafer.

The total resistance of a typical 60 μm sensor was around 150 Ω, and about 220 Ω for a 30 μm sensor. The thermal coefficient of resistance, χ, was measured in still air in constant current mode and was found to be 0.0016 K^{-1}. During the operation of the NSTAPs, the temperature overheat α was kept between 0.5 and 0.75, resulting in heating the filament up to about 450-510 K. Here $\alpha = (T - T_0)/T_0$, where T is the operating temperature of the filament and T_0 is the temperature of the ambient fluid. It was found that at higher temperature overheat $\alpha > 0.8$ (resulting in the operating temperature above 540 K), the platinum filament resistance started to drift over time due to the overheating and probe damage was also observed. Therefore all sensors were kept below 510 K and in that case no change in resistance was noted during operation. A half hour annealing in the flow was still done before operating the sensor for the first time, to assure a constant resistance; the change in resistance, if any, was always below 1% and occurred within the first 5 minutes of operation. Throughout numerous experiments the resistance remained constant, even if the sensor was used for many months, and failure of sensors was usually caused by poor handling or dust particles hitting the sensor in the flow.

2.4.2 Temporal response

By manufacturing very small sensors such as NSTAP, we can alleviate the problem of spatial resolution in measurements of turbulence. We also need to achieve adequate frequency response. In our applications, hot-wire probes and NSTAPs are

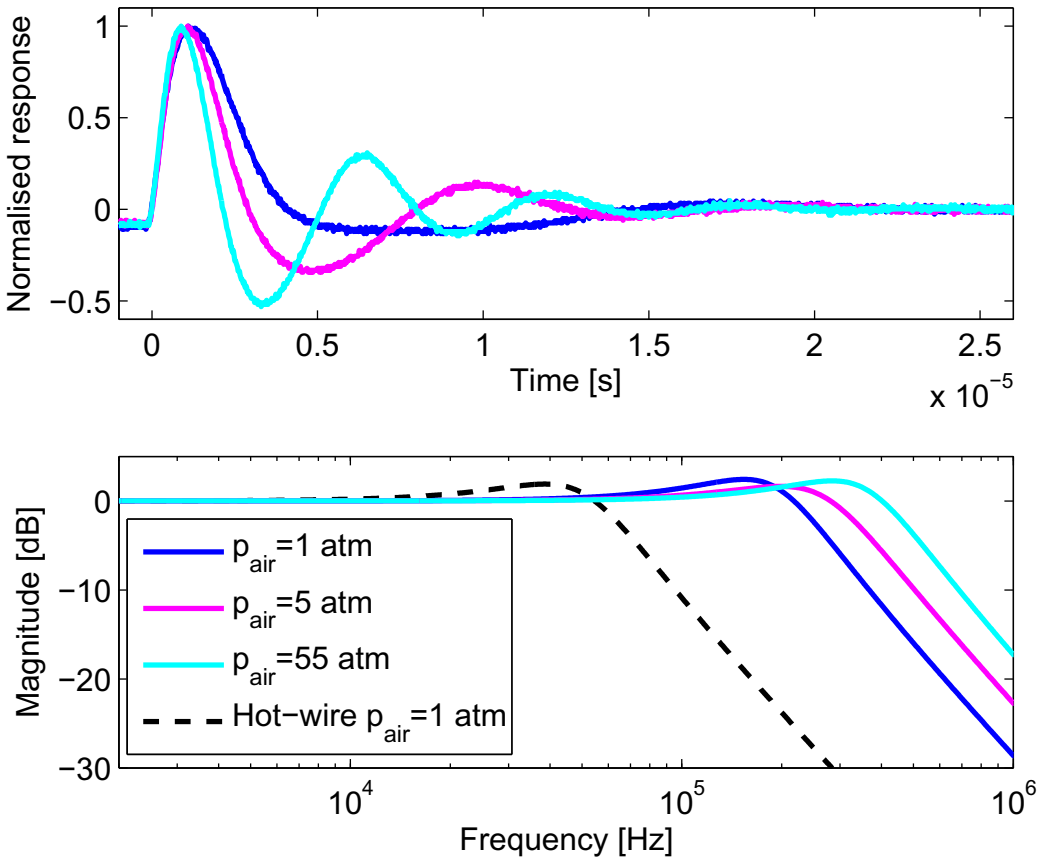

Figure 2.9: Temporal response of the NSTAP at different ambient air pressures. a) Square-wave response; b) attenuation in signal with frequency (Bode diagram), where 0 dB indicates unity gain.

powered by the same anemometer system, a Dantec Streamware Constant Temperature Anemometer, which provides a very low noise to signal ratio (much less than $\mathcal{O}(10^{-3})$). The response of the system can be described approximately as a second order system with a cut-off frequency f_c and a damping factor ξ [Perry and Morrison, 1971], and an optimal response in terms of a flat frequency response occurs with $\xi \approx 0.4$.

To determine f_c and ξ, a square wave input to the system can be used, and a typical response of a 60 μm NSTAP is shown as a blue curve in Figure 2.9(a), with frequency response of 195 kHz. The cut-off frequency can be estimated as $f_c = 1/1.3\tau_w$, where

τ_w is the time during which the signal has first decayed to 3% of its maximum value, and the damping factor ξ can be found by comparing to a theoretical response from a second order system. NSTAPs are especially useful for measurements in very high Reynolds number facilities, such as those at Princeton where high Reynolds numbers are achieved using compressed air [Jiménez et al., 2010, Zagarola and Smits, 1998]. Therefore the frequency response of an NSTAP at three different ambient air pressures $p_{air} = [1; 5; 55]$ was investigated at a flow velocity $U = 10$ m/s and at temperature overheat of 0.73. We found that with increasing pressure, the frequency response estimated from impulse response increased from f_c =195, to 275, to 360 kHz, and the corresponding damping factors become ξ =0.55, 0.31, and 0.21. Hence the system becomes less stable at higher pressures (due to higher heat transfer rates at higher pressures) while the frequency response is increasing. It must be noted that the true response could be significantly lower for NSTAP as well as conventional wires, based on recent study by N. Hutchins (private communication), being as low as 40 kHz for NSTAP at 5 atm pressures. But even this much lower response would result in well-resolved data, only loosing $< 0.5\%$ of the energy in the flow (assuming the response to be 40 kHz at 5 atm and 10 m/s). Using f_c and ξ, the gain function for velocity fluctuations (the Bode diagram) can be estimated (assuming a second-order system), as shown in Figure 2.9(b). For comparison, a typical conventional hot-wire response at U =10 m/s is also shown, with $f_c = 50$ kHz and $\xi = 0.45$, as taken from the study by Ashok et al. [2012]. The NSTAP clearly captures a wider range of frequencies and this range is even more expanded at higher pressures.

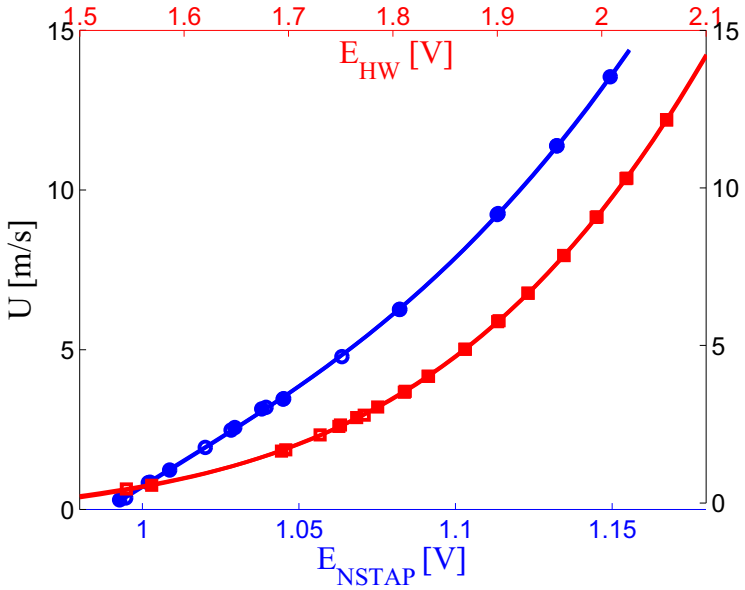

Figure 2.10: NSTAP and hot-wire calibration. Open symbols: pre-calibration, filled symbols: post-calibration.

2.5 Testing and validation

2.5.1 Calibration

The gain of the system (that is, its sensitivity) is found by performing a calibration. The NSTAP can be operated using a standard anemometer system, here a Dantec CTA with 1:1 bridge and an external resistor. To calibrate the system, the sensor is inserted into a flow of known velocity, and the output voltage is recorded over the velocity range that will be encountered in the actual experiment. To help determine the sensitivity (the slope of the voltage–velocity relationship, $\mathrm{d}E/\,\mathrm{d}U$), a fourth-order polynomial was fitted to the data (further details of the procedure can be found in Vallikivi et al. [2011]). Calibrations are performed before and after each experiment to monitor any possible drift in sensitivity, and temperature correction proposed by Hultmark and Smits [2010] was used to correct for the temperature changes in the flow (correction being usually below 0.2°C).

Two calibration curves obtained using a typical 60 μm NSTAP are shown in

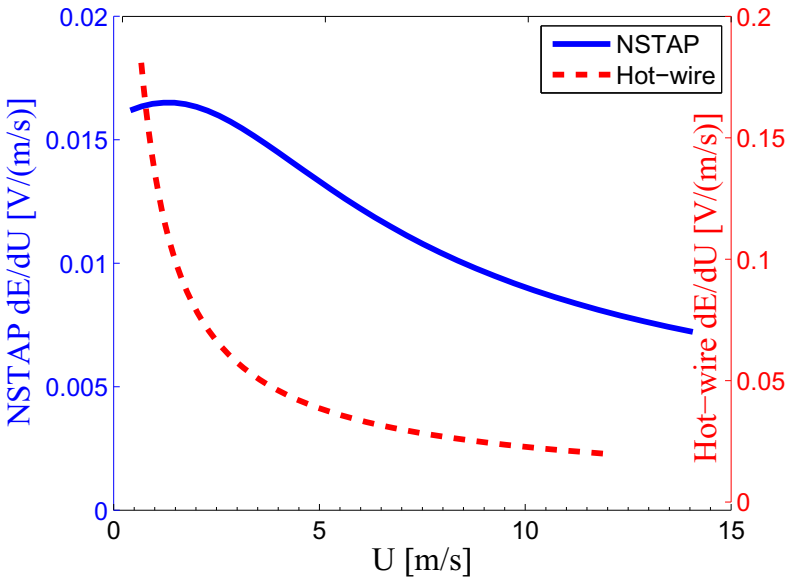

Figure 2.11: NSTAP and hot-wire sensitivity (dE/dU). Open symbols: pre-calibration, filled symbols: post-calibration.

Figure 2.10, together with a similar calibration obtained for a conventional hot-wire probe (platinum-10% rhodium Wollaston wire with diameter 2.5 μm and length 0.5 mm). The voltage output for the NSTAP is smaller than that of the hot-wire because of the smaller size of the sensor, but both sensors follow a very similar curve well described by the polynomial fit. The agreement between the pre- and post-calibration is excellent for both sensors (below 0.2% for $U > 2$ m/s), indicating almost negligible changes in the cold resistance of the sensor, which we have found to be typical for NSTAPs.

Conventional hot-wires are known to be very accurate method for low-velocity measurements, due to the increasing sensitivity at lower velocities, as can be seen from Figure 2.11. The NSTAP shows a similar behavior, however, at very low velocities the sensitivity flattens out. This is due to the miniature size of the sensor, as for low velocities the heat transfer is dominated by natural convection instead of forced convection (a similar behavior was noted by Ligrani and Bradshaw [1987b] while using miniature hot-wires).

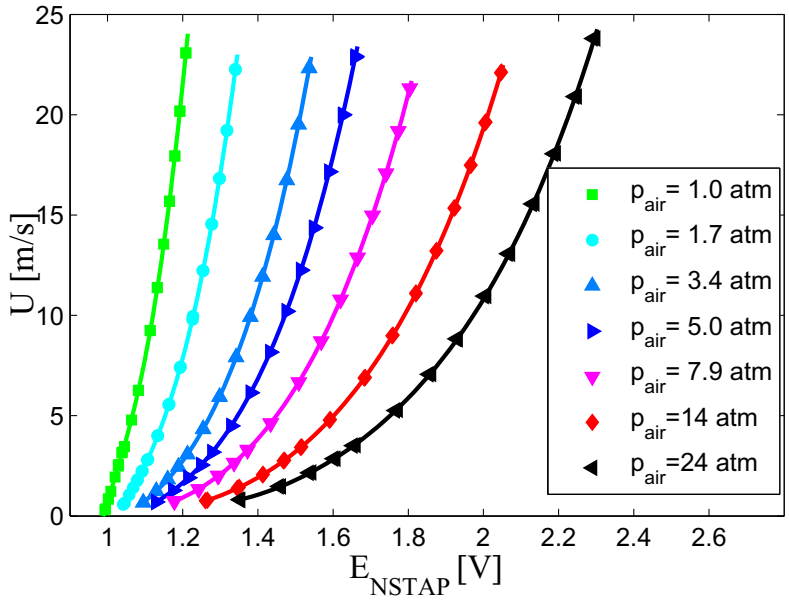

Figure 2.12: Calibration curves of NSTAP (60 μm) operation at different ambient air pressures p_{air}.

Figure 2.12 shows how the calibration of a 60 μm NSTAP changes with ambient pressure p_{air}. As the pressure increases, the output voltage increases, making the signal less noisy, and due to the higher density of the ambient air the performance of the sensors at low velocities is improved. Experiments have also been conducted with NSTAPs in a different facility at Max Plank Institute of Dynamics and Self-Organization, where pressurized SF_6 is used as the ambient fluid [Bewley et al., 2014], and the NSTAPs have been shown to operate equally well under those conditions. Some example calibration curves in SF_6 at different pressures p_{SF_6} are shown in Figure 2.13. Even though the range of velocities covered in these calibrations is smaller than for the calibrations in air, it is evident that the NSTAP behaves well and could be used for velocity measurements in SF_6.

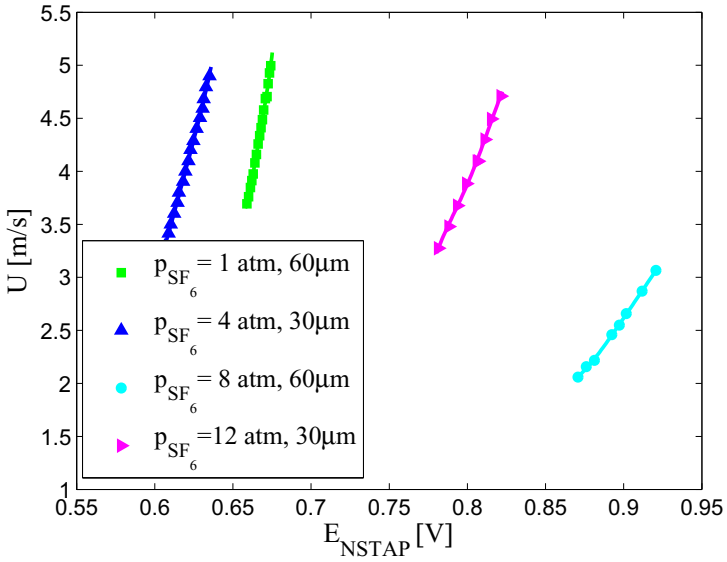

Figure 2.13: Calibration curves for two NSTAPs (30 and 60 μm length) in SF_6 at different pressures p_{SF_6}.

2.5.2 Pitch and yaw sensitivity

To evaluate the performance of the NSTAP further, the response to a change in flow angle was studied, namely the dependence on pitch angle θ and yaw angle ψ. Pitch is defined as rotation around y-axis and yaw around z-axis according to the coordinate system shown in Figure 2.2.

Hot-wire sensors are usually considered to be relatively insensitive to pitch angle changes, as long as the angles are small enough Bruun [1995]. One would expect to see a similar trend for an NSTAP if the response of the sensor is not affected by aerodynamic interference caused by the supporting silicon structure. Additionally, the NSTAP sensor filament is a ribbon with a high aspect ratio, rather than a circular sensor as used in a hot-wire probe. The comparisons between probes are shown in Figure 2.14, where the "effective" velocity U_e (the velocity as indicated by the sensor) has been normalized by the mean velocity U_m measured at $\theta = 0°$, that is, the "true" velocity. For large pitch angles, the effects of pitch on the NSTAP response is significant, having an error up to 5%. It must be noted that for many applications,

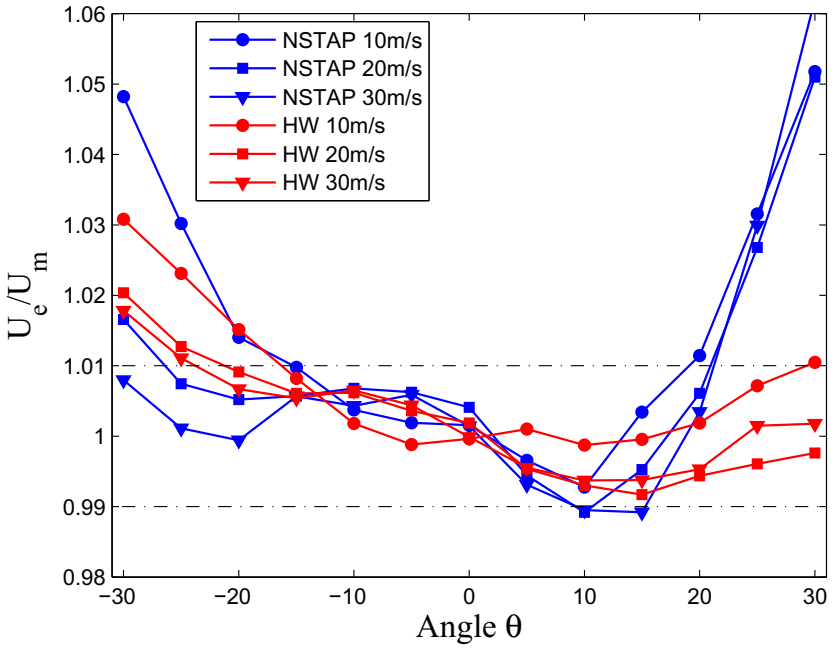

Figure 2.14: Pitch angle dependence of an NSTAP and a hot-wire probe (HW).

this angle is usually much smaller. If only pitch angles in the range $\theta = \pm 10°$ are considered, the hot-wire probe and NSTAP show a very similar response, both having deviations well below 1%.

The hot-wire response to yaw angle changes is often assumed to follow a simple cosine cooling law, where the effective velocity is given by $U_e = U_m \cos\psi$ and ψ is the yaw angle [Bradshaw, 1971, Bruun, 1995]. The response of the NSTAP is compared to that of a typical hot-wire probe in Figure 2.15 and both probes follow the cosine law closely. To illustrate the cosine behavior better, the same data are plotted against $\cos\psi$ in Figure 2.15(b). For small angles both sensors agree well with each other, as well as with the expected response. For large angles, the NSTAP deviates somewhat from the $\cos\psi$ line, which is reasonable considering that the supporting structure will start to protrude ahead of the sensor. Again, for most applications, angles larger than 10° are rarely encountered, and for $-10° < \psi < 10°$ the deviation for both sensors from the cosine cooling law is less than 1%.

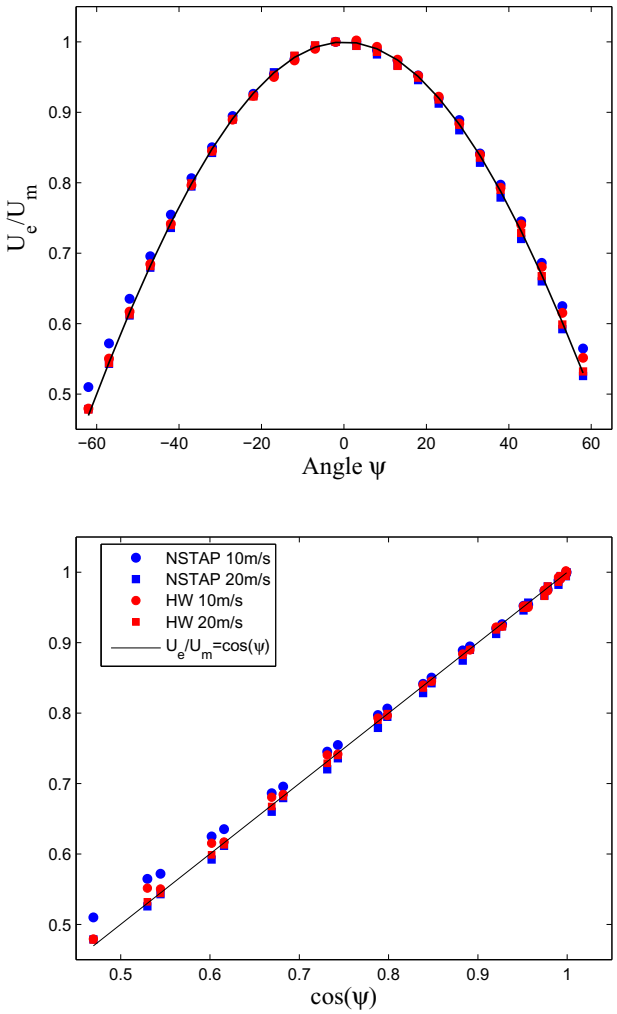

Figure 2.15: Yaw angle dependence of an NSTAP and a hot-wire probe (HW). Top - dependence on ψ; Bottom - dependence on $\cos\psi$. The cosine cooling law is shown as the solid line.

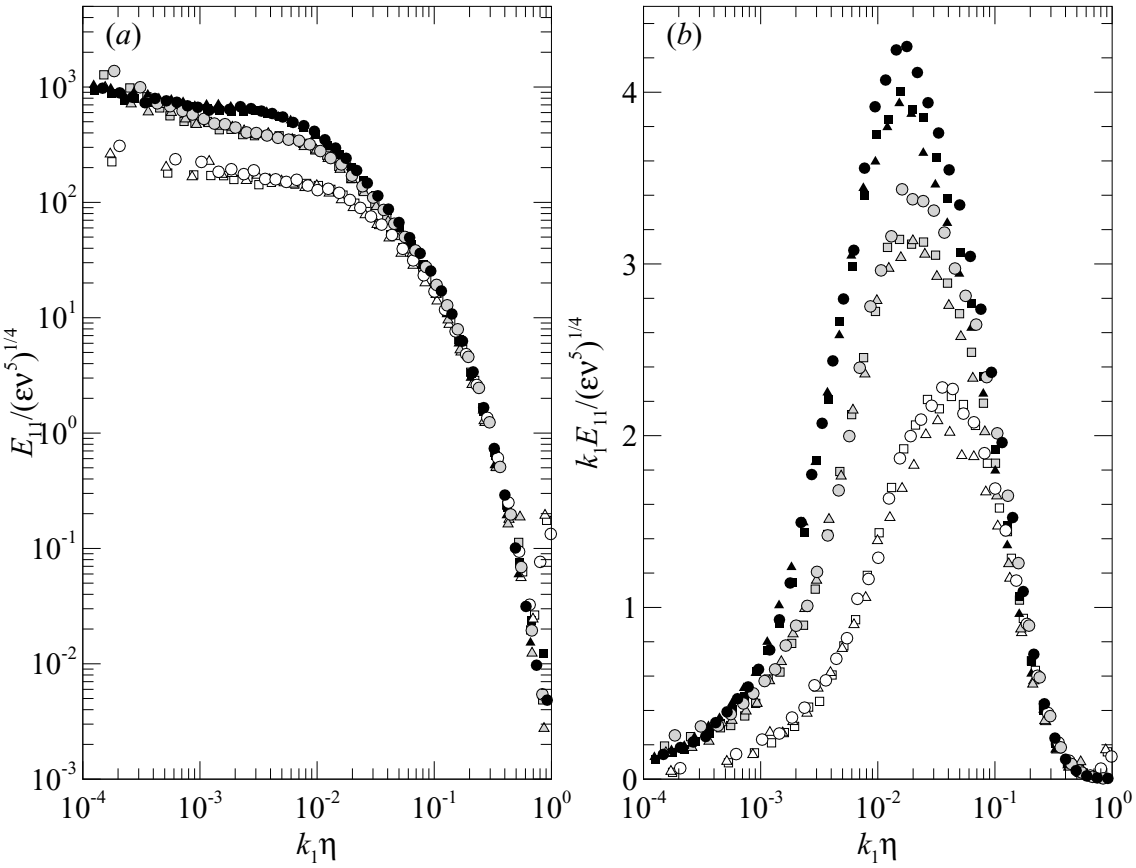

Figure 2.16: Measured streamwise wavenumber spectra in grid turbulence normalized by the Kolmogorov scales in (a) standard and (b) pre-multiplied form. Results for ◯, 60 μm NSTAP; □, 0.5 mm probe; and △, 1.5 mm probe are shown for $U_\infty = 10$ m/s (hollow symbols), $U_\infty = 20$ m/s (gray symbols) and $U_\infty = 30$ m/s (filled symbols) shown.

2.5.3 Turbulence measurements

Grid turbulence

The first turbulence measurements with NSTAPs were performed by Bailey et al. [2010], who used the original design, shown in Figure 2.1(D). Measurements were performed in grid-generated turbulence and compared to conventional hot-wire probes with a range of sensor lengths. The results showed a good agreement between all the probes.

The wavenumber spectra $\Phi_{uu}(k_1)$ are shown in Figure 2.16, where the streamwise wavenumber is taken as $k_1 = 2\pi f / \langle U_1 \rangle$ and f is the frequency. Figure 2.16(a) illustrates that the NSTAP provides virtually the same overall response as the conventional probes, even at low wavenumbers where end conduction effects would be expected to be important. However, the wavenumber distribution of turbulent kinetic energy is better illustrated by plotting the power spectra in pre-multiplied form as in Figure 2.16(b). When viewed in this form, the reduced spectral response of the larger probes becomes much more readily apparent. At low velocity the 0.06 mm NSTAP and 0.5 mm hot wire probe are in excellent agreement and both measure an energy level that is slightly higher than that of the 1.5 mm probe. In grid turbulence, the relevant length scale for spatial filtering effects can be argued to be the Kolmogorov length scale $\eta_K = \left(\frac{\nu^3}{\varepsilon}\right)^{1/4}$, where ε is the average rate of dissipation of turbulent kinetic energy. As velocity increases, the Kolmogorov length scale decreases, ℓ/η_K increases, and we see that the energy measured by even the 0.5 mm probe decrease relative to the NSTAP. This illustrates the importance of minimizing filtering effects in order to acquire reliable measurement results.

Pipe flow

Vallikivi et al. [2011] described an experiment in fully developed turbulent pipe flow, conducted in part to help validate NSTAP behavior in wall bounded turbulent flow. Measurements of the streamwise component of velocity were performed using 60μm NSTAP and compared with the data obtained using a conventional hot wire probe with $\ell_w = 0.4$ mm and diameter of 2.5μm.

Mean flow as well as turbulent fluctuations were shown to have a very good agreement between the different sensors. Figure 2.17(a) shows distributions of the streamwise variance $u^{+2} = \overline{u^2}/u_\tau^2$. It can be seen that in the outer flow for all three Reynolds numbers the NSTAP data agree remarkably well with the hot-wire data, and an inner

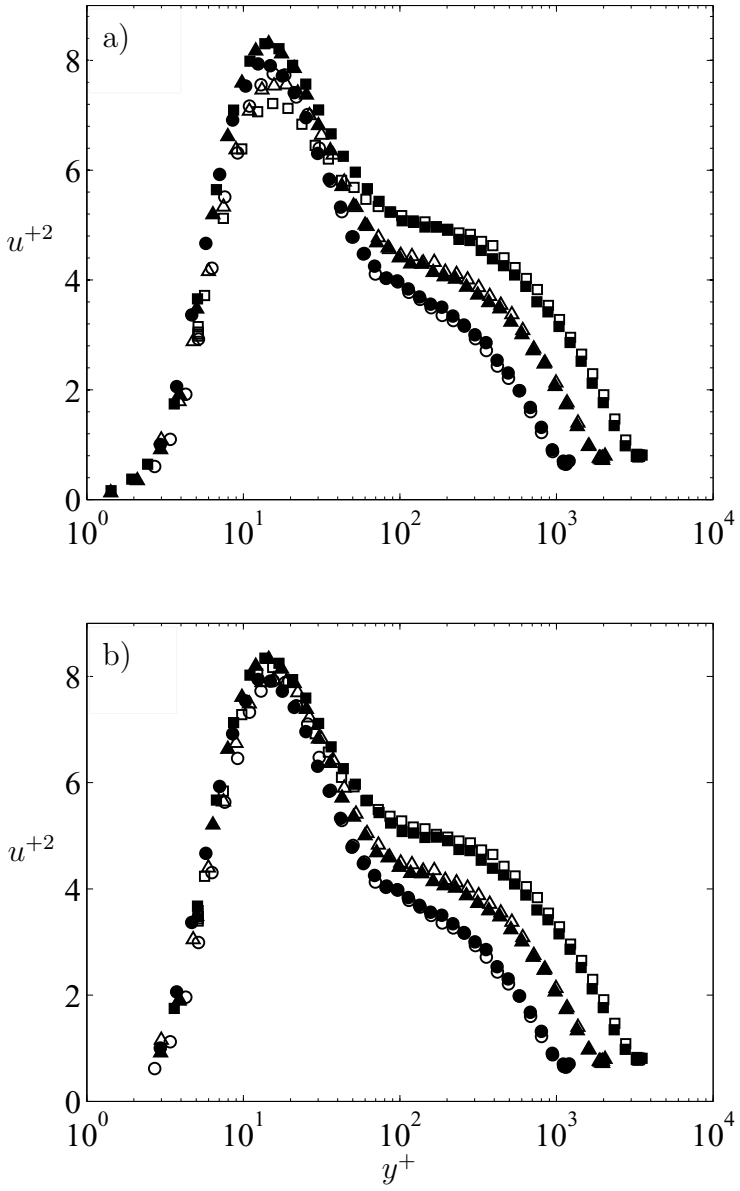

Figure 2.17: Streamwise turbulence intensity profiles in turbulent pipe flow a) uncorrected and b) corrected for spatial filtering; measured with NSTAP (filled symbols) and conventional hot-wire (hollow symbols) at ○, $Re_D = 45000$; △, $Re_D = 80000$; □, $Re_D = 150000$.

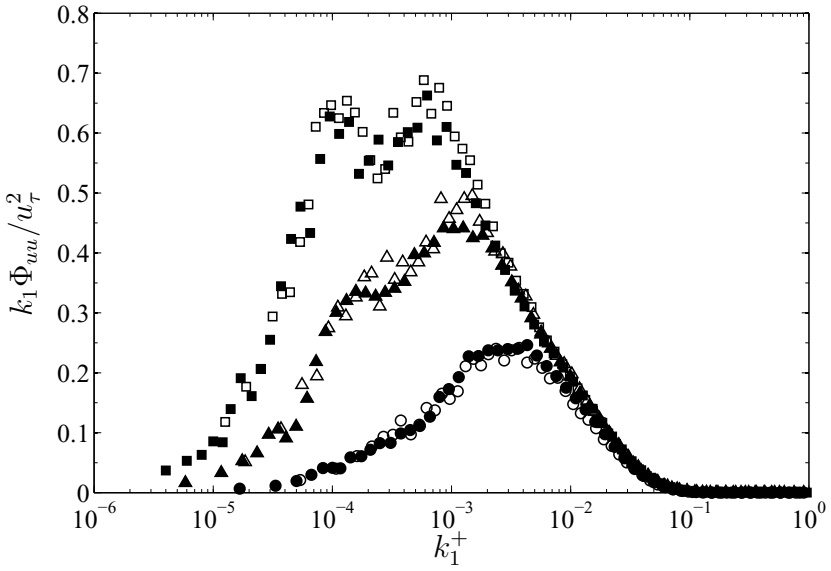

Figure 2.18: Pre-multiplied energy spectra of the streamwise velocity signal in pipe flow in outer region at $y^+ = 1000$; measured with NSTAP (filled symbols) and conventional hot-wire (hollow symbols) at ○, $Re_D = 45000$; △, $Re_D = 80000$; □, $Re_D = 150000$.

peak in intensity at $y^+ \approx 15$ is seen in each profile. However, discrepancies due to spatial filtering are observed in the near wall region, increasing with Reynolds number, that is, for $y^+ < 15$ at $Re_D = 45,000$, $y^+ < 25$ at $Re_D = 80,000$ and $y^+ < 50$ at $Re_D = 150,000$. For the NSTAPs, $1.0 \leq \ell^+ \leq 3.1$, and the profiles agree in every respect at each Reynolds number (as can be seen in Figure 2.17(a)), demonstrating that no significant spatial filtering effects are present. However, for the hot-wire data, $7 \leq l_w^+ \leq 20.6$, and some filtering is evident even at the lowest Reynolds number in the region $y^+ < 15$.

To account for the effects of spatial filtering, the correction function proposed by Smits et al. [2011b] was used (described in Chapter 1.3.1. In Figure 2.17(a) the turbulence intensity distributions are shown without this correction, and in Figure 2.17(b) they are shown with this correction applied. The corrected hot wire and NSTAP data collapse onto a single curve for each Reynolds number, even in near-wall region where spatial filtering effects were significant prior to correction. As the correction method

proposed by Smits et al. [2011b] has been validated at similar Reynolds numbers, the collapse of the profiles shows the correct behavior of the sensors.

The frequency spectra Φ_{uu} were also studied for both NSTAP and conventional hot wire probes, with local mean velocity as the convection velocity. In Figure 2.18 the premultiplied one-dimensional streamwise energy spectra $\Phi_{uu}k_1$ are shown for $y^+ = 1000$, where the spatial filtering effects are small and the hot-wire and NSTAP show excellent agreement.

2.6 End-conduction effects

In order to finish the evaluation of the NSTAP performance, the end-conduction effects need to also be taken into account. Chapter 1.3.2 discussed the importance of end-conduction effects on the sensor, introducing an empirical criterion $\ell/d > 200$ for avoiding such effects for conventional hot-wires. Recently a more rigorous analysis was done by Hultmark et al. [2011], who demonstrated that end-conduction effects of a regular hot-wire reduce with Reynolds number such that the sensing length of a hot-wire probe can be halved with a 15-fold increase in the Reynolds number based on the sensor width. Hultmark et al. [2011] defined a new non-dimensional end-conduction parameter Γ and show that a for conventional hot-wires, $\Gamma > 14$ is necessary to avoid any attenuation in the turbulent fluctuations.

This criterion was derived for a circular cross-section hot-wire filament, but in the case of NSTAP the filament is more like a ribbon, with a rectangular cross-section. Therefore the parameter characterizing end-conduction effects needs to be re-defined to allow for arbitrary cross-sections, and we call this new parameter Λ.

2.6.1 Theoretical Analysis

We derive a new end-conduction criterion following Betchov [1948] and Hultmark et al. [2011]. The temperature distribution in a hot-wire for steady state can be expressed as

$$\textit{Resistive heating} = \textit{Heat convection to the ambient} + \textit{Heat conduction to prongs}, \tag{2.6.1}$$

$$r(x)I^2 = P_s h\left(T(x) - T_0\right) + \frac{\mathrm{d}q(x)}{\mathrm{d}x}, \tag{2.6.2}$$

where

$$q(x) = -k_w A_c \frac{\mathrm{d}T(x)}{\mathrm{d}x}. \tag{2.6.3}$$

Here, x is the coordinate along the sensor measured from the center of the sensor, $r(x)$ is the resistance per unit length at the sensor temperature $T(x)$, I is the current through the sensor, T_0 is the ambient temperature, P_s is the perimeter of the cross-section, A_c is the area of the cross-section, k_w is the thermal conductivity of the sensor and h is the convective heat transfer coefficient.

Using the relationship

$$r(x) = r_0\left[1 + \chi\left(T(x) - T_0\right)\right], \tag{2.6.4}$$

where χ is the thermal coefficient of resistance of the sensor material and r_0 is resistance per unit length at ambient temperature, Equation 2.6.2 can be rewritten as a differential equation

$$r(x)I^2 = \frac{P_s h}{\chi r_0}(r - r_0) - \frac{k_w A_c}{\chi r_0}\frac{\mathrm{d}^2 r(x)}{\mathrm{d}x^2}. \tag{2.6.5}$$

Using the boundary conditions $r'(0) = 0$ and $r(\ell/2) = r_0$ (assuming that stubs are

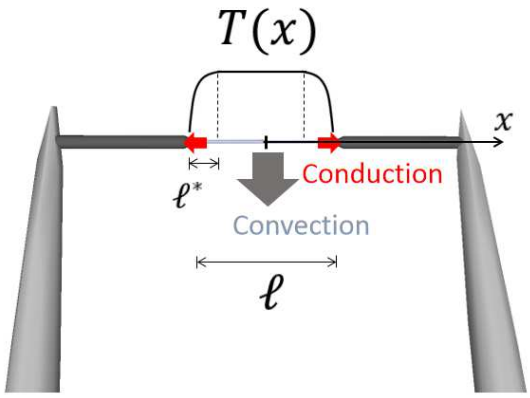

Figure 2.19: Sketch of a conventional hot-wire. $T(x)$ is the temperature distribution of the wire, ℓ the wire length and ℓ^* the cold length.

perfect heat sinks), we obtain

$$r(x) = \frac{r_0 A}{A - I^2}\left[1 - \frac{I^2}{A}\frac{\cosh\frac{x}{\ell^*}}{\cosh\frac{\ell/2}{\ell^*}}\right], \tag{2.6.6}$$

$$A = \frac{P_s h}{\chi r_0}, \tag{2.6.7}$$

$$\ell^* = \sqrt{\frac{k_w A_c}{\chi r_0 (A - I^2)}}. \tag{2.6.8}$$

that expresses the resistance distribution along the sensor filament. The parameter ℓ^* was introduced by Betchov [1948] as the "cold length," which denotes the length of the wire that is affected by end-conduction to the prongs, as shown in Figure 2.19. If this cold length is much smaller than the total wire length, the sensor could be considered free of end-conduction effects.

In order to estimate the severity of end-conduction effects for a sensor, we first estimate the heat transfer through conduction to be

$$q_{cond} = -k_w A_c \frac{\mathrm{d}T(x)}{\mathrm{d}x} = \frac{k_w A_c}{\chi r_0}\frac{\mathrm{d}r(x)}{\mathrm{d}x} \tag{2.6.9}$$

$$= \frac{k_w A_c r_0 I^2}{\ell^* \chi r_0 (A - I^2)}\left[\frac{\sinh\frac{x}{\ell^*}}{\cosh\frac{\ell/2}{\ell^*}}\right]. \tag{2.6.10}$$

Estimating this heat transfer at the stubs gives

$$q_{stub} = q_{cond}|_{x=\ell/2} = \frac{1}{\ell^*} \frac{k_w A_c r_0 I^2}{\chi r_0 (A - I^2)} \left[\tanh \frac{\ell/2}{\ell^*} \right]. \tag{2.6.11}$$

Assuming that the half length of the sensor $\ell/2 >> \ell^*$ (at least 3 times bigger), $\tanh \frac{\ell/2}{\ell^*} \approx 1$, and using the expression for the cold length, q_{stub} becomes

$$q_{stub} = \ell^* r_0 I^2. \tag{2.6.12}$$

The total heat transfer out of the filament is

$$q_{tot} = \overline{R} I^2 = \ell \gamma r_0 I^2, \tag{2.6.13}$$

where $\overline{R}$ is the total resistance of the filament, $r_0 \ell$ is total cold resistance, and $\gamma = \frac{\overline{R}}{r_0 \ell}$ is the resistance overheat ratio. Comparing the total heat flux to the heat lost to stubs, we can write

$$\frac{q_{tot}}{2q_{stub}} = \frac{\ell \gamma r_0 I^2}{2\ell^* r_0 I^2} = \frac{\ell \gamma}{2\ell^*} = \Lambda \tag{2.6.14}$$

where Λ is the desired non-dimensional parameter describing the end-conduction effects. It must be noted that the definition of Λ is slightly different from parameter Γ defined by Hultmark et al. [2011], differing by a factor 2, so that $\Lambda = \Gamma/2$. This difference comes from the fact that Hultmark et al. [2011] compared total heat flux to heat lost to one stub, but does not change any qualitative conclusions made by Hultmark et al. [2011], just changes the numerical value of the constant.

This new parameter Λ can now be rewritten, using the definition of the cold length, as

$$\Lambda = \frac{1}{2} \ell \gamma \sqrt{\frac{h P_s}{k_w \gamma A_c}}. \tag{2.6.15}$$

The convective heat transfer coefficient can be rewritten in terms of the Nusselt

number as $h = \mathrm{Nu}k_f/\ell_c$, where k_f is thermal conductivity of the ambient fluid and ℓ_c is a characteristic length in direction of a growing boundary layer. Expressing the surface area of the filament as $A_s = P_s\ell$, the general form of the non-dimensional coefficient becomes

$$\Lambda = \frac{1}{2}\sqrt{\frac{\ell}{\ell_c}\frac{A_s}{A_c}\frac{k_f}{k_w}\gamma\mathrm{Nu}}. \tag{2.6.16}$$

Circular sensor filament

From this general form of Λ any type of cross-section filaments can be analyzed. For a circular cross-section with diameter d and characteristic length $\ell_c = d$ this parameter becomes

$$\Lambda = \frac{\ell}{d}\sqrt{\frac{k_f}{k_w}\gamma\mathrm{Nu}}, \tag{2.6.17}$$

similar to expression for Γ introduced by Hultmark et al. [2011]. For this cylindrical filament case Nu can be estimated as $\mathrm{Nu} = (0.35 + 0.56Re_c^{0.52})Pr^{0.3}$, as shown in Fand [1965].

Rectangular sensor filament

For a rectangular cross-section, as for an NSTAP with $\ell_c = \ell_w$,

$$\Lambda = \frac{1}{2}\sqrt{\frac{\ell}{\ell_w}\frac{2(\ell_h + \ell_w)\ell}{\ell_h\ell_w}\frac{k_f}{k_w}\gamma\mathrm{Nu}} \approx \sqrt{\frac{1}{2}\frac{\ell^2}{\ell_w\ell_h}\frac{k_f}{k_w}\gamma\mathrm{Nu}}. \tag{2.6.18}$$

where ℓ_w and ℓ_h are respectively the width and the height of the filament, and $\ell_w >> \ell_h$ for the second approximation. For a plate type of geometry, the Nusselt number can be approximated as $\mathrm{Nu} = 0.664\mathrm{Pr}^{0.33}Re_c^{0.5}$ [Incropera et al., 2011].

2.6.2 Validation

The new end-conduction parameter Λ depends on the geometry of the sensor but also on many other parameters. Because the NSTAP is primarily designed to be used in

pressurized facilities, we will analyze the behavior of Λ for the NSTAP at different ambient pressures. Figure 2.20 shows that the value of Λ depends on the ambient air pressure, for a hot-wire as well as for a NSTAP with different geometry (with ℓ=30 or 60 μm, and ℓ_w = 1 or 2 μm). The figure demonstrates well the increase in Λ as the ambient pressure (and therefore the characteristic Reynolds number) increases. It also shows that for any NSTAP geometry used, the criteria of $\Lambda > 7$ is difficult to meet by only increasing the pressure.

The experiments described in Chapter 2.5.3 were all made using an NSTAP with dimensions $60 \times 2 \times 0.1\mu$m, which is shown as the blue dashed line in Figure 2.20. No evidence of end-conduction effects were observed for the measurements by Bailey et al. [2010] in grid turbulence nor by Vallikivi et al. [2011] in turbulent pipe flow, both measured in air at atmospheric conditions, with free stream velocities above 4 m/s. The hot wires used in these studies had $5 < \Lambda < 15$, and agreed well with each other, while for the NSTAP these conditions corresponded to $\Lambda > 1.7$. Though the NSTAP value was much lower than for the hot wires, an excellent agreement between probes was seen, suggesting that there were no significant end-conduction effects in either case. To be on the safe side, we choose $\Lambda > 2.5$ as our condition for avoiding end-conduction effects. This is much lower than $\Lambda > 7$ proposed by Hultmark et al. [2011], suggesting that the criteria on Λ may depend on the sensor geometry, or that the theoretical analysis might be oversimplified.

From Figure 2.20 it is clear that a 30 μm NSTAP, even with 1 μm width, will not satisfy $\Lambda > 7$ in any reasonable range of pressure. But if we use assume that for NSTAP $\Lambda > 2.5$ is sufficient, we can see that for a $30 \times 1 \times 0.1\mu$m sensor the criteria is fulfilled at 7 atm and for a $30 \times 2 \times 0.1\mu$m filament at 16 atm. To verify this proposal, in Figure 2.21 we compare two sets of data at the same flow conditions measured with 60 μm and 30 μm NSTAPs having a 2 μm width (marked as symbols in Figure 2.20). The agreement between two data sets for $y^+ > 100$ is very good and well within

experimental error. These data were taken in turbulent pipe flow (described in detail in Chapter 3) at $Re_D = 4.0 \times 10^6$ and at 46 atm pressure. The mean velocity on the sensor varied from 5 to 12 m/s for $y^+ > 100$ where the two sensors agree well. It must be noted that to avoid any confusion due to possible spatial filtering effects, the correction suggested by Smits et al. [2011b] and described in Chapter 1.3.1 was applied in Figure 2.21(b). The 60 μm sensor has $\Lambda > 7$, whereas the 30 μm sensor only has $\Lambda = 2.75$ at 10 m/s (and even lower at lower velocities). The results present a convincing argument that for an NSTAP sensor $\Lambda > 2.5$ is a sufficient criterion for avoiding end-conduction effects. This corresponds to $\ell/d = 85$ for a cylindrical wire, being surprisingly lower than reported minimum ℓ/d for hot-wire sensors, suggesting some other geometrical effects could be effecting the response. A study incorporating wider range of sensor geometries and flow conditions is needed to make any final conclusions.

2.7 Conclusion

We have described the design and fabrication process of a novel Nano-Scale Thermal Anemometry Probe (NSTAP), which can resolve velocity fluctuations down to 30μm with a frequency response that can exceed 300 kHz based on square wave response. The small size of NSTAP allows it to measure velocities very close to the wall, down to 15 μm. The complete fabrication process includes the formation of a three-dimensional silicon structure using deep reactive ion etching combined with the RIE lag effect. The 3D structure is shaped to reduce aerodynamic interference, but the particular technique demonstrated here can easily be adapted to form many other 3D silicon structures for other applications.

Many sensors with different dimensions have been fabricated and tested in various flows, and have been shown to have similar behavior as conventional hot-wire

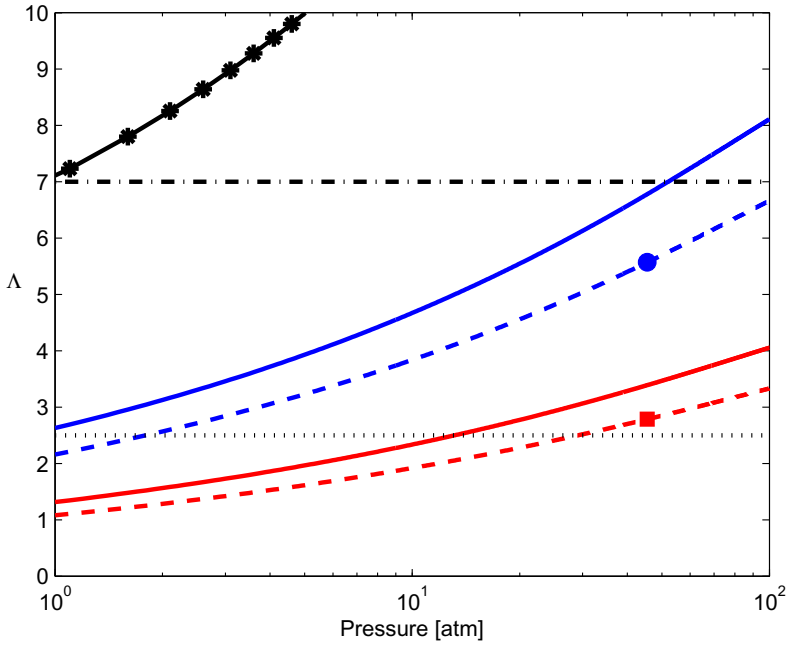

Figure 2.20: Parameter Λ dependance on ambient pressure and sensor geometrical parameters, at 10 m/s flow velocity. (*) - Hot-wire with $\ell/d = 200$; (blue) - NSTAP with ℓ=60 μm; (red) - NSTAP with ℓ=30 μm; (solid line) - NSTAP with $\ell_w = 1\mu$m ; (dashed line) - NSTAP with $\ell_w = 2\mu$m; $\circ$ and $\square$ - conditions of Figure 2.21; (dash-dot line) - $\Lambda = 7$; (dotted line) - $\Lambda = 2.5$

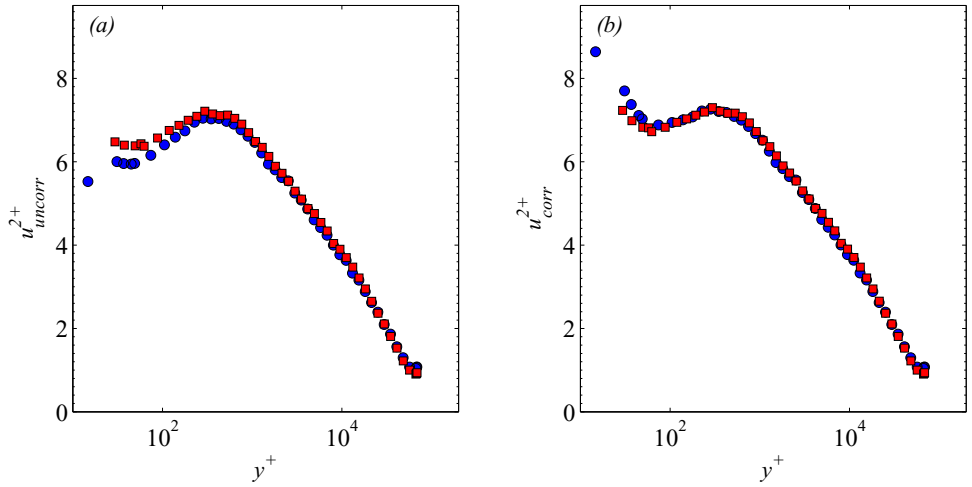

Figure 2.21: Comparison between 60 micron NSTAP ($\circ$) and 30 micron NSTAP ($\square$) in smooth-walled pipe flow at $p = 46$ atm and 10 m/s bulk velocity, (a) uncorrected and (b) following correction for spatial filtering effects.

anemometers. The NSTAP can be operated in different gases over a wide range of ambient pressures, with minimal drift and simple calibration techniques. In addition, the probes are relatively insensitive to small pitch angles ($\pm 10^{\circ}$), and over the same range of angles the sensitivity to yaw follows a cosine behavior, which follows the response observed for conventional hot-wires.

An expression was derived for a parameter $\Lambda = \frac{1}{2}\sqrt{\frac{\ell}{\ell_c}\frac{A_s}{A_c}\frac{k_f}{k_w}\gamma \mathrm{Nu}}$, characterizing the end-conduction effects for a filament with an arbitrary cross-section. The experimental validation showed that fulfilling a criteria of $\Lambda > 2.5$ is sufficient to avoid end-conduction effects for an NSTAP.

The NSTAP have been shown to give excellent agreement with conventional hot wire anemometers in isotropic homogeneous turbulence as well as in shear flows, in cases where no spatial and temporal filtering occurs. At the same time the sensors provide an improved spatial and temporal resolution compared to any other technique available. Therefore NSTAP appears to provide a powerful new tool for accurate turbulence measurements, where spatial and temporal resolution are vital.

Chapter 3

Turbulent pipe flow

3.1 Introduction

When the flow is hydraulically smooth such that the smallest eddy scales are much larger than the roughness elements, classical scaling arguments indicate that the flow scaling can be divided into two regions, an "inner region" and an "outer region" [Millikan, 1938, Perry and Abell, 1975], as described in Chapter 1. In the inner region, where viscosity is important, the characteristic velocity scale is the friction velocity u_τ and the characteristic length scale is the viscous length scale, $\eta = \nu/u_\tau$. In the outer region, where viscosity is not important, the characteristic velocity scale remains the friction velocity u_τ (at least at a sufficiently high Reynolds number, see Zagarola and Smits [1998]), but the characteristic length scale is now the shear layer thickness, which in a pipe is its radius R.

3.1.1 Mean flow

Classical scaling works very well for the mean velocity profile in fully-developed smooth pipe flow, as comprehensively demonstrated by Zagarola and Smits [1998] and McKeon et al. [2004a], among others [Marusic et al., 2010c, Smits et al., 2011a]. The

near-wall region follows a universal behavior when scaled using inner scaling. In particular, McKeon et al. [2004a] concluded that at sufficiently high Reynolds numbers there exists a viscous sublayer for $y^+ \leq 5$, where the inner-scaled velocity $U^+ = U/u_\tau$ varies linearly with y^+, a buffer region for $5 \leq y^+ \leq 50$, and a power-law-like region for $50 \leq y^+ \leq 600$ described by $U^+ = Cy^{+\gamma}$, where C and γ are Reynolds-number independent constants. Here, $y^+ = yu_\tau/\nu$, where y is the distance from the wall. This power-law region has a clear resemblance to the mesolayer introduced for pipe flow by Wosnik et al. [2000], who argued that in this region there is insufficient scale separation between the energy and dissipation ranges for inertially dominated turbulence to exist. Beyond this power-law region, McKeon et al. [2004a] noted that a "true" logarithmic region appears, from approximately $y^+ = 600$ up to about $y/R = 0.12$, and then a universal wake region in outer coordinates fills out the remainder of the profile.

We can express the mean velocity variation (assuming that the convection terms are negligible) in the so-called overlap region in either inner scaling according to,

$$U^+ = \frac{1}{\kappa} \ln y^+ + B, \tag{3.1.1}$$

or in outer scaling as in:

$$U_{cl}^+ - U^+ = -\frac{1}{\kappa} \ln \frac{y}{R} + B^*. \tag{3.1.2}$$

This result has classically been found through similarity hypotheses [von Kármán, 1930], mixing length concepts [Prandtl, 1925], asymptotic matching [Millikan, 1938], dimensional analysis [c.f. Buschmann and Gad-el Hak, 2009] or, more recently, high Reynolds number asymptotic analysis [George and Castillo, 1997, Jiménez and Moser, 2007]. Here, U is the mean streamwise velocity, and $U^+ = U/u_\tau$. Furthermore, $U_{cl}^+ = U_{cl}/u_\tau$, where U_{cl} is the mean velocity on the centerline and R is the radius of

the pipe. Using Equation (3.1.1) and (3.1.2), we can also write

$$U_{cl}^{+} = \frac{1}{\kappa} \ln R^{+} + B + B^{*}. \tag{3.1.3}$$

The von Kármán constant κ, and the additive constants B and B^{*}, were originally thought to be universal. But since von Kármán [1930] proposed a logarithmic region of mean flow, there has been a remarkable variation in the values of these constants. The reviews of experimental data by Coles [1956] and Coles and Hirst [1968] led to the values of $\kappa = 0.40$ to 0.41 being generally accepted, and the values $\kappa = 0.41$, $B = 5.2$ and $B^{*} = 0.65$ became commonly cited [Bradshaw and Huang, 1995, Huffman and Bradshaw, 1972, Schlichting and Gersten, 2000]. More recent experiments, however, have suggested that these constants could depend on the flow under consideration [Nagib and Chauhan, 2008], or that the convection terms present in boundary layers act to alter the velocity profile compared to fully developed channel and pipe flows where they are strictly zero, appearing as a change in the constants [George, 2007]. For example, in turbulent boundary layers Österlund et al. [2000] found $\kappa = 0.384$, $B = 4.17$ and $B^{*} = 3.6$, while measurements in channel flows made by Zanoun et al. [2003] indicated $\kappa = 0.37$ and $B = 3.7$. In pipe flow McKeon et al. [2004a] found $\kappa = 0.421$, $B = 5.60$ and $B^{*} = 1.20$, whereas Monty [2005] reported $\kappa = 0.386$ in a different pipe facility (and at lower Reynolds number). Zanoun et al. [2003] pointed out that values of κ from 0.33 to 0.43 and B from 3.5 to 6.1 have been proposed, with no apparent convergence in time. A more recent review, together with a historical perspective on logarithmic mean flow scaling and the associated constants, is provided by Örlü et al. [2010].

Many of these estimates of κ were based on regression fits to Equation (3.1.1) or its derivative, which can easily lead to bias errors, especially when the lower and upper limits of the logarithmic region are still being debated (see, for exam-

ple, Marusic et al. [2010c] and Smits et al. [2011a]). To avoid such errors for pipe flow, additional means for obtaining κ were employed by Zagarola and Smits [1998] and McKeon et al. [2004a]. One way, based on integrating Equation (3.1.1) from the wall to the centerline and assuming complete similarity of the mean velocity profile, uses the Reynolds number dependence of the friction factor $\lambda = 8(u_\tau/\overline{U})^2$, where $\overline{U}$ is the area weighted bulk velocity (for details see Zagarola and Smits [1998]). With $Re_D = 2\overline{U}R/\nu$, the friction law gives

$$1/\lambda^{1/2} = \frac{1}{2\kappa\sqrt{2}\log e}\log\left(Re_D\lambda^{1/2}\right) + C_2, \tag{3.1.4}$$

where C_2 is an empirical constant. For pipe flow, this approach has the advantage that u_τ can be found with high precision by measuring the pressure drop along the pipe, and so Equation (3.1.4) can give an alternate estimate of κ.

Despite these precautions, the pipe flow results of Zagarola and Smits [1998] and McKeon et al. [2004a] have been disputed, including arguments that the Pitot profiles required a turbulence correction [Nagib and Chauhan, 2008, Perry et al., 2001]. Such disputes could not be addressed without complementary thermal anemometry measurements made in the same facility, which have since been obtained. In Chapter 3.3, we aim to use these data to establish the best estimate for the value of von Kármán's constant for the flow in a hydraulically smooth pipe, together with its uncertainty levels.

The upper and lower limits of the logarithmic region in pipe flow are still under discussion. As noted, Zagarola and Smits [1998] and McKeon et al. [2004a] observed a lower bound close to $y^+ = 600$, while Hultmark et al. [2012] observed a lower limit closer to 800 using data presented here. Recently, Marusic et al. [2013] evaluated high Reynolds number measurements from boundary layer and pipe flow experiments, including those of Hultmark et al. [2012], and suggested based on several previous

studies that a conservative lower limit for fitting data could be $y^+ = 3Re_\tau^{0.5}$ (the middle of the log region). This conclusion can only hold at high Reynolds numbers, at least for pipe flow, since no logarithmic region was observed by McKeon et al. [2004a] for $Re_\tau < 5000$. As to the upper limit, Zagarola and Smits [1998] suggested $0.07R$, whereas McKeon et al. [2004a] indicated an upper bound of $0.12R$ and Marusic et al. [2013] used $0.15R$ for a mix of pipe and boundary layer flows.

3.1.2 Reynolds stresses

Despite these ambiguities, it appears that classical scaling describes the behavior of the mean velocity well. In contrast, it is not so clear that the turbulent stresses follow a similar scaling, especially with regard to the streamwise component $\overline{u^2}$. Within the near wall region, for example, the distribution of $u^{2+} = \overline{u^2}/u_\tau^2$ shows a distinct peak at $y^+ \approx 15$, the so-called "inner peak". However, the variation of this peak with Reynolds number is currently a topic of debate, with recent studies arriving at contradictory conclusions. In pipe flow, for instance, Ng et al. [2011] found that the magnitude of the inner peak increased with Reynolds number, whereas Hultmark et al. [2010], Vallikivi et al. [2011] and Hultmark et al. [2012] each found that its magnitude was constant with Reynolds number, although its precise value is not clear. For channel flows and boundary layer flows the picture seems clearer in that there is a general consensus that the peak value increases with Reynolds number [DeGraaff and Eaton, 2000, Hutchins and Marusic, 2007, Jiménez and Hoyas, 2008, Klewicki and Falco, 1990, Marusic and Kunkel, 2003]. It is worth noting, however, that its rate of increase has not yet been established with any certainty, where, for example Hutchins and Marusic [2007] proposed an increase in peak u^{2+} of 2.22 per decade in Re_τ, while Marusic et al. [2010a] suggest a possible value as low as 0.90 per decade. The question is important in that it informs our understanding of inner/outer layer interactions. Marusic et al. [2010b] suggested that the increase in the near-wall

peak for boundary layers occurs through a superposition and modulation coupling between the inner and outer regions of wall turbulence, and given that boundary layers, channel flows, and pipe flows have different geometrical constraints it would not be surprising to see differences in the structure and organization of the outer layer turbulence, and its interaction with the near-wall motions.

Further from the wall, some studies have reported the appearance of a second peak (the so-called "outer peak") at high Reynolds number. For instance, Morrison et al. [2004] observed its appearance in pipe flows for $Re_\tau \geq 8560$. These measurements covered the range $1.8 \times 10^3 \leq Re_\tau < 101 \times 10^3$, and used hot-wires with $14.1 < \ell^+ < 385$, where $\ell^+ = \ell u_\tau / \nu$, and ℓ is the wire length.* The effects of spatial filtering in this investigation were obviously substantial at the higher Reynolds numbers, especially near the wall, and preferential filtering of near-wall data could have led to the appearance of a "false" outer peak [Hutchins et al., 2009]. To more precisely establish the nature of this outer layer behavior, spatial filtering effects need to be minimized. In this respect, Hutchins et al. [2009] and Smits et al. [2011b] demonstrated that to avoid all spatial filtering effects close to the wall, ℓ^+ must be smaller than 4. Smits et al. [2011b] further showed that the requirements on ℓ^+ can be relaxed linearly with the distance from the wall outside of the inner peak, and proposed a correction for inadequately resolved data for wall-bounded flows on smooth surfaces.

3.2 Experimental methods

3.2.1 Experimental Facility

The experiments were conducted in the Princeton University/ONR Superpipe, which is a closed-return pipe facility, designed to produce high Reynolds number pipe flow

*The lowest Reynolds number case at $Re_\tau = 1500$ should be excluded as it has since been found to have a poor low velocity calibration.

through pressurizing the working fluid, described in detail by Zagarola and Smits [1998] and Langelandsvik et al. [2007]. A sketch of the whole facility is shown in Figure 3.1(A) and the test section in Figure 3.1(B).

Two different test pipes with different relative roughnesses were used, one "smooth" and one "rough". A commercial steel pipe was used as a rough pipe, described by Langelandsvik et al. [2007], with an average inner radius of $R = 64.92$ mm and a surface roughness $k_{rms} = 5$ μm, giving $k_{rms}/R = 7.7 \times 10^{-5}$. Langelandsvik et al. [2007] demonstrated that this pipe is hydraulically smooth up to $Re_\tau \approx 13 \times 10^3$ and fully rough for $Re_\tau \geq 101 \times 10^3$.

The smooth pipe was the same as that described by Zagarola and Smits [1998], McKeon et al. [2004a], and Morrison et al. [2004], with an average inner radius of $R = 64.68$ mm and a surface roughness of $k_{rms} = 0.15$ μm, resulting in a relative roughness of $k_{rms}/R = 2.3 \times 10^{-6}$. This pipe has been previously demonstrated to be hydraulically smooth for $Re_\tau < 217 \times 10^3$ ($Re_D < 13.5 \times 10^6$) [McKeon, 2003, McKeon et al., 2004a], which includes all Reynolds numbers tested in the current study. Prior to the experiments in the smooth pipe, the test pipe was disassembled to accommodate rough pipe experiments, and then reassembled using optical inspection of every connection to minimize mismatches between sections.

For both pipes the measurement station was located $392R$ downstream from the entrance, to assure fully developed flow. The streamwise pressure gradient in the pipe was measured with 21 pressure taps over a distance of $50R$ to obtain the friction velocity, u_τ.

3.2.2 NSTAP measurements

In order to acquire data with adequate spatial and temporal resolution, Nano-Scale Thermal Anemometry Probes (see Chapter 2) were used for all velocity measurements reported here. An image of a representative 60 μm probe of the design used is shown

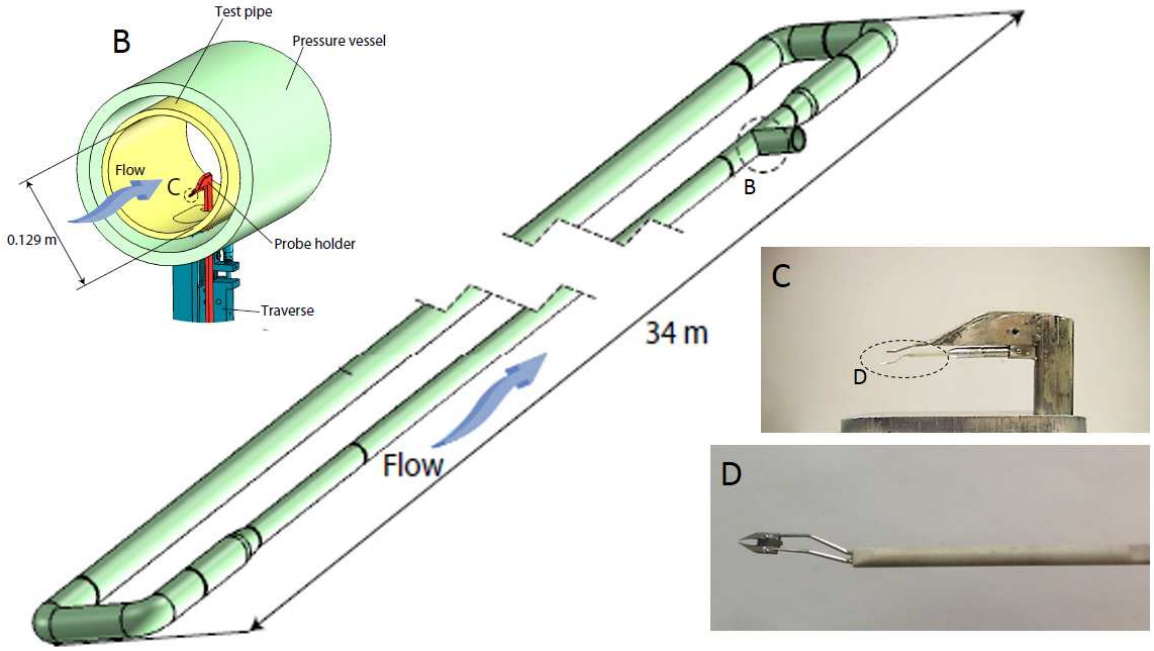

Figure 3.1: Experimental setup for pipe flow. (A) ONR Superpipe sketch; (B) Close-up of the test section with the pressure vessel, test pipe, probe holder, and traverse; (C) Close-up of the probe holder; (D) A typical NSTAP mounted onto prongs.

in Figure 2.1F.

The NSTAP was operated using a Dantec StreamLine constant temperature anemometry system in the 1:1 bridge mode with an external resistor heating the NSTAP to a wire temperature of approximately 450 K. The measured frequency response from squarewave test was always above 150 kHz in still air, which increased to more than 300 kHz at the highest Reynolds number. The data were low-pass filtered using an eighth-order Butterworth filter at 150 kHz and digitized using a 16-bit A/D board (NI PCI-6123) at a rate of 300 kHz. A stepper motor traverse with a linear encoder with 0.5 μm resolution (SENC50 Acu-Rite Inc.) was used to position the probe. The initial distance between the wall and the wire, y_0, was determined using a depth measuring microscope (Titan Tool Supply, Inc.) allowing for 5 μm precision in determining y_0.

The NSTAP was calibrated using the pressure difference between a 0.89 mm Pitot tube and two 0.4 mm static pressure taps located in the pipe wall at the same streamwise location. The pressure difference was measured using four different

Case	Surface	Re_D	Re_τ	p_a [atm]	$\langle U \rangle$ [m/s]	$\frac{\nu}{u_\tau}$ [μm]	ℓ [μm]	ℓ^+	y_0 [μm]	y_0^+	k_{rms}^+	Symbol
1	Smooth	81×10^3	1,985	0	9.48	33	60	1.8	14	0.4	0.00	★
2	Smooth	146×10^3	3,334	0.67	10.1	19	60	3.1	14	0.74	0.01	▼
3	Smooth	247×10^3	5,412	2.40	8.40	12	60	5.0	14	1.2	0.01	▶
4	Smooth	512×10^3	10,481	5.43	9.37	6.2	60	9.7	14	2.3	0.02	▲
5	Smooth	1.1×10^6	20,250	10.8	10.5	3.2	60	18.8	14	4.4	0.05	■
6	Smooth	2.1×10^6	37,690	22.5	10.5	1.7	60	35.0	14	8.2	0.09	♦
7	Smooth	4.0×10^6	68,160	45.6	10.4	0.95	60	63.2	14	15	0.16	
8	Smooth	4.0×10^6	68,371	45.9	10.3	0.95	30	31.7	28	29	0.16	◀
9	Smooth	6.0×10^6	98,190	69.7	10.6	0.66	30	45.5	28	43	0.23	●
10	Rough	993×10^3	19,316	6.88	14.8	3.4	60	17.9	28	8.5	1.49	■
11	Rough	2.0×10^6	36,676	13.3	16.3	1.8	60	33.9	28	16	2.82	♦
12	Rough	3.8×10^6	69,118	22.7	19.2	0.93	60	63.9	28	30	5.32	◀
13	Rough	5.6×10^6	100,530	34.3	19.2	0.65	60	92.9	28	44	7.74	●

Table 3.1: Experimental conditions of NSTAP measurements in pipe flow.

pressure transducers depending on the Reynolds number. For the lowest Reynolds number, a Datametrics 1400 transducer with a 2,488 Pa range was used, and for the higher Reynolds numbers three different Validyne DP15 transducers with ranges 1,379 Pa, 8,618 Pa and 34,473 Pa were employed. The Pitot tube measurements were corrected for static tap Reynolds number effects with the correlation proposed by McKeon and Smits [2002] and for viscous effects using the correlation identified by McKeon et al. [2003]. The streamwise pressure gradient was acquired using a 133 Pa MKS Baratron transducer for the lowest Reynolds number and a 1,333 Pa MKS transducer for the higher Reynolds numbers. Each pressure transducer was individually calibrated over its full range (with calibration uncertainties reported in Chapter 3.2.3). The ambient fluid temperature change during a given profile ranged from 0.3° C to 2.0° C over the full Reynolds number range, and the data were corrected using the temperature correction outlined by Hultmark and Smits [2010].

For calibration, the Pitot probe was positioned above the NSTAP (as can be seen in Figure 3.1(C)), and the distance between probes was measured using the depth measuring microscope. The probes were then positioned symmetrically on opposite sides of the pipe centreline. For all pressure measurements, sufficient time was given for the pressure within the pressure tubing to reach a steady state and long averaging times were used to minimize the effects of transients on the average. 14 calibration points were used both before and after each measurement and a fourth order polynomial fit was used to find the calibration coefficients. The rest of the experiment closely followed the procedures described by Hultmark et al. [2010].

Data were acquired for $81 \times 10^3 < Re_D < 60 \times 10^6$, with the Superpipe pressurized for $Re_D \geq 150 \times 10^3$. The flow conditions examined in this study using NSTAP are listed in Table 3.1 and the estimated experimental uncertainties are listed in Table 3.2. Cases 1 to 9 were measured in the smooth pipe, and Cases 10 to 13 were measured in the rough pipe. Here, p_a is the ambient pressure, and y_0 is the initial distance from

Source	Uncertainty ±
Pressure (static and total)	0.4%
Temperature	0.1%
Ambient pressure	0.2%
Density, ρ	0.3%
Dynamic viscosity	0.4%
Friction velocity, smooth flow, u_τ	0.8%
Friction velocity, rough flow, u_τ	1.6%
Viscous length scale, ν/u_τ	0.9%
Wall normal position zero, y_0	5 μm
Wall normal position precision, y	0.5 μm/m
Distance between Pitot and hot wire	15 μm
Wall normal distance in inner scaling, y^+	0.53 + 0.9%
Calibration error due to calibration velocity	0.4%
Calibration error due to curve fitting	1.8%
Mean velocity derived from hot wire, U	2.2%
Mean velocity in inner scaling (smooth), U^+	2.3%
Mean velocity in inner scaling (rough), U^+	2.7%
Variance of velocity, $\overline{u'^2}$	3.0%
Variance of velocity in inner scaling (smooth), u^{2+}	3.4%
Variance of velocity in inner scaling (rough), u^{2+}	4.7%

Table 3.2: Uncertainty estimates in pipe flow.

the wall.

3.2.3 Pitot measurements

In order to evaluate the differences in mean velocity profiles acquired in Superpipe over the last 15 years, an overview of all the results and thorough error analysis was performed. In addition to previously available data and NSTAP data described above, a new set of Pitot measurements was conducted.

A Pitot tube with 0.40 mm diameter was used to measure dynamic pressure and the static pressure was measured using two 0.40 mm static pressure taps located in the pipe wall. This Pitot diameter was comparable to the 0.30 mm and 0.89 mm

Case	Re_D	Re_τ	p_a [atm]	$\langle U \rangle$ [m/s]	$\frac{\nu}{u_\tau}$ [μm]	d^+	k^+_{rms}
1P	80×10^3	1,956	0.00	9.42	33	12	0.00
2P	144×10^3	3,329	0.00	17.1	19	21	0.01
3P	244×10^3	5,379	0.70	16.7	12	33	0.01
4P	468×10^3	9,744	2.49	15.9	6.6	60	0.02
5P	980×10^3	19,011	6.82	14.9	3.4	118	0.04
6P	1.97×10^6	36,065	13.5	16.3	1.8	223	0.08
7P	3.84×10^6	66,286	22.5	19.8	0.98	410	0.15
8P	6.00×10^6	100,280	41.0	17.5	0.65	620	0.23
9P	10.57×10^6	169,690	74.0	18.0	0.38	1,050	0.39

Table 3.3: Experimental conditions of Pitot measurements in Superpipe with smooth wall.

diameter Pitot tubes used in previous Pitot studies in the Superpipe (McKeon [2003] and Zagarola [1996] respectively), and was equal to $0.006R$ or approximately 1000 viscous lengths at the highest Reynolds number measured.

The pressure difference was measured using a Datametrics 1400 transducer with a 2,488 Pa range for all atmospheric pressure cases, and Validyne DP15 transducers with ranges 1,379 Pa, 8,618 Pa, 34,474 Pa and 82,737 Pa for the pressurized cases, depending on the pressure. For the streamwise pressure gradient measurements, a 133 Pa MKS Baratron transducer was used for atmospheric cases and a 1,333 Pa MKS transducer or Validyne DP15 34,474 Pa transducer was used for pressurized cases. All pressure transducers were carefully calibrated prior to use. For calibrating the lowest pressure range, a liquid manometer with uncertainty of less than $\pm 0.40\%$ of the reading was used, whereas for the intermediate range Validyne transducers an Ametek pneumatic dead weight tester was used with accuracy of $\pm 0.05\%$. The tunnel pressure was measured using Validyne DP15 transducers with 345 kPa, 3,447 kPa and 27,579 kPa ranges, and these were calibrated using an Amthor dead weight pressure gauge tester with accuracy of $\pm 0.1\%$ of the reading.

Data were acquired at $Re_D \approx 80 \times 10^3, 150 \times 10^3, 250 \times 10^3, 500 \times 10^3, 1 \times 10^6, 2 \times 10^6, 4 \times 10^6, 6 \times 10^6$, and 10×10^6. The experimental conditions are given in Table 3.3. To position the probe, a stepper motor traverse was used equipped with a linear

optical encoder with a resolution of 0.5 μm (SENC50 Acu-Rite Inc.), similarly to the NSTAP setup described in Chapter 3.2.2.

3.2.4 Bias error effects

Uncertainties may be divided into bias errors and precision errors. Here, we treat precision uncertainty as the expected variation which would occur amongst repeated measurement of the same quantity as reflected through experimental scatter. Bias error is more difficult to identify and we treat it as a consistent deviation between a measured and a true quantity as introduced by the experimental setup, procedure or analysis. The estimated errors for the data sets under consideration are provided in Table 3.4 where uncertainty values derived from stated manufacturer values are treated as bias error. Here we discuss several additional sources of bias error which can play a role in estimates of κ, and investigate the impact of each source on the estimate. All referred datasets and estimates are described in Chapter 3.3.

Impact of Pitot probe corrections

Pitot probe corrections for shear, near-wall, viscous and finite static tap size, are discussed in great detail in many sources [see, for example Tavoularis, 2005, Tropea et al., 2007]. With the exception of eliminating data points less than two probe diameters from the surface, the complete correction suite used here is described in Bailey et al. [2013] and has been demonstrated to result in mean velocities measured with Pitot tubes agreeing with those measured by hot-wires to within 1%. This difference therefore can be used as an approximation of the bias error which can be expected in the measured mean velocity. However, the source of this bias should not be considered exclusive to the Pitot and the accuracy of its corrections, but can equally be attributed to uncertainty in the hot-wire mean velocity.

Of particular interest for the Pitot measurements is the magnitude of the correc-

tion for turbulence effects which has previously been observed to significantly bias the estimate of κ found using mean flow profiles [Nagib and Chauhan, 2008, Perry et al., 2001]. To assess the effect of this correction on estimates of κ we repeated the analysis without the turbulence correction. The effect of not using the turbulence correction was found to be an increase in estimated κ of +2% when determined using Equation (3.1.1) and bias it -0.2% and +0.2% when using Equation (3.1.3) and (3.1.4) respectively.

Initial probe position

The effects of initial probe position are discussed in detail in Örlü et al. [2010] which illustrates how accurate determination of wall position is necessary to correctly deduce mean and turbulence quantities. In the Superpipe, the wall layer thickness is 64.68 mm and, at $Re_D = 1.3 \times 10^7$, the viscous length is only 300 nm. Therefore, an inaccurate estimate of wall position can have significant effect on the mean velocity profile. To minimize this zero position error, the ZS data set used a capacitance-based method to determine the zero position to within 40 μm, and the MLJMS data set used electrical contacts between the probe and surface to identify the initial probe position with a cited accuracy of 5 μm. For the MMJS data, no details were available regarding how the initial probe distance was determined. For the HVBS and VS data, initial probe position was determined via depth measuring microscope, with the zero location marked using an electrical contact and a 5 μm uncertainty is estimated. Note that these cited values are likely to underestimate the true bias, which can arise from errors in estimating Pitot probe diameter, probe orientation with respect to the wall, hot-wire probe distortion and rotation relative to the wall plane, the method used to measure wall distance, and the possibility that electrical contact is rarely made at a clearly defined and repeatable point [Hutchins and Choi, 2002]. These errors are also further compounded in the Superpipe facility due to lack of optical access to the

measurement station and therefore the inability to directly verify the position of the probe relative to the wall.

To illustrate how uncertainty can propagate into the estimate of κ, we artificially biased the zero position of the VS data set by +50 μm (12.5% of the probe diameter, corresponding to a bias of approximately 1.5 viscous unit at the lowest Reynolds number and 125 viscous units at the highest Reynolds number). For κ estimated from Equation (3.1.1), there was a resulting bias in κ of -1% at $Re_D = 1 \times 10^6$ to -3% for $Re_D \geq 4 \times 10^6$ corresponding to changes in κ from -0.004 to -0.01. As might be expected, the effect on the estimates of κ using Equation (3.1.4) and (3.1.3) were much less, corresponding Reynolds number dependent bias in κ estimate from -0.01% to -0.05% using Equation (3.1.4) and +0.005% to +0.05% using Equation (3.1.3).

Estimate of area averaged flow velocity from discrete data

An associated error to that of initial probe position, which could have a noticeable effect on the estimate of κ using Equation (3.1.4), is the numerical integration scheme used to determine the area averaged velocity to calculate the Reynolds number. As the Reynolds number increases, and the inner layer thins accordingly, there is a potential Reynolds number dependent bias introduced into any estimate of area averaged velocity due to an inability to resolve this high shear region. This compounds any error introduced by the order of the numerical integration scheme used. In this study, we have used second-order-accurate trapezoidal integration and, where necessary, have extrapolated the profile down to the wall with data measured at lower Reynolds numbers and assuming wall-scaling is valid. Not performing this extrapolation process was found to have a surprisingly significant effect on κ determined using Equation (3.1.4), with a bias in κ of typically +3%,+0.4%,+1% and +1% for the ZS, MLJMS, MMJS and VS data sets respectively. For the HVBS data set, the closest measurement point was always within the buffer layer and the extrapolation process

was not required.

Hot-wire drift

In hot-wire anemometry, the most sensitive issue in experiments is a proper calibration of the sensor and some drift in the response is an inherent part of the measurements. Even the smallest drift during measurements can cause significant errors, especially when estimating mean velocities. For the HVBS data, a calibration was conducted on the centerline at 14 flow velocities before and after each profile and agreement of the calibration curves was used as a validation condition for acceptance of the profile. Then all 28 points were combined to fit the calibration curve used for all data processing. In Figure 3.2*a* all calibration curves are shown and in Figure 3.2*b* the relative difference, U_{rel}, between each pre- and post-measurement calibration and the combined calibration U_{comb} is illustrated (where relative velocity is given as $U_{rel} = (U_{cal} - U_{comb})/U_{comb}$ and relative voltage as $E_{rel} = (E_{cal} - E_{min})/(E_{max} - E_{min})$). It can be seen that, for most cases, the relative difference between calibration curves is below 1%.

To estimate the error from this minimal drift, all data were processed using pre- and post-measurement calibrations separately and values of κ were compared to the values found using combined calibration curves. Despite the agreement apparent in Figure 3.2, regression fit to Equation (3.1.1) showed differences in κ of up to 1.1%, whereas fits to Equation (3.1.3) and (3.1.4) had variations up to 6.3% and 5.5% respectively. Additionally, an interpolation scheme was also attempted to transition between pre- and post-measurement calibration curves over the course of the profile measurements. When this was employed, the estimate of κ from regression fit was found to vary up to 0.6% and estimates from Equation (3.1.3) and (3.1.4) varied 4.6% and 4.6% respectively. Therefore it can be seen that even a slight variation in probe response over the course of a profile measurement will significantly impact the

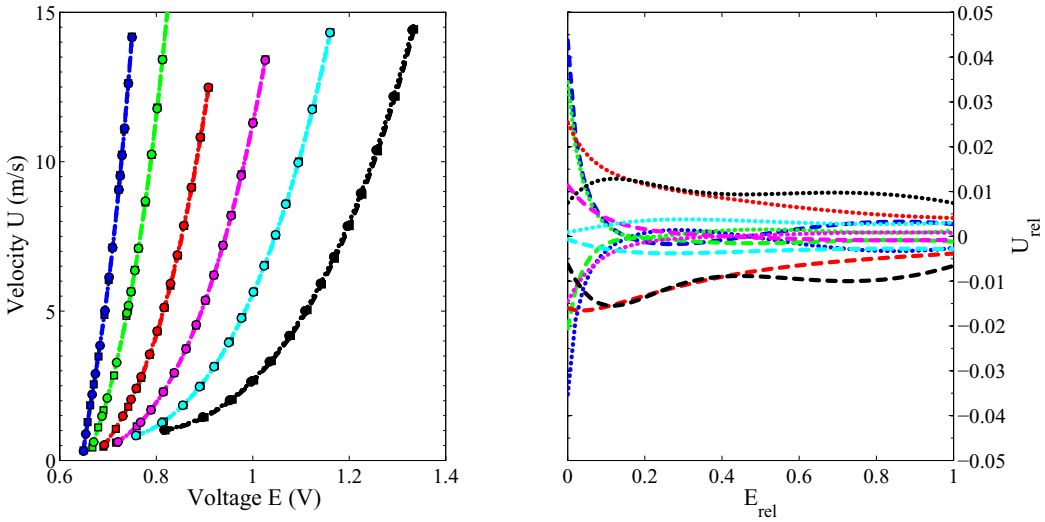

Figure 3.2: Calibration points and curves for all cases in HVBS data set. Dashed line and circles indicate pre-calibraton fit, dotted line and squares post-calibration fit. (a) Shows calibration points and according fitted curves; (b) shows the relative difference U_{rel} of the calibrations compared to the combined calibration fit.

estimate of κ and thus mean velocity measurements with hot-wires must be treated with caution.

Use of multiple transducers over a large Reynolds numbers range

The advantage of the Superpipe is not strictly the high Reynolds numbers it can achieve, but principally its large achievable Reynolds number range. It is this large operating range, achieved by pressurizing the working fluid, that makes the use of Equation (3.1.3) and (3.1.4) feasible for obtaining estimates of κ. It is also the insensitivity of Equation (3.1.3) and (3.1.4) to the bias errors, discussed in Chapter 3.2.4, which makes them attractive for estimating κ. However, measuring the quantities in Equation (3.1.3) and (3.1.4) accurately over the range of Superpipe operating conditions requires the use of multiple pressure transducers of varying sensitivity, each of which requires individual calibration. Therefore, the final source of bias error to be described is the error associated with using multiple transducers to measure the quantities used in Equation (3.1.3) and (3.1.4). We will see that significant errors can

arise from even slight differences in the calibrations between the different transducers.

To illustrate the impact this error could have on the estimate of κ, we re-analyzed the MV data set after artificially adding a -1% error in the Pitot transducer for $2.5 \times 10^5 \leq Re_D \leq 1 \times 10^6$ and 1% error for $Re_D \geq 6 \times 10^6$. Whereas κ determined by Equation (3.1.1) changed by 0.5% and -0.5% respectively in the affected Reynolds number ranges, κ determined from Equation (3.1.3) and (3.1.4) were found to change by -1.5% to -8%, depending on the Reynolds number range used for the fit. A similar analysis conducted with the bias applied to the pressure gradient transducer resulted in a 1% to 8% change in κ using Equation (3.1.3) and (3.1.4) and -0.5% and +0.5% using Equation (3.1.1). Estimates of κ were found to be much less sensitive to bias errors in the transducer used to measure the Superpipe operating pressure, with a negligible effect on estimates using Equation (3.1.1) and only a 0.1% to 0.5% bias resulting when using Equation (3.1.3) and (3.1.4).

3.3 The von Kármán's constant

With the addition of the new Pitot tube data, five complete data sets now exist on the mean velocity distribution in the Princeton/ONR Superpipe at Reynolds numbers ranging across $81 \times 10^3 \leq Re_D \leq 1.8 \times 10^7$. These profiles were taken using Pitot tubes, conventional hot-wires and nano-scale thermal anemometry probes (NSTAPs). Here, we aim to use these data to establish the best estimate for the value of von Kármán's constant for the flow in a hydraulically smooth pipe, together with its uncertainty levels.

The five data sets on the mean velocity in the Princeton University/ONR Superpipe are the Pitot data of Zagarola and Smits [1998] (denoted ZS) and McKeon et al. [2004a] (denoted MLJMS), the conventional hot-wire data of Morrison et al. [2004] (denoted MMJS) whose mean flow results taken with hot-wire probes of sensing length of 500 and 250 μm have not previously been published, the nano-scale thermal anemometry probe results of Chapter 3.2.2, Hultmark et al. [2012, 2013] (denoted HVBS), and the new Pitot data set acquired specifically for the present study (denoted VS, see Chapter 3.2.3). A comparison of mean velocity profiles and Re_D dependence of λ from all data sets is provided in Figure 3.3.

The particular flow conditions for each data set are given in the appropriate references where further descriptions of each experiment may also be found. For the present analysis, to avoid any potential biasing by surface roughness effects, ZS and MLJMS data for $R_\tau > 2.17 \times 10^5$ ($Re_D > 13.5 \times 10^6$) have been excluded. In addition, the $Re_D = 6 \times 10^6$ data from MMJS and HVBS experienced relatively large temperature changes resulting in anemometer drift, and so have also been excluded. Finally, the $Re_D = 5.5 \times 10^4$ case of MMJS was excluded due to errors identified in the probe calibration data [Hultmark et al., 2010].

All Pitot data sets (ZS, MLJMS, VS) were processed using the static tap and shear corrections proposed by McKeon and Smits [2002] and McKeon et al. [2003], with

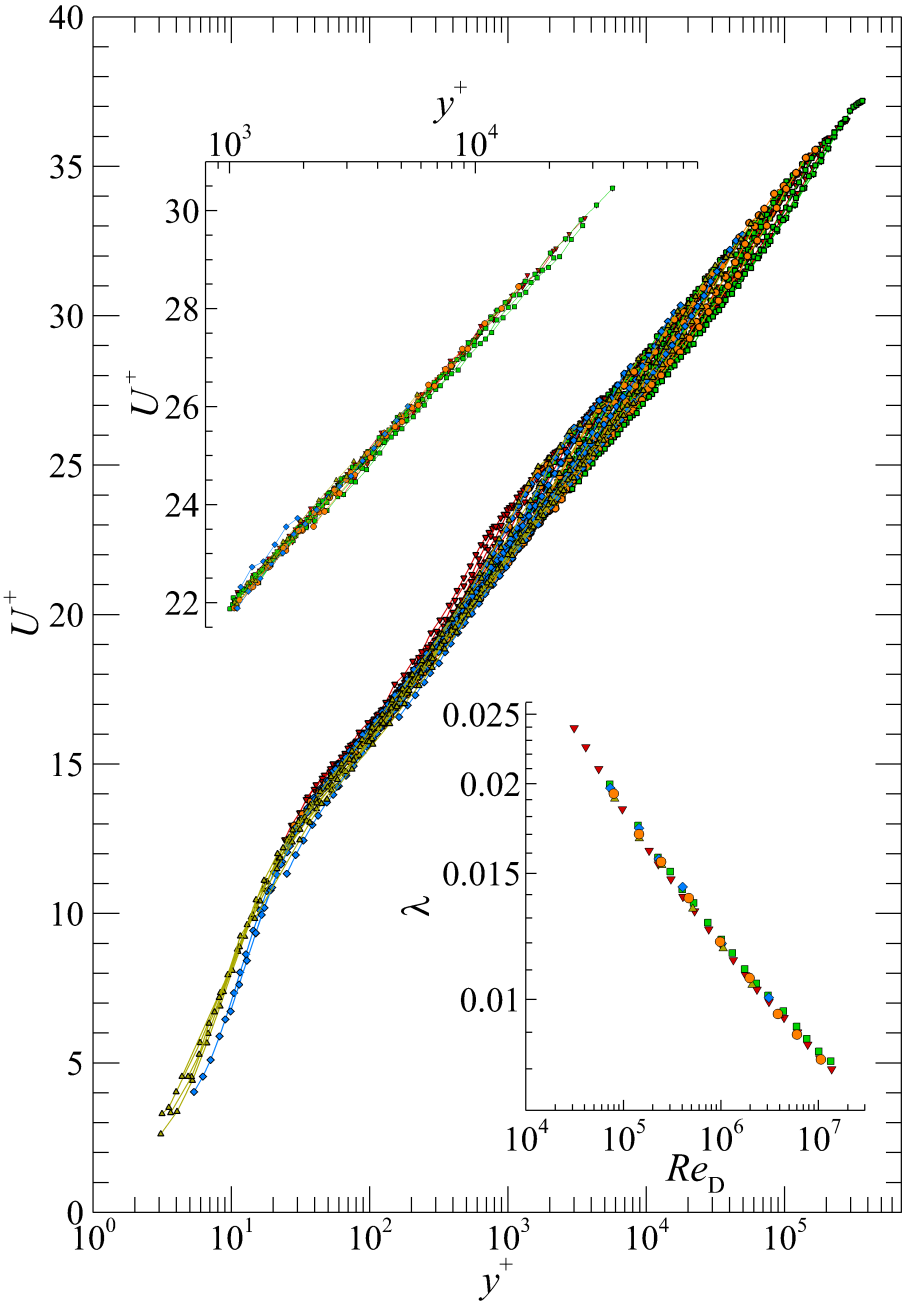

Figure 3.3: Comparison of all mean velocity profiles included in the current study: (▽) ZS; (□) MLJMS; (◇) MMJS; (○) VS; and (△) HVBS. Inset in upper left shows only data points falling in the range $1000 < y^+ < 0.1Re_\tau$. Inset in the lower right shows friction factor dependency on Re_D for all data sets.

Data set	ZS		MLJMS		MMJS		HVBS		VS	
Source	bias	prec.	bias	prec.	bias	prec.	bias	prec.	bias	prec.
Pitot differential	±0.4%	±0.8%*	±0.4%	±0.6%*	N/A		N/A		±0.4%	0.8%*
Pitot corrections	±1%†	±0.3%‡	±1%†	±0.3%‡	N/A		N/A		±1%†	0.3%‡
Hot-wire precision	N/A		N/A		±0%	±0.4%*	±0%	±0.4%*	N/A	
Hot-wire caln.	N/A		N/A		±1%	±0%	±1%	±0%	N/A	
Anemometer drift	N/A		N/A		±1%	±0%	±1%	±0%	N/A	
y position (μm)	118	5	41	5	41	5	5.25	0.5	13.25	0.5
Tunnel pressure	±0.3%		±0.3%		±0.3%		±0.3%		±0.3%	
Pressure gradient	±(0.17–0.83)%		±(0.17–0.83)%		±(0.17–0.68)%		±(0.17–0.68)%		±(0.17–0.68)%	
Temperature	±0.05%		±0.05%		±0.05%		±0.05%		±0.05%	
Dynamic viscosity	±0.8%		±0.8%		±0.8%		±0.8%		±0.8%	
Pipe radius	±0.06%	±0%	±0.06%	±0%	±0.06%	±0%	±0.06%	±0%	±0.06%	±0%

Table 3.4: Bias and precision uncertainty estimates. Where a single value is stated across both bias and precision columns, the same value was used for both bias and precision uncertainty. *Value estimated from data scatter. †Value estimated based on results of Bailey et al. [2013]. ‡Value estimated from scatter in measured velocity gradient.

the additional turbulence correction and associated near-wall correction discussed by Bailey et al. [2013]. As done by McKeon et al. [2004a], we discard Pitot data from measurement points lying less than two probe heights from the surface. To estimate the turbulence intensity required for applying the turbulence correction, the streamwise turbulence intensity of HVBS is used for $Re_D \leq 6 \times 10^6$. For Pitot cases at higher Reynolds numbers, the turbulence intensity was estimated by assuming that the logarithmic scaling observed by HVBS was valid throughout the layer.

A comparison of the newly acquired VS Pitot data set to the HVBS NSTAP data set taken at the same Reynolds numbers is provided in Figure 3.4. The results demonstrate negligible differences between the two data sets, after all applicable corrections have been applied.

The fitting of Equation (3.1.1), (3.1.3) and (3.1.4) to the data were conducted using the linearized form of the equations applying a least-squares approach (implemented through the MATLAB function polyfit). The fit to Equation (3.1.1) therefore returned κ^{-1} and B; to Equation (3.1.3) it returned κ^{-1} and $(B + B^*)$; and to Equation (3.1.4) it returned $(2\sqrt{2}\kappa \log e)^{-1}$ and C_2. Here, we only consider the values of κ and do not examine the additive coefficients in any detail. For fitting to Equation (3.1.3), U_{cl}^+ was determined by a cubic fit to the three data points straddling the centerline, although there was a negligible difference when compared to the same estimate using the measurement point located at the pipe centerline.

Estimates for the experimental uncertainties used in the uncertainty analysis are listed in Table 3.4. In most cases, given that much of the facility and instrumentation used was largely unchanged, these follow the values provided by ZS. Additional sources of bias error are discussed in Chapter 3.2.4, and the Monte Carlo based error analysis approach used to estimate the uncertainty in κ is described in Bailey et al. [2014].

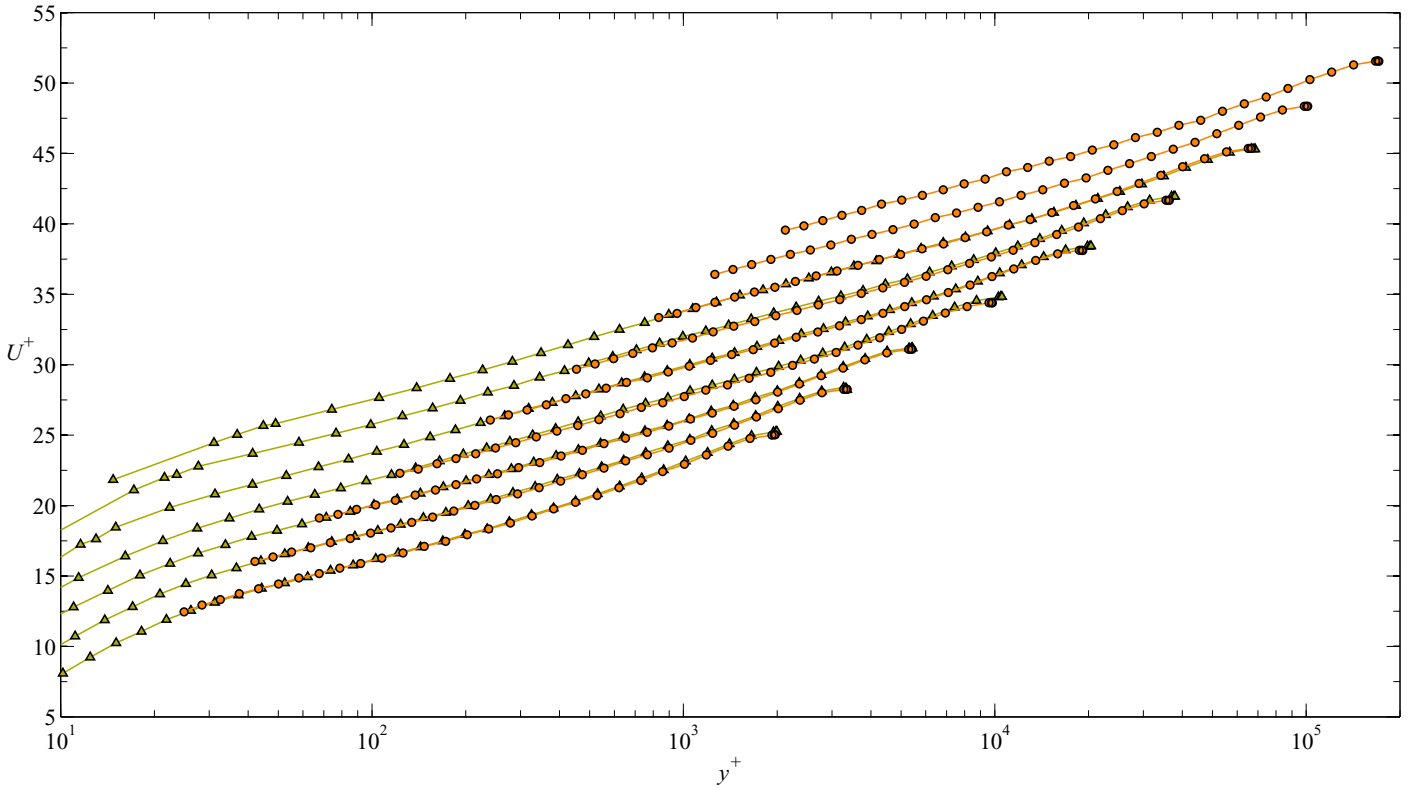

Figure 3.4: Comparison of (○) VS Pitot and (△) HVBS mean velocity profiles at $Re_D = 80 \times 10^3, 150 \times 10^3, 250 \times 10^3, 500 \times 10^3, 1 \times 10^6, 2 \times 10^6$ and 4×10^6. Note that successive Reynolds numbers are shifted vertically by $2u_\tau$ for clarity.

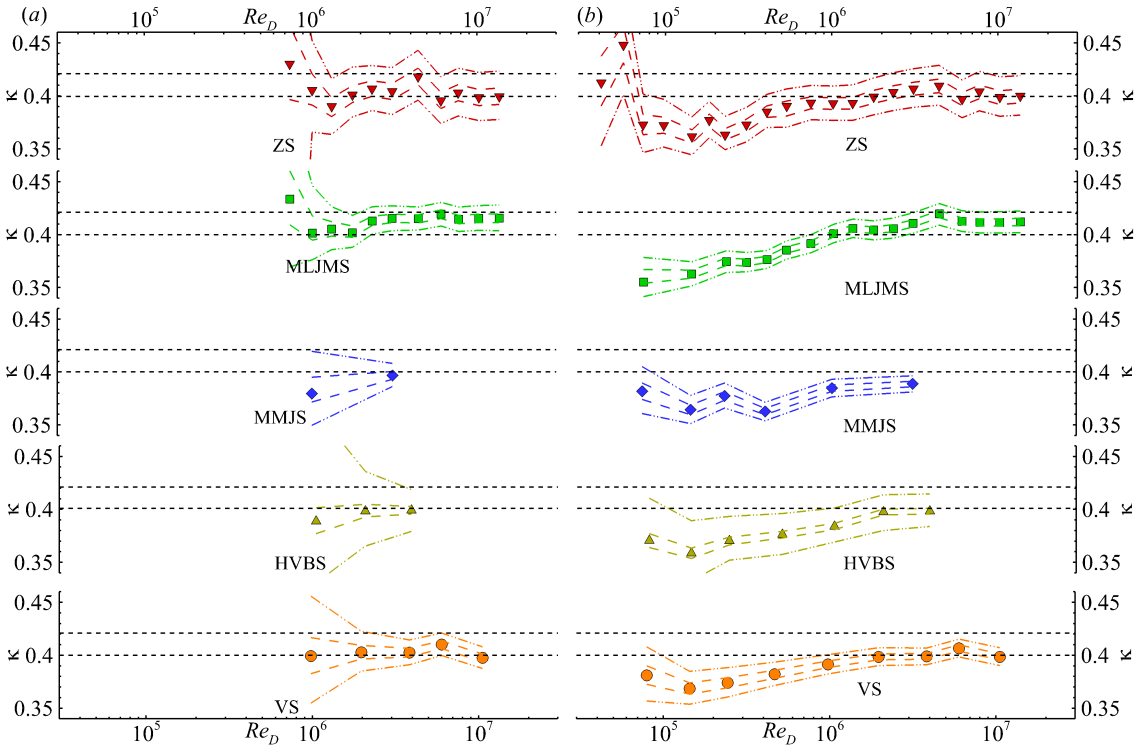

Figure 3.5: Value of κ as estimated from least-squares fit of Equation (3.1.1) to the mean velocity profiles measured at different Reynolds numbers for the range of data points lying in the range (*a*) $1000 < y^+ < 0.1Re_\tau$ and (*b*) $3(Re_\tau)^{1/2} < y^+ < 0.15Re_\tau$. Dash-dot-dot lines indicate 95% confidence limits and dashed lines indicate 50% confidence limits. Black dashed lines indicate the values of $\kappa = 0.40$ and $\kappa = 0.421$.

3.3.1 κ from the mean velocity profile

We first find κ using a least-squares fit of Equation (3.1.1) to each individual velocity profile within the range $y^+ > 1000$ to $y/R < 0.1$. These values were selected to ensure that the fit was unambiguously contained within the range where a log law has been found to hold in this flow ($y^+ > 800$ to $y/R < 0.15$), and this choice is not meant to suggest a particular range of validity of the logarithmic scaling.

The results are presented in Figure 3.5*a* and suggest a Reynolds number independent value of κ, but with large variations in experimental uncertainty across the Reynolds number range and between measurements. Note that, with regards to uncertainty, there appears to be no advantage to using either thermal anemometry or

Pitot tube measurement approaches, because the largest uncertainty is associated with the smallest number of data points falling within the acceptance range and used for the regression fit. Thus, the uncertainty levels generally decrease with increasing Re_D. The exception is the early data set of ZS, where the higher uncertainty levels are mostly due the relatively large Pitot probe used by ZS so that fewer measurement points fall within the fitting range. The most likely values for κ vary considerably among the data sets. For the earlier Pitot probe profiles, the ZS values lie between 0.39 and 0.43, while the MLJMS data set suggests 0.4 to 0.42 (consistent with McKeon et al. [2004a]'s previous estimate of 0.421 at high Reynolds number). Both thermal anemometry cases give estimates of κ varying between 0.38 and 0.40, whereas the most recent Pitot data set indicates a value between 0.40 and 0.41.

In addition to the conservative range ($y^+ > 1000$ to $y/R < 0.1$), the proposed overlap layer range of $3(Re_\tau)^{0.5} < y^+ < 0.15Re_\tau$ of Marusic et al. [2013] was also used to determine κ. The resulting estimate was found to be Reynolds number dependent for $Re_D \lesssim 2 \times 10^6$, as shown in Figure 3.5*b*. Note that $y^+ = 3(Re_\tau)^{0.5} \approx 600$ at $Re_D \approx 2 \times 10^6$, corresponding to the lower limit observed by McKeon et al. [2004a]. Above this Reynolds number the values of κ estimates become very close for the two different limits. Wide variation in the κ values was seen for any lower limits below $y^+ \approx 800$ but for larger $y^+ > 800$, the change of the limit resulted in minimal change in the value of κ within each separate profile. Virtually identical results were observed when the upper limit was reduced to $y/R = 0.1$, suggesting that the Reynolds number dependence is caused by too low lower limit. Therefore, below $Re_D \approx 2 \times 10^6$ the current results do not support the Reynolds number dependent lower limits used by Marusic et al. [2013] in pipe flow.

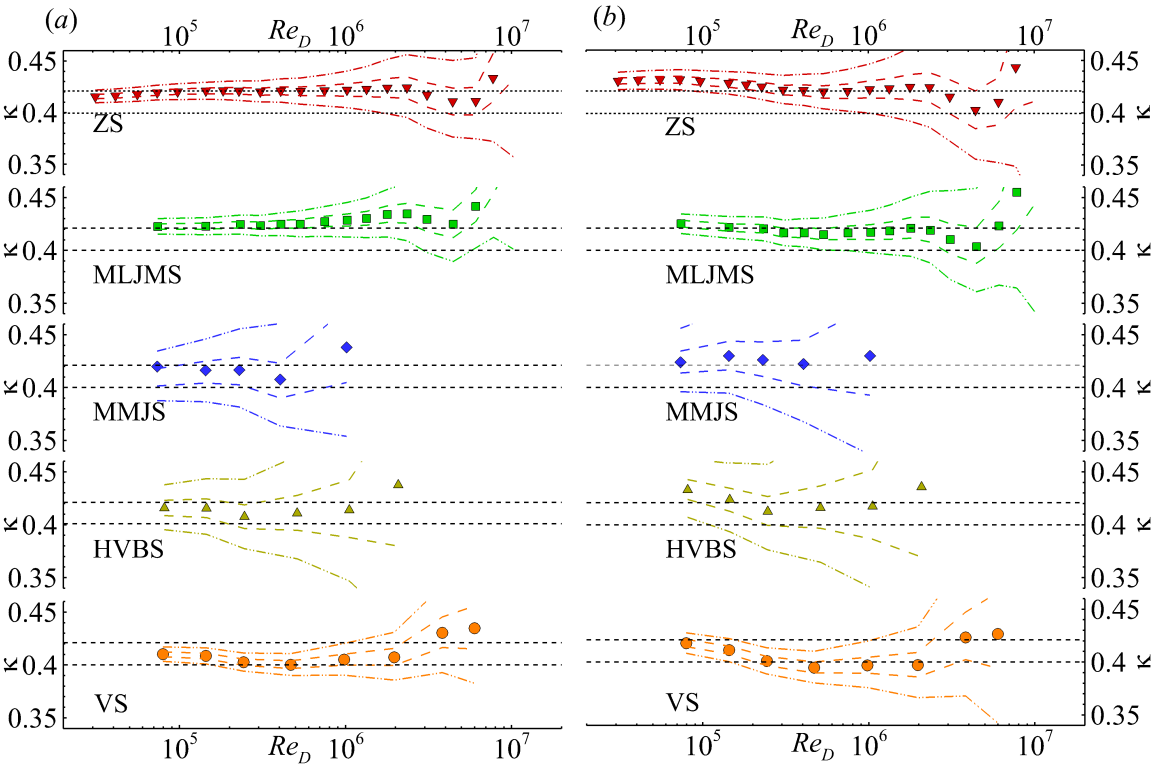

Figure 3.6: Value of κ estimated from least-squares fit of (a) Equation (3.1.4) (friction factor fit) and (b) Equation (3.1.3) (centerline velocity fit) shown as a function of the lowest Reynolds number case used for the regression fit. Dash-dot-dot lines indicate 95% confidence limits and dashed lines indicate 50% confidence limits.

3.3.2 κ from bulk properties

Although regression fits to the mean velocity profiles can provide an estimate of κ, the procedure is sensitive to the range of y^+ values selected for fitting, and to small errors in u_τ [see, for example Örlü et al., 2010]. However, for pipe flow a valid estimate of κ must satisfy Equation (3.1.1) and (3.1.2), and Equation (3.1.3) and (3.1.4). Therefore, given a sufficient Reynolds number range, one can also estimate κ from the Reynolds number dependence of the bulk flow properties. This was the approach taken by Zagarola and Smits [1998] and McKeon et al. [2004a].

Figure 3.6 shows the value of κ estimated by fitting Equation (3.1.4) and (3.1.3) to the centerline velocity data and the friction factor data, respectively. The results are shown as a function of the lowest Reynolds number included in the fit. For example,

for the highest Reynolds number shown κ was estimated from fitting only the two highest Reynolds number cases; each successively lower Reynolds number data point on the figure represents the results from a curve fit with one additional point included in the fit. Hence the lowest Reynolds number plotted represents the estimate of κ determined from fitting the entire data set.

As noted by McKeon et al. [2004a] with respect to the MLJMS data set, we see that for $Re_D > 300 \times 10^3$ the estimates for all data sets become Reynolds number independent, except for the highest Reynolds number values where the number of points in the fit are reduced and the uncertainty increases significantly. For $Re_D > 300 \times 10^3$, fitting Equation (3.1.4) or (3.1.3) gives similar values, although the latter estimate is subject to slightly higher uncertainty because it relies on a single measurement of U_{cl}^+ at each Reynolds number. The ZS, MLJMS and MMJS data sets return a value of $\kappa \approx 0.42$ consistent with the McKeon et al. [2004a] estimate of $\kappa = 0.421$. However the more recent HVBS and VS data indicate $\kappa \approx 0.41$ and 0.40, respectively. In addition, we see that the uncertainties in the thermal anemometry data sets are much higher than that of the Pitot data sets, primarily because the thermal anemometry data cover a smaller and lower Reynolds number range. A fit of Equation (3.1.4) was also applied to the high Reynolds number friction factor data of Swanson et al. [2002] [tabulated in McKeon et al., 2004b]. The resulting estimate of κ was found to depend strongly on the Reynolds number range selected for the fit, varying between 0.41 and 0.5.

3.3.3 Discussion

The different estimates of κ from each data set are summarized in Figure 3.7. For the regression fit to Equation (3.1.1) we use the value determined from the highest Reynolds number case, where the uncertainty is lowest due to the number of data points in the logarithmic region. For the estimates determined from regression fits

to Equation (3.1.3) and (3.1.4), we use the value determined from fitting to $Re_D > 3 \times 10^5$, which comprises the range where the estimate becomes Re_D independent and the uncertainties are lowest due to the number of data points included in the fit.

If we assume that the log law is valid, then Equation (3.1.1), (3.1.3) and (3.1.4) must be simultaneously valid and inspection of Figure 3.7*a* reveals two important points. First, no single value of κ is within the 95% uncertainty bounds of all five data sets. This indicates that one or more sources of uncertainty remain undetected while also reflecting the difficulty inherent in determining κ experimentally. Second, the estimates obtained by fitting Equation (3.1.3) and (3.1.4) are consistently higher than those obtained by fitting Equation (3.1.1), suggesting that these undetected errors are consistently biasing the estimate.

Many factors contribute to the overall uncertainty, but the primary ones are the estimate of y_0, the method chosen to integrate the mean velocity profile near the wall in order to find $\overline{U}$, drift in the thermal anemometry measurements, and turbulence corrections to the Pitot probe data (see Chapter 3.2.4). For example, the turbulence correction influences the value of κ obtained by fitting Equation (3.1.1) by 2% and a relatively small (0.08% of R) uncertainty in the wall distance can change κ by up to 3%, whereas estimates obtained by fitting Equation (3.1.3) and (3.1.4) are nearly unaffected by these factors. On the other hand, the estimates obtained using Equation (3.1.3) and (3.1.4) are very sensitive to the different pressure transducers used to obtain the velocity and pressure gradient, as well as the integration methods for estimating bulk properties. Estimates obtained from the hot-wire data are extremely sensitive to any type of drift, where estimates obtained using Equation (3.1.3) and (3.1.4) can be influenced by up to 6% even with high-quality calibrations with less than 1% drift. Overall, it can be seen that there is no measurement technique or method of analysis that could be identified as the most precise.

Although the 95% confidence intervals indicate that no value of κ is supported by

all data sets, within each data set there exists a range of possible values, following the assumption that Equation (3.1.1), (3.1.3) and (3.1.4) must be simultaneously valid. Thus ZS indicates $0.41 < \kappa < 0.42$; MLJMS indicates $0.41 < \kappa < 0.43$; MMJS indicates $0.39 < \kappa < 0.41$; HVBS indicates $0.39 < \kappa < 0.41$; and VS indicates $0.39 < \kappa < 0.41$. However, since these ranges represent an overlap of three separate 95% confidence ranges, the confidence of κ lying within this range for each data set is actually lower. This is demonstrated by the probability density functions (pdfs) shown in Figure 3.7*b*, which were compiled from combining all three methods used to estimate κ using the uncertainty analysis described in Bailey et al. [2014]. We see that the most probable value of κ is 0.40 for the three most recent data sets, arising from reduced uncertainty in the fitting of Equation (3.1.1) at high Reynolds numbers combined with the higher uncertainty in fitting Equation (3.1.3) and (3.1.4) for these data sets. Conversely, the ZS and MLJMS data sets indicate the most probable value of κ is 0.42 due to the agreement between the fits of Equation (3.1.3) and (3.1.4) (and reduced uncertainty) for these data sets.

Using these p.d.f.s, it can also be determined that the confidence of κ being within the intervals of overlap in 95% confidence for the three techniques is approximately 50% or less for the ZS, MLJMS, MMJS and HVBS data sets (i.e., a 50% chance that $0.41 < \kappa < 0.42$, $0.41 < \kappa < 0.43$, $0.39 < \kappa < 0.41$, and $0.39 < \kappa < 0.41$ respectively). In comparison the agreement between the three estimates of κ for the VS data set results in a 73% confidence that $0.394 < \kappa < 0.408$, indicating that this data set is the one least affected by undetected bias errors. The 95% confidence interval for this data sets combining the three approaches was found to be $0.389 < \kappa < 0.411$.

Thus, if we consider only the single VS data set, we could therefore conclude that $\kappa = 0.40 \pm 0.01$. However, doing so would necessarily assume that only this data set was free of undetected bias errors which affected all previous data sets. Such filtering of data sets, although not completely arbitrary, is not prudent and therefore

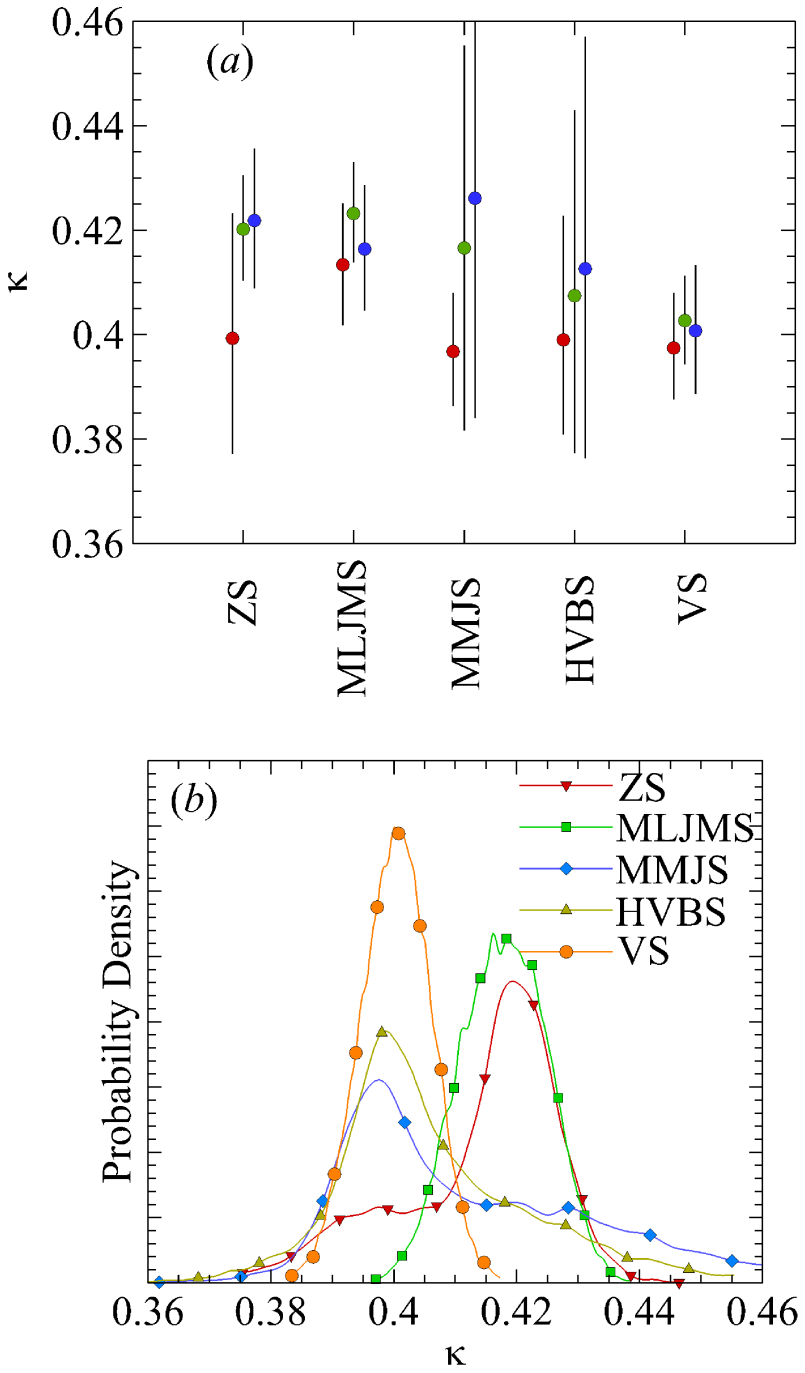

Figure 3.7: (a) Values of κ estimated from each data set with error bars indicating 95% confidence interval. For each data set, the value on the left is obtained from the regression fit to Equation (3.1.1); the one in the center is from the regression fit to Equation (3.1.3); and the one on the right is from the regression fit to Equation (3.1.4). (b) Probability density functions of κ for each data set found by combining uncertainty of all three estimates.

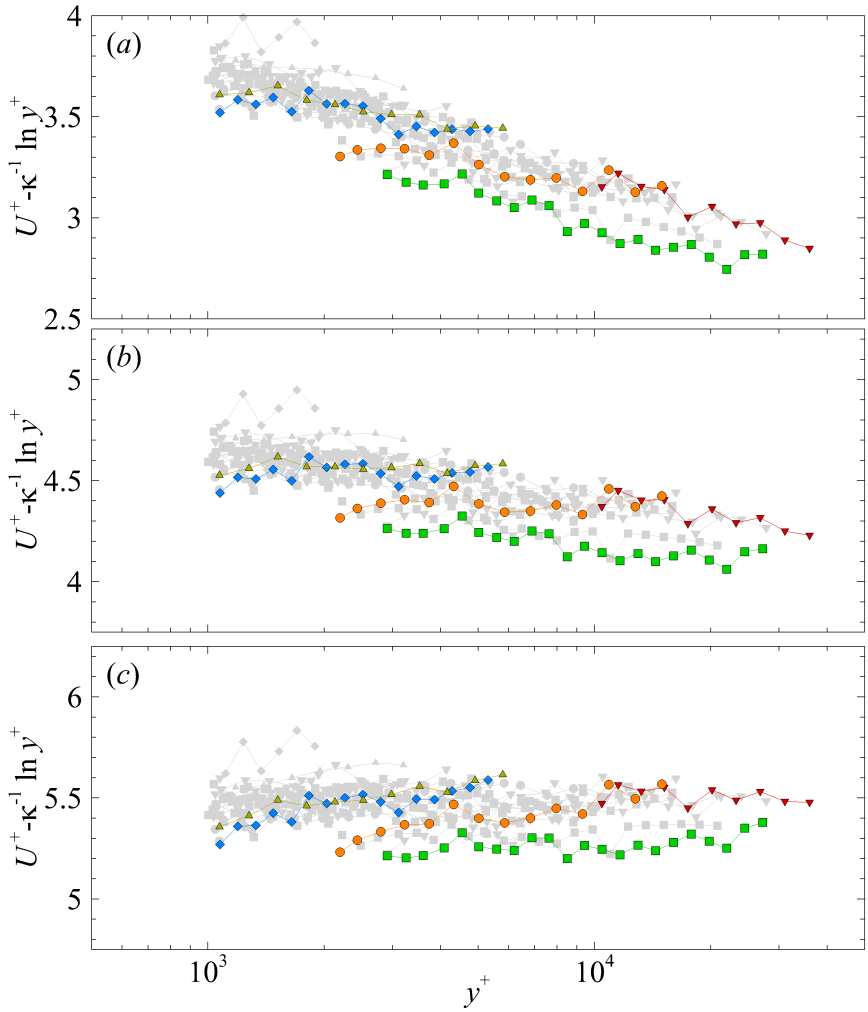

Figure 3.8: Plots of $U^+ - \kappa^{-1} \ln y^+$ within the range $1000 < y^+ < 0.1Re_\tau$ for (a) $\kappa = 0.38$; (b) $\kappa = 0.40$ and (c) $\kappa = 0.42$: $(\triangledown)$ ZS; $(\square)$ MLJMS; $(\diamond)$ MMJS; $(\circ)$ VS; and $(\triangle)$ HVBS. Highlighted profiles are the highest Reynolds number profiles for each data set.

we must consider the complete collection of data. This lack of consensus suggests the actual uncertainty in κ is likely to be higher than that given by any single data set, and a more conservative estimate is $\kappa = 0.40 \pm 0.02$. The profiles in the range $1000 < y^+ < 0.1Re_\tau$ are compared to this range of κ in Figure 3.8*b*, in which the logarithmic region should appear constant and equal to B over the entire overlap layer. These results suggest a value of $B = 4.5 \pm 0.3$ when $\kappa = 0.40$.

This estimate of κ is identical to the recent values found for channel flow by

Jiménez and Moser [2007] and Schultz and Flack [2013], and the uncertainty limits are consistent with the currently accepted values for boundary layers of $\kappa = 0.38$ to 0.39 [Marusic et al., 2013, Nagib and Chauhan, 2008, Österlund et al., 2000]. It would appear, therefore, that the present results support the existence of a universal value of κ. However, inspection of Figure 3.8 which shows the quantity $(U^+ - \kappa^{-1} \ln y^+)$ for $\kappa = 0.38$, 0.4 and 0.42, provides little support for the proposed boundary layer value of $\kappa = 0.38$ within the current pipe flow results. It should also be noted that the present results required a large range of Reynolds number and the use of the most conservative estimate of the logarithmic region to date to obtain a Reynolds number independent estimate of κ. To obtain a comparable estimate for turbulent boundary layers and channels would require significantly more data with $Re_\tau > 10,000$ than is currently available (at least for data accompanied by an independent skin friction measurement).

This is in stark contrast to the recent trend of citing experimentally determined values of κ to high precision (i.e. 0.436 for pipe flow [Zagarola and Smits, 1998], 0.384 for turbulent boundary layers [Nagib and Chauhan, 2008, Österlund et al., 2000], 0.421 for pipe flows [McKeon et al., 2004a], 0.386 and 0.389 for pipe and channel flows [Monty, 2005], 0.387 for the atmospheric surface layer [Andreas et al., 2006]. In the Zagarola and Smits [1998] and McKeon et al. [2004a] studies at least, this level of precision appears overly optimistic.

3.3.4 Conclusions

For the first time, all available smooth-wall mean flow data sets from the Princeton Superpipe were analyzed to determine the von Kármán constant, κ, using three different methods. Due to its large Reynolds number range and controlled conditions, this facility offers a unique opportunity to estimate the value of κ and its attendant uncertainty.

Unlike most prior studies investigating the value of κ for pipe flow, we do not limit our analysis to a single data set. We find no clear consensus on the value of κ obtained from multiple data sets measured largely independently in the same facility, even following the application of all known corrections and taking into account all the known uncertainties. This suggests the actual uncertainty in κ is likely to be higher than given for any single data set studied. Contrary to what has been suggested in previous work, we found that differences between values of κ cannot be attributed only to the differences between hot wire anemometry and Pitot tube measurements. The present results also did not support the recently proposed Reynolds number dependent logarithmic region limits of $3\sqrt{Re_\tau} < y^+ < 0.15Re_\tau$ [Marusic et al., 2013], at least for pipe flows below $Re_\tau \approx 40,000$.

Based on all our observations, we therefore estimate the value of κ for high Reynolds number pipe flow to be 0.40 ± 0.02.

The fact that, even with this facility, using modern instrumentation, the value of κ can only be determined to within this precision is a notable result. In order to obtain a more precise estimate of κ, improved experimental techniques are required, accompanied with carefully conducted experiments and analysis. It should also be noted that evaluation of κ in turbulent boundary layers is even more challenging, given that measurements of u_τ are less accurate.

3.4 Logarithmic scaling of turbulence

Despite these uncertainties regarding the value of κ, the mean velocity scaling behavior is reasonably well established. Finding the equivalent scaling behavior for the turbulence quantities, however, has been particularly elusive. The Reynolds number scaling of the streamwise Reynolds stress, u^{2+}, which describes the intensity of the turbulence, has been the subject of intensive research. NSTAP measurements have provided us a unique opportunity to measure instantaneous velocities at extremely high Reynolds numbers. Here, we report the scaling behavior of u^{2+} over an unprecedented range of Re_τ and degree of accuracy. NSTAP data were acquired in a smooth pipe for Reynolds numbers ranging between $2 \times 10^3 < Re_\tau < 98 \times 10^3$ (cases 1-6 and 8-9 in Table 3.1). The calibration and data analysis techniques were described in Chapter 3.2.2.

3.4.1 Inner scaling

Figure 3.9 shows the values corrected for spatial filtering [Smits et al., 2011b] of u^{2+} as a function of distance from the wall in inner scaling, y^+, for all Reynolds numbers measured. We begin by examining the results in the near-wall region. Of particular interest in this region is the scaling behavior of the near-wall peak in u^{2+} located at $y^+ \approx 15$. This peak is associated with the location where the turbulence production rates are highest. In the past, it had been postulated that the near-wall turbulence was driven solely by the presence of the wall and therefore u^{2+} would depend on inner variables alone. Earlier studies appeared to support this hypothesis, but results from the high Reynolds number atmospheric surface layer and direct numerical simulations at low Reynolds numbers indicate that the magnitude of this peak is Reynolds number dependent due to interaction between near-wall eddies and those further from the wall [Smits et al., 2011a]. In contrast, recent low Reynolds

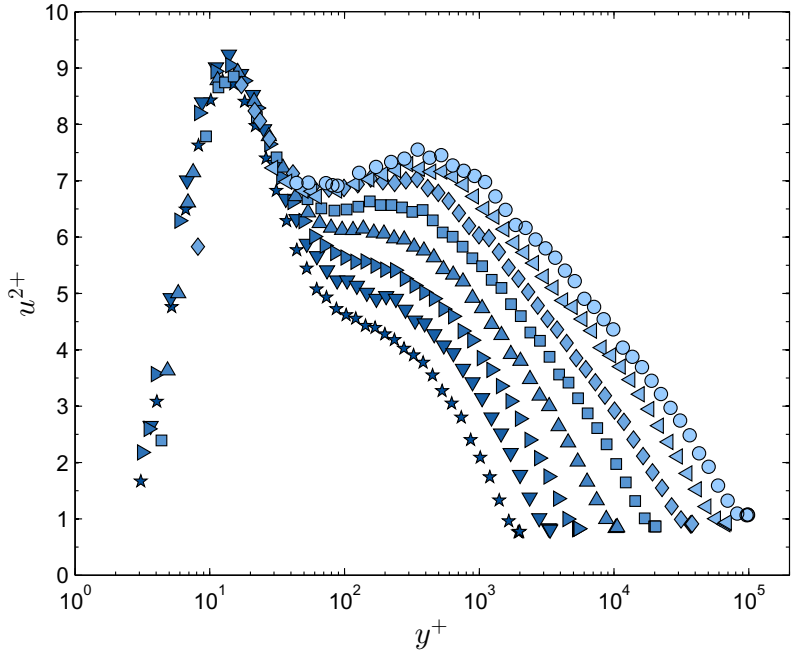

Figure 3.9: Inner scaled turbulence fluctuations for $2 \times 10^3 < Re_\tau < 98 \times 10^3$. ☆, $Re_\tau = 2.0 \times 10^3$; ▽, $Re_\tau = 3.3 \times 10^3$; ▷, $Re_\tau = 5.4 \times 10^3$; △, $Re_\tau = 10.5 \times 10^3$; □, $Re_\tau = 20.3 \times 10^3$; ◇, $Re_\tau = 38 \times 10^3$; ◁, $Re_\tau = 68 \times 10^3$; ○, $Re_\tau = 98 \times 10^3$; Symbols as indicated in Table 3.1.

number results from the Superpipe, presented by Hultmark et al. [2010], indicate that the near-wall peak is independent of Reynolds number, and collapses in inner variables. However, Hultmark et al. [2010] measurements were performed with conventional hot-wire probes and therefore cover a limited Reynolds number range, that may have been too small to reveal an inner peak growth beyond that of experimental uncertainty.

For the results shown in Figure 3.9, it is evident that the magnitude of the inner peak is invariant with Reynolds number, within the range of 9.0 ± 0.3, agreeing with the expected u^{2+} measurement uncertainty of ± 0.3 at this location. This observation applies for $3.3 \times 10^3 < Re_\tau < 20 \times 10^3$ (for higher Reynolds numbers the inner peak was below the measurement point closest to the wall). Note that this value is somewhat higher than those previously reported in lower Reynolds number studies in this fa-

cility; 7.7 using un-corrected hot-wire probes for $691 < Re_\tau < 3336$ [Hultmark et al., 2010], and 8.1 using an NSTAP for $1133 < Re_\tau < 3312$ [Vallikivi et al., 2011]. It is possible, therefore, that the uncertainty in measuring u^{2+} is concealing a slow growth of the inner peak. This problem is compounded by the temporal resolution required to fully capture the turbulence, which may help to explain the difference between the two low Reynolds number data sets: the usual frequency response of a hot wire is considerably lower than that of a typical NSTAP.

This result is in contrast to previous experience with turbulent boundary layers at moderate Reynolds numbers, where the growth of the inner peak is seen to go hand-in-hand with an increasing influence of large-scale outer eddies on the near-wall dynamics. This modulation has been proposed as the basis for a near-wall model for Large Eddy Simulations by Marusic et al. [2010b], but this seems unnecessary for pipe flows where this interaction appears to be minimally significant, or even entirely absent. In this study, new results in high Reynolds number boundary layer are described in Chapter 5, where the behavior of streamwise Reynolds stress in boundary layers will be further discussed.

3.4.2 Outer scaling

In addition to the inner peak at $y^+ \approx 15$, the results presented in Figure 3.9 also reveal the presence of an outer peak between $100 < y^+ < 800$ for the three highest Reynolds numbers measured. Morrison et al. [2004] reported similar behavior, but their observations are sometimes dismissed because at their highest Reynolds numbers $\ell^+ = 385$, and spatial filtering undoubtedly had a significant impact on their measurements. However the current results demonstrate that the existence of this outer peak is a feature of high Reynolds number turbulence, and not simply an artifact of spatial filtering. Furthermore, we can find the position of the outer peak as a function of Reynolds number as $y_p^+ = 0.23(Re_\tau)^{0.67}$. This is slightly different

compared to the findings of Morrison et al. [2004] who found $y_p^+ = 1.8(Re_\tau)^{0.52}$ which is most likely because of the limitations on their data, including a more limited range of Reynolds numbers.

The presence of an outer peak has several important implications for wall-bounded turbulence at extreme Reynolds numbers. First, none of the many turbulence models that exist today will predict its appearance, representing a fundamental flaw in turbulence modeling. Second, at some high Reynolds number the outer peak magnitude could exceed that of the inner peak, simply because the magnitude of the inner peak is a constant multiple of u_τ, and the magnitude of the outer peak is a Reynolds number dependent factor of u_τ. Such behavior reflects a shift in the turbulence production away from the wall with increasing Re_τ as a consequence of the continually increasing separation of scales. Although the rate of turbulence production will always be a maximum closest to the wall, our results imply that the peak production will increasingly occupy a smaller physical region in the flow as the Reynolds number increases. As illustrated in Figure 3.10, although the production rates are lower further away from the wall, turbulence will be produced over an increasingly larger area relative to that corresponding to the near wall production.

The location where the outer peak develops is above $y^+ > 50$, a region where the mean flow is traditionally expected to scale logarithmically. Within this region, Townsend [1976] hypothesized that turbulence production and dissipation should be in equilibrium. However, the development of the outer peak implies that such an equilibrium does not exist in the region of the outer peak ($y^+ \lesssim 800$) since the presence of the peak indicates production exceeds dissipation here. As a result, we should not expect true logarithmic scaling of the mean flow this close to the wall, entirely consistent with the results of McKeon et al. [2004a], who found that logarithmic scaling in the mean flow did not emerge until $y^+ \gtrsim 600$.

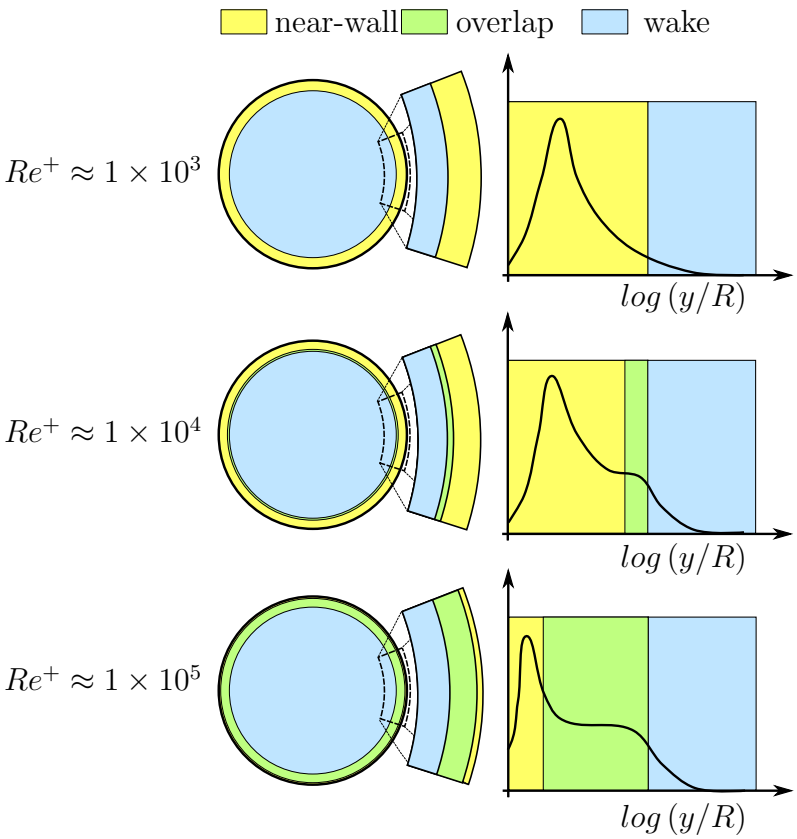

Figure 3.10: Schematic of the different regions of the flow at different Reynolds numbers. To the left in physical space and to the right on a logarithmic axis. The graph shows the production of turbulence kinetic energy in pre-multiplied form (so that equal areas under the graph corresponds to equal contributions to the total production).

3.4.3 Logarithmic region in turbulence

We now shift our attention to this logarithmically scaled region, which forms as an overlap layer between inner and outer scaled regions of the mean flow (that is, the region where $600\nu/u_\tau \leq y \leq 0.15R$).

Logarithmic scaling of the turbulent fluctuations was first predicted by Townsend [1976] who used the attached eddy hypothesis to show that the streamwise and spanwise Reynolds stresses should follow the logarithmic variation given by

$$u^{2+} = B_1 - A_1 \ln\left[\frac{y}{R}\right] \tag{3.4.1}$$

within a region where the eddies scale on y, that is, within the overlap region where the mean velocity displays logarithmic scaling. The spectral assumptions leading to this relation are described in Chapter 7.1. Subsequently, Perry and Abell [1977] used a similarity analysis of the spectral behavior of turbulence in smooth and rough pipe flows to suggest that, in the overlap region,

$$u^{2+} = B_1 - A_1 \ln\left[\frac{y}{R}\right] - F(y^+)^{-0.5} \tag{3.4.2}$$

with $B_1 = 3.53$, $A_1 = 0.8$ and $F = 6.06$. The viscous term was intended to capture the contribution of the smallest eddies to the total intensity such that Equation (3.4.2) asymptotes to Equation (3.4.1) at sufficiently high Reynolds number . Perry et al. [1986] extended the measurements of Perry & Abell and refined the constants to $B_1 = 2.67$ and $A_1 = 0.9$. These pipe flow studies were performed at relatively low Reynolds numbers ($1610 \leq Re_\tau \leq 3900$) and therefore the viscous correction term was always significant.

The existence of the logarithmic region described by Equation (3.4.1) had never been fully validated due to a very limited range of Reynolds numbers achieved in

previous experimental studies, whereas our current experiments cover two orders of magnitude in Reynolds numbers. By plotting the streamwise turbulent fluctuations against y/R, as in Figure 3.11, our results conclusively demonstrate the existence of such a logarithmic behavior for the turbulence intensity. A regression fit of the three highest Reynolds numbers indicates that $B_1 = 1.48 \pm 0.30$ and $A_1 = 1.24 \pm 0.10$.

The measurements presented here are the first to show that the logarithmic scaling only becomes evident for $y/R < 0.15$ once $Re_\tau \gtrsim 20 \times 10^3$ and increasing in spatial extent with Reynolds number until it spans more than a decade in y/R, or 10% of the pipe radius, at the highest Reynolds number measured.

One particularly interesting observation which we can make from Figure 3.11 is that the Reynolds number at which the logarithmically-scaled u^{2+} region appears is approximately the same as the one where the outer peak emerges. Because the logarithmic region extends all the way to the outer peak, we can infer that the outer peak forms as a result of increased scale separation between the inner-scaled turbulent motions produced at the wall and the outer-scaled turbulent motions produced further from the wall.

We have seen that inner scaling in u^{2+} is observed for $y^+ < 80$, and outer scaling is observed for $y^+ > 800$. The intermediate range between these two limits approximately corresponds to that of the power-law-like region in the mean flow, suggesting that in this region the mean flow follows inner scaling, even though there is insufficient scale separation for the fluctuations to form an overlap region — dissipative scales are not fully separated from the energy-containing scales. It was found that the onset of outer scaling, that is, the lower limit of the logarithmic region, corresponds (approximately) to the location where $y/\eta \approx 100$, where η is the Kolmogorov length scale, which gives an estimate of the required scale separation. These observations are consistent with the mesolayer described by Hultmark [2012] which shows up as an offset in the logarithmic behavior of the fluctuations. This concept is also

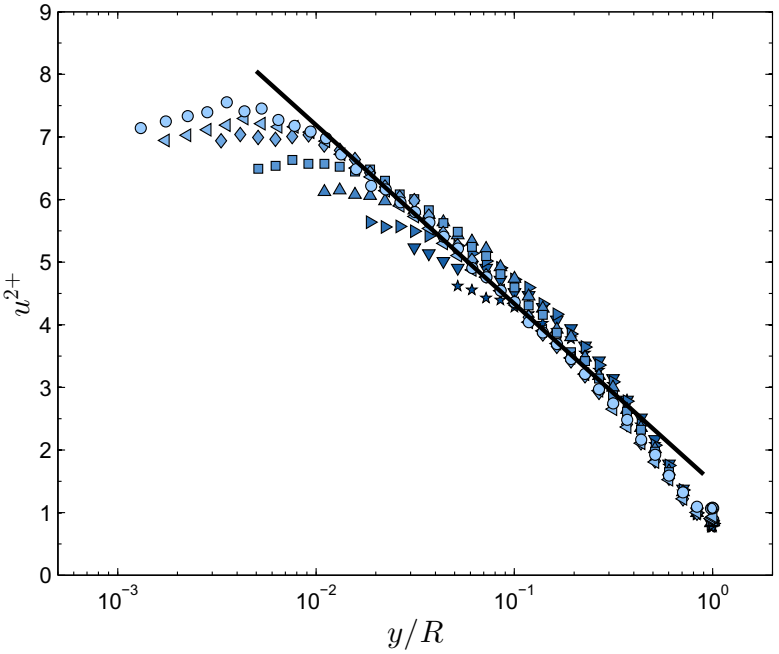

Figure 3.11: Outer scaled turbulence fluctuations for $2 \times 10^3 < Re_\tau < 98 \times 10^3$. Solid line is the log-law of the turbulent fluctuations. Only data for $y^+ > 100$ shown for clarity. Symbols same as in Figure 3.9 and indicated in Table 3.1.

consistent with the presence of a viscous term, as included by Perry et al. [1986] in Equation (3.4.2), since both terms act to reduce the fluctuations compared to the logarithmic equivalence closer to the wall.

We can now seek to relate the turbulence scaling to the mean velocity scaling. We find that when comparing profiles of the fluctuating and mean velocities for very high Reynolds numbers, as is done in Figure 3.12, the same regions identified by McKeon et al. [2004a] for the mean velocity profile are also clearly observed in the turbulence profile. The region where the inner peak in u^{2+} exists ($y^+ \lesssim 50$) corresponds to the near-wall region, where the mean velocity and turbulence profiles scale on inner variables. The region between the inner and outer peaks is a blending region where the mean profile exhibits a power law behavior ($50 \lesssim y^+ \lesssim 800$). Further away from the wall, both the mean and turbulence intensity follow a logarithmic behavior extending up to $y/R = 0.15$. Finally, an outer region can be identified for $y/R > 0.15$

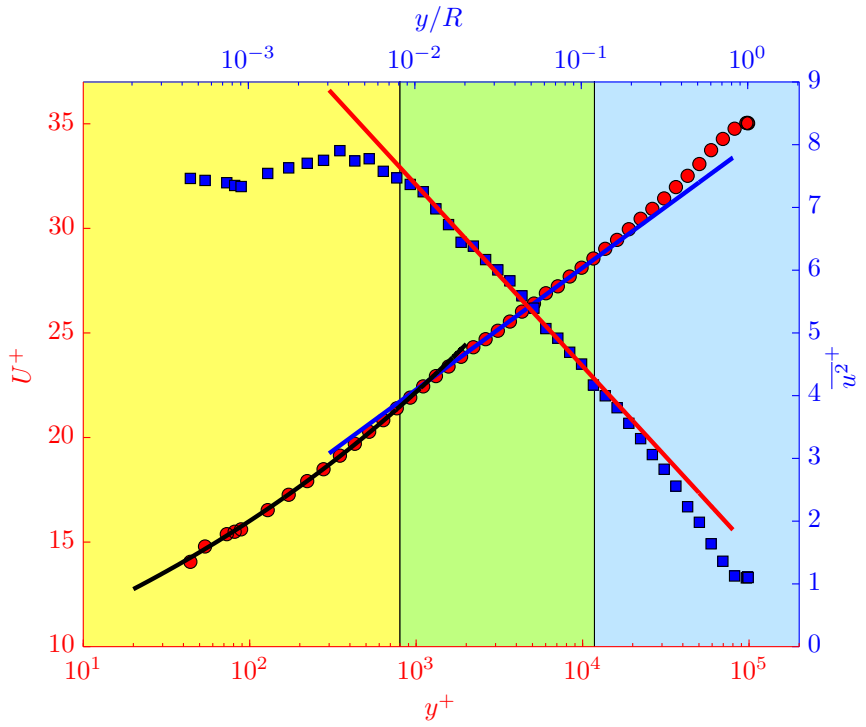

Figure 3.12: Comparison of mean velocity and turbulence streamwise fluctuation profiles for $Re_\tau = 98 \times 10^5$. Red symbols are mean velocities, blue solid line the log-law for the mean velocity and the black solid line is the power-law for the mean velocities as described by McKeon et al. [2004a]. Blue symbols are the turbulence fluctuations and the red solid line is the log-law for the fluctuations, as reported in this chapter. The colors of the different regions are the same as in Figure 3.10.

where the mean velocity and the turbulence intensity scale using outer variables.

These four regions are only truly distinct at the extremely high Reynolds numbers measured in the current study. For lower Reynolds numbers, no separation exists between $y^+ < 800$ and $y/R > 0.15$ and therefore the logarithmic region is not evident, neither in the mean velocity nor in the turbulence. This high degree of correspondence was previously unknown, and presents an important simplification in the modeling of wall-bounded turbulence. It must be noted that the nature of the mean flow power law scaling for $y^+ < 800$ can create the (misleading) impression of logarithmic scaling. Examples can be found in the literature of observations of logarithmically scaled mean flow at Reynolds numbers as low as $Re_\tau \sim O(10^2)$, however here we show that to achieve the scale separation to produce a distinct logarithmically scaled

layer, $Re_\tau \sim O(10^4)$.

3.4.4 Conclusions

The measurements reveal that high Reynolds number turbulence displays a previously unknown similarity to the mean velocity distribution, in that the near-wall behavior is Reynolds number independent (corresponding to the viscous and buffer layer regions in the mean velocity), there is a transitional regime that links the near-wall region to the logarithmic region (corresponding to McKeon et al. [2004a] power law region), and there is an outer region that spans the same range as that seen in the mean flow, both for the logarithmic region and the wake region.

It was observed that the nature of the interface between the inner-scaled near-wall region and outer-scaled logarithmic region produces a peak in the streamwise Reynolds stress distribution, which appears at the same Reynolds number where the logarithmic region becomes established. This confirms earlier observations in high Reynolds number flows, where a similar outer peak has been noted. The onset of the logarithmic region is found at location where the wall distance is equal to about 100 times the Kolmogorov length scale.

Thus, our results suggest that modeling wall-bounded turbulent flows at extreme Reynolds numbers can be greatly simplified. In particular, at these extremely high Reynolds numbers the logarithmically scaled overlap layer will increasingly dominate the near wall flow, occupying as much as 12% of the pipe radius, whereas the inner-scaled region at these Re_τ values will occupy much less than 1%. Correspondingly, a greater percentage of turbulence production will also move to the overlap layer and, at extremely high Reynolds numbers, the near-wall turbulence production cycle will ultimately become irrelevant. In the limit of infinite Reynolds number, the entire flow will scale only with y/R, and one of the essential difficulties with wall-bounded turbulence, which is that it is a two-scale problem, will vanish.

Chapter 4

Turbulence in rough-wall pipe flow

4.1 Introduction

One of the more important concepts for the understanding of turbulent flows over rough surfaces is Townsend's hypothesis [Townsend, 1976], which states that if the height of the shear layer, R, is much larger than the roughness height, k, the only effect of the roughness is to change the boundary condition by changing the wall shear stress. In all other respects, the flow far from the roughness elements is independent of the wall roughness. That is, when the mean flow and turbulent fluctuations are scaled by the friction velocity the profiles are universal, although the mean velocity profile in inner coordinates will be shifted downward by an amount that depends on the roughness.

Townsend's hypothesis has been confirmed by many authors [see for example Allen et al., 2007, Flack et al., 2005, Kunkel et al., 2007], although some studies found the geometry of the roughness to be important through its effect on the turbulence, especially in the transitionally rough regime. Jiménez [2004] noted that most of these studies had large values of the relative roughness ratio k/R, and he proposed that the influence of the geometry of the roughness on the outer flow should diminish

as $k/R \to 0$ since the information of the roughness reaches the outer flow after a long series of eddy interactions. He further stated that high quality experiments are needed with simultaneous small k/R and large k^+ values, which implies very high Reynolds numbers. This was attempted by Kunkel et al. [2007], who investigated the validity of Townsend's hypothesis by comparing measurements taken in two pipes with different surface roughness for Reynolds numbers up to $Re_\tau = 100 \times 10^3$. One pipe was smooth ($k^+_{rms} < 0.25$), and other was rough so that $k/R = 3.9 \times 10^{-5}$ with k^+_{rms} up to 11, where k_{rms} is the rms roughness height [Shockling et al., 2006]. The results supported Townsend's hypothesis, but the authors noted that experimental errors due to, for example, spatial and temporal filtering of the hot-wire signal added to the uncertainty, especially close to the wall where the two flows showed significant differences.

Here, we are concerned with the scaling behavior of hydraulically smooth, transitionally rough, and fully rough pipe flow at very high Reynolds numbers with small relative roughness. We examine measurements in pipe flow at Reynolds numbers Re_D from 81×10^3 to 6.0×10^6. In terms of the friction Reynolds number, Re_τ, this corresponds to $2.0 \times 10^3 \leq Re_\tau \leq 101 \times 10^3$; all experimental conditions are described in Chapter 3 and listed in Table 3.1.

4.2 Mean velocity

The mean velocity profiles for all Reynolds numbers in the smooth and rough pipes obtained using NSTAP are shown in Figure 4.1, plotted in inner coordinates. For the smooth-wall data set, it is clear that inner scaling collapses the data well up to the wake region whereas the rough-wall pipe, as expected, demonstrates a progressive downward shift of the profiles as k^+_{rms} increases. In all cases, the profiles display the

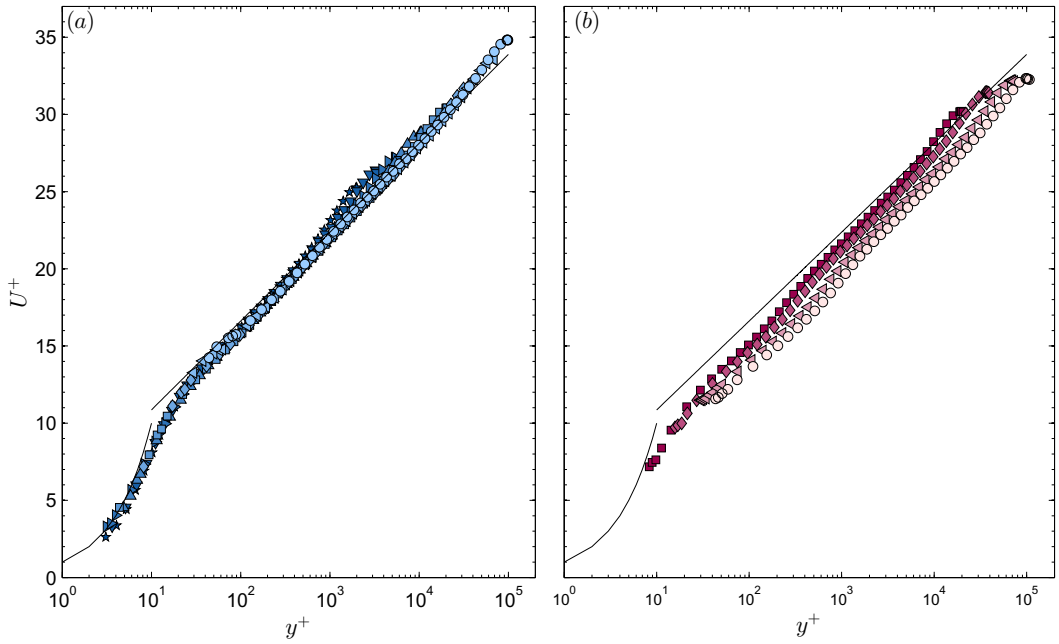

Figure 4.1: Mean velocity profiles for (a) smooth and (b) rough-wall cases: ☆, $Re_\tau = 2.0 \times 10^3$; ▽, $Re_\tau = 3.3 \times 10^3$; ▷, $Re_\tau = 5.4 \times 10^3$; △, $Re_\tau = 10.5 \times 10^3$; □, $Re_\tau = 20.3 \times 10^3$; ◇, $Re_\tau = 38 \times 10^3$ (smooth), $Re_\tau = 37 \times 10^3$ (rough); ◁, $Re_\tau = 68 \times 10^3$ (smooth), $Re_\tau = 69 \times 10^3$ (rough); ○, $Re_\tau = 98 \times 10^3$ (smooth), $Re_\tau = 101 \times 10^3$ (rough). Symbols as indicated in Table 3.1 and lines show linear and log-law.

anticipated region of logarithmic dependence given by

$$U^+ = \frac{1}{\kappa} \ln y^+ + B - \Delta U^+, \tag{4.2.1}$$

where ΔU^+ is the Hama roughness function [Hama, 1954]. The values $\kappa = 0.40$ and $B = 5.1$ found in 3.3 are used throughout current study.

Shift in mean velocity profiles described by Townsend [1976] is compensated by the Hama roughness function ΔU^+. Its magnitude depends on k^+_{rms} and the particular nature of the roughness. The value of ΔU^+ as a function of the equivalent sand grain roughness height, k_s, is compared in Figure 4.2 to that found in the same pipe by Langelandsvik et al. [2007], who used Pitot tubes to acquire the mean velocity data. Langelandsvik et al. [2007] found that $k^+_s = 1.6 k^+_{rms}$, which, given the good agreement shown Figure 4.2, was also assumed for our experiments.

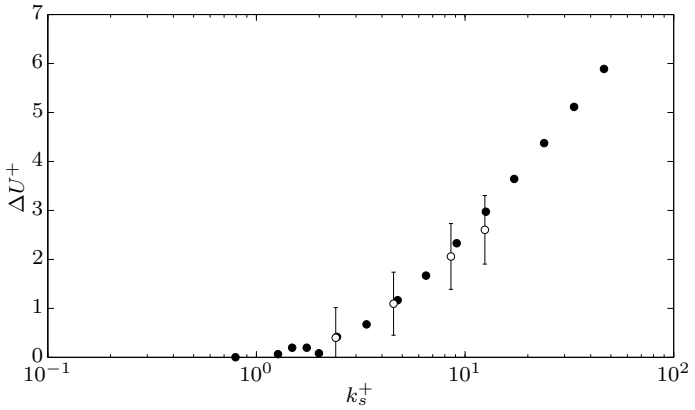

Figure 4.2: Hama roughness function as a function of non-dimensionalized roughness height $k_s^+ = 1.6k_{rms}^+$ from current study (hollow symbols) and from Langelandsvik et al. [2007] (filled symbols).

To better examine the range of applicability of this logarithmic scaling we define the functions

$$\Psi_1 = U^+ - \frac{1}{\kappa}\ln y^+ - B - \Delta U^+ \tag{4.2.2}$$

and

$$\Psi_2 = U_{cl}^+ - U^+ + \frac{1}{\kappa}\ln\left[\frac{y}{R}\right]. \tag{4.2.3}$$

Figure 4.3 shows the variation of Ψ_1 for the three highest Reynolds number cases in inner coordinates for both smooth and rough walled pipes and Figure 4.4 shows the corresponding variation of Ψ_2 in outer coordinates. To better extract the range of validity for the log law, the value of κ used to evaluate Ψ_1 and Ψ_2 for each profile is the one determined from regression fit within the range $1000 < y^+ < 0.1Re_\tau$ for that particular profile. In all smooth cases, the regression fit value was $\kappa = 0.397 \pm 0.001$ and for rough wall cases $\kappa = 0.383 \pm 0.002$, all of which are consistent with the overall uncertainty range $\kappa = 0.40 \pm 0.02$ found in Chapter 3.3.

In Figure 4.3*a*, the lower bound of the logarithmically scaled region appears at $y^+ \approx 800$ with the upper bound at $y/R \approx 0.15$ as illustrated in Figure 4.4*a*. As shown in Figure 4.4*b*, this upper bound describes the upper limit of the logarithmically-scaled region for the rough-walled cases as well. However, Figure 4.3*b*, indicates that the

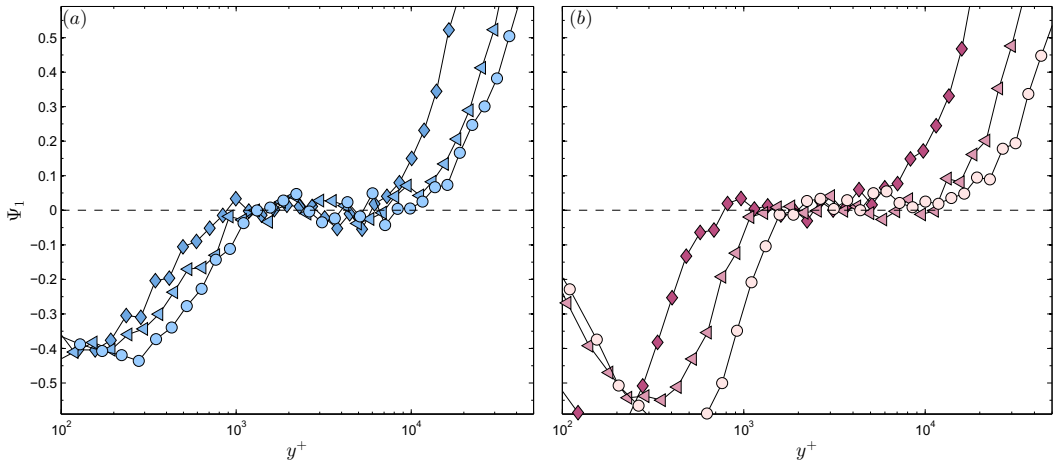

Figure 4.3: The function Ψ_1 defined by Equation (4.2.2) for the three highest Re_τ smooth-wall cases in (a) and rough-wall cases in (b). Symbols as in Figure 4.1 and indicated in Table 3.1.

lower limit for the rough-walled cases is not fixed in inner units and instead appearing fixed at $y/k_{rms} \approx 260$ ($y/R \approx 0.02$) as shown in Figure 4.4b. Given that the upper extent of the roughness sublayer can be expected to be driven by the inertial eddies introduced by the roughness elements, it is perhaps not surprising that the lower limit scales with k_{rms} rather than ν/u_τ. The value of 260, however, greatly exceeds the expected extent of the roughness sublayer (2-5k_{rms}) described by Raupach et al. [1991], suggesting a much greater region of influence of roughness in the present case. However, it should also be noted that for the roughness in the present experiment, the parameter k_{rms} only partially describes the roughness geometry. As observed in Langelandsvik et al. [2007], the surface features for this roughness have spanwise and streamwise scales of dimensions much greater than k_{rms}. Furthermore, considering that viscous effects for the smooth pipe are noticeable up to $y^+ = 800$, or 160 times the viscous sublayer thickness, it is not unlikely that the roughness sublayer of the rough pipe has an equivalent ratio for its region of influence.

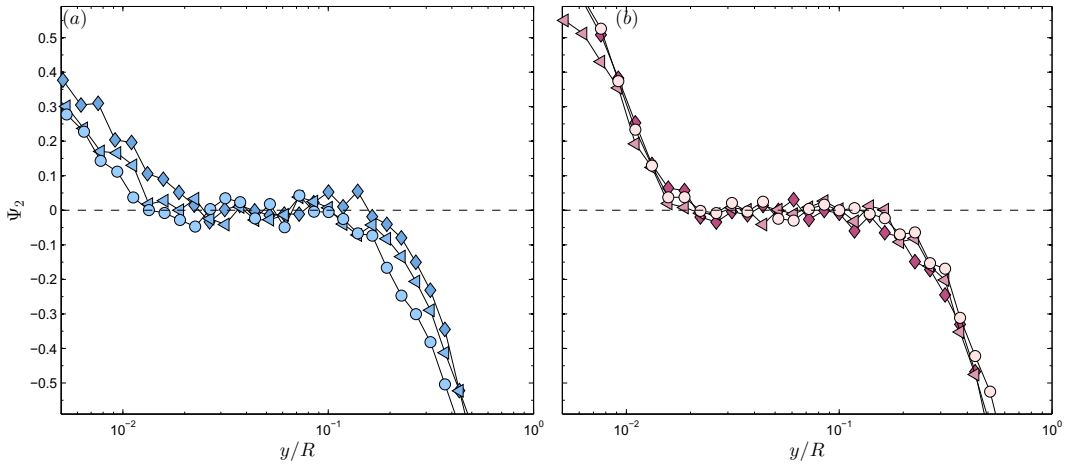

Figure 4.4: The function Ψ_2 defined by Equation (4.2.3) for the three highest Re_τ smooth-wall cases in (a) and rough-wall cases in (b). Symbols as in Figure 4.1 and indicated in Table 3.1.

4.3 Streamwise Reynolds stress

Profiles of the streamwise Reynolds stress u^{2+} for the smooth and rough-wall pipes at all Reynolds numbers are shown in Figure 4.5*a*-*b*.

It is important to consider spatial filtering effects to assure that the data has been sufficiently resolved. Table 3.1 shows that the requirement $\ell^+ < 4$ is only met at the lowest two Reynolds numbers even with the NSTAP, and the maximum value of ℓ^+ was 46 for the smooth case and 93 for the rough case at $Re_\tau = 1 \times 10^5$. To compensate for spatial filtering effects in the smooth wall data, the correction proposed by Smits et al. [2011b] was applied in Chapter 3.4. For the rough wall data, the effects of spatial filtering are potentially more severe, but the correction proposed by Smits et al. [2011b] has not been validated for measurements over rough walls. In general the spatial filtering effects are mostly confined to the near-wall region ($y^+ < 200$) leaving the logarithmic and wake regions essentially unaffected.

As discussed in Chapter 3.4 for the smooth-wall cases, the Superpipe results provide strong support the existence of logarithmic scaling of the streamwise turbulence component within the overlap layer. To illustrate this result, the streamwise Reynolds

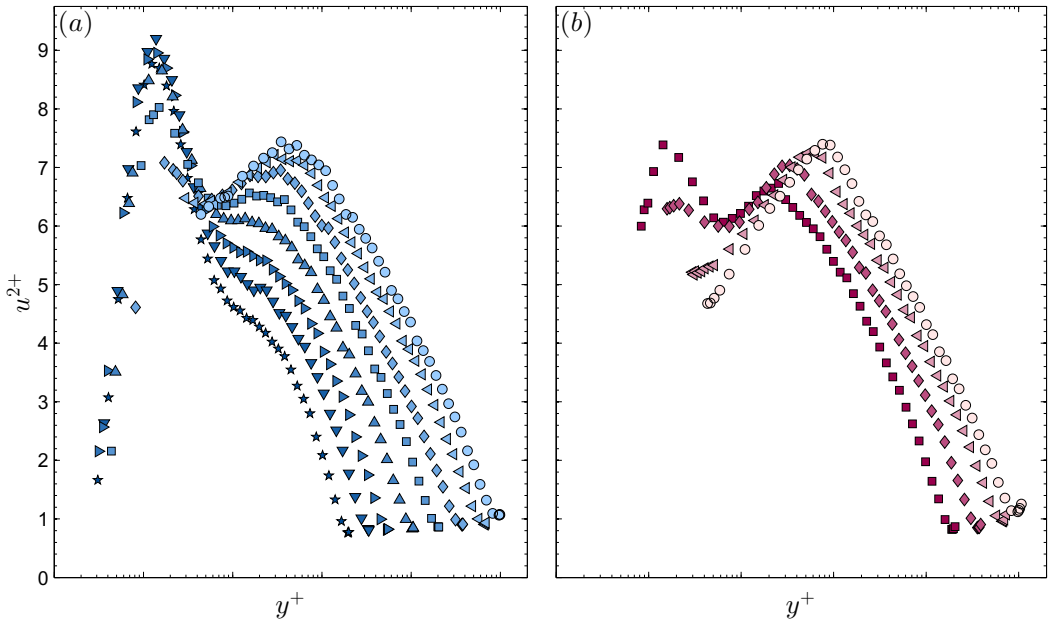

Figure 4.5: Inner scaled streamwise Reynolds stress profiles in the (a) smooth pipe and (b) rough pipe. The same profiles corrected for spatial filtering effects following Smits et al. [2011b] are shown in (c) and (d) respectively. Symbols as in Figure 4.1 and indicated in Table 3.1.

stress results are shown in Figure 4.6a using outer scaling, displaying only the results for $y^+ > 100$ and at the four highest Reynolds numbers, where F is negligible in Equation (3.4.2). The corresponding rough-wall results are given in Figure 4.6b. The outer peak is readily apparent as an unambiguous feature of both smooth and rough pipe flows, and it seems to be particularly well delineated in the rough wall cases. However, unlike the smooth-walled cases, which have a Reynolds number dependent location, as noted in Chapter 3.4, the outer peak appears to be at a fixed location of $y/k_{rms} = 100$ ($y/R = 0.008$), at least for the three highest Reynolds numbers. These figures also highlight the emergence of a logarithmic region for u^{2+} in both smooth and rough-wall flows. A regression fit of the data between $y^+ = 800$ and $y/R = 0.15$ returns $A_1 = 1.24 \pm 0.06$ and $B_1 = 1.48 \pm 0.15$ for the smooth-wall cases, and $A_1 = 1.25 \pm 0.05$ and $B_1 = 1.55 \pm 0.21$ for the rough-wall cases.

To better examine the range of applicability of this logarithmic scaling we define

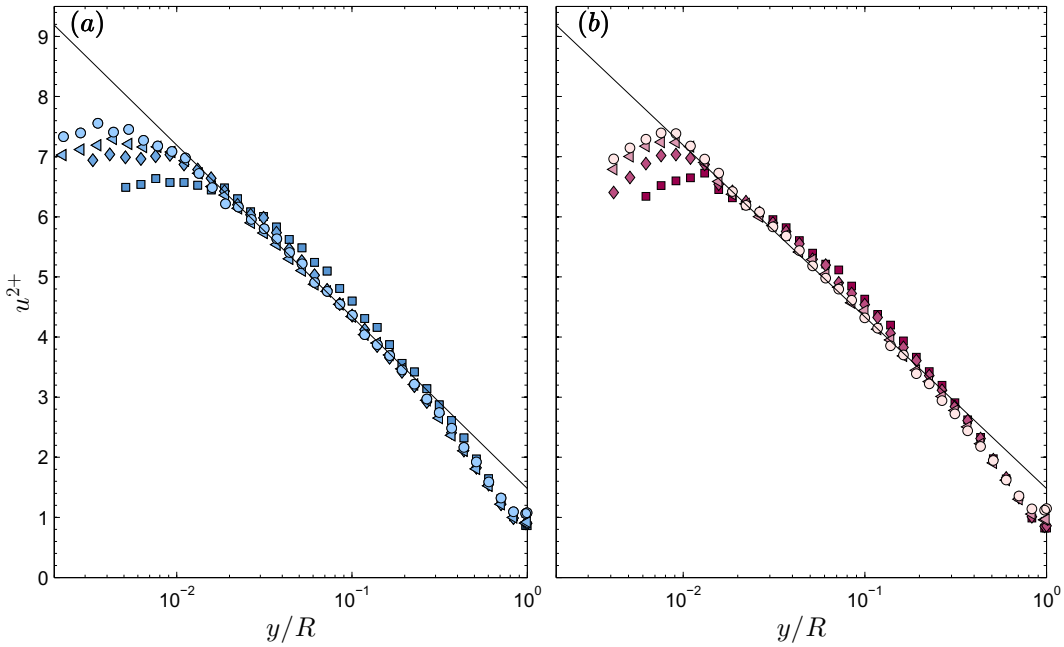

Figure 4.6: Outer scaled streamwise Reynolds stress profiles of four highest Reynolds numbers of (a) smooth and (b) rough-wall data sets. Symbols as in Figure 4.1 and indicated in Table 3.1, with solid line indicating Equation (3.4.1) and constants $A_1 = 1.24$ and $B_1 = 1.48$.

a function

$$\Psi_3 = u^{2+} + A_1 \log \frac{y}{R} - B_1. \tag{4.3.1}$$

Figure 4.7 displays Ψ_3 as a function of inner and outer scaling for the smooth-wall (Figure 4.7*a-b*) and rough-wall cases (Figure 4.7*c-d*). We see that for the smooth-wall case, within data scatter, the streamwise Reynolds stress follows logarithmic scaling over the the same range where the mean flow displays logarithmic scaling of $800 < y^+ < 0.15Re_\tau$. For the rough-wall case, the upper limit for the logarithmic region appears at $y/R = 0.15$, with the lower limit scaling with k_{rms} (or R) rather than ν/u_τ, as in the case of the mean flow. The lower limit appears at $y/k_{rms} = 260$ ($y/R = 0.02$) with a consistent deviation below logarithmic scaling between $y/k_{rms} = 100$ and 260 for all rough-wall cases. For the rough-wall pipe flow at sufficiently high Reynolds number, these results indicate that the Reynolds stress obeys outer scaling for $y/k_{rms} > 260$, and there is an overlap between inner and outer scaling between

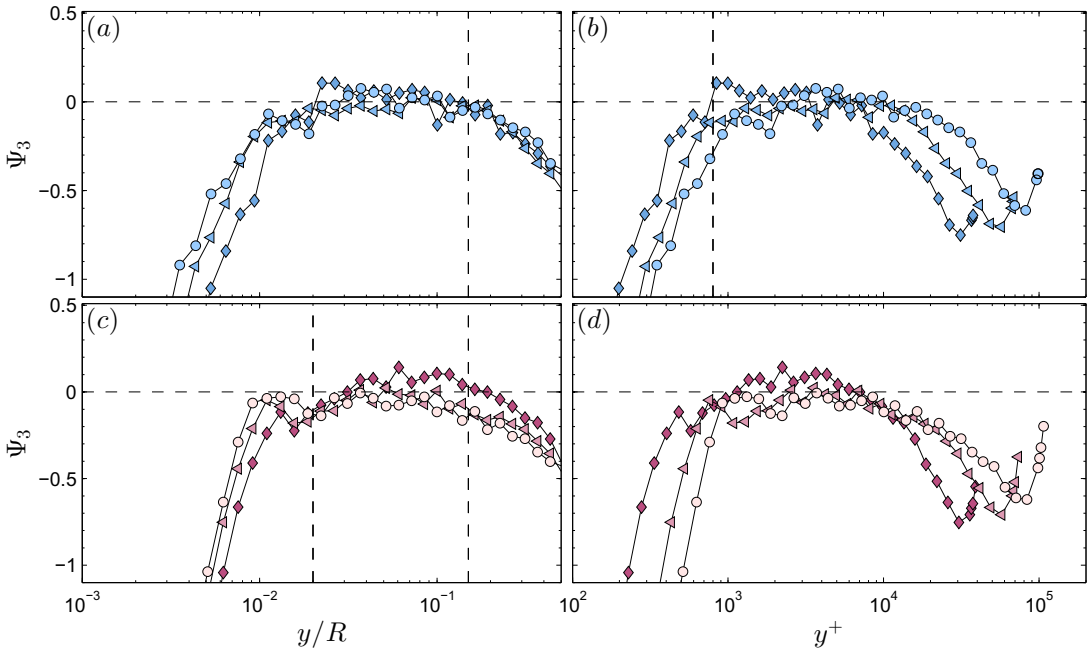

Figure 4.7: Function Ψ_3 defined by Equation (4.3.1). Smooth wall: the three highest Reynolds numbers in (a) outer scaling, (b) inner scaling. Rough wall: the three highest Reynolds numbers in (c) outer scaling, (d) inner scaling. Symbols as in Figure 4.1 and indicated in Table 3.1. The vertical dashed lines in (a) and (b) mark the location where $y/R = 0.15$, and $y^+ = 800$ respectively. In (c) the vertical dashed lines indicate the locations where $y/k_{rms} > 260$ and $y/R > 0.15$.

$y/k_{rms} = 260$ and $y/R = 0.15$.

The mean velocity and the streamwise Reynolds stress distributions are shown together in Figure 4.8, where the wall-normal locations corresponding to the upper and lower limits of the logarithmic mean velocity and Reynolds stress variation are marked by dashed lines. We see that the mean velocity and the turbulence intensity display their respective logarithmic variations over essentially the same range of wall normal distances. This duality occurs for the smooth and rough wall experiments.

We have seen that the mean velocity and the streamwise turbulence intensity each display a logarithmic behavior over the same spatial extent, in both smooth and rough-wall flows. In this region, an outer-scaled log-law must also be valid for the mean velocity,

$$U_{cl}^+ - U^+ = -\frac{1}{\kappa} \ln \frac{y}{R} + B^*, \tag{4.3.2}$$

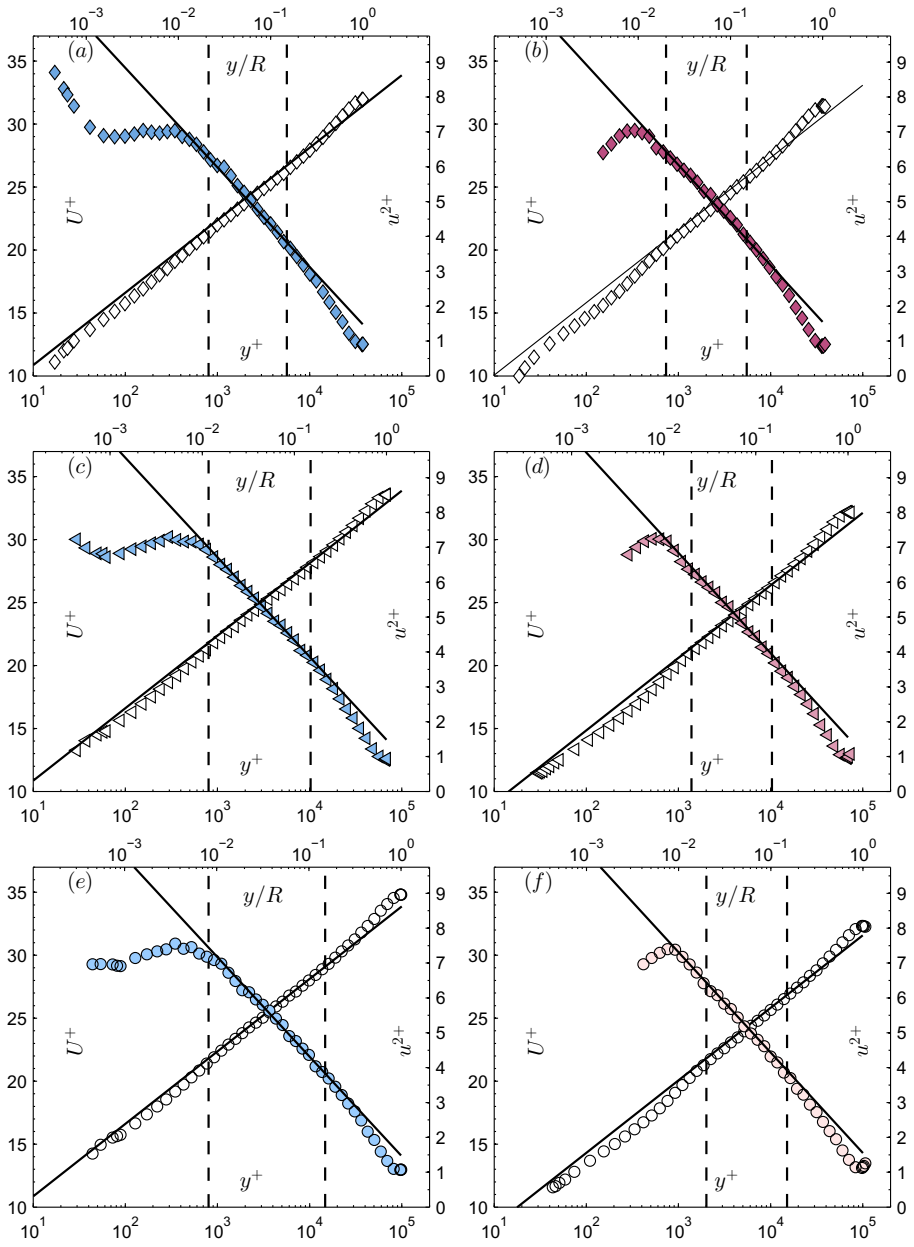

Figure 4.8: Comparison of mean (hollow symbols) and streamwise Reynolds stress (solid symbols) profiles for: (*a*) smooth-wall pipe at $Re_\tau = 38 \times 10^3$; (*b*) rough-wall pipe at $Re_\tau = 37 \times 10^3$; (*c*) smooth-wall pipe at $Re_\tau = 68 \times 10^3$; (*d*) rough-wall pipe at $Re_\tau = 69 \times 10^3$; (*e*) smooth-wall pipe at $Re_\tau = 98 \times 10^3$; and (*f*) rough-wall pipe at $Re_\tau = 101 \times 10^3$. The solid lines represent Equation (4.2.1) and (3.4.1) and dashed lines indicate their region of validity.

where U_{cl}^{+} is the inner-scaled mean centerline velocity and B^{*} is another empirical constant, found here to be approximately 1.0. Equation (4.3.2) and (3.4.1) yield

$$u^{+2} = B_1 - A_1\kappa B^{*} + A_1\kappa\left(U_{cl}^{+} - U^{+}\right) \tag{4.3.3}$$

That is, the variance in the logarithmic region should be a linear function of the velocity defect, which removes uncertainty due to ΔU^{+}, with the further advantage that any uncertainty in the wall position will be eliminated because the fluctuations and the mean are measured at the same point*. This result is plotted in Figure 4.9, for $y^{+} > 100$. And it is clear that the data follow this linear variation $u^{2+} \sim U^{+}$, particularly for the three highest Reynolds numbers where the viscous damping term of Equation (3.4.2) is negligible. This result contradicts conventional eddy viscosity or mixing length arguments, where the stresses are related to velocity gradients ($u^2 \sim (\partial U/\partial y)^2$) not velocity U itself.

4.4 Higher order moments of streamwise velocity

The Reynolds stress describes only the second central moment of velocity, and it is also interesting to explore the behavior of the higher order moments, especially the third and fourth order central moments, $u^{3+} = \overline{u^3}/u_\tau^3$ and $u^{4+} = \overline{u^4}/u_\tau^4$, respectively. Morrison et al. [2004] found no evidence of scaling of the higher order moments but their results were potentially dominated by spatial filtering effects and, as observed by Bailey et al. [2010], spatial filtering effects are amplified with increasing order of moment. Although the NSTAP offers an improvement over conventional hot-wires, for the majority of the Reynolds numbers measured $\ell^{+} > 4$ and therefore the effects of spatial resolution cannot be neglected on the higher order moments. Hence, we limit the analysis to wall-normal locations where the spatial filtering correction of

*This presentation was suggested to us by P. H. Alfredsson of KTH.

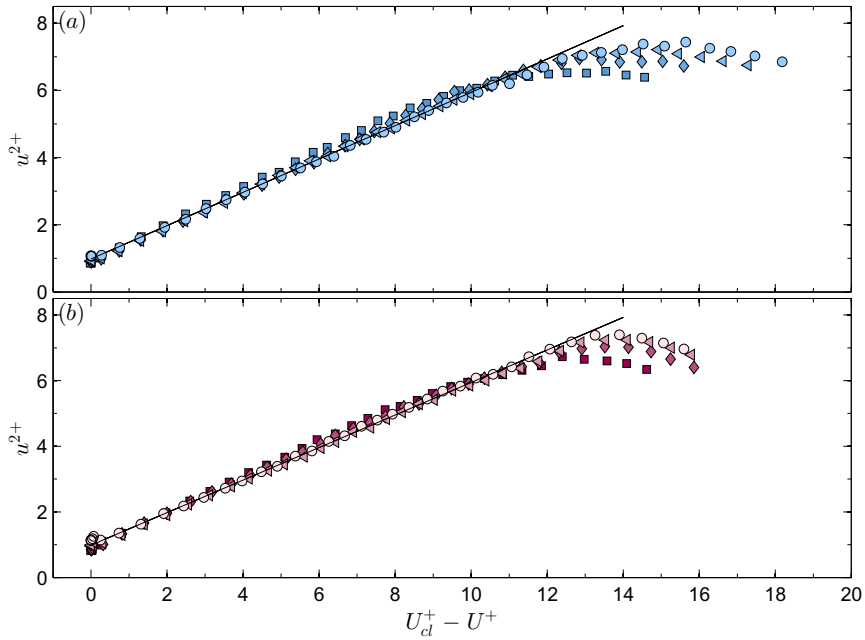

Figure 4.9: Cross plot of streamwise Reynolds stress and mean velocity data for (a) smooth and (b) rough-wall data sets, for the four highest Reynolds numbers and $y^+ > 100$. Symbols as in Figure 4.1 and indicated in Table 3.1, with solid line indicating Equation (4.3.3). Symbols as in Figure 4.1.

Smits et al. [2011b] predicts attenuation of u^{2+} to less than 3%.

The skewness and flatness profiles are shown for the three highest Reynolds numbers in Figure 4.10 for $y^+ > 100$ using outer coordinates. At these high Reynolds numbers, the results depend only weakly on Reynolds number and roughness effects. Although the flatness remains approximately constant at 2.7 throughout the logarithmic layer, slightly below the Gaussian value, the skewness varies over the same range of y/R, and it does not appear that the pipe flow results follow the same self-similar behavior in the logarithmically scaled region observed in turbulent boundary layers [Tsuji et al., 2005].

We will return to the skewness after considering the scaling of u^{4+}. For a Gaussian distribution, we expect that the flatness is equal to 3, so that $u^{2+} = (u^{4+}/3)^{0.5}$. We see from Figure 4.10 that the flatness in the logarithmic region is close to Gaussian at a value of about 2.7, so we explore the wall-normal dependence of $(u^{4+})^{0.5}$ (see

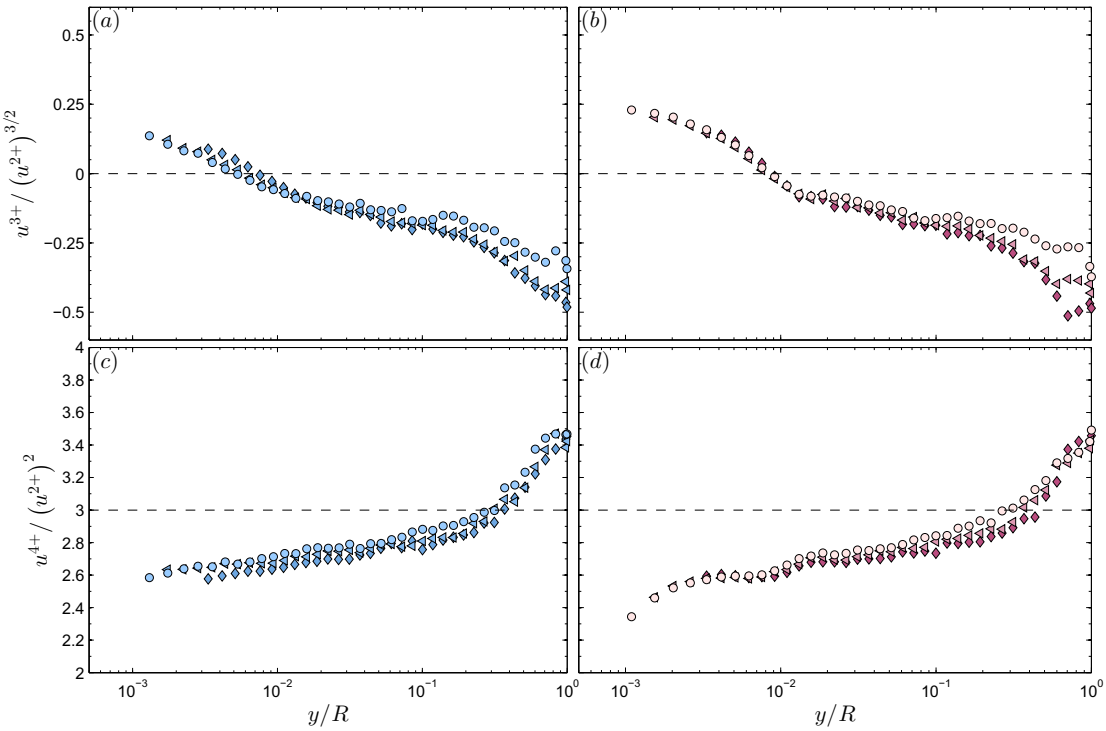

Figure 4.10: Profiles of skewness from the (a) smooth- and (b) rough-walled pipes in outer coordinates for the three highest Reynolds numbers. Corresponding flatness profiles shown in (c) and (d) for smooth-walled and rough-walled pipes respectively. Only data points above $y^+ = 100$ shown for clarity. Symbols as in Figure 4.1 and indicated in Table 3.1.

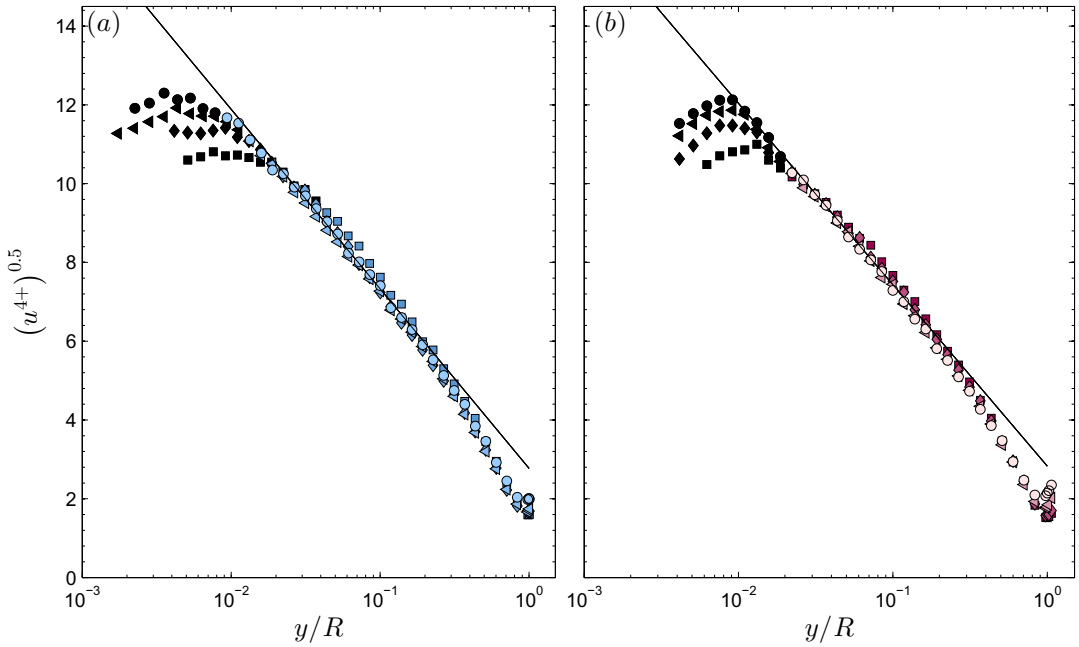

Figure 4.11: Profiles of $(u^{4+})^{0.5}$ from the (a) smooth- and (b) rough-walled pipes in outer coordinates. Symbols as in Figure 4.1 and indicated in Table 3.1, with data points below $y^+ = 800$ for the smooth-walled flow and $y/k_{rms} = 260$ for the rough-walled flow indicated using black symbols. For clarity, only the four highest Reynolds numbers are shown and only for $y^+ > 100$. Solid line is Equation (4.4.1).

also Meneveau and Marusic [2013]). Figure 4.11 shows that there is strong evidence for the existence of a logarithmically scaled region in $(u^{4+})^{0.5}$ over the same Reynolds number range where logarithmic scaling is evident in u^{2+}, closely following

$$(u^{4+})^{0.5} = D_1 - C_1 \log\left[\frac{y}{R}\right] \tag{4.4.1}$$

with $D_1 = 2.78 \pm 0.46$ and $C_1 = 1.98 \pm 0.16$ for the smooth pipe and $D_1 = 2.83 \pm 0.25$ and $C_1 = 2.00 \pm 0.06$ for the rough pipe. Note that for the smooth wall, $B_1\sqrt{3} = 2.6 \approx D_1$, and $A_1\sqrt{3} = 2.17 \approx C_1$, as expected if the p.d.f. followed a normal distribution (we obtain 2.73 and 2.05 if instead we use 2.7, the measured value of the flatness). Similar results are found for the rough wall experiments.

Figure 4.11 also indicates that, for sufficiently high Re_τ, this logarithmic region extends over the same range of wall distance as for the mean velocity and Reynolds

stress. To illustrate this point, the data points that lie below the lower logarithmic limits have been indicated in Figure 4.11 using solid symbols. It therefore appears that the logarithmic scaling extends beyond the second moment due to the near-normality of the velocity p.d.f. in the log layer.

Returning to the skewness behavior, Mathis et al. [2009] noted that there is an indication that the skewness reflects modulation of the near wall flow by outer-scaled eddies. Similarly, the lack of scaling in the even moments within the logarithmic region at lower Reynolds numbers may indicate a significant interaction between the outer-scaled and inner-scaled eddies due to insufficient scale separation. Interestingly, once a logarithmically scaled region forms, comparison of Figures 4.10 and 4.11 reveals that the location where the outer peak forms at high Re_τ closely corresponds to the location where $u^{3+} = 0$. Hence, it would appear that the outer peak is related to the modulation of the near-wall flow. We also note that, although potentially attributable to experimental uncertainty, the weak Reynolds number dependence in u^{3+} in the outer and logarithmic layers suggests that complete similarity does not exist.

4.5 Conclusions

Measurements of the streamwise component of the velocity in fully-developed pipe flow for two pipes with different surface roughness conditions were analyzed; one machined to provide a hydraulically smooth surface and the other consisting of a commercial steel pipe with irregular elements of small relative roughness.

A strong duality between the scaling of the mean velocity profile and the turbulence fluctuations was observed, with an inner-scaled region extending to $y^+ \approx 50$ occupying the same span as the combination of the viscous sublayer and the buffer region in the mean velocity profile. A wake region in the turbulence intensity scales

with y/R and extends outwards from $y/R > 0.15$, similar to that of the mean flow. More interestingly, a logarithmic behavior of the streamwise Reynolds stress under hydraulically smooth, transitionally rough, and fully rough conditions was observed for Reynolds numbers higher than $Re_\tau > 20 \times 10^3$, in a region corresponding to the logarithmic scaling in the mean flow. This extends the results shown in Chapter 3.4 to include transitionally rough and fully rough flows. In addition, in this region of logarithmic scaling, the streamwise turbulence intensity scales with the mean velocity defect, which contradicts conventional eddy viscosity or mixing length arguments.

It was observed that the nature of the interface between the inner-scaled near-wall region and outer-scaled logarithmic region produces a peak in the streamwise Reynolds stress distribution, which appears at the same Reynolds number where the logarithmic region becomes established. This confirms earlier observations in high Reynolds number flows, where a similar outer peak has been noted. The onset of the logarithmic region is found at a location where the wall distance is equal to $\sim$100 times the Kolmogorov length scale.

Additionally, higher-order statistics were investigated and it was shown that, in the logarithmic region the square root of the fourth-order moment also displays a logarithmic region in y/R. The behavior of higher order statistics is further discussed in Chapter 6, where the results are also compared with high-order statistics from turbulent boundary layer.

Chapter 5

Turbulent boundary layer flow

5.1 Introduction

The scaling of turbulent wall-bounded flows with Reynolds number has been the subject of considerable interest (see Chapter 1, Marusic et al. [2010c], Smits et al. [2011a], Smits and Marusic [2013]). Boundary layers, pipe flows and channel flows are often assumed to scale with the same variables, namely the friction velocity $u_\tau = \sqrt{\tau_w/\rho}$ and either the viscous length scale ν/u_τ for the inner region of the flow, or the boundary layer thickness δ (radius R for pipes, half height h for channels) for the outer flow. The validity and applicability of these scaling behaviors at high Reynolds numbers is still an open subject.

5.1.1 Mean Flow

For turbulent boundary layers at sufficiently large Reynolds numbers, one can expect an overlap region between the inner and outer scaling of the flow, similarly to the pipe flow discussed in Chapter 3.1. In this log-region (or turbulent wall region), the

mean velocity U can be expected to behave logarithmically, expressed as

$$U^+ = \frac{1}{\kappa} \log y^+ + B. \tag{5.1.1}$$

In recent years, with advancing measurement techniques and facilities, high quality measurements over a wide range of Reynolds numbers have been reported, with some evidence showing that in different wall-bounded flows the start and extent of the logarithmic region, and the value of the von Kármán constant may vary. More extended discussion on mean flow scaling is given in Chapter 3.1.

The start of the log-law region was commonly assumed to be located at $y^+ = yu_\tau/\nu = 30 - 50$, but recent studies indicate values as high as $y^+ = 800$ for pipe flows (Chapter 3.4.3, Hultmark et al. [2012]) and for boundary layers, recently a Reynolds number dependent lower limit of $y^+ = 3Re_\tau^{0.5}$ was used by Marusic et al. [2013] (as a conservative lower bound), where $Re_\tau = u_\tau \delta/\nu$. As to the outer limit, values in the literature range from $y/\delta = 0.08$ to 0.3, Marusic et al. [2013] suggesting $y/\delta = 0.15$. The values of the von Kármán constant reported in the past have also varied over a considerable range, with values as low as 0.38 in a boundary layer (Österlund et al. [2000]) and as high as 0.42 in a pipe (McKeon et al. [2004a]). More recently, the value of 0.38 given by Nagib and Chauhan [2008] has garnered considerable experimental support, although the maximum Reynolds number Re_τ for this data set did not exceed 10,000. In Chapter 3.3 it was shown that there is a large error associated with estimating the slope of the mean flow, yielding an estimate of von Kármán constant in pipe flow with wide error bar $\kappa = 0.40 \pm 0.02$ even when u_τ is well known. For boundary layers one would expect an even larger variation due to the difficulty in estimating friction velocity.

5.1.2 Turbulence intensities

The scaling of turbulent intensities in boundary layers has not been so widely studied. The main reason being the difficulties in conducting experiments at high Reynolds numbers and being able to spatially and temporally resolve the turbulent fluctuations. Whereas many studies on turbulent boundary layers have been made, only few of them reported Reynolds stresses with reasonable resolution at high enough Reynolds numbers where scale separation could be expected. The most notable study was made by DeGraaff and Eaton [2000] using Laser Doppler Anemometry to resolve all three components of velocity instantaneously for up to $Re_\tau \approx 14,000$. They found that the streamwise Reynolds stresses did not scale with u_τ^2 even in the near-wall region and proposed a mixed scaling with $u_\tau^2\sqrt{C_f/2}$ instead. It must be noted though, that they did not have direct measurements of wall shear stress and used Coles log law [Coles, 1956] for estimating u_τ.

As already described in Chapter 3.1, Townsend [1976] and Perry et al. [1986] suggested that logarithmic behavior in fluctuations should occur in the overlap region if large enough scale separation is reached in the flow. This logarithmic behavior was first observed experimentally by Hultmark et al. [2012] in pipe flow, followed by Marusic et al. [2013] who showed this scaling also applies in boundary layers, and Huisman et al. [2013] who showed it for turbulent Taylor-Couette flow. In the inertial subrange the turbulent fluctuations can be described with

$$u^{2+} = B_1 - A_1 \ln \frac{y}{\delta}, \tag{5.1.2}$$

where A_1 is a Townsend-Perry constant and B_1 is an additive constant, at least for a fixed Reynolds number. Marusic et al. [2013] compared four different flows and suggested $A_1 = 1.26$ for all flows compared, where the boundary layer data studied had a maximum $Re_\tau \approx 18,000$.

In order to establish these and other parameters more precisely, it is necessary to obtain high quality and high resolution experimental data over a very large range of Reynolds numbers. At Princeton, we have the facilities and the instrumentation to make these measurements possible. Here we describe well resolved turbulent zero pressure gradient boundary layer measurements at 2,600< Re_τ <72,000.

5.2 Experimental methods

5.2.1 Experimental Facility

The boundary layer measurements were conducted in the High Reynolds Number Test Facility (HRTF) at Princeton University Gas Dynamics Laboratory (shown in Figure 5.1(a)). It is a closed-loop wind tunnel with air as the working fluid that can be compressed up to 220 atm, thus decreasing the kinematic viscosity and therefore allowing to achieve and study a wide range of Reynolds numbers in laboratory conditions. The wind tunnel has a maximum speed of 12 m/s and freestream turbulence intensity levels between $0.3 - 0.6\%$. The tunnel has two working sections, each 2.44 m long with a 0.61 m outer and 0.49 m inner diameter. The sketch of the tunnel is shown in Figure 5.1(b) and the tunnel itself has been described in further detail by Jiménez et al. [2010].

A 2.06 m flat plate model with an elliptic leading edge was mounted in the downstream test section of the wind tunnel. A 1 mm square trip wire, located at 76 mm from the leading edge, was used to trip the boundary layer and the measurement station was located 1.82 m downstream of the trip wire. The schematic of the setup is shown in Figure 5.1(c). The aluminum surface of the plate was carefully polished to a mirror finish. The surface roughness was estimated using an optical microscope and comparator plates and found to be less than 0.15μm, corresponding to $k^+_{rms} < 0.4$ at the highest Reynolds number studied. Therefore all experiments reported here

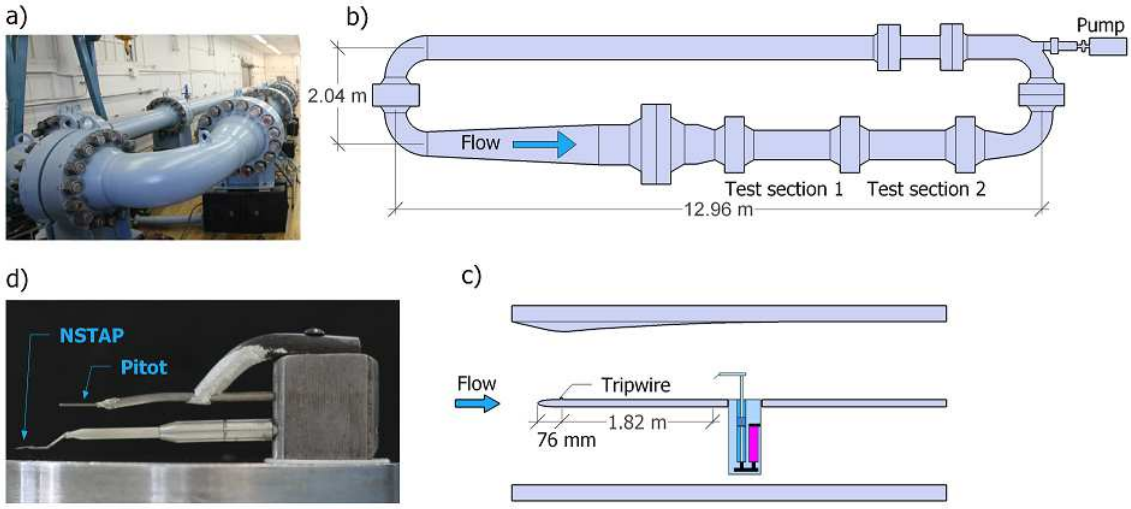

Figure 5.1: The Princeton High Reynolds Number Test Facility (HRTF). a) Photo of the facility, b) sketch of the tunnel, c) sketch of the boundary layer setup, d) image of the probe holder with an NSTAP and Pitot probe.

pertain to a hydraulically smooth surface.

The pressure distribution in the circular test section was adjusted using a "blister" insert attached to the tunnel wall on the opposite side of the plate, as shown in Figure 5.1(c). The pressure distribution was measured using 18 streamwise and 15 spanwise pressure taps, and the insert was adjusted to minimize the pressure gradient. The local streamwise pressure gradient parameter (or acceleration parameter) $K_p = \frac{\nu}{U_\infty^2}\frac{\mathrm{d}U_\infty}{\mathrm{d}x} = \frac{\nu}{\rho u_\tau^3}\frac{\mathrm{d}p}{\mathrm{d}x}$ was found to be always smaller than 1×10^{-8}, as shown in Figure 5.2. This value is an order of magnitude smaller than that reported in some previous studies (for example DeGraaff and Eaton [2000] reported $K_p < 1.1\times10^{-7}$), and therefore this flow is considered to be free of pressure gradient effects.

5.2.2 NSTAP measurements

In the current study, two Nano-Scale Thermal Anemometry Probes (described in Chapter 2) were used, one with filament length $\ell = 60\mu$m and cross-section $0.1\times2\mu$m

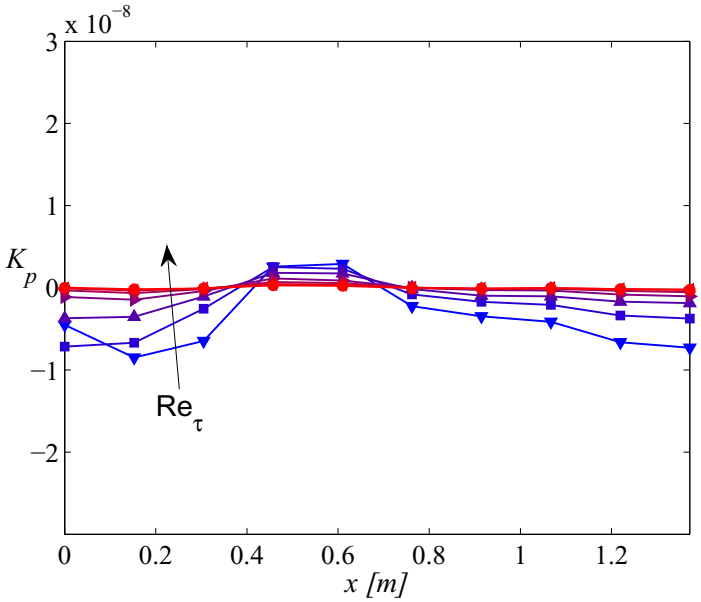

Figure 5.2: The pressure gradient parameter K_p for all Reynolds numbers studied varying with upstream location x.

and second one with $\ell = 30\mu$m and $0.08 \times 1.5\mu$m cross-section. An image of a representative 30μm probe of the design used is shown in Figure 2.7.

The sensors were operated using a Dantec Streamline Constant Temperature Anemometry system with a 1:1 bridge, keeping the heated filament at a temperature of about 450 K. The frequency response, determined from a square wave test, was always above 150 kHz in still air, which increased to more than 300 kHz at the highest Reynolds number. The data were low-pass filtered using an eighth-order Butterworth filter at 150 kHz and digitized using a 16-bit A/D board (NI PCI-6123) at a rate of 300 kHz. The sensor was traversed in wall-normal direction y using a stepper motor traverse with a Numeric Jena LIK22 encoder resolution of 0.05 μm (the NSTAP sensor with probe holder is shown in Figure 5.1). The initial wall-normal distance y_0 of the NSTAP probe was measured using a depth measuring microscope (Titan Tool Supply Inc.) which provided accuracy of 5 μm.

The NSTAP was calibrated using the pressure difference between a 0.4 mm Pitot

tube and two 0.4 mm static pressure taps located in the pipe wall at the same streamwise location. The Pitot tube measurements were corrected for static tap Reynolds number effects with the correlation proposed by McKeon and Smits [2002] and for viscous effects using the correlation identified by McKeon et al. [2003]. The ambient fluid temperature change during a given profile ranged from 0.7° C to 10.0° C over the full Reynolds number range, and the data were corrected using the temperature correction outlined by Hultmark and Smits [2010].

For calibration, the Pitot probe was positioned above the NSTAP (similar to the pipe setup shown in Figure 3.1(C)) and the probes were then positioned in the free stream 45 mm above the surface, well above the height of boundary layer thickness δ. For all pressure measurements, sufficient time was given for the pressure within the pressure tubing to reach a steady state, and long averaging times were used to minimize the effects of transients on the average. Then, 14 calibration points were used before and after each profile measurement and a fourth order polynomial fit was used to find the calibration coefficients.

Data were acquired for $3 \times 10^3 < Re_\tau < 73 \times 10^3$, corresponding to $8.4 \times 10^3 < Re_\theta < 235 \times 10^3$ (where $Re_\theta = U_\infty \theta / \nu$ is the Reynolds number based on momentum thickness θ). The tunnel was pressurized for all cases and the experimental conditions using NSTAP are listed in Table 5.1 (cases 1-7). Here, p_a is the ambient pressure, and y_0 is the initial distance from the wall. The values of u_τ used in this table are those derived using the skin friction correlation proposed by Fernholz and Finley [1996].

The spatial resolution of the sensor is shown in viscous units as ℓ^+ in Table 5.1, demonstrating the extent of spatial resolution achieved at these very high Reynolds numbers. It can be seen that NSTAP size is comparable to the viscous scales at the lowest Reynolds number case, but at the highest Reynolds number even the miniature NSTAP probe cannot resolve turbulence down to the viscous scales. Therefore the spatial filtering correction by Smits et al. [2011b] was used for turbulence fluctuations

u^{2+}, unless noted otherwise.

5.2.3 Pitot measurements

In addition to the NSTAP, a Pitot probe was also used to measure the mean velocity profiles. A Pitot probe with diameter d_p =0.20 mm, in conjunction with two 0.4 mm static pressure taps in the plate, was used. The pressure difference was measured using a DP15 Validyne pressure transducer with a 1.40 kPa range which was calibrated against a liquid manometer. The initial wall distance y_0 of the Pitot probe was measured using a depth measuring optical microscope and the probe was traversed in wall-normal direction y using a stepper motor traverse, as described in Chapter 5.2.2.

The Pitot measurements were corrected following Bailey et al. [2013] using the static tap correction (outlined by McKeon et al. [2003]), viscous and shear corrections following Zagarola and Smits [1998] and the near-wall correction proposed by MacMillan [1957]. The data for wall distances smaller than two Pitot tube diameters were neglected in calculations, in order to avoid possible biases introduced by the Pitot correction methods and wall distance determination, similar to pipe experiments described in Chapter 3.2.3.

Measurements were taken for $2.8 \times 10^3 < Re_\tau < 65 \times 10^3$, corresponding to $9.4 \times 10^3 < Re_\theta < 223 \times 10^3$. The experimental conditions for all cases are given in Table 5.1 (cases 8-14).

5.2.4 Friction Velocity

Finding the friction velocity u_τ in boundary layer flows is always difficult as there is no simple way to obtain a direct measurement. Here, we find u_τ by estimating the skin friction coefficient $C_f = 2u_\tau^2/U_\infty^2$ using different methods to determine the uncertainty bounds.

First, measurements using the 0.2 mm Pitot probe as a Preston tube were used

Case	Sensor	Re_θ	Re_τ	p_a [atm]	U_∞	$\frac{\nu}{u_\tau}$ [μm]	ℓ or d_p [μm]	ℓ^+ or d_p^+	y_0 [μm]	y_0^+	Symbol
1	NSTAP	8.4×10^3	2,622	4.4	9.08	10	60	5.8	40	3.9	
2	NSTAP	15.1×10^3	4,635	8.1	9.21	5.9	60	10	40	6.8	
3	NSTAP	26.9×10^3	8,261	15	9.29	3.4	60	17	40	12	
4	NSTAP	46.7×10^3	14,717	30	9.33	1.8	60	33	40	22	
5	NSTAP	80.6×10^3	25,062	57	9.46	1.0	30	29	20	19	
6	NSTAP	113×10^3	40,053	105	9.50	0.6	30	47	20	31	
7	NSTAP	235×10^3	72,526	213	9.55	0.4	30	75	20	50	
8	Pitot	9.4×10^3	2,841	4.4	9.40	10	200	20	130	13	
9	Pitot	16.0×10^3	4,835	8.0	9.51	5.9	200	34	130	22	
10	Pitot	28.4×10^3	8,622	15	9.61	3.4	200	59	130	38	
11	Pitot	50.7×10^3	15,256	28	9.64	1.8	200	109	130	70	
12	Pitot	90.6×10^3	26,609	57	9.53	1.0	200	197	130	126	
13	Pitot	147×10^3	43,481	107	9.58	0.6	200	329	130	211	
14	Pitot	223×10^3	65,129	214	9.55	0.4	200	506	130	324	

Table 5.1: Experimental conditions of NSTAP and Pitot measurements in HRTF. Cases 1 to 7 were taken using the NSTAP with sensor length ℓ, and Cases 8 to 14 were taken using the Pitot probe with diameter d_p.

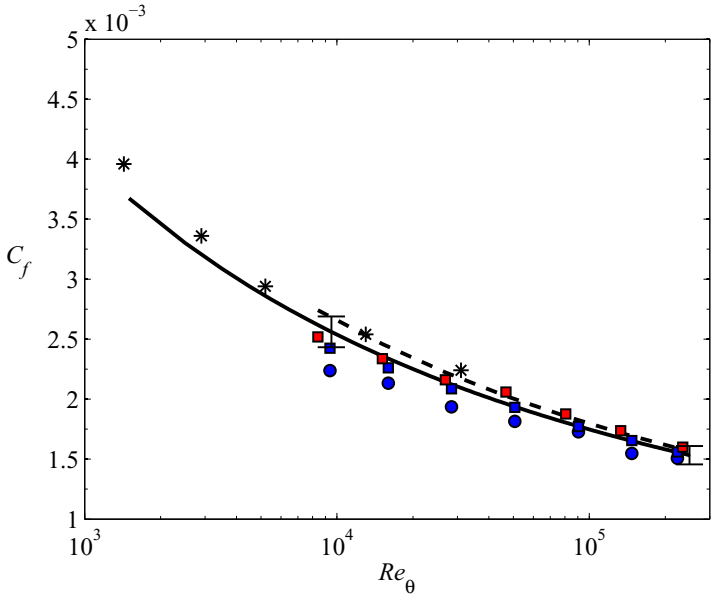

Figure 5.3: Skin friction coefficient C_f: ∘, Preston tube; □, Clauser fit for Pitot data sets; ■, Clauser fit for NSTAP data sets Clauser [1956]; ∗, DeGraaff and Eaton [2000]; solid line, Fernholz and Finley [1996]; dashed line, Gaudet and Winter [1973]. Error bars indicate ±5%.

to estimate the skin friction (Patel [1965], Zagarola et al. [2001]). Second, a Clauser chart technique [Clauser, 1956] was used to estimate C_f from mean profiles of both sensors, where the log-law (with $\kappa = 0.40$ and $B = 5.1$ Coles [1956]) was fitted to the velocity profiles for $200\nu/u_\tau < y < 0.15\delta$ for the NSTAP and Pitot tube mean velocity profiles. These results are compared in Figure 5.3 to the skin friction correlation proposed by Fernholz and Finley [1996] and data from one of the few high Reynolds number direct measurements of skin friction using a drag plate, reported by Gaudet and Winter [1973]. For comparisson, values from DeGraaff and Eaton [2000] found using the Clauser chart fit are also shown. All the different estimates lie within 5%, except the values from the Preston tube showing a larger variation.

To evaluate the effect of the constants chosen for Clauser chart method on the magnitude of friction velocity, four different sets of constants were used to estimate u_τ. The sets chosen were $\kappa = 0.40, B = 5.1$ [Coles, 1956]; $\kappa = 0.38, B = 4.1$

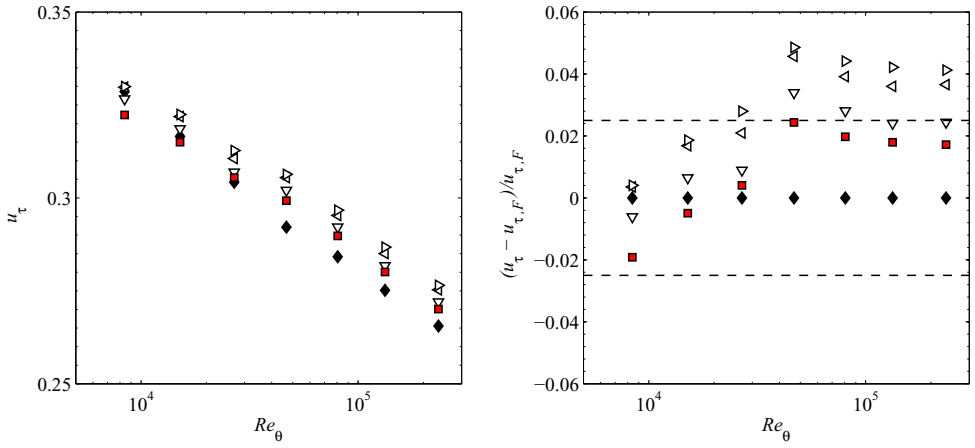

Figure 5.4: Friction velocity for NSTAP data, (a) absolute values of u_τ and (b) relative difference from Fernholz relation $u_{\tau,F}$. $\diamond$, Fernholz relation; $\square$, Clauser chart with $\kappa = 0.40, B = 5.1$ [Coles, 1956]; $\triangledown$ Clauser chart with $\kappa = 0.38, B = 4.1$ [Österlund et al., 2000]; $\triangleleft$, Clauser chart with $\kappa = 0.39, B = 4.3$ [Marusic et al., 2013]; $\triangleright$, Clauser chart with $\kappa = 0.41, B = 5.0$ [Huffman and Bradshaw, 1972].

[Österlund et al., 2000]; $\kappa = 0.39, B = 4.3$ [Marusic et al., 2013]; and $\kappa = 0.41, B = 5.0$ [Huffman and Bradshaw, 1972], and the resulting values of u_τ are shown in Figure 5.4. The overall trends are similar between the different estimates, and from Figure 5.4(b) it can be seen that the Coles constants (used throughout this dissertation for mean profile analysis) give an estimate within 5% compared to the Fernholz relation.

In light of this level of agreement among the different estimates of C_f, the value from the Fernholz correlation is used for finding friction velocity u_τ for all subsequent data analysis. It must be noted that these indirect methods all depend in one way or another to the presence of a logarithmic layer with fixed and pre-chosen values for the von Kármán constant, and therefore no definitive conclusions can be made about the logarithmic behavior based on the experiments reported here.

5.3 Mean flow and turbulence intensities

5.3.1 Mean flow and bulk properties

The mean velocity profiles from the NSTAP and Pitot measurements are shown and compared in Figure 5.5 in inner variables. Good collapse of the profiles can be seen in Figure 5.5(a) from the linear region at the wall (where $y^+ = U^+$, shown as a solid line) throughout the near-wall region. The logarithmic region is evident for all cases, though only for a very small region at the lowest Reynolds number. In order to better show the comparison between the profiles, Figure 5.5(b) shows each profile shifted by a constant factor of $\Delta U^+ = 5$. The data show an excellent agreement between the profiles throughout the whole boundary layer for all Reynolds numbers.

Comparing the NSTAP and Pitot profiles showed agreement within 2% for most of the data, which is within expected experimental error, as the uncertainty in measurements of U under these experimental conditions is estimated to be as high as 2.2%. Larger differences of up to 4% occurred for $Re_\tau = 15 \times 10^3$ (Case 4) and this is probably due to the decrease in stability of the CTA bridge as the Reynolds number is increased. A much more stable 30μm sensor with smaller cross-section was fabricated and used for three highest Reynolds numbers. This flexible fabrication which allows to tailor sensors according to specific needs of the experiment demonstrates another advantage of these novel sensors, in addition to the improved spatial and temporal resolution.

In the outer layer of boundary layer, the flow is assumed to be independent of viscosity and outer scales depend only on global properties of the flow. Generally the proper outer scaling is considered to be given as the velocity deficit law

$$\frac{U_\infty - U}{U_c} = f\left(\frac{y}{\delta}\right) \tag{5.3.1}$$

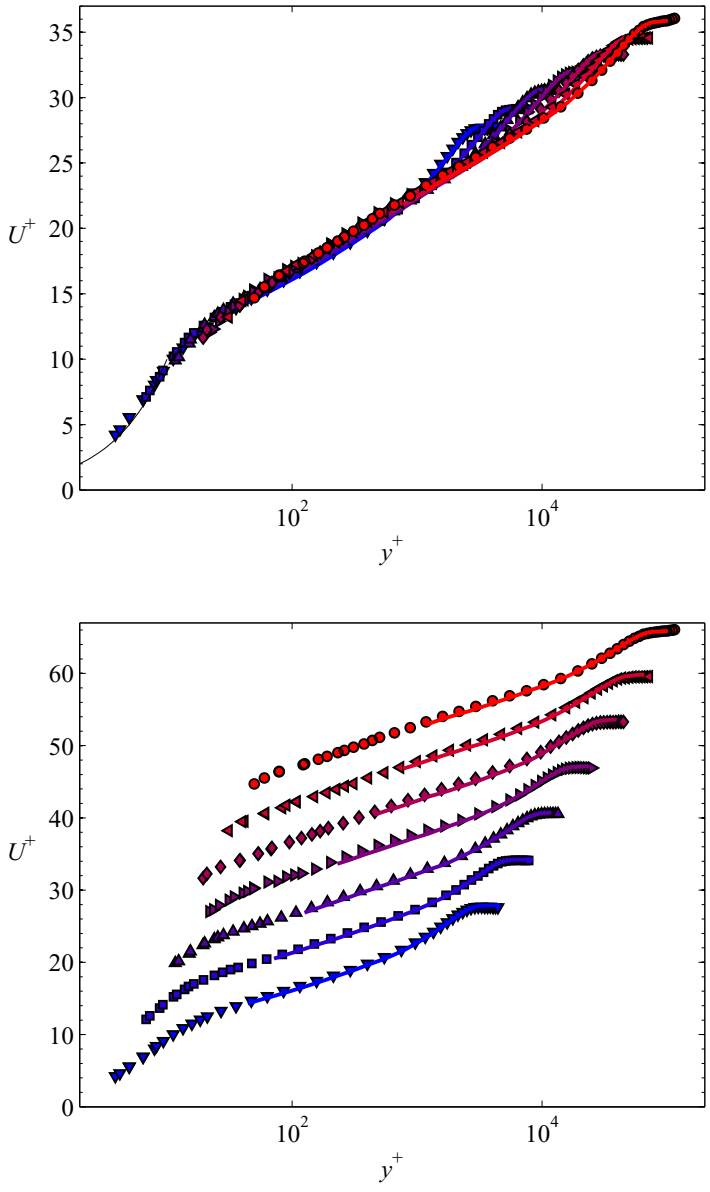

Figure 5.5: Mean velocity profiles measured with NSTAP probe (symbols) and Pitot tube (lines) in inner coordinates. Solid line shows the viscous sublayer relationship $U^+ = y^+$ for $y^+ \leq 10$. a) All mean profiles in inner coordinates; b) Each mean profile shifted by $\Delta U^+ = 5$ for clarity. Symbols as indicated in Table 5.1.

introduced by Clauser [1956], where outer characteristic velocity was given as $U_c = u_\tau$. Here, the friction velocity is considered to only play a role to match the inner and outer layer velocity. All mean velocity deficit profiles scaled with δ and u_τ are shown in Figure 5.6(a) and a reasonable agreement can be seen. An alternative scaling, only depending on bulk parameters, was suggested by Zagarola and Smits [1998] who showed that for pipe flow $U_c = U_{cl} - \langle U \rangle$ was a more appropriate scaling parameter (U_{cl} is center-line velocity in pipe and $\langle U \rangle$ is the bulk velocity). Zagarola and Smits [1998] also extended this scaling argument to boundary layers, where outer velocity scale U_c is proportional to the mass flux deficit in the boundary layer

$$u_0 = U_\infty \int_0^1 \left(1 - \frac{U}{U_\infty}\right) d\left(\frac{y}{\delta}\right) = \frac{\delta^*}{\delta} U_\infty, \tag{5.3.2}$$

where $\delta^* = \int_0^\delta \left(1 - \frac{U}{U_\infty}\right) \mathrm{d}y$ is the displacement thickness. In Figure 5.6(b) all mean velocity profiles are shown with this alternative outer scaling and a significantly better collapse of profiles can be noted. In turbulent pipe, the flow is driven by a pressure gradient that is inherently connected to the skin friction and therefore it is reasonable to assume the outer flow to scale with u_τ. On the other hand, in boundary layers there is no such connection between the outer flow and the skin friction, and one would expect the outer flow to have no specific dependence on the wall friction. Therefore there is no fundamental reason to expect the outer part of the mean profiles to scale with u_τ. Additionally, an advantage of this u_0 scaling is that it does not require any skin friction estimate, which could introduce a large error bar. Upon a closer inspection of Figure 5.6(a), it can be seen that the Pitot profiles seem always to be slightly higher than the NSTAP profiles, and this disagreement (probably due to the uncertainty in C_f) is eliminated by using u_0 as a scaling parameter. Therefore it is suggested that the scaling proposed by Zagarola and Smits [1998] serves as a more general outer scaling (with less uncertainty) for the mean flow in boundary layers,

especially at lower Reynolds numbers.

Table 5.2 lists the boundary layer thickness $\delta = \delta_{99}$, as well as the displacement thickness δ^*, the momentum thickness $\theta = \int_0^\delta \frac{U}{U_\infty}\left(1 - \frac{U}{U_\infty}\right) dy$, and the shape factor $H = \delta^*/\theta$ for each case. For estimating δ^* and θ, trapezoidal integration was used and the near-wall region was interpolated using lower Reynolds number cases that cover full near-wall region. Figure 5.7 shows the bulk properties from the current experiment. For comparison, the data from DeGraaff and Eaton [2000], the functions suggested by Coles [1956] (with log-law constants κ=0.40 and B=5.1, as used by Coles [1956]) and the asymptotic values $\theta/\delta = 0.0767$, $\delta^*/\delta = 0.0894$ and $H = 1.17$ suggested by George and Castillo [1997], are also shown. The experimental values of DeGraaff and Eaton [2000] agree well with the current data (where the NSTAP and Pitot data are in good agreement). The functions suggested by Coles [1956] are very sensitive to the chosen log law constants and the wake function. Even though all the trends are similar, some significant differences can be seen among the values, especially for the shape factor H. Additionally it can be seen that the values are decreasing with Reynolds number and are still far from the asymptotes suggested by George and Castillo [1997].

In order to visualize the extent of the logarithmic layer in the profiles we use the parameter Ψ_1, where

$$\Psi_1 = U^+ - \frac{1}{\kappa} \ln y^+ - B. \tag{5.3.3}$$

In the region where the log law should apply, plotting Ψ_1 against the wall-normal positions a horizontal line should be evident, assuming that reasonable κ was chosen (throughout this dissertation $\kappa = 0.40$ and $B = 5.1$ are used). In Figures 5.8(a) and 5.8(b) this function is shown in inner and outer wall coordinates, respectively, with each Reynolds number shifted by $\Delta\Phi = 2$, and dashed lines indicating the respective zero values for each Reynolds number. From Figure 5.8 it is clear that the outer limit of the logarithmic layer agrees well with $y/\delta = 0.15$, which is also indicated on the

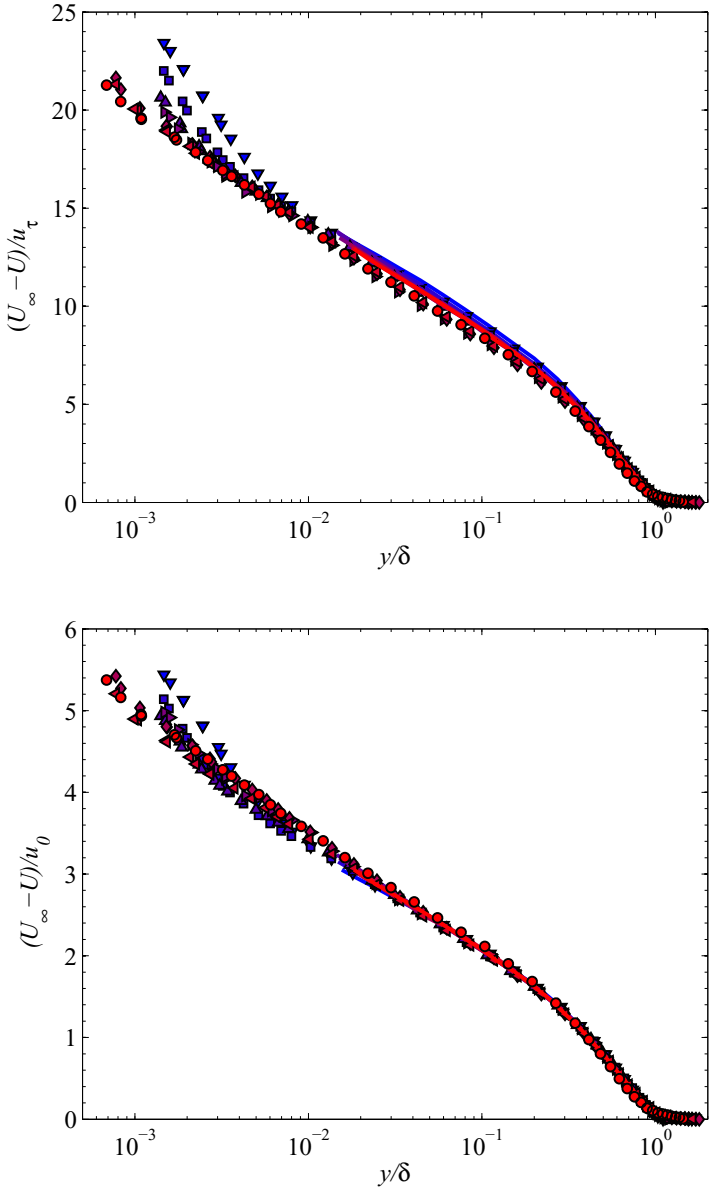

Figure 5.6: Mean velocity profiles measured with NSTAP probe (symbols) and Pitot tube (lines). a) All mean profiles in outer coordinates, where U is scaled with u_τ; b) All mean profiles in outer coordinates, where U is scaled with $u_0 = \frac{\delta^*}{\delta} U_\infty$. Symbols as indicated in Table 5.1.

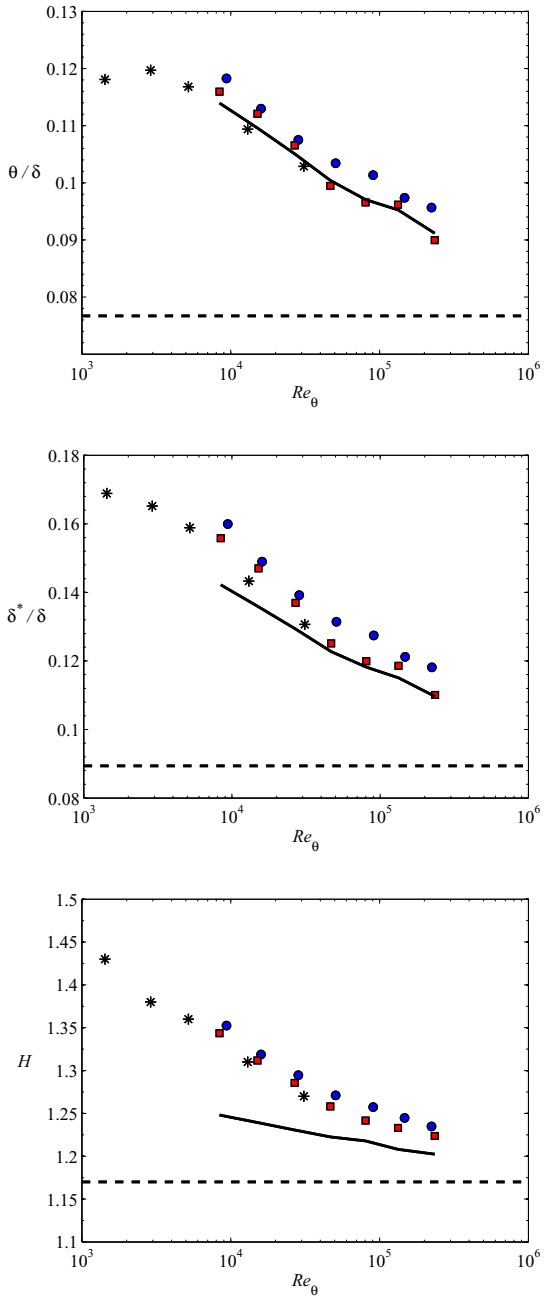

Figure 5.7: Bulk properties with varying Reynolds number. ○, Pitot data; ■, NSTAP data; ∗, DeGraaff and Eaton [2000]; solid line, Coles [1956]; dashed line, asymptotic value from George and Castillo [1997].

Table 5.2: Bulk properties. All dimensional quantities are given in mm.

Case	δ [mm]	δ^* [mm]	θ [mm]	H	$C_f \times 10^3$
1	27.2	4.24	3.15	1.34	2.62
2	27.3	4.01	3.06	1.31	2.36
3	28.4	3.89	3.02	1.29	2.14
4	27.0	3.38	2.68	1.26	1.96
5	25.7	3.09	2.49	1.24	1.80
6	25.8	3.06	2.48	1.24	1.68
7	29.1	3.20	2.62	1.22	1.55
8	28.7	4.59	3.39	1.35	2.57
9	28.6	4.26	3.23	1.32	2.33
10	29.1	4.05	3.13	1.29	2.12
11	28.1	3.69	2.90	1.27	1.94
12	27.0	3.44	2.73	1.26	1.77
13	26.5	3.21	2.58	1.24	1.65
14	25.7	3.04	2.46	1.23	1.56

plots with the error bar locations.

All profiles are slightly curved near the wall, which could indicate the presence of a mesolayer with a power law like behavior as found in pipe flow by McKeon et al. [2004a]. NSTAP data indicates log-region anywhere above $y^+ = 100$ or even lower whereas pitot data does not resolve such near-wall region for higher cases. $y^+ = 3Re_\tau^{0.5}$ suggested by Marusic et al. [2013] as a conservative inner bound for fitting profiles (and the middle of log-region) is denoted with inner error bars in Figure 5.8. Unfortunately this inner region is very close to the wall in physical coordinates and could be affected by uncertainties in the measurements near the wall therefore we can make no final conclusions on the inner limit of the logarithmic layer. Nevertheless it is clear that a much lower inner limit can be observed than found at similar Reynolds numbers in pipe flow ($y^+_{min} = 600-800$ seen in McKeon et al. [2004a], Hultmark et al. [2013]).

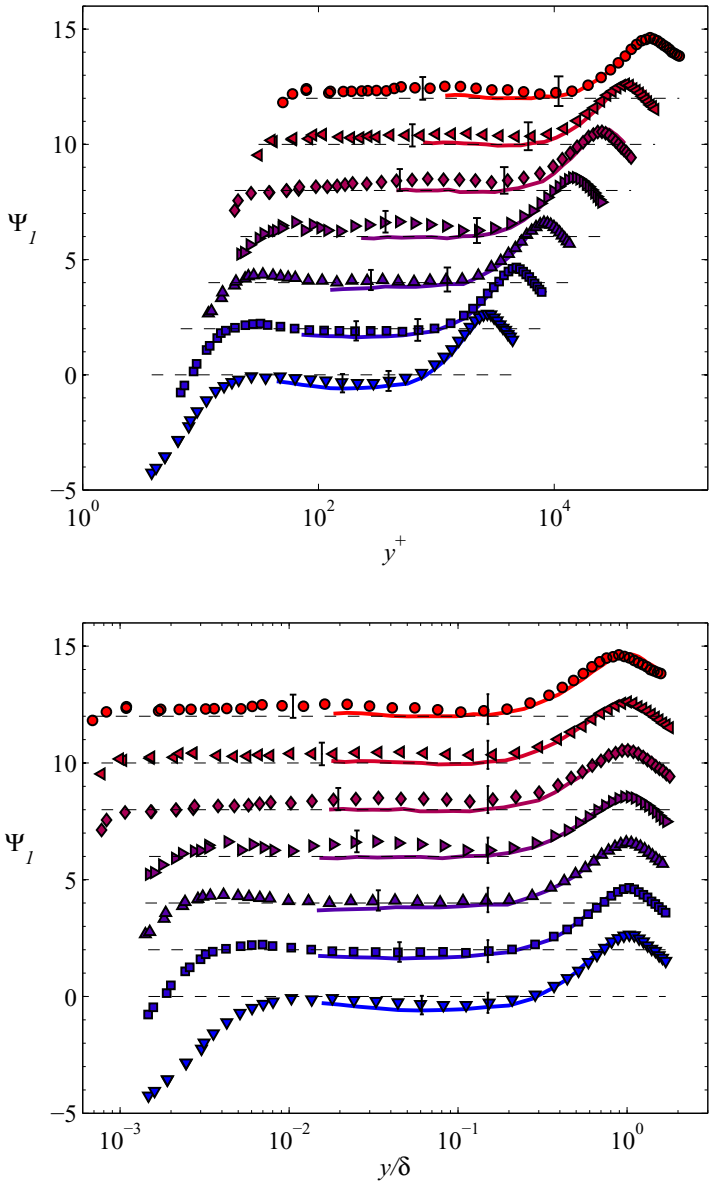

Figure 5.8: Parameter Ψ_1 in a) inner coordinates and b) outer coordinates. Profiles have been shifted by $\Delta\Psi_1 = 2$ for clarity, error bars of 2.2% U are shown at locations $y^+ > 3Re_\tau^{0.5}$ and $y/\delta = 0.15$. Symbols as indicated in Table 5.1.

5.3.2 Streamwise Reynolds stresses

The great advantage of using NSTAPs for velocity measurements is their superior spatial and temporal resolution (Table 5.1 lists the sensor length in viscous units ℓ^+). At lower Reynolds number, all viscous time and length scales can be expected to be resolved, but for higher Reynolds numbers even NSTAP measurements suffer from spatial filtering effects, with ℓ increasing up to 75 times the viscous length. Therefore u^{2+} has been corrected using the spatial filtering correction introduced by Smits et al. [2011b], which has been shown to work well in many different wall-bounded flows. The correction has less than 1% effect on most of the flow, but becomes more significant near the wall, so that at $y^+ = 100$ the correction is already 3%, 5% and 10% for the three highest Reynolds numbers.

In addition to spatial filtering, there are other uncertainties introduced near the wall, such as the uncertainty in initial wall location y_0 (about 5μm), the calibration sensitivity due to low mean velocity, possible asymmetrical temperature profiles around the sensor, to name a few.

Profiles of the streamwise turbulent stress u^{2+} are shown in inner and outer coordinates in Figure 5.9. A good agreement between the profiles is seen near the wall, with a peak near $y^+ \approx 15$, as expected. The inner peak values for the three lowest Re_τ are $u_I^{2+} = [8.3; 8.1; 7.7]$. After applying the spatial filtering correction suggested by Smits et al. [2011b], all values collapse to $u_I^{2+} = 8.44 \pm 0.02$. So the available data show no Reynolds number trend in the inner peak value for turbulent boundary layers for $3,000 \leq Re_\tau \leq 10,000$. However, only the three lowest Reynolds number cases can be measured at such small y^+, so less than a decade in Re_τ is covered. At the same time, in near-wall region the errors increase (wall-distance, calibration sensitivity at low U, etc). Therefore if peak is increasing logarithmically with Re, this could be simply masked by experimental error.

The outer region shows a clear variation with Re_τ, and a Reynolds number de-

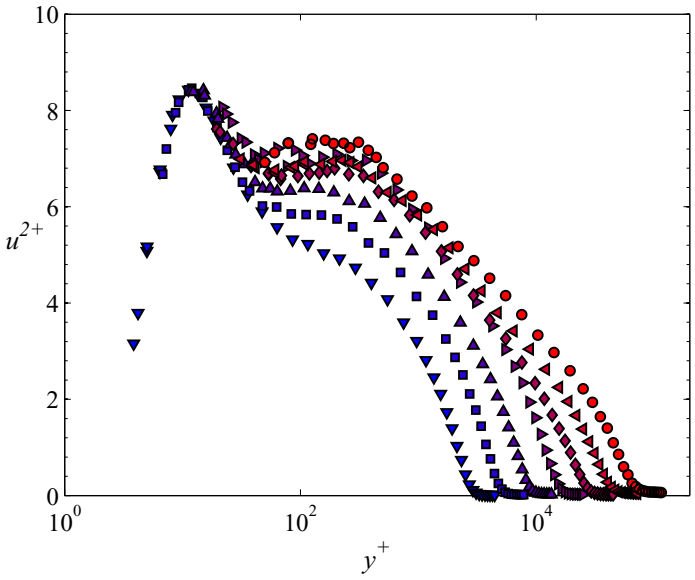

Figure 5.9: Streamwise turbulent stress u^{2+} profiles in inner coordinates. Symbols as indicated in Table 5.1.

pendent second peak emerges for higher Reynolds numbers. The value of streamwise Reynolds stress at the outer peak u^{2+}_{II}, that is where the profile starts to decay logarithmically, was found for each Reynolds number (for the three lowest cases there is no peak, but just a shoulder, so an inflection point was used to estimate the peak value). These values are shown in Figure 5.10, together with the values from the pipe flow in Chapter 3.4, and it can be seen that the magnitudes of the outer peaks are very similar in these two flows. The data where a genuine peak can be observed, indicating where u^{2+} starts to decay (for $Re_\tau > 20,000$), is shown with filled symbols in Figure 5.10. It was found that the peak magnitudes follow $u^{2+}_{II} = 0.49\ln(Re_\tau)+1.7$ in pipe and $u^{2+}_{II} = 0.47\ln(Re_\tau)+2.0$ in boundary layer and these fits are very similar, suggesting a similar behavior of u^{2+}_{II} in these two flows. The location of the peaks is discussed in Chapter 7.3.4.

Recently, Pullin et al. [2013] proposed an analysis suggesting a logarithmic increase in the outer peak value u^{2+}_{II} with two possible relations: $u^{2+}_{II} = 0.42\ln(Re_\tau) + 2.82$ and $u^{2+}_{II} = 0.63\ln(Re_\tau)+0.33$ (depending on the relation governing the location

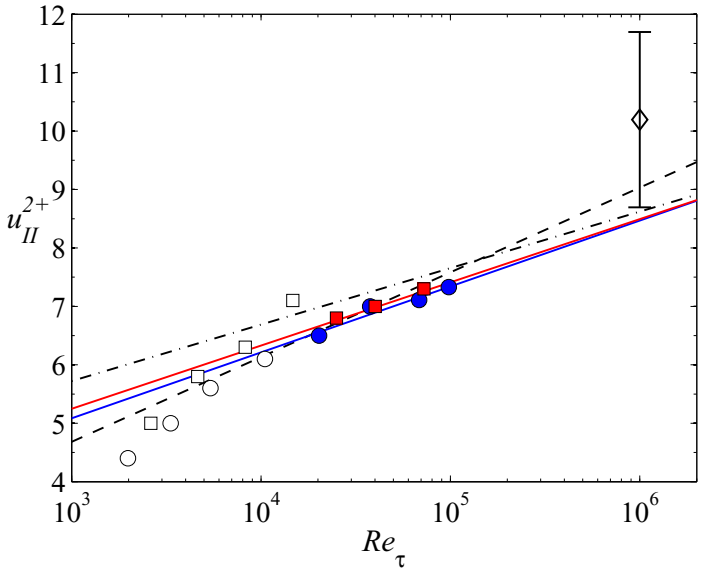

Figure 5.10: Magnitudes of the outer peak in u^{2+} for pipe ($\circ$) and boundary layer ($\square$).(Filled symbols) data for $Re_\tau > 20,000$; (solid blue line) Best fit to pipe data as $u_{II}^{2+} = 0.49\ln(Re_\tau) + 1.7$; (solid red line) Best fit to boundary layer data as $u_{II}^{2+} = 0.47\ln(Re_\tau) + 2.0$; ($\Diamond$) data from atmospheric boundary layer [Metzger et al., 2007]; (dashed line) $u_{II}^{2+} = 0.63\ln(Re_\tau) + 0.33$ from Pullin et al. [2013] and (dash-dot line) $u_{II}^{2+} = 0.42\ln(Re_\tau) + 2.82$ from Pullin et al. [2013].

of the peak) and both of these relations are shown in Figure 5.10. The relations suggested by Pullin et al. [2013] agree well with the magnitude of the peaks, as well as the curve fit, supporting the hypothesis that the turbulence is asymptotically attenuated when approaching infinite Reynolds number. This means that with increasing Reynolds number the locations of the inner peak (at constant y^+) and the outer peak (varying as $\ln(Re_\tau)$) are both moving closer to the wall in physical coordinates, diminishing as $Re_\tau \to \infty$ and the asymptotic state of the wall layer is slip-flow bounded by a vortex sheet at the wall [Pullin et al., 2013]. It should be noted that if all boundary layer cases are considered, the peak was found to follow $u_{II}^{2+} = 0.34 + 0.63\ln(Re_\tau)$, which is very close to Pullin et al. [2013] relation.

Figure 5.11(a) shows all profiles of streamwise Reynolds stress in outer scaling, y scaled with boundary layer thickness. The scaling does not collapse the profiles

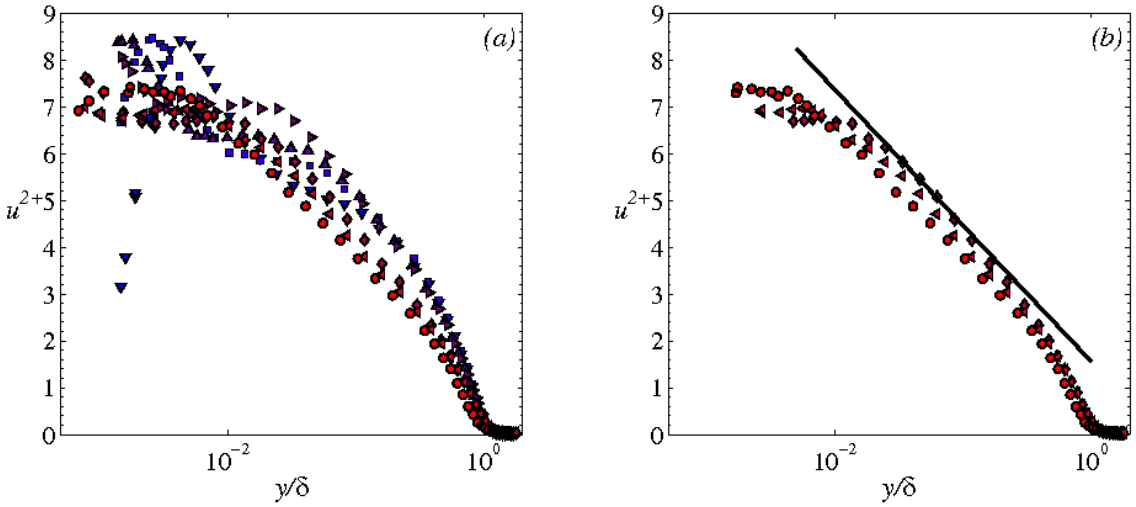

Figure 5.11: Streamwise turbulent stress u^{2+} profiles in outer coordinates. (a) Profiles for all Re_τ; (b) Profiles at $Re_\tau > 20,000$ and $y^+ > 100$, solid line indicating Equation (5.1.2) with $A_1 = 1.24$ and $B_1 = 1.48$. Symbols as indicated in Table 5.1.

well and a clear shift with increasing Reynolds numbers can be observed, especially at the lowest Reynolds numbers. The mixed scaling of fluctuations using $u_\tau U_\infty$, introduced by DeGraaff and Eaton [2000], gives a qualitatively similar collapse as the conventional scaling, therefore the conventional scaling u_τ^2 is used in current analysis.

At highest Reynolds numbers ($Re_\tau > 20,000$) logarithmic behavior described by Equation (5.1.2) can be observed starting after the outer peak in variance at about $y^+ > 300$. This logarithmic behavior can be seen in Figure 5.11(b), where cases for $Re_\tau > 20,000$ and $y^+ > 100$ are shown only, with solid line showing Equation (5.1.2) (with $A_1 = 1.24$ and $B_1 = 1.48$ from the results in pipe flow in Chapter 3.4). There is clear logarithmic behavior, though with some variation in the additive constant, as there is no collapse in the profiles. Similarly to the mean flow, we can introduce a parameter Ψ_3, where

$$\Psi_3 = u^{2+} - A_1 \ln \frac{y}{\delta} - B_1. \tag{5.3.4}$$

In the region where the log law should apply, plotting Ψ_3 against the wall-normal position should reveal a horizontal line.

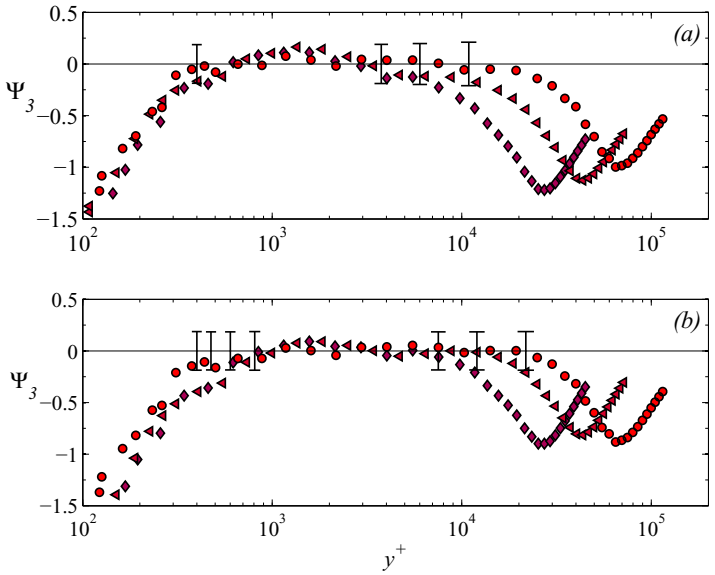

Figure 5.12: Turbulence intensities logarithmic behavior shown with Φ_2 in inner coordinates. Constants found a) in region $400 < y^+ < 0.15Re_\tau$, b) in region $3Re_\tau^{0.5} < y^+ < 0.3Re_\tau$, with error bar locations indicating according limits. Symbols as indicated in Table 5.1.

In Figures 5.12 and 5.13 the function Ψ_3 is shown in inner and outer coordinates, respectively. In the top plots of both figures, the constant A_1 and B_1 were found from a regression fit to the data between $400 < y^+ < 0.15Re_\tau$ for each case. In the bottom plots of both figures, A_1 and B_1 were found from a fit to the data between $3Re_\tau^{0.5} < y^+ < 0.3Re_\tau$. The value and Reynolds number dependence of these constants is more thoroughly discussed in Chapter 6. The inner and outer limits are indicated on the plots with the error bar locations, where error bars indicate a $\pm 3\%$ variation (not accounting for the uncertainty of estimating u_τ).

Compared to the mean flow function Ψ_1 shown in Figure 5.8, there is much more variation in the turbulent intensities, which is due to the higher uncertainty in instantaneous measurements. Nevertheless, a significant region of the profiles follows the logarithmic behavior, and for $Re_\tau = 70,000$ it extends over about 1.7 decades in y. Analyzing Figures 5.12 and 5.13 shows that $3Re_\tau^{0.5} < y^+ < 0.3Re_\tau$ provides a more

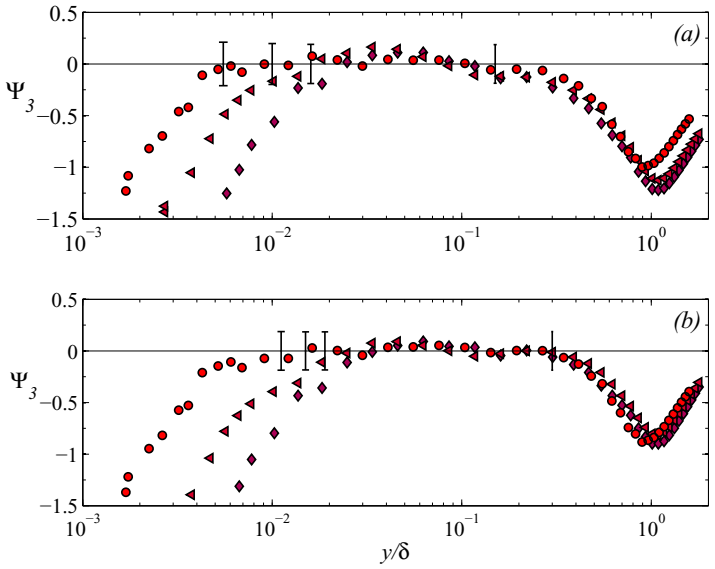

Figure 5.13: Turbulence intensities logarithmic behavior shown with Φ_2 in outer coordinates. Constants found a) in region $400 < y^+ < 0.15Re_\tau$, b) in region $3Re_\tau^{0.5} < y^+ < 0.3Re_\tau$, with error bar locations indicating according limits. Symbols as indicated in Table 5.1.

flat and collapsing Ψ_3 indicating that the logarithmic behavior is well determined by these limits. This is in contrast to results in pipe flow, where a fixed inner limit of logarithmic behavior was observed. A higher upper limit ($y/\delta = 0.3$) is also different from pipe flow, where an outer limit of $y/\delta = 0.15$ was observed. This can be explained by the different outer boundary conditions of these flows; in the pipe, u^{2+} sustains a constant value at the center-line, whereas in boundary layer there is first intermittency and finally the fluctuations decrease to zero in the free-stream.

5.3.3 Logarithmic regions in the mean and the variance

In pipe flow the logarithmic regions in mean flow and fluctuations were observed to occur in the same physical region. For boundary layer flows, profiles of U^+ and u^{2+} are shown in Figure 5.14 for the six highest Reynolds numbers. Solid lines indicate Equation (5.1.1) and (5.1.2), and dashed lines show the limits of the overlapping

logarithmic region, $y+ = 400$ and $y/\delta = 0.15$. Clearly, both the mean and the variances follow a logarithmic behavior within these limits, and for the mean flow the behavior extends to much lower values of y^+. This could indicate the presence of an intermediate range below $y+ = 400$, which is similar to the power-law region observed by McKeon et al. [2004a] in pipe flows. In this region, the mean flow follows inner scaling, even though there is insufficient scale separation for the fluctuations to form an overlap region as dissipative scales are not fully separated from the energy-containing scales. This region was first introduced as a mesolayer in boundary layers by George and Castillo [1997], who suggested that the logarithmic law in mean flow includes a Reynolds number dependent offset, which diminishes with increasing wall-normal distance until $y^+ \approx 300$, after which the true logarithmic behavior is observed. This approach was expanded by Hultmark [2012], who proposed an alternative theory for the logarithmic behavior for the streamwise Reynolds stresses in turbulent pipe flow. The observations made here support the existence of such a mesolayer in boundary layers, where the flow is still affected by viscosity, showing up as a decrease in the fluctuations, similarly to pipe flow analysis by Hultmark [2012].

5.4 Conclusions

Well-resolved zero pressure gradient turbulent boundary layer measurements for 2,600< Re_τ <72,000 have been reported and analyzed. Seven different Reynolds numbers were studied with two different experimental techniques. First, Pitot measurements were conducted for establishing the mean behavior; then, NSTAP (with 60μm and 30μm sensors) were used to provide the temporal and spatial resolution for turbulence studies. Different indirect methods for estimating the skin friction factor were used and shown to agree within 5%. Bulk properties of Pitot and NSTAP profiles agreed well, and followed the expected behavior, agreeing with previous experiments

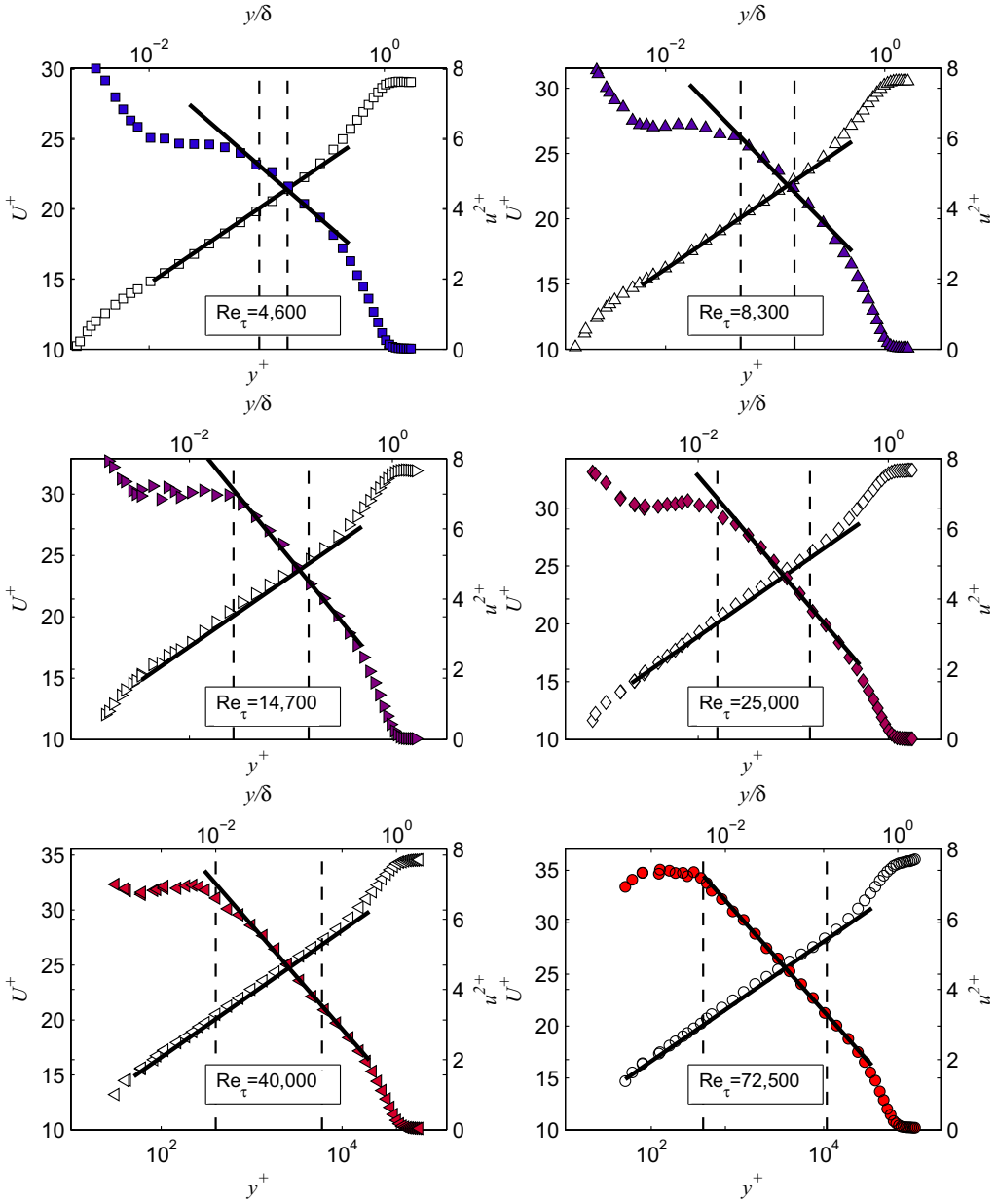

Figure 5.14: Mean profiles (empty) and turbulence intensities (filled) for cases 2-7. (dashed lines) limits of logarithmic region y=400 and $y^+ = 0.15Re_\tau$. Symbols as indicated in Table 5.1.

[DeGraaff and Eaton, 2000] and empirical relations [Coles, 1956].

The mean velocity profiles showed a good agreement between two measurement techniques and an extended logarithmic region was observed. In the outer region of the flow, the characteristic velocity $u_0 = \frac{\delta^*}{\delta} U_\infty$ proposed by Zagarola and Smits [1998] was shown to be a more suitable scale than u_τ for the mean velocity.

Streamwise Reynolds stresses were obtained with high spatial resolution ($6 < \ell^+ < 75$), using NSTAP measurements. The turbulent fluctuations were found to scale well with viscous scales near the wall, but they did not scale well with u_τ in the outer coordinates. A logarithmic region in turbulent fluctuations was observed for $Re_\tau \geq 20,000$, with constants close to the ones found from pipe flow in Chapter 3.4.3. A logarithmic behavior in variances was observed over a region $400 < y^+ < 0.3Re_\tau$, and it was shown that the mean and variances both show the log-behavior for $400 < y^+ < 0.15Re_\tau$. In addition, log-like behavior in mean profiles was seen even closer to the wall, suggesting the existence of a mesolayer, as introduced by George and Castillo [1997].

Chapter 6

Higher order moments in boundary layers and pipes

6.1 Introduction

The similarity and differences between boundary layer and pipe flow at high Reynolds numbers has always been a topic of discussion. All wall bounded flows are governed by similar scale separation and similar scaling can be found. On the other hand, the outer boundary conditions are different, and if fully developed pipe flow has no streamwise gradient by definition, it is only approximately true for the boundary layers. Here we have a unique opportunity to compare experimental results from both of these flows at very high Reynolds numbers, using smooth pipe data from Chapter 3 together with boundary layer data described in this Chapter, both acquired with the NSTAP. In order to make reasonable comparisons, six different cases with matching Reynolds numbers have been chosen for comparison, and properties of all cases are listed in Table 6.1. From here on, only these data are considered in the analysis. For consistancy we use a single notation δ to denote the outer length scale, that is boundary layer thickness for bondary layer data and pipe radius for pipe flow.

Case	Pipe		Boundary layer		Symbol
$Re_\tau \approx$	Re_τ	ℓ^+	Re_τ	ℓ^+	
3×10^3	3,334	3.1	2,622	5.8	▼
5×10^3	5,412	5.0	4,635	10	■
10×10^3	10,481	9.7	8,261	17	▲
20×10^3	20,250	18.8	25,062	29	♦
40×10^3	37,690	35.0	40,053	47	◀
70×10^3	68,371	31.7	72,526	75	●

Table 6.1: Cases chosen for pipe and boundary layer comparison.

Streamwise fluctuations u^{2+} for both flows in outer coordinates are shown in Figure 6.1. Only data for $y^+ > 100$ have been shown for clarity and only cases where $Re_\tau \geq 20,000$, that is, where a distinct logarithmic region in fluctuations occurs in both of these flows (as shown in Chapter 3 for pipe flow). We found the constants in Equation (5.1.2) to be independent of Reynolds number with values $A_1 = 1.24$ and $B_1 = 1.48$ for pipe flow and in Figures 6.1(a) and (b), Equation (5.1.2) with these constants is shown. Later, Marusic et al. [2013] found the constants be same for pipes and boundary layers with values $A_1 = 1.26$ and $B_1 = 1.56$, which equally well fit the data. As observed previously, it is clear that boundary layer data is not ideally collapsed by the outer scaling, but it can be seen that the magnitude as well as the slope of logarithmic region is in good agreement with pipe flow, suggesting that only B_1 might be Reynolds number dependent. The Reynolds number dependence of these constants will be discussed further below.

In order to further examine the similarities of these two flows, the behavior of higher order moments is also analyzed. NSTAP measurements allow high resolution data and also makes it possible to investigate higher order moments. Figure 6.2 shows the probability density function $P(u)$, and the premultiplied pdf $u^{2p}P(u)$, where $2p = [2, 6, 10]$ indicates the p'th even moment, for a representative boundary layer case ($Re_\tau \approx 70,000$ at $y^+ = 800$). For comparison, the same profiles for a Gaussian distribution are shown with solid lines. These profiles assure the convergence of the

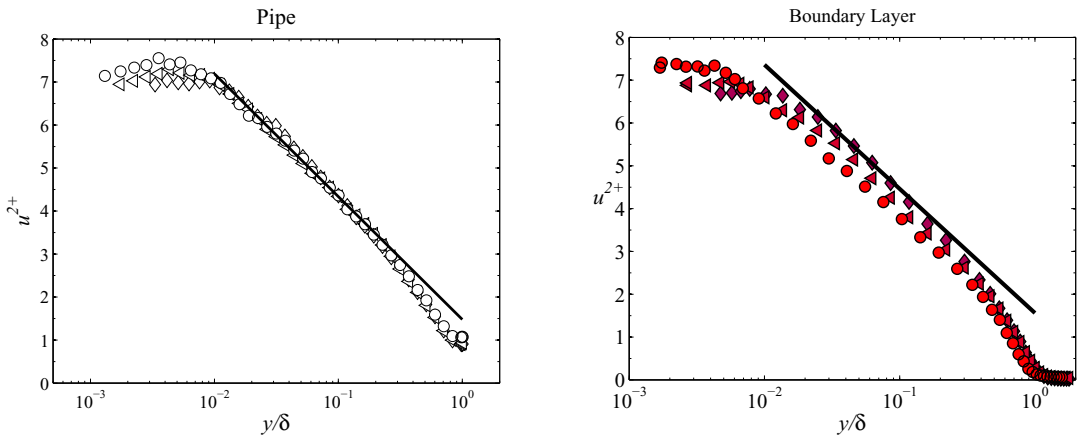

Figure 6.1: Comparison of turbulent fluctuations in pipe and boundary layer in outer coordinates for $Re_\tau > 20,000$ and $y^+ > 100$. Solid line shows Equation (5.1.2) with $A_1 = 1.26$ and $B_1 = 1.56$ from pipe flow. Symbols as indicated in Table 6.1.

higher order moments. As discussed in Chapter 2, the frequency response of the sensor could be lower than estimated with squarewave test. To assure accuracy of the results, moments were also calculated from data filtered at 50 kHz. It was found that at highest Reynolds number, the magnitude of the filtered moments differed less than 2% from the unfiltered moments, and for lower cases the difference diminished. As the differences were not significant, full moments from unfiltered data are used in the analysis.

6.2 Skewness and kurtosis

The skewness $S = \langle u^3 \rangle / \langle u^2 \rangle^{3/2}$ for both flows is shown in Figures 6.3 in inner and outer coordinates accordingly. A very similar behavior can be observed in both flows, with the skewness slightly positive near the wall for $y^+ < 200$ and becoming negative further away in the log-region and outer flow. For pipe flow, the viscous scaling (Figure 6.3(a)) does not collapse the profiles and the values show a Reynolds number dependence. Interestingly, for the boundary layer (Figure 6.3(b)), the skewness is well collapsed in the log-region $100 < y^+ < 0.15Re_\tau$ before increasing in the wake,

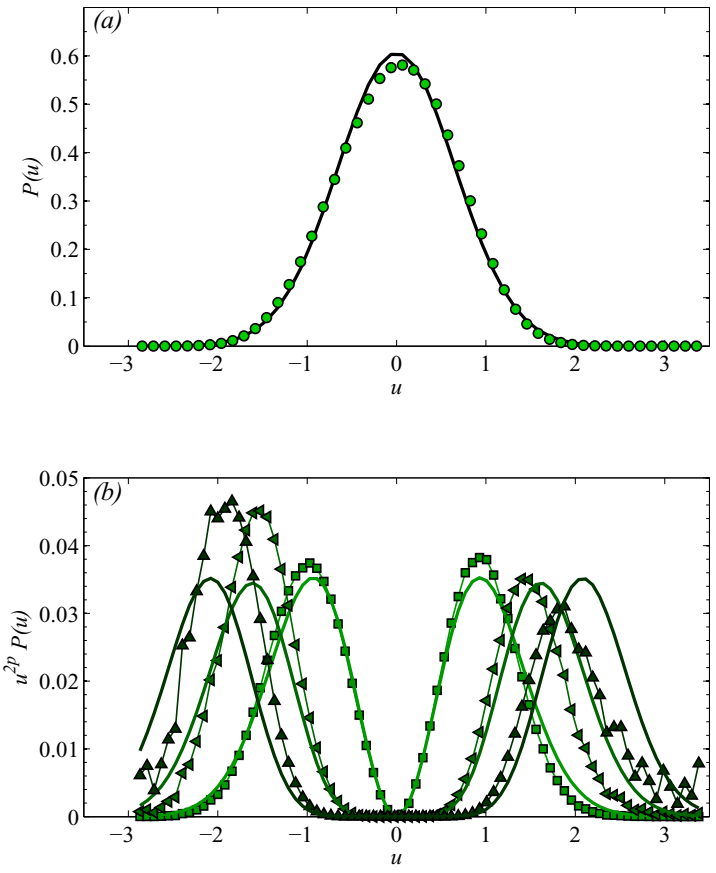

Figure 6.2: p.d.f and premultiplied p.d.f for Gaussian distribution (solid lines) and current boundary layer data at $Re_\tau = 70 \times 10^3$, $y^+ = 800$. (a) shows $P(u)$ (●) and (b) shows premultiplied p.d.f. for moments $2p = 2$ (■), $2p = 6$ (◀) and $2p = 10$ (▲).

where S scales with outer variables (Figure 6.3(c,d)). For Gaussian statistics $S = 0$, and for both flows we see sub-Gaussian behavior. In pipe flow, we see a Reynolds number dependence throughout the flow, with S becoming negative depending on Reynolds number from $y^+ = 100$ to $y^+ = 450$ and slowly decreasing from there until the pipe centerline. For the boundary layer, on the other hand, the skewness profiles are well collapsed, and we see all profiles change sign at $y^+ = 200$ and reach a value of $S \approx -0.1$ before decreasing in the wake. Mathis et al. [2009] observed that the skewness behaves similarly to the amplitude modulation function, suggesting that the skewness reflects modulation of the near wall flow by outer-scaled eddies. Collapse of the profiles suggests that sufficient scale separation might have been reached at higher Reynolds numbers, agreeing with our observations of the behavior of the variance.

The kurtosis $K = \langle u^4 \rangle / \langle u^2 \rangle^2$ in inner and outer scaling is shown in Figures 6.4. All the values are slightly below 3, with $K \approx 2.7$, indicating again a sub-Gaussian behavior. The scaling with inner coordinates in Figure 6.4 (a,b) shows a similar behavior for both flows, with some dependence on the Reynolds number, but it must be kept in mind that spatial filtering effects increase for higher order moments and therefore this could be masking the true behavior of K. In outer scaling (Figure 6.4 (c,d)), pipe and boundary layer flows also show the same values and behavior of K, having some Reynolds number dependence (or just indicating effects of spatial filtering). Therefore no significant conclusions can be made, except the observation that pipe and boundary layer show essentially identical behavior of kurtosis.

6.3 High-order even moments

The attached eddy hypothesis, first introduced by Townsend [1976], states that the length scales of eddies are proportional, and their population density is inversely proportional, to the distance from the wall. Meneveau and Marusic [2013] describe

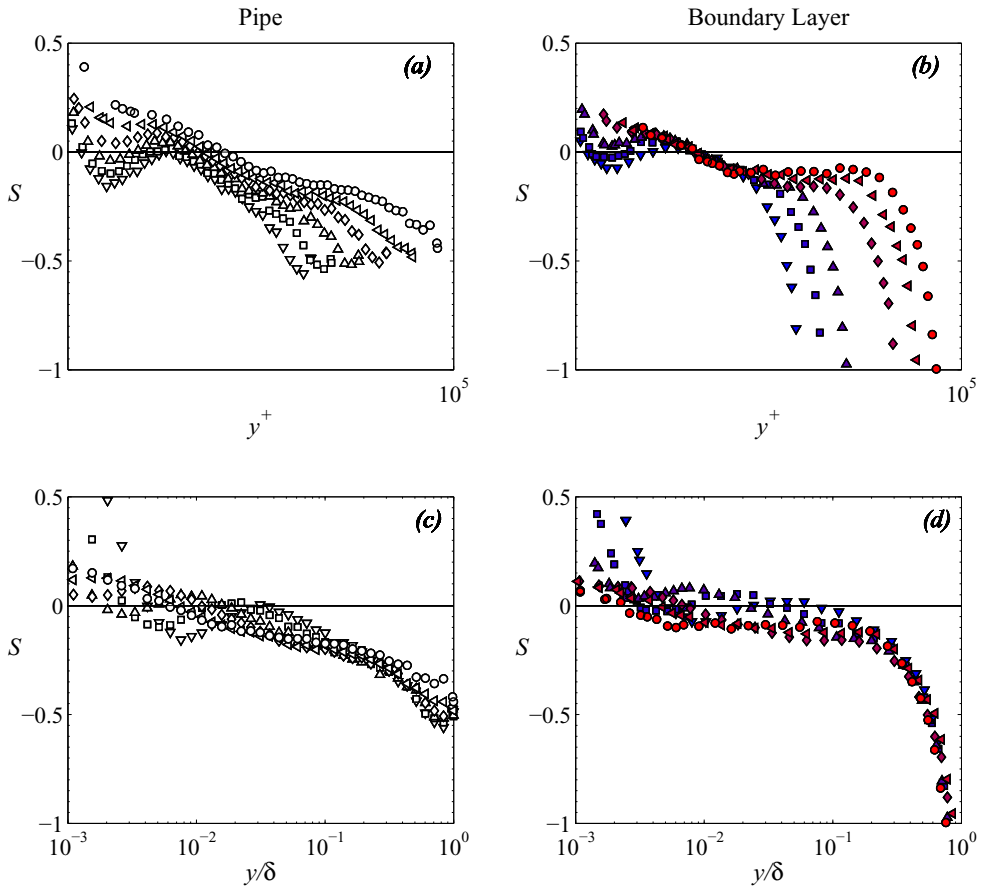

Figure 6.3: Skewness in inner coordinates (a,b) and outer coordinates (c,d). Empty symbols indicate Pipe flow (a,c) and filled boundary layer (b,d). Symbols as indicated in Table 6.1.

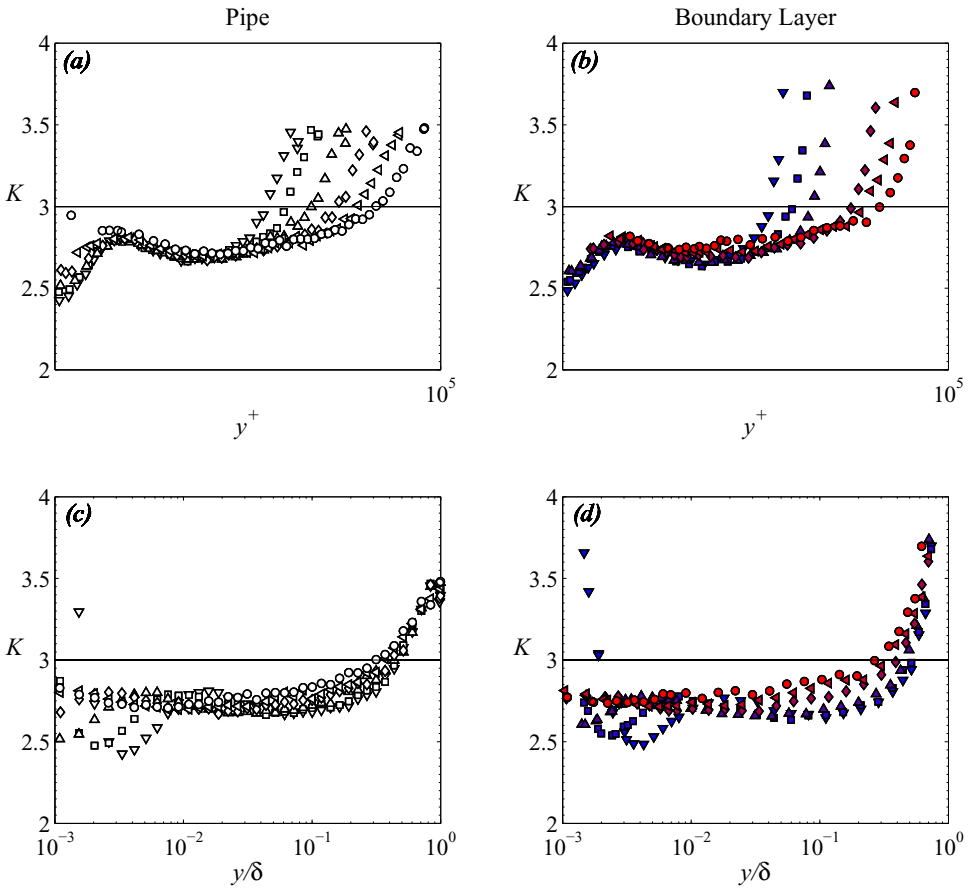

Figure 6.4: Kurtosis in inner coordinates (a,b) and outer coordinates (c,d). Empty symbols indicate Pipe flow (a,c) and filled boundary layer (b,d). Symbols as indicated in Table 6.1.

that if the summands are assumed to be statistically independent (as in the case of non-interacting eddies), Equation (5.1.2) is consistent with the attached eddy hypothesis. Furthermore, they show by using the central limit theorem that the pth root of moments of velocity fluctuations could be expected to behave according to

$$\left\langle \left(u^+\right)^{2p} \right\rangle^{1/p} = B_p - A_p \ln(y/\delta), \tag{6.3.1}$$

where A_p and B_p are constants, at least at fixed Reynolds number. This equation, introduced by Meneveau and Marusic [2013], is the generalized logarithmic law for high-order moments. They looked at the validity of this law in boundary layers with Re_τ up to 19,000 and found good agreement between Equation (6.3.1) and experiments. The behavior of high-order moments was noted to be sub-Gaussian with the possibility of having a universal value of A_p. Here we extend this analysis to both pipe flow and boundary layer at even higher Reynolds numbers.

Moments up to 12th order have been calculated and analyzed, and the behavior was found to be similar for all even moments studied. Figure 6.5 shows the pth roots of the pth even moments $\left\langle \left(u^+\right)^{2p} \right\rangle^{1/p}$, for $2p = 2,\ 6,\ 10$ (the data for $2p = 4,\ 8,\ 12$ show the same trends). Results for both pipe (empty symbols) and boundary layer (filled) flows are shown for six matching Reynolds numbers, as listed in Table 6.1. For higher moments, a qualitatively similar behavior can be seen as for the variances, with an inner peak at about $y^+ = 15$ having a Reynolds number independent value, a blending region in the mesolayer ($30 < y^+ < 300$), and a logarithmic behavior in the log-region. The results from the pipe and the boundary layer agree very well throughout most of the flow, with the only differences in the outer layer due to the different outer boundary conditions, as expected. Some differences can also be seen in the near-wall region, around $y+ \approx 15$, where pipe flow has a slightly higher peak value and smaller spatial filtering effects, because ℓ^+ is smaller for the pipe (listed in

Table 6.1). Here, no spatial filtering correction has been used for any moments, as there is no well-established corrections, and so caution must be used when drawing any conclusions for $y+ < 100$. Finally, it appears that the inner limit of the logarithmic range is at higher y^+ for pipe flows, as seen for the variances.

Figure 6.5(b, d, f) show results in outer coordinates for $Re_\tau \geq 20,000$, that is, for the three highest Reynolds numbers. The solid line indicates Equation (6.3.1) with constants A_p and B_p found from a regression fit to the pipe flow profile at $Re_\tau = 70,000$ ($A_1 = 1.13$ and $B_1 = 1.17$, $A_6 = 2.48$ and $B_3 = 3.31$, $A_5 = 3.44$ and $B_5 = 6.73$ respectively). Similarly to the behavior of the variances, the higher moments show a good collapse between pipe and boundary layer flows, though the boundary layer data again shows some Reynolds number dependence. For the higher moments the collapse between profiles actually improves in the log-region, clearly showing a wide range of logarithmic behavior.

Following Equation (6.3.1), constants A_p and B_p were found by regression fit to each profile; that is separately for each flow, Reynolds number and moment. In order to avoid biases from the range chosen, and to try to determine the best range, different ranges were used for fitting, with the inner limit varying as $y^+_{min} = [3Re_\tau^{0.5}; 200; 400; 600; 800]$ and keeping a constant outer limit at $(y/\delta)_{max}$ =0.15. A minimum of four points in each profile were used for determining the constants, otherwise the profile was discarded as not having a sufficiently extensive logarithmic region.

The Perry-Townsend constant A_p in Equation (6.3.1), as a function of moment, is shown in Figure 6.6, for five different ranges for both flows. For Gaussian statistics, $A_{p,G} = A_1 \left[(2p-1)!!\right]^{1/p}$, where !! denotes double factorial, and this result is shown as the solid line in Figure 6.6. It is clear that for both pipe and boundary layer flows, all the constants have a sub-Gaussian behavior, as was previously observed by Meneveau and Marusic [2013] for boundary layers. For smaller y^+_{min} values for the

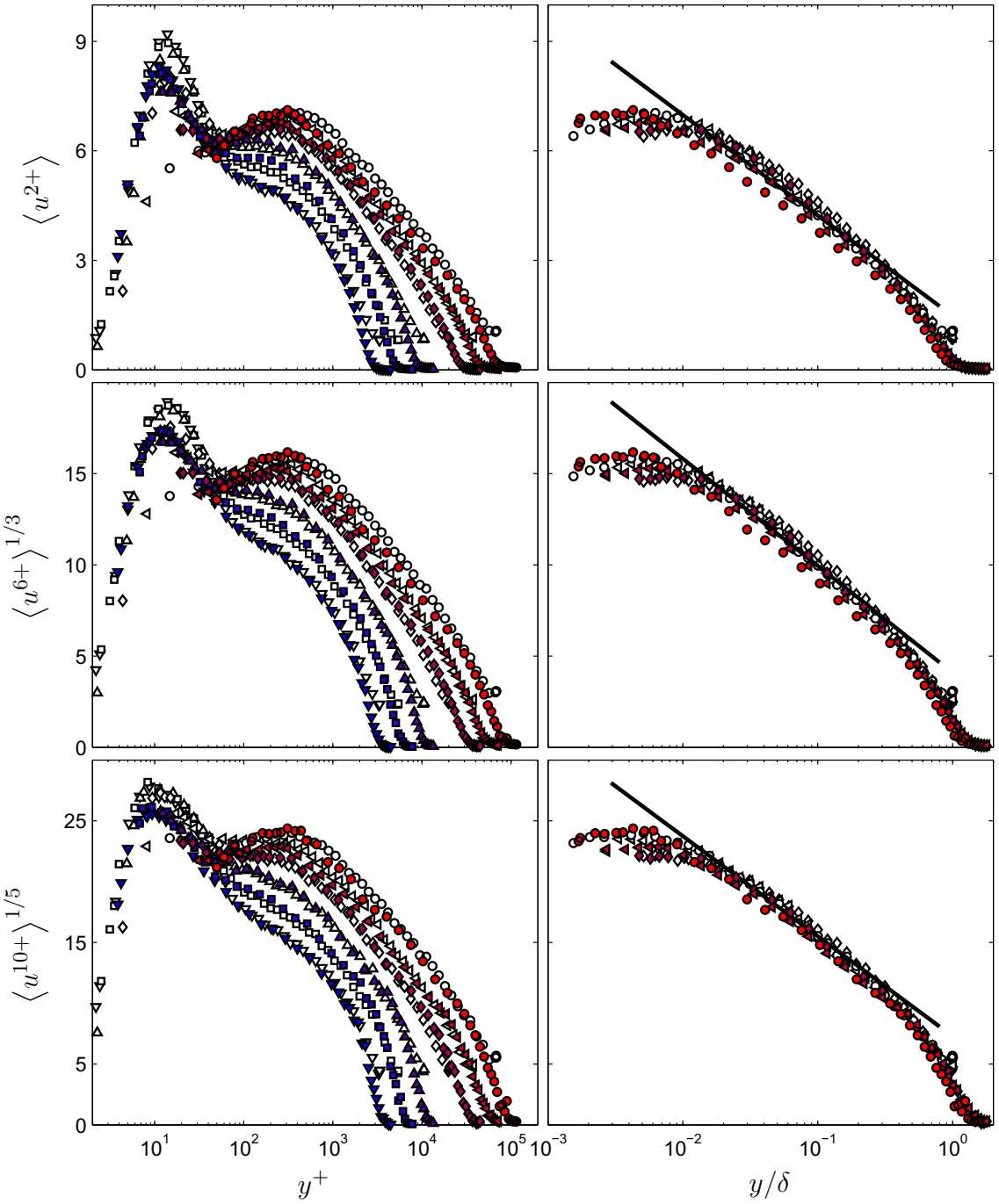

Figure 6.5: Higher order moments $2p = 2$ (a,b), $2p = 6$ (c,d), $2p = 10$ (e,f). Plots (a,c,e) show data for all Re_τ in inner coordinates. Plots (b,d,f) show data in outer coordinates, for $Re_\tau \geq 20,000$ and $y^+ > 100$. Symbols as indicated in Table 6.1.

fit limit, one can see a clear Reynolds number variation in the values of A_p between cases, as well as change in value with changing limit. For pipe flow, A_p was found to become independent of Re_τ for $y^+_{min} \geq 600$, and the value $y^+_{min} = 3Re_\tau^{0.5}$ was found to be a poor estimate for inner limit. In contrast, for boundary layer flows $y^+_{min} = 3Re_\tau^{0.5}$ proves to be a good inner limit and the constants found from there are similar to ones for conservative ranges with $y^+_{min} \geq 600$. It must be noted, however, that for boundary layer the Reynolds number dependence is already negligible at $y^+_{min} = 400$. Assuming that the more conservative range gives a more precise estimate of the constant, it can be argued that values using a higher y^+_{min} better represent the true value. It was found empirically that a good representation of the asymptotic constant value of the slope is given by $A_p \sim (2p-1)^{1/2}$ for both pipe and boundary layer (shown in dashed line in Figure 6.6), rather than the Gaussian variation (shown as a solid black line).

It may be concluded that if large enough value of y^+_{min} is chosen, A_p does not depend on Reynolds number in neither pipe nor boundary layer flows. The only outlier, the highest Reynolds number case for the boundary layer, has a slightly lower value of A_p, which is probably due to the difficulties in estimating the higher order moments (especially the 12th moment) given the limited spatial resolution of the probe at the very highest Reynolds numbers. For outer limit of the log-region, $y/\delta = 0.15$ was found to be the best limit for both flows (even though for the variances measured in the boundary layer, a logarithmic behavior was observed extending as far as up to $y/\delta = 0.3$).

Figure 6.7 shows the variation of the additive constant B_p in Equation (6.3.1) as a function of moment and Reynolds numbers, for different ranges of fitting. Similar to behavior of the slope A_p, for low values of y^+_{min} there is a large variation of the constant. For both flows, a more constant value of B_p is reached as the inner limit is increased. For pipe flow, again, $y^+_{min} \geq 600$ seems to be the start of the range where B_p becomes independent of Reynolds number, whereas $y^+_{min} \geq 3Re_\tau^{0.5}$ proves to be a poor choice.

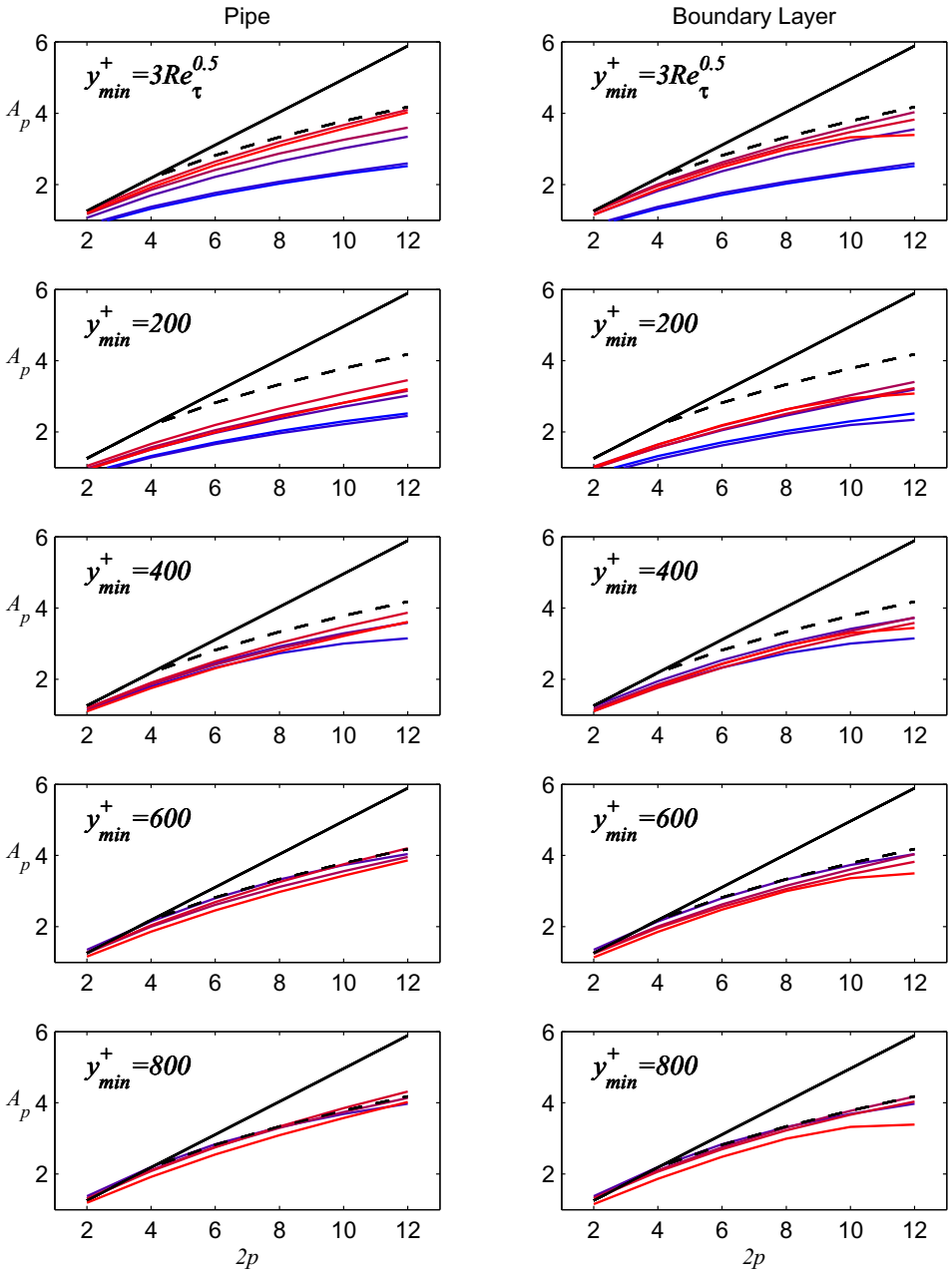

Figure 6.6: Perry-Townsend constant A_p for even moments $2p$ for the fitting range $y^+ = [y^+_{min}, 0.15Re_\tau]$. The solid black line shows the slope of a Gaussian distribution, and the dashed line shows the empirical fit $A_p = 1.26(2p-1)^{1/2}$. Colors as indicated in Table 6.1.

Interestingly though, for the boundary layer the behavior of B_p with a change in y^+_{min} is different from that observed for the slope. For $y^+_{min} \geq 3Re_\tau^{0.5}$, a clear dependence on Re_τ can be observed, as well as for any limits below $y^+_{min} = 600$. However, for a conservative limit of $y^+_{min} \geq 600$, the additive constant in boundary layers also seems to reach an asymptotic value independent of Re_τ. This is in contrast to the findings by Meneveau and Marusic [2013], who found B_p to depend on Re_τ (as could be seen here for $y^+_{min} \geq 3Re_\tau^{0.5}$ which is what they used as their inner limit). However it must be kept in mind that less than a decade of Reynolds numbers can be studied and therefore any Reynolds number dependence could just be within experimental error.

6.4 Conclusions

Following the results above, it could be argued that to reach true independence of Reynolds number for the higher order moments, the log-region defined by $600 < y^+ < 0.15Re_\tau$ should be considered for both pipe and boundary layer flows. For the boundary layer, $y^+_{min} \geq 3Re_\tau^{0.5}$ seems to be a reasonable estimate for the inner limit of the logarithmic behavior for the mean flow and the turbulent stresses, but for higher-order moments this lower limit leaves the additive constant B_p varying with Reynolds number. Therefore, even though a sufficient separation between inner and outer scaling has been reached for mean and variances, higher-order moments still have some viscous effects present in the range $3Re_\tau^{0.5} \leq y^+_{min} \leq 600$ (for $Re_\tau < 40,000$, where this region excists). At the same time, a universal log-region defined by $600 \leq y^+ \leq 0.15Re_\tau$ for both pipe and boundary layer would support the hypothesis of similarity of wall-bounded flows in the inner region of the flow. These bounds also define a minimum Reynolds number where this similarity occurs to be $Re_\tau \approx 4,000$ (being much higher than previously believed, as discussed in Smits et al. [2011a]), and therefore a decade of true scale separation could only be seen above $Re_\tau = 40,000$.

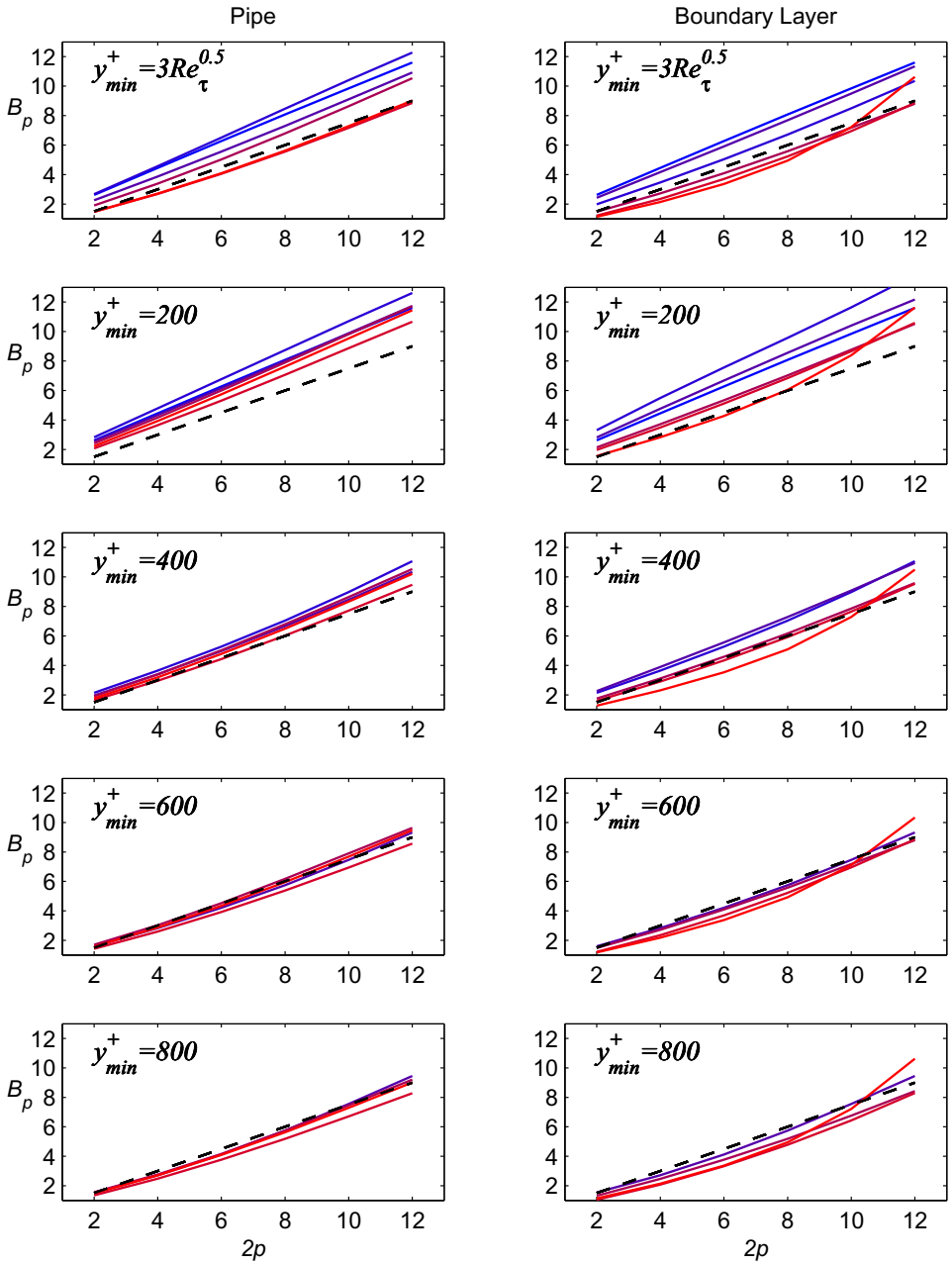

Figure 6.7: Additive constant B_p for even moments $2p$ for the fitting range $y^+ = [y^+_{min}, 0.15Re_\tau]$. The dashed line shows the empirical fit $B_p = \frac{3}{4}2p$. Colors as indicated in Table 6.1.

Chapter 7

Spectra in turbulent wall-bounded flows

7.1 Introduction

In the previous chapters, the statistics of turbulent pipe and boundary layer flow were studied. We saw that there are scaling laws for different regions of the flow and we can estimate the behavior of the flow with changing Reynolds number. We also found that the mean velocity, the variations and even the higher order moments all demonstrate a logarithmic behavior in the inertial sublayer ($800 \lesssim y^+ \lesssim 0.15Re_\tau$ in pipes, and $3Re_\tau^{0.5} \lesssim y^+ \lesssim 0.15Re_\tau$ in boundary layers). However, one of the important questions in turbulence is to understand how the energy injected at large scales is transported to the small scales and dissipated, the so-called the energy cascade. Here, spectral analysis becomes useful. Unfortunately, experimentally measuring the full three-dimensional energy spectrum is extremely difficult, as one needs fully resolved three-dimensional velocity data. Instead, we can often only examine the power spectral density of the streamwise velocity fluctuations Φ_{uu}, so that $\int_0^\infty \Phi_{uu}(k_x)\,\mathrm{d}k_x = u^2$.

In the logarithmic region, where $\nu/u_\tau \ll y \ll \delta$, the turbulence spectrum is usually

divided into three regions: a low wavenumber range that scales with the characteristic shear layer length scale δ; an intermediate wavenumber range that scales will the wall-normal distance y; and a high wavenumber range that scales with the Kolmogorov length η_K. As shown by Perry et al. [1986], we expect that at high enough Reynolds numbers, there will be an overlap of the low and intermediate wavenumber regions, described by

$$\frac{\Phi_{uu}(k_x\delta)}{U_{C1}^2} = g_1(k_x\delta) = \frac{A_{1s}}{k_x\delta}, \tag{7.1.1}$$

or

$$\frac{\Phi_{uu}(k_x y)}{U_{C1}^2} = g_2(k_x y) = \frac{A_{1s}}{k_x y}, \tag{7.1.2}$$

where U_{C1} and U_{C2} are the respective characteristic velocities, A_{1s} is a universal constant, $k_x = 2\pi/\lambda_x$ is the streamwise wavenumber, and λ_x is the streamwise wavelength. This overlap relation is often referred to as the inverse power law [Perry et al., 1986] or alternatively the k_x^{-1} law.

Similarly, an overlap of the intermediate and high wavenumber regions would be expected, with

$$\frac{\Phi_{uu}(k_x y)}{U_{C2}^2} = g_2(k_x y) = \frac{K_0}{\kappa^{2/3}(k_x y)^{5/3}}, \tag{7.1.3}$$

or

$$\frac{\Phi_{uu}(k_x \eta_K)}{u_K^2} = g_3(k_x \eta_K) = \frac{K_0}{(k_x \eta_K)^{5/3}}, \tag{7.1.4}$$

which is referred to as the $k_x^{-5/3}$ law, and the region is often called the inertial sub-range. Here u_K is the Kolmogorov velocity, $K_0 \approx 0.5$ is the Kolmogorov constant, and $\kappa \approx 0.4$ is the von Kármán constant [Perry et al., 1986]. The Kolmogorov length η_K and velocity u_K can be expressed as a function of viscosity ν and the total dissipation rate ε, as $\eta_K = (\nu^3/\varepsilon)^{1/4}$ and $u_K = (\nu\varepsilon)^{1/4}$.

The characteristic velocities at large and intermediate wavelengths can be assumed to be equal to the friction velocity (which is reasonable considering the scaling in the

statistics) so that $U_{C1} \sim U_{C2} \sim u_\tau$. Now, by integrating over the named spectral regions, the streamwise turbulence intensity u can be found as

$$u^{2+} = B_{1s} - A_{1s} \ln\left[\frac{y}{\delta}\right] - F(y^+)^{-0.5}, \tag{7.1.5}$$

where A_{1s} and F are universal constants and B_{1s} is a large-scale constant, as shown in Perry et al. [1986]. As $y^+ \to \infty$ (that is where $y >> \nu/u_\tau$) this relation becomes

$$u^{2+} = B_1 - A_1 \ln\left[\frac{y}{\delta}\right], \tag{7.1.6}$$

suggested first by Townsend [1976] and observed experimentally in Chapters 3 and 5 for pipes and boundary layers. Here we have dropped subscript s from the constants A_1 and B_1 with the assumption that this is the correct reasoning for explaining the logarithmic behavior in the variances.

Based on reasoning of Perry et al. [1986], the k_x^{-1} region would be expected to appear together with the $k_x^{-5/3}$ region in the region where the turbulent fluctuations show a logarithmic behavior. The existence of a k_x^{-1} law is important to establish, as it also plays an important role in many turbulence models, especially in the framework of Townsend's attached eddy framework [Marusic and Kunkel, 2003, Marusic et al., 1997, Perry and Chong, 1982, Perry and Li, 1990, Townsend, 1976]. Whereas an inertial subrange with $k_x^{-5/3}$ has been observed in many experiments, the k_x^{-1} has only been seen in laboratory flows at high Reynolds number over a very limited spatial extent by Nickels et al. [2005], although several authors report its presence in the atmospheric boundary layer (see, for example, Högström et al. [2002], Katul and Chu [1998]). We should note, however, that Hultmark [2012] suggested an alternative derivation for Equation (7.1.6) without involving the spectral overlaps and k_x^{-1} region.

Existence of k_x^{-1} region would indicate a complete similarity. Morrison et al. [2004] found no such overlap region in pipe flow between low and intermediate wavenumber

regions, showing an incomplete similarity behavior. They suggested that there is no complete similarity because even though inner scaling (y and u_τ) may properly scale the spectrum at intermediate wavenumbers, these wavenumbers might be too small for simultaneous scaling with outer variables (δ and u_τ). They also speculated that a different velocity scale might be considered for outer scaling which would then make complete similarity impossible.

The energy distribution in wavenumber space represented by the spectrum can also help to understand the structure of the turbulent shear flows and the behavior of coherent structures in these flows. Large scale coherent structures in the turbulent wall region and outer flow have been observed both in boundary layers (Kovasznay et al. [1970], Balakumar and Adrian [2007]) and pipes (Kim and Adrian [1999], Guala et al. [2006]) and are usually referred to as Large Scale Motions (LSMs). These structures are usually about 2-3δ in streamwise and 1-1.5δ in spanwise direction and are often associated with occurrence of bulges of turbulent fluid at the edge of the wall layer. They carry a significant amount of the Reynolds shear stress and play an important role in turbulent transport [Ganapathisubramani et al., 2003].

Recent advances in visualization techniques have revealed the existence much longer meandering structures in wall shear flows. In pipe flows these structures are usually referred to as Very Large Scale Motions (VLSMs), observed by many authors [Bailey and Smits, 2010, Guala et al., 2006, Kim and Adrian, 1999], and extending up to $20R$ in the streamwise direction [Monty et al., 2007]. Similar very large scale coherent structures have been observed in the turbulent wall region of boundary layers, extending up to 20δ [Hutchins and Marusic, 2007] in length, and denoted as superstructures (SS). Hutchins and Marusic [2007] found that these superstructures seem to scale with the boundary layer thickness δ, that they have a meandering nature, and that they are present only in the turbulent wall region, compared to VLSMs that extend throughout the outer flow of pipes and channels. It is important

to note that when inferred from single point statistics, these lengths are usually much shorter, 6δ and 10-15R respectively, due to the meandering nature of these large coherent structures [Hutchins and Marusic, 2007]. The differences between VLSM and SS may simply be due to the different boundary conditions imposed by open and confined geometry flows [Monty et al., 2009].

In the spectra, it is often true that here are two distinct maxima observed, one in the near-wall region associated with the near-wall energy production around the inner peak in u^{2+} at about $y^+ \approx 15$ (we shall call this the *inner spectral peak*), and one in the outer region associated with the VLSMs or SSs (we shall call this the *outer spectral peak*). The location and magnitude of the outer spectral peak is still an open question, as these very large coherent structures together with the outer spectral peak can only be seen at high Reynolds numbers where the scale separation is large enough. Hutchins and Marusic [2007] observed this outer spectral peak associated with superstructures for $Re_\tau \geq 2,000$ in boundary layers, and found that the magnitude of the peak increases with Reynolds number. It was located at about $y/\delta \approx 0.06$ and $\lambda_x/\delta \approx 6$. This observation was made on data with a maximum $Re_\tau \approx 7,300$, and it was noted that a larger range of Reynolds number is needed to make further conclusions. A considerably larger range, $2,800 < Re_\tau < 19,000$, was available to Mathis et al. [2009], who studied the large scale amplitude modulation on the small scale structures in boundary layers. At these Reynolds numbers, the footprint of superstructures and the associated outer spectral peak was clearly evident. They found that the large-scale intensity in the log-region increases with Reynolds number, and results in increase in amplitude modulation on the near-wall small-scale structures (suggesting that the increase in outer spectral peak energy was connected to the increase in the near-wall peak in u^{2+}). Based on their more extensive Reynolds number range, Mathis et al. [2009] suggested that the outer spectral peak is located at about $y^+ \approx 3.9Re_\tau^{0.5}$ (which they associated with the middle of the log layer with

bounds $100 < y^+ < 0.15Re_\tau$). They also found that this location collapsed well with the zero magnitude of the amplitude modulation (which was also very similar to the skewness profile of the velocity).

All these observations have been made at relatively moderate Reynolds numbers, and there remains the question whether these reported trends persist with increasing Reynolds number, or if some Reynolds number independent self-similar flow will emerge once the scale separation is large enough. Here, we have the unique opportunity to study the spectra from well-resolved high Reynolds number experiments in pipe and boundary layer at comparable Reynolds numbers, up to $Re_\tau \approx 70,000$.

7.2 Experiments

In previous Chapters (3 and 5), high Reynolds number experiments were described in pipe flow up to $Re_\tau \approx 100,000$, and in a zero pressure gradient boundary layer up to $Re_\tau \approx 70,000$. The NSTAP sensor (described in Chapter 2) allows a very high temporal resolution (up to 300 kHz) together with its good spatial resolution (down to 30μm). Here we compare spectra for six matching Reynolds numbers (as we did for the high-order moments in Chapter 6): $Re_\tau \approx 3\times10^3$; 5×10^3; 10×10^3; 20×10^3; 40×10^3; 70×10^3, with properties listed in Table 7.1. The outer characteristic length scale is denoted as δ throughout this chapter, corresponding interchangeably to the boundary layer thickness for boundary layers and the pipe radius for pipes.

We are interested in looking at the spatial spectrum of the energy associated with the streamwise fluctuations. Taylor's hypothesis [Taylor, 1938] was used to covert the frequency spectrum to the spatial spectrum by assuming that the local turbulent field is "frozen" while it is carried past the sensor by some large scale characteristic velocity. Here we use the local mean velocity $U(y)$ as the convection velocity at each wall-normal location. Rosenberg et al. [2013] gives an extended discussion on the

Case	Pipe			Boundary layer			Symbol
$Re_\tau \approx$	Re_τ	ℓ^+	f_s^+	Re_τ	ℓ^+	f_s^+	
3×10^3	3,334	3.1	12.6	2,622	5.8	9.5	▼
5×10^3	5,412	5.0	9.7	4,635	10.2	5.6	■
10×10^3	10,481	9.7	4.8	8,261	17.5	3.4	▲
20×10^3	20,250	18.8	2.4	25,062	29.2	1.1	♦
40×10^3	37,690	35.0	1.4	40,053	46.6	0.7	◀
70×10^3	68,371	31.7	0.8	72,526	74.7	0.5	●

Table 7.1: Cases chosen for pipe and boundary layer spectra comparison. ℓ^+ is the wire length in viscous units and f_s^+ is sampling frequency in viscous units.

implications of using the Taylor's hypothesis at these Reynolds numbers in pipe flow, and they conclude that the hypothesis works relatively well, except very close to the wall where it can introduce significant distortions.

For all cases studied, the original sampling frequency f_s in experiments was 300 kHz. This corresponded to $12.6 < f_s^+ < 0.80$ for the pipe flow and $9.47 < f_s^+ < 0.45$ for the boundary layer flow (shown in Table 7.1, where $f_s^+ = f_s\nu/u_\tau^2$ is the sampling frequency in viscous units. To avoid the effects of temporal filtering (which will change with Reynolds number), a low-pass filter with a cut off at $f^+ = 0.5$ was used to remove any frequencies higher than f_s^+ for the worst case. This filtered spectra was compared to the original, and it was confirmed that filtering did not alter any results or conclusions.

In order to find the Kolmogorov length and velocity scales, the rate of dissipation ε needs to be determined. An estimate of the mean dissipation rate was found using an isotropic estimate, that is by integrating the one-dimensional dissipation spectrum according to

$$\varepsilon = 15\nu \int_0^\infty k_x^2 \Phi_{uu}\, \mathrm{d}k_x. \tag{7.2.1}$$

Bailey et al. [2009] studied the local dissipation scales in the same pipe facility with hot-wires at slightly lower Reynolds numbers and found the isotropic relation to be a reasonable estimate. However, for the highest Reynolds number cases the dissipation

spectra is not fully covered by the measurements, decreasing the accuracy of the ε estimate.

7.3 Results and discussion

Spectra at three different Reynolds numbers are shown in figure 7.1 for pipe flow (a,c,e) and boundary layer flow (b,d,f) at $0.001 \leq y/\delta \leq 0.5$. At the lowest Reynolds number, a small $k_x^{-5/3}$ region can be observed for $y/\delta \geq 0.05$ for both flows, being more significant for boundary layer. The pipe flow appears to display a k_x^{-1} region for intermediate wall locations, whereas this is not evident for the boundary layer. As the Reynolds number increases, the $k_x^{-5/3}$ region extends for both flows over a longer wavenumber range and starts emerging closer to the wall. The k_x^{-1} also appears in pipe flow at some wall locations over a short extent.

7.3.1 The $k_x^{-5/3}$ dependence

The spectra in Kolmogorov scaling, $\Phi_{uu}/\left(\varepsilon\nu^5\right)^{1/4}$, is shown in figure 7.2 for $0.001 \leq y/\delta \leq 1.0$ at $Re_\tau \approx 20 \times 10^3$ for pipe flow (a) and boundary layer flow (b). The Kolmogorov scaling collapses the data well for all wall-normal locations at high wavenumbers, and as the y/δ increases a clear $k_x^{-5/3}$ range emerges for both flows, extending up to two decades in $k_x\eta_K$ and dropping off at $k_x\eta_K \approx 0.1$. The energy at large length scales (smaller k_x) increases with y, but for $y/\delta > 0.15$ (the outer edge of turbulent wall region) the energy at large scales starts to decrease in the wake region (denoted as dashed lines). However, the $k_x^{-5/3}$ region continues to increase with increasing wall distance. This observation agrees well with inertial subrange scaling arguments, which suggest that the $k_x^{-5/3}$ region emerges when the separation between large energetic scales and small dissipative scales is large and the flow can be considered nearly isotropic. For boundary layer at larger y/δ values the spectra

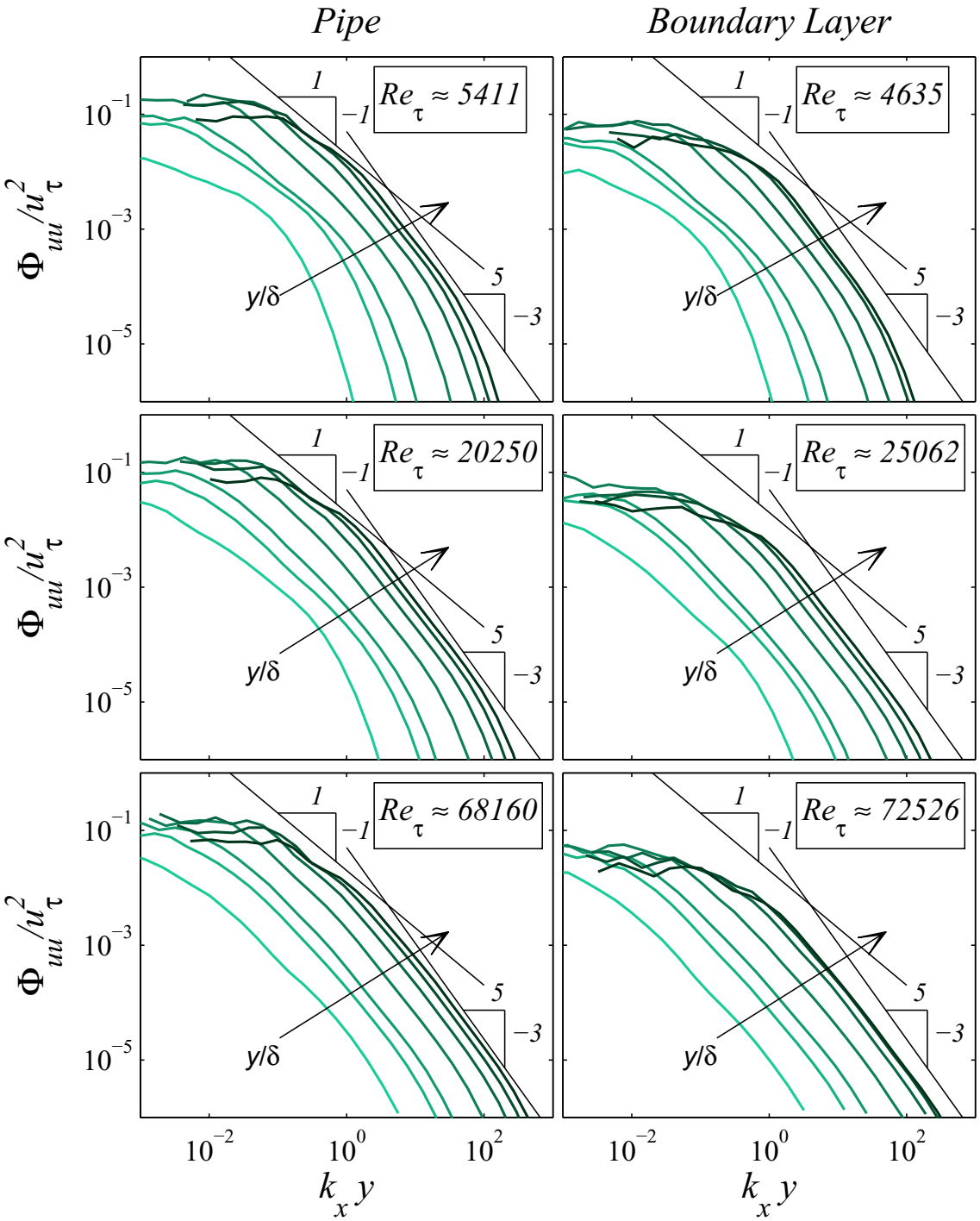

Figure 7.1: Spectra Φ_{uu}/u_τ^2 with varying $y/\delta \approx 0.001; 0.005; 0.01; 0.05; 0.15; 0.3; 0.5$ at three different $Re_\tau \approx 5,000; 20,000; 70,000$ for pipe and boundary layer. Arrow indicates increasing wall-normal distance.

departs from $k_x^{-5/3}$ behavior at higher wavenumbers than in pipe flow, which can be explained with the intermittency in the outer boundary layer.

By assuming Kolmogorov scaling to be valid at all Reynolds numbers, the error in finding total dissipation ε can be estimated for each Re_τ by examining the lack of collapse of the experimental spectra in Kolmogorov scaling. This error in Kolmogorov sectrum $\Phi_{uu}/\left(\varepsilon\nu^5\right)^{1/4}$ was found to be increasing with Re_τ in range $0.5\% - 4\%$ for the pipe and $1\% - 5\%$ for the boundary layer, with the exception of the boundary layer case with $Re_\tau \approx 70,000$ where error was as large as about 25%. Because Φ_{uu} varies as $\varepsilon^{1/4}$, the uncertainty range for dissipation would be 2% to16% for the pipe and 4% to 20% for the boundary layer (except for the boundary layer at $Re_\tau \approx 70,000$ where the error may be as high as 100%).

We can also examine the inertial subrange behavior with changing Reynolds number. Figure 7.3 shows Kolmogorov spectra for all Reynolds numbers in this study, at a single wall normal location $y/\delta = 0.5$. The Kolmogorov scaling collapses all the cases well above $k_x\eta_K \approx 0.015$ (with only a slight disagreement at $Re_\tau = 70 \times 10^3$ for boundary layers, due to difficulties in estimating ε). As the Reynolds number increases, the separation between the energy production range and the dissipation range increases. This can clearly be seen in figure 7.3, where the $k_x^{-5/3}$ extends further out to smaller $k_x\eta_K$ with increasing Re_τ.

The behavior of pipe and boundary layer spectra was found to be identical in Kolmogorov variables for $Re_\tau \geq 5 \times 10^3$, which indicates that the small wavelengths in the turbulent wall region and in the wake are independent of the flow geometry at these high Reynolds numbers. To demonstrate this point further, in figure 7.4 both pipe (dashed line) and boundary layer (solid line) spectra are plotted on top of each other for $y/\delta = 0.05$ and $y/\delta = 0.5$. The Kolmogorov constant was found to be $K_0 = 0.51 \pm 0.03$ for pipe and $K_0 = 0.52 \pm 0.03$ for boundary layer data using a least square fit in the inertial subrange for $0.05 < y/\delta < 0.5$.

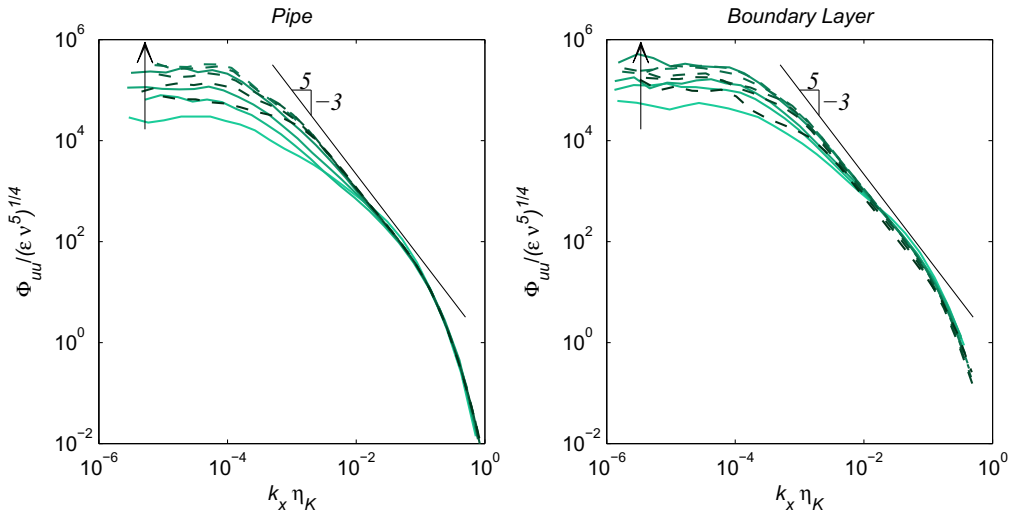

Figure 7.2: Kolmogorov spectra at $Re_\tau \approx 20,000$ with varying $y/\delta \approx 0.001$; 0.005; 0.01; 0.05; 0.15; 0.3; 0.5; 0.7; 1.0 for pipe and boundary layer. Wall locations $y/\delta \leq 0.15$ marked with solid lines and $y/\delta > 0.15$ marked with dashed lines. Arrow indicates the increase in y/δ until $y/\delta = 0.15$.

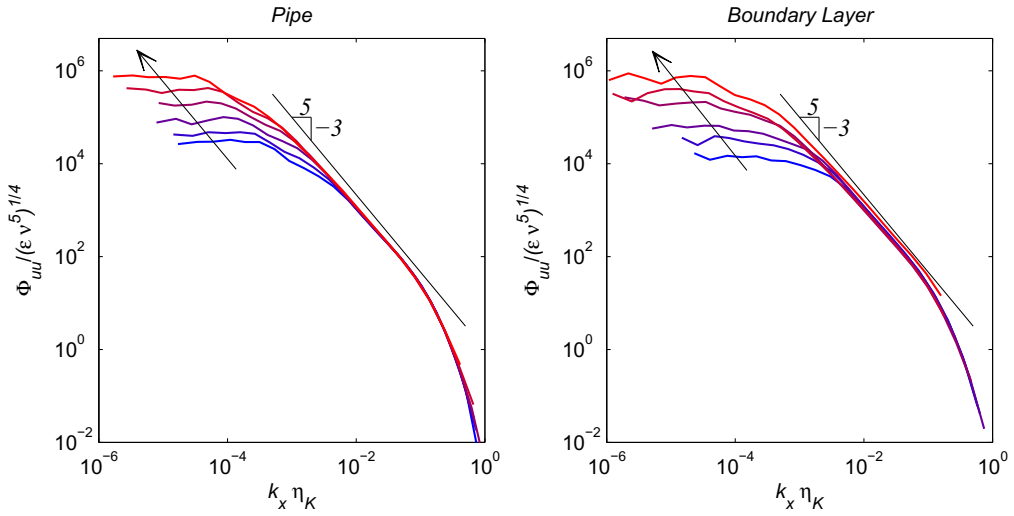

Figure 7.3: Kolmogorov spectra with varying $Re_\tau \approx 3,000$; 5,000; 10,000; 25,000; 40,000; 70,000 at $y/\delta \approx 0.5$, with arrow indicating increase in Re_τ.

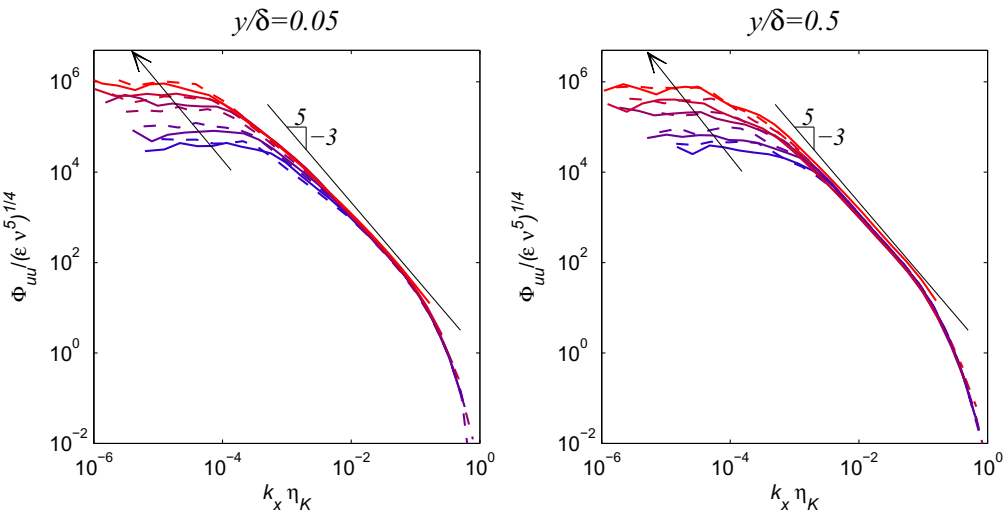

Figure 7.4: Kolmogorov spectra with varying $Re_\tau \approx 5,000$; 10,000; 25,000; 40,000; 70,000 at $y/\delta \approx 0.05$ and $y/\delta \approx 0.5$, comparison between pipe (dashed line) and boundary layer (solid line). Arrow indicating increase in Re_τ.

7.3.2 The k_x^{-1} dependence

To consider the k_x^{-1} dependence, spectra are shown in pre-multiplied form as $k_x\Phi_{uu}/u_\tau^2$ in Figures 7.5 and 7.6 for $Re_\tau = 5,000$ and $Re_\tau = 70,000$ respectively. In this representation, the k_x^{-1} region would show up as plateau in the spectra. For both cases, spectra in the turbulent wall region $3Re_\tau^{0.5} < y^+ < 0.15Re_\tau$ are shown using solid lines (the region where a logarithmic behavior was found in the mean and variances and where k_x^{-1} region would be expected based on Perry et al. [1986] analysis), and spectra in the wake region $0.15 < y/\delta < 0.7$ are shown using dashed lines.

First, we consider the lower Reynolds number cases shown in figure 7.5. For low wavenumbers (larger wavelengths), a good collapse is seen with δ scaling, and at higher wavenumbers (smaller wavelengths), k_x scales well with wall-normal distance y. This is true especially in the turbulent wall region, with departures from these scalings appearing towards the wake. If an overlap region between these two scalings existed with the same characteristic velocity u_τ, this pre-multiplied representation would

result in a plateau in the profile. As one can see, there is no clear plateau region evident in the data, for neither pipe nor boundary layer. However, in either case one could postulate a small plateau region in a couple of cases for a wall-normal location around $y/\delta = 0.15$, but this behavior disappears closer to the wall, as well further from the wall. Also, no region exists where both scalings would collapse the data, hence there is incomplete similarity, and no full similarity exists, similar to discussion in Morrison et al. [2004]. This observation suggests that any plateau seen here is just an artifact of the decrease in the energy at small wave-numbers, bringing down the peak to form a shoulder, and forming an approximate plateau at some locations near the outer edge of turbulent wall region. Similar trends can be observed for higher Reynolds number cases.

Second, we consider the high Reynolds numbers cases. Spectra for $Re_\tau = 70,000$ are shown in figure 7.6 and again, the scalings with y and δ collapse respective ranges of the wavenumber for $3Re_\tau^{0.5} < y^+ < 0.15Re_\tau$ but no overlap between these scalings is evident suggesting an incomplete similarity. As at low Reynolds number, at some y/δ locations near 0.15, single spectra show some flattening, but this seems to be due to the change in the peak energy wavelengths for different wall locations. Therefore no k_x^{-1} dependence is evident for neither pipes nor boundary layers; small flat regions seem to indicate the outer bound of the turbulent wall region, where the wavelengths with highest energy are decreasing, but there is no collapse with y and δ scaling over the same interval in wavenmuber.

Morrison et al. [2004] suggested existence of incomplete similarity due to u_τ not being the appropriate velocity scale for outer scaling. del Álamo et al. [2004] suggested that the large wall-attached motions do not scale with u_τ because their contribution to the Reynolds stress is limited by the impermeability of the wall and proposed a logarithmic correction to the k_x^{-1} spectrum as $k_x\Phi_{uu} = \beta u_\tau^2 \log(2\pi\alpha^2/(k_x y)$. This function with fitted constants $\alpha = 2$ and $\beta = 0.2$ agreed well with the experimental

and numerical spectra studied by del Álamo et al. [2004] in the range $y < \lambda_x < 10y$ ($0.63 < k_x y < 6.3$). This relation is shown using a red dashed line in Figures 7.5(c,d) and 7.6(c,d) using constants from del Álamo et al. [2004], with range $y < \lambda_x < 10y$ shown as solid line. For $Re_\tau = 5,000$, a small interval in wavenumber agrees with this relation for pipe flow, similar to the suggested bounds $0.63 < k_x y < 6.3$, but the boundary layer spectra seem to have a different slope. At $Re_\tau = 70,000$, this relation agrees with the data over a wider range than that suggested by del Álamo et al. [2004], but again for the boundary layer the slope should be varied to agree better, possibly indicating that the constant β could vary with Reynolds number ($\beta = 0.23$ and 0.19 were found better fits for $Re_\tau = 5,000$ and 70,000 respectively).

In chapter 3.4, we found that the streamwise turbulent stress u^{2+} scaled well with outer variables u_τ and δ in both the turbulent wall region and in the wake. In this outer region, Φ_{uu} should also scale with outer variables at large wavelengths. The pre-multiplied spectra for all Reynolds numbers at four different locations $y/\delta = 0.05$; 0.1; 0.15; 0.5 are shown in figure 7.7. Based on the observations on the scaling of u^{2+} in pipe and boundary layer flows, better collapse with outer variables would be expected in pipe flow. This can indeed be concluded from figure 7.7, where spectra in pipe flow (a,c,e) show better collapse than spectra in boundary layer flow (b,d,f). In boundary layers, the energy at large scales is decreasing and more energy is relocated to higher wave-numbers. However, if boundary layer spectra show a clear trend with Reynolds number, there is some variation in pipe flow as well, showing a slight decrease in the energy with increasing Reynolds number. This could be the effect of spatial filtering, which would re-locate energy from higher wave-numbers to lower ones by averaging over the sensor length, even though the sensor length at highest Reynolds number corresponds to $k_x^+ = 0.08$ or $k_x\delta = 6 \times 10^3$ and therefore should not play a significant role. Alternatively, this shift in profiles could be a result of using Taylor's hypothesis.

For pipe flow (figure 7.7, on the left) at $y/\delta = 0.15$, a plateau region can be seen for

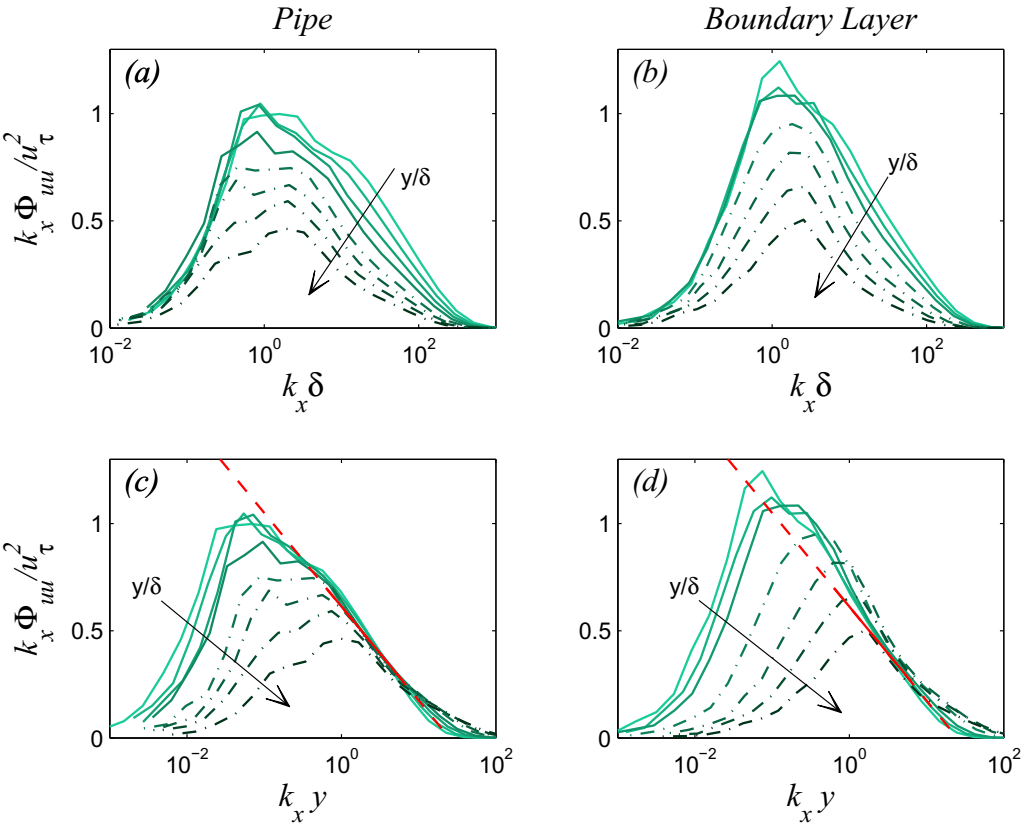

Figure 7.5: Pre-multiplied spectra $k_x\Phi_{uu}/u_\tau^2$ at $Re_\tau \approx 5,000$ for pipe and boundary layer with varying y/δ. (Solid line) $3/Re_\tau^0.5 < y/\delta+ < 0.15$; (dash-dotted line) $0.15 < y/\delta+ < 0.7$. Arrow indicates increase in y. (dashed line) relation proposed by del Álamo et al. [2004], with solid line for $0.63 < k_x y < 6.3$.

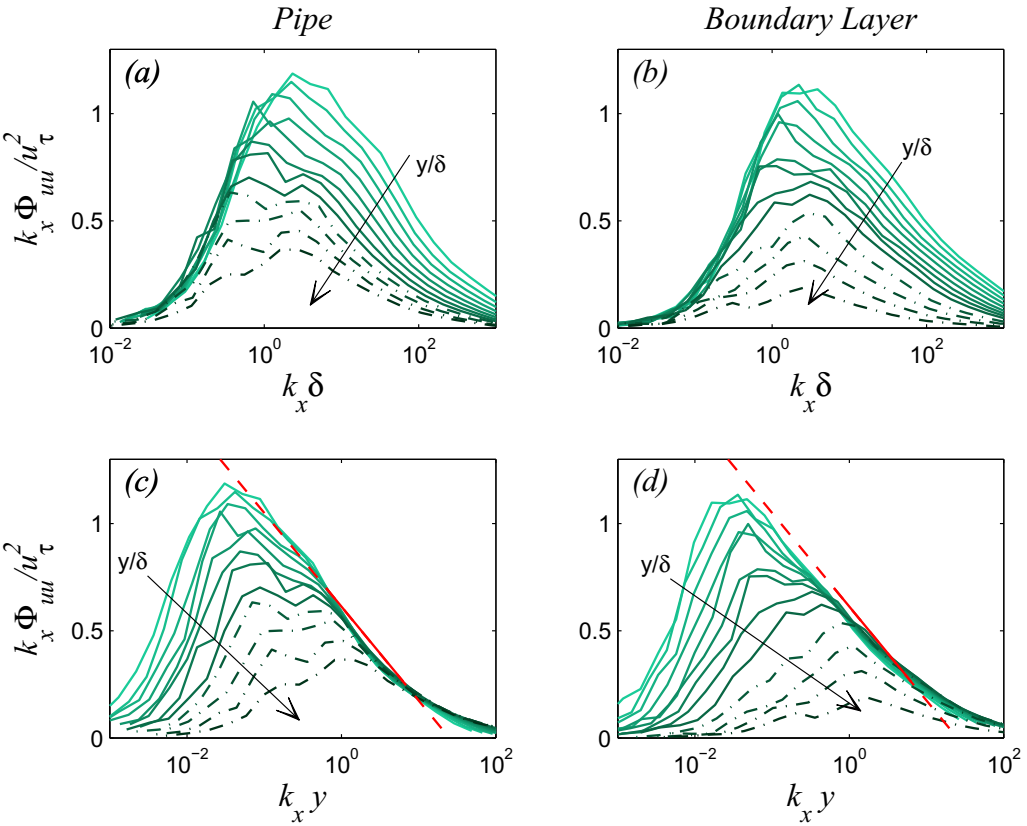

Figure 7.6: Pre-multiplied spectra $k_x\Phi_{uu}/u_\tau^2$ at $Re_\tau \approx 70,000$ for pipe and boundary layer with varying y/δ. (Solid line) $3/Re_\tau^0.5 < y/\delta+ < 0.15$; (dash-dotted line) $0.15 < y/\delta+ < 0.7$. Arrow indicates increase in y. (dashed line) relation proposed by del Álamo et al. [2004], with solid line for $0.63 < k_x y < 6.3$.

each Reynolds number, with the magnitude 0.6 to 0.8, which is close to the constant $A_1 = 0.8$ found by Perry and Abell [1977]. But if other y locations are considered, a clear trend can be seen, where closer to the wall the peak in energy is at lower k_x and further from the wall this VLSM peak decreases while the peak of LSM at higher k_x increases. This suggests that the k_x^{-1} region observed at $y/\delta \approx 0.15$ is just the region where these two peaks are approximately the same magnitude, showing up as two small bumps, feigning a true k_x^{-1} region. If this behavior is an inherent aspect of the turbulent wall region, some plateau would be expected to appear at all locations where $y/\delta < 0.15$. However, from figure 7.7 at $y/\delta = 0.05$ and 0.1 this does not seem to be the case. For the boundary layer, there are no pronounced two peaks in energy, and instead only one peak associated with superstructures is evident. For boundary layer flow (figure 7.7, on the right), some small regions with k_x^{-1} behavior can be seen for maybe $y/\delta = 0.05$ and $y/\delta = 0.1$ at the higher Reynolds numbers, but there is no indication of a constant magnitude of this region, as there is clear decrease of energy with Reynolds number. An alternative theoretical approach was recently suggested by Hultmark [2012], who showed a logaritmic behavior in variances without involving spectral arguments and therefore not needing a k_x^{-1} region in spectra to explain the log behavior.

7.3.3 Scaling of spectral peaks

We now consider the coherent large wavelength motions and the scaling behavior of the inner and outer spectral peaks. In pipe flow, Rosenberg et al. [2013] identified distinct Reynolds number independent scaling for LSM and VLSM peaks in each wall-normal region. Near the wall at $y^+ < 12$, a single peak scales with y, where $k_x y \approx 0.07$. At $y^+ = 12$, the low and high wavenumber loci bifurcate, where the LSM peak scales first with the viscous length ν/u_τ ($k_x^+ \approx 0.006$) and for $y^+ > 67$ with y as $k_x y \approx 0.4$ in turbulent wall region. Surprisingly, Rosenberg et al. [2013] found that

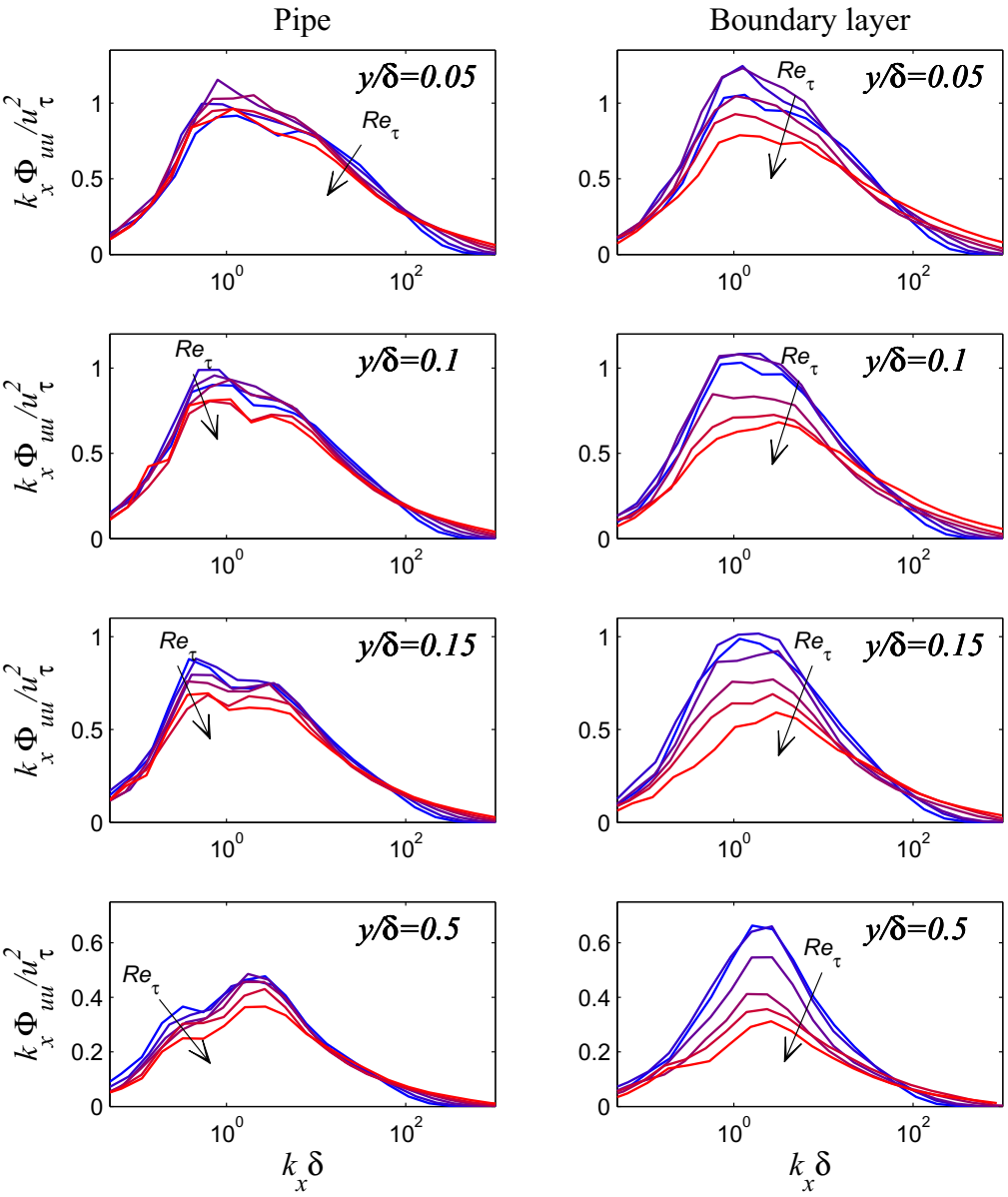

Figure 7.7: Pre-multiplied spectra with varying Reynolds number at fixed wall-normal locations $y/\delta \approx 0.05; 0.1, 0.15; 0.5$ for pipe (left) and boundary layer (right). Arrows indicate the increasing Reynolds number from $Re_\tau = 3,000$ to $Re_\tau = 70,000$.

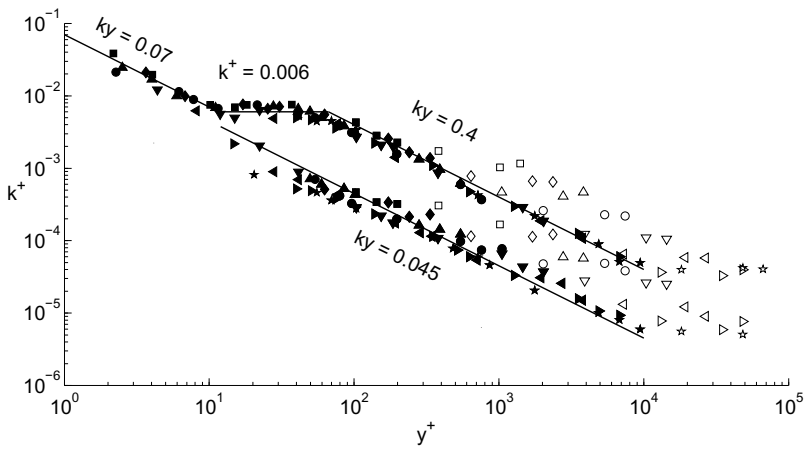

Figure 7.8: Spectral peak locations in inner coordinates for pipe. Filled symbols denote $y/\delta < 0.1$ and open symbols $y/\delta > 0.1$. Figure from Rosenberg et al. [2013].

the VLSM peak also scaled with wall-normal location y in the turbulent wall region ($k_x y \approx 0.045$), and not with δ as seen in boundary layers by Hutchins and Marusic [2007]. Finally, for $y/\delta > 0.1$ both spectral peaks scale with the pipe radius (here labelled as δ): the VLSM peak as $k_x\delta \approx 0.45$, and the LSM peak as $k_x\delta \approx 2.6$. Figures 7.8 and 7.9 (from Rosenberg et al. [2013]) show the locations of these spectral peaks and the described trends in inner and outer coordinates respectively.

We now apply the methodology used by Rosenberg et al. [2013] for analyzing the spectral peaks in pipe flow for finding the spectral peaks in the boundary layer flows. In order to estimate the wavenumber peak location, a Gaussian curve in $\log(k_x)$ was fitted to the data locally at each peak. At locations where the second peak was more difficult to identify, because it appeared more as a narrow shoulder rather than a distinct peak (the LSM peak in the region $100 < y^+ < 0.15$), a cubic spline was used to fit data locally and the point of inflection was used as an estimate of the peak location. The spectral peak at higher wavenumbers is identified as the LSM peak, as done for pipe flows, and the peak at lower wavelengths is considered to be the SS (superstructure) peak, similar to the VLSM peak seen in pipes.

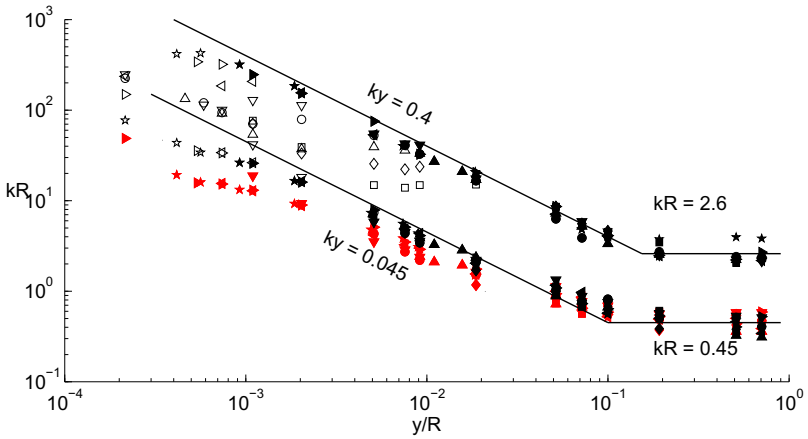

Figure 7.9: Spectral peak locations in outer coordinates for pipe. Filled symbols denote $y^+ > 67$ and open symbols $y^+ < 67$. The red points denote the lower wavenumber peaks assuming the convection velocity is spatially uniform and equal to the bulk velocity. The shaded region, obtained from the survey of Wu et al. [2012], represents the approximate scatter of previous data-sets. Figure from Rosenberg et al. [2013].

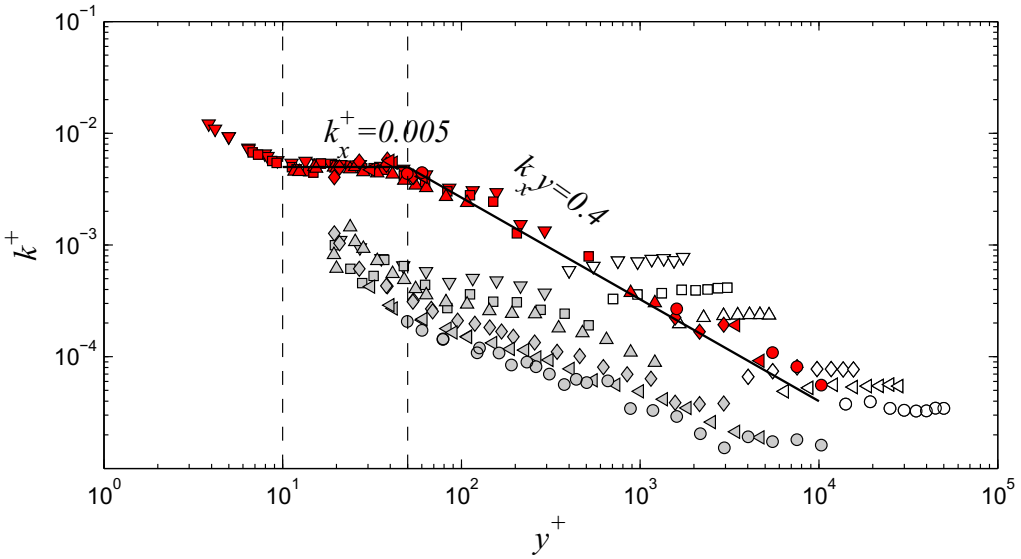

Figure 7.10: Spectral peak locations in inner coordinates for boundary layer. (Filled red symbols) peaks associated with near-wall structures and LSMs; (Filled gray symbols) peaks associated with SS; (Open symbols) peak loci at $y/\delta > 0.15$; (dashed lines) $y^+ = 10$ and $y^+ = 50$; symbols are according to Table 7.1.

The locations of the spectral peaks scaled with viscous variables are shown in Figure 7.10. In the near-wall region, for $y^+ < 10$, a single peak is observed, scaling with the wall-normal distance and located at about $k_x y \approx 0.05$ ($\lambda_x \approx 125y$). It is important to note that this scaling is purely the result of the local mean velocity used as convection velocity when applying Taylor's hypothesis, which is not a good approximation in this region. For $y^+ < 10$, the mean velocity has a nearly linear profile $U^+ \approx y^+$, and this makes $k_x y$ constant in this region. If no Taylor hypothesis were applied, the inner peak scales purely with the viscous time scale, being constant at $f^+ \approx 0.008$, or $t^+ \approx 125$.

Near $y^+ \approx 10$, which is close to where the turbulent kinetic energy has its maximum, there is a bifurcation in the loci of the peaks, so that the peak associated with larger wavenumbers (LSMs) starts scaling with the viscous length η and goes as $k_x^+ \approx 0.005$ (or $\lambda_x \approx 1250\eta$). This LSM peak dominates the spectrum to about $y^+ \approx 50$, after which the locus of the peak starts to scale with y, its magnitude becomes small, and it only appears as a small shoulder in the pre-multiplied spectrum. The magnitude of this LSM peak is much weaker than in pipe flow, indicating a lower energy content in the LSMs for boundary layers, but its location scales with y as in pipe flow, going as $k_x y \approx 0.4$.

In figure 7.10 the trends for each region described above are shown. The peaks scaling with inner variables, associated with near wall and large scale motions below $y/\delta < 0.15$, are shown with filled symbols, to better visualize the trends. The loci of the second peak, emerging for $y^+ > 10$ and associated with superstructures, are shown in gray symbols, and the peak loci for $y/\delta > 0.15$ are shown with empty symbols.

In figure 7.11 the same peak loci are shown in outer coordinates. Here, the peak loci associated with superstructures (larger wavelengths, smaller wavenumbers), are shown with solid symbols, and the loci associated with near-wall and LSMs

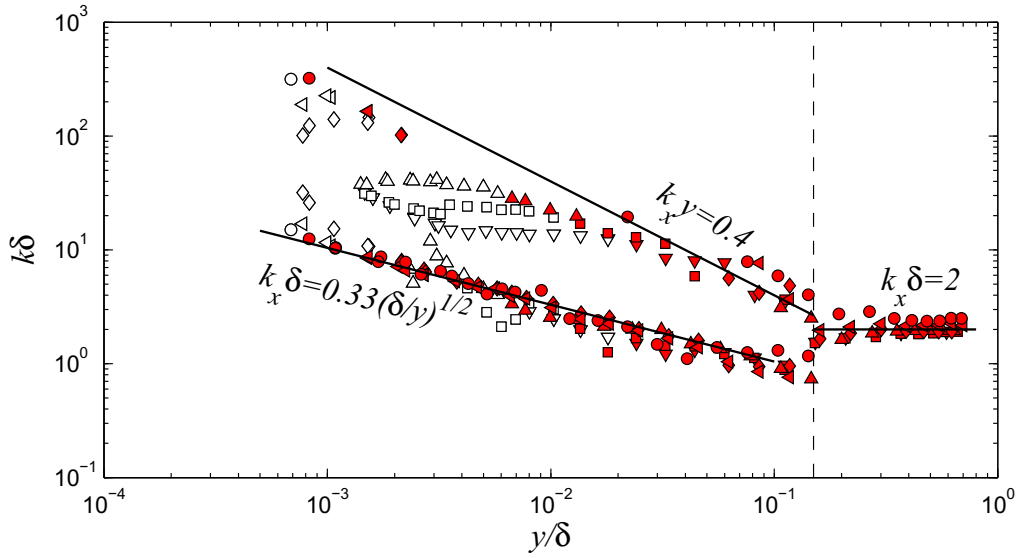

Figure 7.11: Spectral peak locations in outer coordinates for boundary layer. (Filled red symbols) peaks in region $50 < y^+ < 0.15Re_\tau$; (Open symbols) peaks for $y^+ < 50$; dashed line $y/\delta = 0.15$; symbols are according to Table 7.1.

shown with empty symbols. It is clear that, in agreement with the observations by Hutchins and Marusic [2007], the superstructures are dictated by the outer scales and the loci of the peaks scale with δ. The location of this peak in the turbulent wall region seems to be Reynolds number independent, with the location of this second peak described by $k_x\delta \approx C(y/\delta)^{-1/2}$, or $k_x^+ \approx C(y^+R_\tau^+)^{-0.5}$, showing simultaneous dependence on wall-normal distance as well as the boundary layer thickness (the constant was found to be $C \approx 0.33$). This trend expressed in terms of the wavelength gives $\lambda_x+ \approx 20(y^+R_\tau)^{0.5}$, which suggests that the region $50 < y^+ < 0.15Re_\tau$ is a transitional phase, where SS are associated with wavelengths $\lambda_x \sim y^{1/2}\delta^{1/2}$. Our previous analysis indicated that in the same region where $50 < y^+ < 0.15Re_\tau$ there was no overlap region between y and δ scaling in the spectra (Chapter 7.3.2).

At the outer edge of the turbulent wall region, at $y/\delta \approx 0.15$, the two peaks (SS peak and LSM peak) merge back together to form a single peak in the spectrum for the rest of the outer region of the flow, at about $k_x\delta \approx 2$. This value corresponds to $\lambda_x \approx$

3δ, which is in agreement with previous observations [Ganapathisubramani et al., 2003].

In pipe flow, Rosenberg et al. [2013] found that the wavelength associated with VLSMs in the turbulent wall region is solely determined by wall distance. The same analysis for pipe flow was done in exact same way as for boundary layer and at every wall normal location (Rosenberg et al. [2013] used only about a third of the data), and the VLSM peak loci was found to scale with δ for $y^+ > 50$, going as $k_x\delta \approx 0.17(y/\delta)^{-0.66}$, compared to $k_x\delta \approx 0.045(y/\delta)^{-1}$ found by Rosenberg et al. [2013]. This indicates that in pipe the VLSM structures are more strongly dependent on radial distance. The peak loci in inner and outer coordinates are shown in Figures 7.12 and 7.13.

Based on the analysis given here, it can be concluded that the LSMs have the same characteristics in confined and open geometries but the superstructures and VLSMs continue to behave differently even at very high Reynolds numbers. The outer flow in pipe flow continues to be characterized by LSMs and VLSMs, whereas in the boundary layer a single peak associated with large energetic structures suggests that the superstructure organization is lost in the wake region leaving only one size of large scale structure with $\lambda_x \approx 3\delta$.

7.3.4 Outer spectral peak

Previous studies by Hutchins and Marusic [2007] and by Mathis et al. [2009] found that the location in inner variables and the value of the maximum in the spectral peak (the outer spectral peak) associated with superstructures varied with Re_τ. Our study includes a range of Reynolds numbers with large separation of scales and therefore provides a great opportunity to study the behavior of this outer spectral peak further. Figure 7.14 shows the magnitude of the superstructure peak at each wall-normal location in inner variables for all Reynolds numbers for pipes (a) and boundary layers

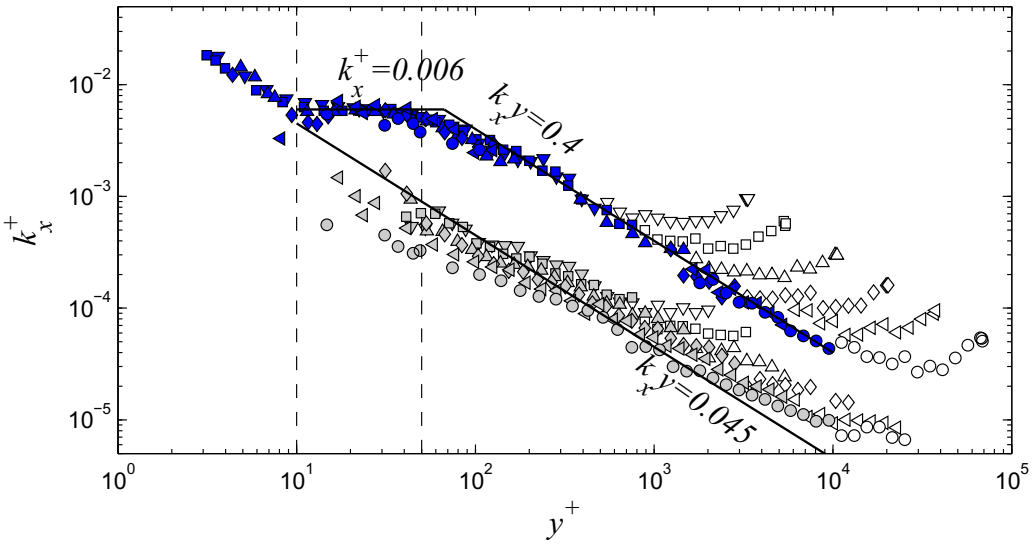

Figure 7.12: Spectral peak locations in inner coordinates for pipe. (Filled blue symbols) peaks associated with near-wall structures and LSMs; (Filled gray symbols) peaks associated with VLSM; (Open symbols) peak loci at $y/\delta > 0.15$; (dashed lines) $y^+ = 10$ and $y^+ = 50$; symbols are according to Table 7.1.

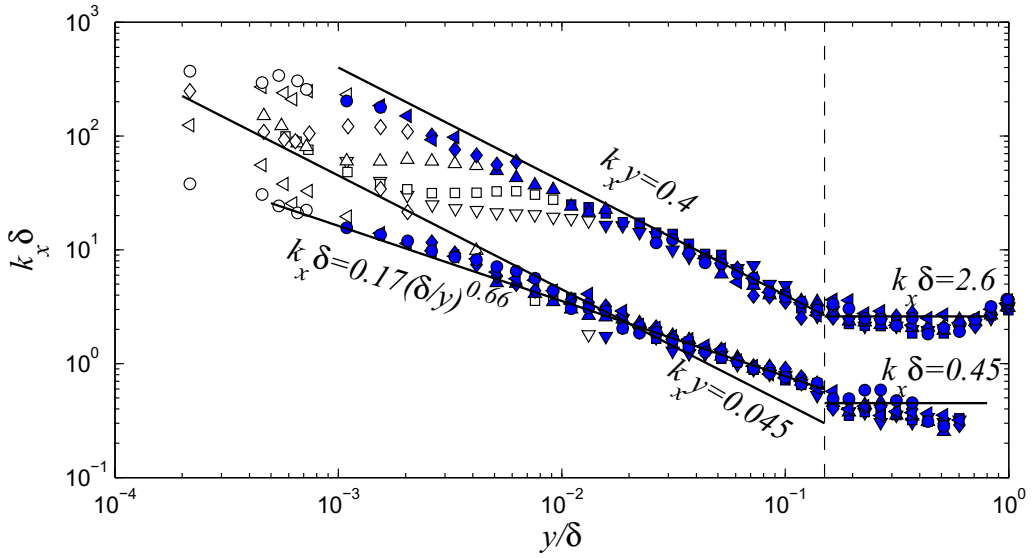

Figure 7.13: Spectral peak locations in outer coordinates for pipe. (Filled blue symbols) peaks in region $50 < y^+ < 0.15Re_\tau$; (Open symbols) peaks for $y^+ < 50$; dashed line $y/\delta = 0.15$; symbols are according to Table 7.1.

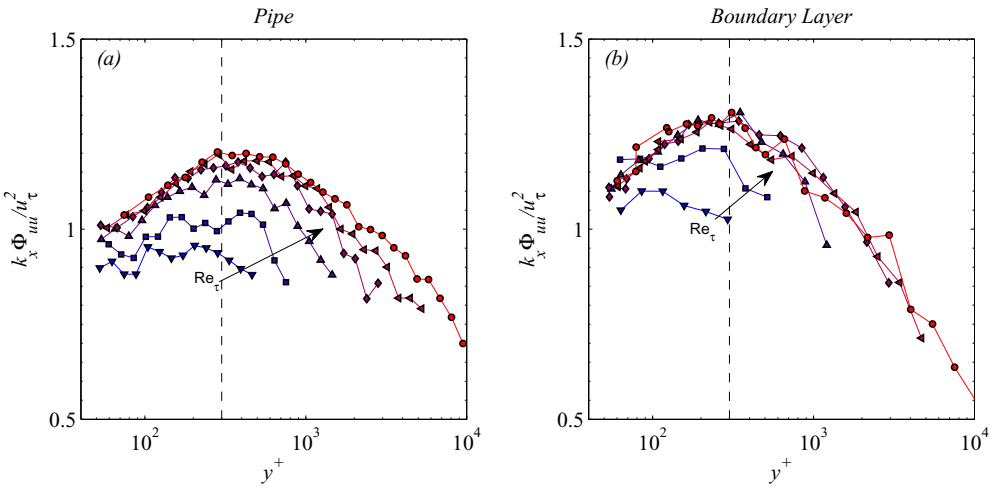

Figure 7.14: Values of $k_x\Phi_{uu}/u_\tau^2$ for $50 < y^+ < 0.15Re_\tau$ associated with a) VLSM in pipe and b) SS in boundary layer. Dashed line shows $y^+ = 300$; arrows indicate the increasing Reynolds number; symbols as shown in Table 7.1.

(b). The location and magnitude of the peaks increases for the three lowest values of Re_τ similar to that seen by Mathis et al. [2009], but for $Re_\tau \geq 10,000$ the profiles appear to collapse in viscous units, so at the highest four Reynolds numbers available, the magnitudes seem to become independent of Reynolds number. This collapse also suggests that the location of the peak does not increase significantly with Reynolds number. Now we will separately discuss the location and magnitude of this outer spectral peak (OSP), corresponding to VLSM and SS for pipes and boundary layers, respectively. It must be noted that this relatively constant magnitude could also just be an artifact of the measurements: due to changing from 60 to 30μm sensor and overall experimental uncertainty.

The wall-normal location of the OSP for all Reynolds numbers is shown in Figure 7.15, together with the boundary layer data and trends from Mathis et al. [2009]. In addition, the location of the outer peak in the variances is shown in the same figure using gray symbols, and the location of the zero crossing in the amplitude modulation function ($R_m = 0$) for the current data are marked with empty symbols (Mathis et al.

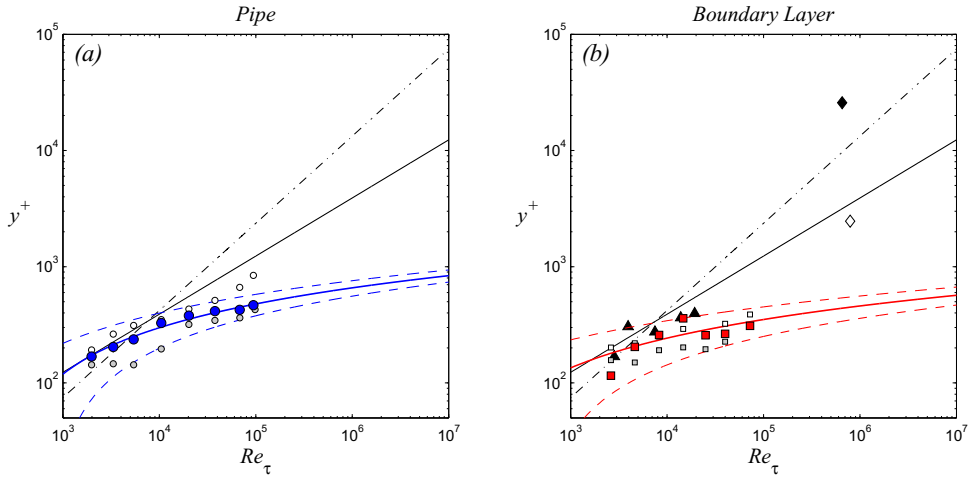

Figure 7.15: Wall-normal location of outer spectral peak varying with Re_τ. (●) all pipe cases from Chapter 3; (■) all boundary layer cases from Chapter 5. a) (solid red line) $y^+ \approx 47 \ln(Re_\tau) - 190$ with error bounds $y^+ = \pm 100$ (dashed red lines); and (solid blue line) $y^+ \approx 78 \ln(Re_\tau) - 420$ with error bounds $y^+ = \pm 100$ (dashed blue lines); (□) location where amplitude modulation $R_m = 0$ for boundary layer; (○) location where $R_m = 0$ for pipe; (■) location where outer peak in u^{2+} for boundary layer; (●) location where outer peak in u^{2+} for pipe; Adapted from Mathis et al. [2009]: (▲) shows the location where $R_m = 0$ in their boundary layer study; (black solid line) $3.9Re_\tau^{0.5}$; (black dash-dotted line) $0.42Re_\tau^{0.75}$; and ◊ denotes atmospheric data, see reference in Mathis et al. [2009].

[2009] found these loci follow the outer spectral peak location).

The outer spectral peak loci were determined by locally fitting Gaussian curves and finding the closest available data-point. As can be seen in Figure 7.15(b), the locations of the boundary layer outer spectral peak (y^+_{OSP}, red markers) at lower Reynolds numbers agree well with the results from Mathis et al. [2009] and follow the $Re_\tau^{0.5}$ trend. But for $Re_\tau \geq 10,000$, the location of the outer peak starts flattening, so that overall the location of the OSP shows a logarithmic behavior in Re_τ as $y^+_{OSP} \approx 47 \ln(Re_\tau) - 190$. The outer peak in the variance and the $R_m = 0$ loci display very similar values and trends to the OSP loci, indicating that all these phenomena occur at approximately same wall-normal distance. It must be kept in mind that the data were acquired in $\Delta y^+ \approx 40$ to 100 increments, and the location of the maximum energy therefore has a comparable uncertainty range. To demonstrate this uncertainty, dashed lines show limits of $y^+ \pm 100$ around the empirical fit.

These trends agree well with the experimental results form Mathis et al. [2009], but indicate much lower values than found in atmospheric studies. In order to verify these trends or disprove them, even higher Reynolds number experiments are needed, or more atmospheric data with better precision.

Peak loci for pipe (blue markers in Figure 7.15(b)) behave in a similar manner to boundary layer, but having less variation, which can be explained by the fact that data for pipe is available for $\Delta y^+ \approx 30-60$ allowing for higher precision. Again, data seems to follow a logarithmic trend with Reynolds number and empirical fit gives $y^+ \approx 78 \ln(Re_\tau) - 420$. The outer peak in variance loci have close values and trends to the OSP loci, whereas $R_m = 0$ locations seem to continue following the $Re_\tau^{0.5}$ trend even for higher Reynolds numbers. This could either indicate that the zero crossing of amplitude modulation does not occur at the same location as peaks in variance and spectra, or that the uncertainty in determining peak values is even higher than estimated. The higher values of y^+ for pipe flow compared to boundary layer agree

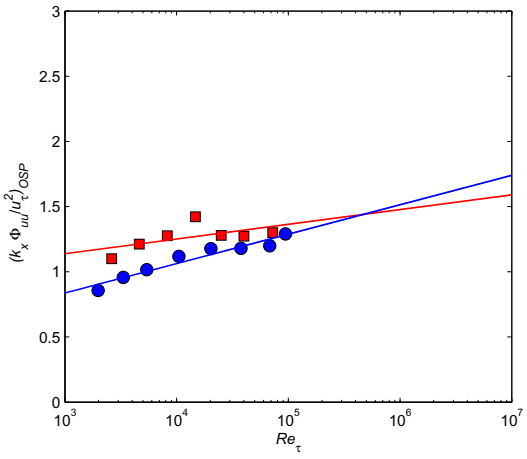

Figure 7.16: Magnitude of the outer spectral peak varying with Re_τ. (●) all pipe cases from Chapter 3; (■) all boundary layer cases from Chapter 5; (solid red line) $k_x\Phi_{uu}/u_\tau^2 = 0.049\ln(Re_\tau) + 0.80$; (solid blue line) $k_x\Phi_{uu}/u_\tau^2 = 0.098\ln(Re_\tau) + 0.16$.

with findings in previous Chapters, where it was concluded that the start of the overlap region is always further from the wall for pipe flow, compared to boundary layer.

It is evident from this discussion that the location of the outer spectral peak varies as $y^+ \sim \ln Re_\tau$ for pipe and boundary layer flows. This result implies that the motions containing high energy are confined in a region almost fixed in y^+ as the Reynolds number increases. Because the viscous length scale decreases with increasing Re_τ in a developing boundary layer, this would mean that the region with high energy and vorticity decreases in physical space and diminishes near the wall (see also the discussion by Pullin et al. [2013]). In the limit of infinite Reynolds number this would recover a potential flow situation with essentially a slip-flow bounded by a vortex sheet at the wall.

The magnitude of the outer spectral peak in $k_x\Phi_{uu}/u_\tau^2$ for each Reynolds number is shown in Figure 7.16. Similar in behavior to the location of this peak, there is an initial increase with Re_τ, but above $Re_\tau > 10,000$ the magnitude of the peak stays

about constant. Again, approximately logarithmic trend can be found by fitting the data, giving $k_x\Phi_{uu}/u_\tau^2 = 0.049\ln(Re_\tau) + 0.80$ for the boundary layer (red), and $k_x\Phi_{uu}/u_\tau^2 = 0.098\ln(Re_\tau) + 0.16$ for the pipe (blue).

This suggests that the energy at the outer spectral peak only has a weak $\ln Re_\tau$ dependence on the Reynolds number. This observation could indicate that the outer peak in the variances, which inevitably will be closely related to the energy in the outer spectral peak, might also not increase indefinitely with Reynolds number, unless the increase in the peak in u^{2+} is supported by spreading energy content over a wider range of k_x, similar to the behavior found for the inner spectral peak in pipe flow by Hultmark et al. [2010]. However, some caution must be exercised in interpreting these results, as some of the trends could be affected by using Taylor's hypotheses, and there is not wide enough range of Re_τ available to strong conclusions. Spatial resolution issues with increasing Re_τ could also play a role, although the sensor size is about three magnitudes smaller than wavelengths associated with these superstructures and would therefore be expected negligible.

It should also be noted that the data-set acquired in the boundary layer at $Re_\tau \approx 15,000$ has been included in Figures 7.15b and 7.16. This case was excluded from most of the comparisons made in this Chapter, mainly because there was no corresponding case in pipe flow, but also due to possible instability of the sensor as mentioned in Chapter 5.3. It was found that the loci of the LSM and SS peaks for that case seem to follow closely the trends described above, and the outer spectral peak for that case was also located at about $y^+ \approx 300$, but this peak had a slightly higher magnitude of $k_x\Phi_{uu}/u_\tau^2$, which could have been caused by insufficient damping of the anemometer bridge.

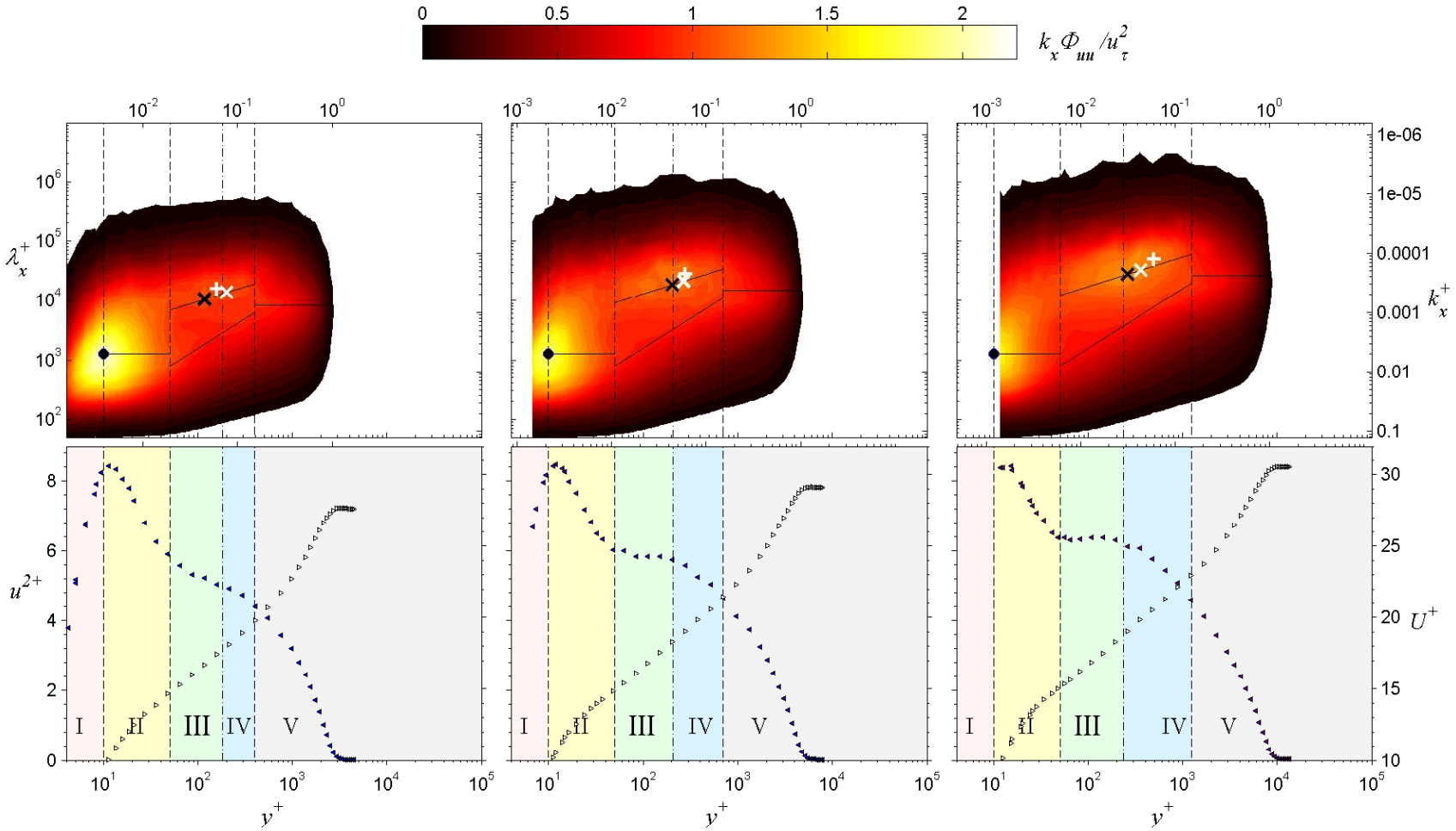

Figure 7.17: Surface plots of spectra at $Re_\tau = 3,000, 5,000, 10,000$. Lines show trends in the loci of peaks shown in Figures 7.10 and 7.11; black × shows location of OSP; white × shows Mathis et al. [2009] suggested OSP location; + shows SS maximum peak found in Hutchins and Marusic [2007].

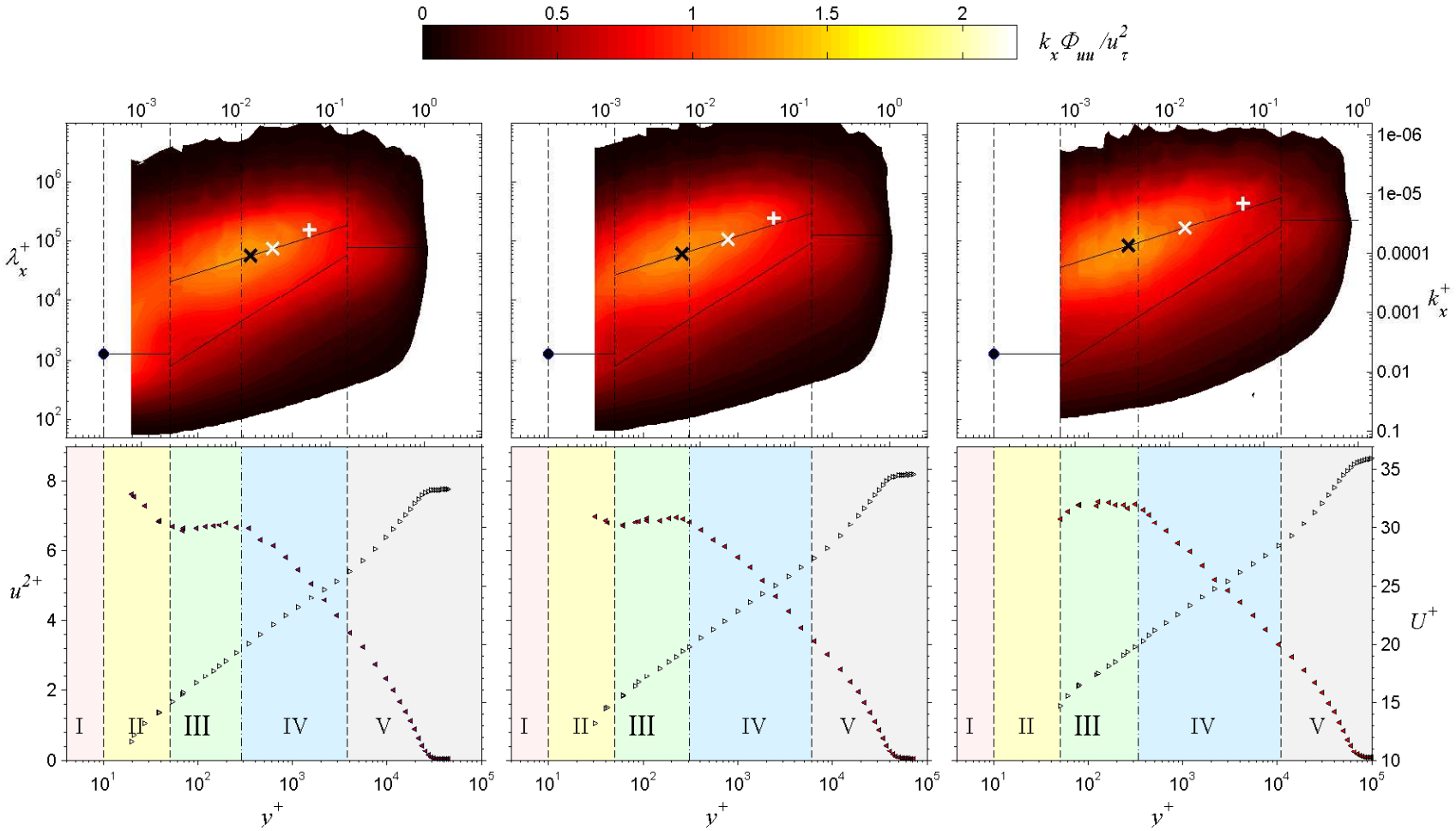

Figure 7.18: Surface plots of spectra at $Re_\tau = 25,000, 40,000, 70,000$. Lines show trends in the loci of peaks shown in Figures 7.10 and 7.11; black × shows location of OSP; white × shows Mathis et al. [2009] suggested OSP location; + shows SS maximum peak found in Hutchins and Marusic [2007].

7.3.5 Wall-normal layers

Full contour maps of the pre-multiplied spectra $k_x\Phi_{uu}/u_\tau^2$ in the boundary layer are shown in Figures 7.17 and 7.18. The scales of y^+, λ^+ and $k_x\Phi_{uu}/u_\tau^2$ are kept constant for all cases for better visual interpretation, and the corresponding mean velocity profiles and u^{2+} profiles are shown below each contour map. The location of the inner spectral peak (•) and the outer spectral peak (×) are shown for each case, as well as the predictions Hutchins and Marusic [2007] (white +) and Mathis et al. [2009] (white ×). The solid lines show the trends in loci of the peaks shown in Figures 7.10 and 7.11.

Based on the results presented in this Chapter, five different wall-normal regions can be identified in the spectral behavior:

Region I: $y^+ < 10$,

where the near-wall structures scale as $\lambda_x/y \approx$ const (or $t^+ \approx$ const without using Taylor hypothesis);

Region II: $10 < y^+ < 50$,

where the near-wall structures scale as $\lambda_x^+ \approx$ const;

Region III: $50 < y^+ < C_1 \ln Re_\tau + C_2$,

where $\lambda_x^+ \sim \sqrt{y^+ Re_\tau}$ in boundary layers and $\lambda_x^+ \sim y^{+2/3} Re_\tau^{1/3}$ in pipes, and the energy associated with SS/VLSMs is increasing;

Region IV:$C_1 \ln Re_\tau + C_2 < y^+ < 0.15 Re_\tau$,

where $\lambda_x^+ \sim \sqrt{y^+ Re_\tau}$ in boundary layer and $\lambda_x^+ \sim y^{+2/3} Re_\tau^{1/3}$ in pipes, the energy associated with SS/VLSMs is decreasing and there is a logarithmic behavior in variances;

Region V: $y/\delta > 0.15$,

where LSMs (and VLSMs in pipe) scale with δ (R in pipes).

To distinguish all the different regions in Figures 7.17 and 7.18, dashed lines show locations of $y^+ = 10$, $y^+ = 50$, and $y/\delta = 0.15$ on each plot, and the empirical relation for the location of the outer spectral peak $y^+ = C_1 \ln Re_\tau + C_2$ (with best fitted coefficients $C_1 = 47$ and $C_2 = -190$) is shown as dash-dotted line.

In *Region I*, the energy associated with near-wall structures is increasing and also total kinetic energy u^{2+} increases rapidly. The mean velocity profile is approximately linear with y^+ and this region can be associated with the linear sublayer. The inner spectral peak location corresponds to $y^+ \approx 10$ and $\lambda^+ \approx 1250$ ($k_x^+ = 0.005$), which can be associated with the peak in the streamwise turbulent stress. Unfortunately only two lowest cases can resolve the near-wall peak as in physical coordinates this peak is located at only 100μm from the wall for lowest Re_τ and this distance is decreasing as Re_τ goes up.

In *Region II*, the energy in the near-wall structures decreases and the wavelength of these structures stays about constant in viscous units at $\lambda_x^+ \approx 1250$. In this region, the rapid decrease of u^{2+} can also be seen associated with the decrease of the near-wall peak in the energy spectra. This region is associated with the buffer layer in the mean velocity.

At the start of *Region III*, at about $y^+ \approx 50$, two energetic peaks in the spectra appear, with most of the energy associated with superstructures located at $\lambda_x \sim \sqrt{y\delta}$, and a weaker peak associated with large scale motions located at about $\lambda_x \approx 20y$. The SS peak continues to increase until about $y^+ \approx C_1 \ln Re_\tau + C_2$, where $C_1 \approx 47$ and $C_2 \approx -190$. This region in u^{2+} can be characterized as a level plateau for lower Reynolds numbers and a slightly rising value for the higher cases. In the mean velocity, an apparent self-similarity has been reached and the profile behaves logarithmically in y^+. This region could be associated with the mesolayer introduced first by George and Castillo [1997], where the mean flow is free of viscous effects but turbulent quantities are still affected by viscosity.

The start of *Region IV* is at $y^+ \approx C_1 \ln Re_\tau + C_2$. This relation denotes the location of the outer spectral peak associated with superstructures, and this is also the location where there is a peak in u^{2+} (if there is one without spatial resolution issues). As for the outer spectral peak, its location agrees well with previous studies for the two lowest Reynolds numbers (which are comparable to the range studied by Hutchins and Marusic [2007]), but as the Reynolds number increases the predictions based on lower Re_τ start to depart more and more from the current data. This is consistent with the finding that the loci of the OSP (dashed-dotted line) varies as $\ln(Re_\tau)$, that is, a weak dependence on Reynolds number. It can be seen that the peak location coincides with the outer peak or the end of plateau seen in total kinetic energy u^{2+}, and therefore marks approximately the beginning of the logarithmic behavior in the variances. This is in contrast to Mathis et al. [2009] who suggested that the peak is associated with the center of the log region in the mean velocity. The disagreement is easily explained by the fact that log region in u^{2+} only shows up at Reynolds numbers larger than those that were available to Mathis et al. [2009]; at lower Re_τ, the peak does seem to be located in about the center of the logarithmic region in the mean velocity but this may just be a coincidence due to the small extent of the log region at lower Reynolds numbers.

Further, in *Region IV*, the energy associated with SS starts to diminish, but the structures are still characterized by $\lambda_x \sim \sqrt{y\delta}$. In this region, the streamwise turbulent stresses start decreasing and follow a logarithmic behavior with y/δ, and $U^+ \sim \ln y^+$ as well. This region is the inertial sublayer, where viscosity does not affect neither the mean flow nor the turbulence (for the higher order moments, even larger wall-normal distances might be needed for self-similarity, as discussed in Chapter 6).

Finally, in *Region V*, everything scales with the outer length scale δ. The SS peak merges with the weak LSM peak, showing up as a single peak associated with large scale structures of $\lambda_x \approx 3\delta$. The turbulent fluctuations diminish and the mean

velocity behaves according to a Reynolds number independent wake function.

It must be noted that the limits used to define these five regions do not serve as the best fitting limits for finding the constants for the various log-region, simply because some blending occurs between these regions. Therefore, more conservative limits should be used for fitting purposes, similar to the discussion by Marusic et al. [2013], where $3Re_\tau^{0.5}$ was chosen as a very conservative inner limit. This is also the reason why more conservative limits were given in Chapters 3 and 5 for the mean velocity and the u^{2+} log layers.

Here, spectral maps of boundary layer were shown only. In pipe flows, very similar trends can be seen and similar regions can be identified, with only a few of differences. First, the LSM peak varies as $\lambda_x \approx 16$, and it is much stronger in magnitude. Second, the VLSM peak (comparable to the SS peak) varies as $\lambda_x \ y^{2/3}\delta^{1/3}$, and the outer spectral peak (and the change from *Region III* to *Region IV*) is located further from the wall, but still varying as $y^+ \approx C_1 \ln Re_\tau + C_2$, with $C_1 \approx 78$ and $C_2 \approx -420$. Finally, in *Region V* the peaks associated with both LSMs and VLSMs can be observed, varying as $\lambda_x \approx 2.4\delta$ and 14δ, respectively, compared to a single peak in boundary layer.

7.4 Conclusions

Streamwise turbulent spectra for Reynolds numbers in the range $3,000 \lesssim Re_\tau \lesssim 70,000$ were studied in pipe and boundary layer flows. In the high wavenumber (low wavelength) region, all spectra in both flows showed an excellent collapse in Kolmogorov scaling with a large $k_x^{-5/3}$ range, increasing with Reynolds number. This observation confirms that the small scales associated with the dissipation are independent of the outer flow geometry.

At intermediate wavelengths, the spectra were found to scale well with y, and at

large wavelengths (small k_x) the spectra scaled with the outer length scale δ or R. But contrary to the predictions by Townsend [1976], no region of overlap of these scalings was seen, and no clear k_x^{-1} behavior. One possible explanation is that the lack of overlap could be due to the different velocity scales in the intermediate and large wavelength regions. A small k_x^{-1} plateau was seen at the outer edge of the turbulent wall region at $y/\delta \approx 0.15$, but it is suggested that this may just be a result of balance between two competing peaks in the spectra.

The magnitudes and loci of the energy peaks associated with LSM and SS in boundary layers (or VLSM in pipes) were also studied. It was found that in boundary layers the near-wall inner spectral peak loci followed $t^+ \approx 125$ for $y^+ \lesssim 10$. At that y^+ location, the loci bifurcated so that the LSM peak first followed $k_x^+ \approx 0.005$ and then $k_x y \approx 0.4$, in close agreement with previous findings in pipe flow. After bifurcation, a peak associated with superstructures emerged, scaling with outer variables and following $\lambda_x + \approx 20(y^+ Re_\tau^+)^{0.5}$ for $50 \lesssim y^+ \lesssim 0.15 Re_\tau$. Outside the logarithmic layer above $y/\delta > 0.15$, the peaks associated with SS and LSM merged into one peak located at about $\lambda_x \approx 3\delta$. Therefore, superstructures in boundary layers are found to have a different behavior compared to the VLSMs in pipe flow, even at these very large Reynolds numbers.

The magnitude and location of the outer spectral peak (the peak associated with SS) was shown to having a very slow logarithmic increase in values with Re_τ. This result suggests that the physical region containing most of the turbulent energy is getting smaller and moving closer to the wall. At infinite Reynolds number, this layer would diminish to a thin vortex sheet at the wall with a slip-flow above it, similar to a potential flow approximation. This asymptotic behavior was previously suggested based on the trends displayed by the outer peak in the turbulent fluctuations by Pullin et al. [2013], and the spectral behavior seems to support their reasoning. Finally, it was shown that the location of outer spectral peak location is closely re-

lated to the outer peak in turbulent fluctuations, a result that is not obvious but expected. Also, the constant magnitude and location of the outer spectral peak could indicate that at these extremely high Reynolds numbers the separation between the energy containing and dissipative ranges has become large enough to allow asymptotic Reynolds number independent behavior of the turbulence.

Based on the behavior of peaks in the energy spectra, together with previous results from the turbulence statistics, five distinct regions were identified: the viscous sublayer up to $y^+ \approx 10$, the buffer layer $10 \lesssim y^+ \lesssim 50$, the mesolayer $50 \lesssim y^+ \lesssim C_1 \ln Re_\tau + C_2$, the inertial sublayer $C_1 \ln Re_\tau + C_2 \lesssim y^+ \lesssim 0.15 Re_\tau$, and the wake region for $y/\delta \gtrsim 0.15$. The most significant difference between pipes and boundary layers was with respect to the start of the inertial sublayer, where constants C_1 and C_2 were found to be different ($C_1 \approx 47$ and $C_2 \approx -190$ for boundary layer and $C_1 \approx 78$ and $C_2 \approx -420$ for pipe).

Chapter 8

Conclusions

The aim of this dissertation was to study and understand the behavior of wall-bounded turbulent flows at very high Reynolds numbers. To achieve that aim, a Nano-Scale Thermal Anemometry Probe was first developed for high resolution turbulence measurements. It was shown that the performance of this novel sensor was superior to conventional measurement technologies, allowing high quality measurements over an unprecedented Reynolds number range.

Two canonical wall-bounded flows were studied: fully developed pipe flow and zero pressure gradient boundary layer flow. The Reynolds number range was from $Re_\tau \approx 2000$ to about 100,000, and the results show that in general these two flows behave very similarly at these high Reynolds numbers. In particular, a logarithmic behavior in turbulent fluctuations was observed in both flows in the region where the logarithmic behavior in mean flow exists, indicating that the scaling of turbulent fluctuations is much more similar to the mean flow scaling than previously believed. This logarithmic behavior is also evident in higher order even moments over the same wall-normal region. The mean velocity data together with data from previous studies was also examined, and extensive error analysis showed that the von Kármán's constant in the log-law can be determined to be $\kappa = 0.40 \pm 0.02$.

In addition to the behavior of the turbulence statistics, the energy distribution for different wavelengths was studied for the longitudinal fluctuations, and again many similarities were found between the pipe and boundary layer. Perhaps the most intriguing observation is that the location and magnitude of the outer spectral peak increases logarithmically in Re_τ, in contrast to power law behavior previously suggested. This logarithmic behavior was also observed in the outer peak in the variances as well as the zero-crossing of the amplitude modulation function. This result suggests that the wall-normal location of the most energetic motions has a very small increase in viscous units, thereby confining the energetic motions in a decreasing physical region near the wall with increasing Reynolds number. In the limit of infinite Reynolds number, this layer would diminish to an infinitesimally thin vortex sheet at the wall with a slip-flow above it, recovering a potential flow approximation for a turbulent flow.

Five distinct wall-normal layers were identified in turbulent wall-shear flows:

- the linear sublayer up to $y^+ \approx 5$;
- the buffer layer $5 \lesssim y^+ \lesssim 50$;
- the mesolayer $50 \lesssim y^+ \lesssim C_1 \ln Re_\tau + C_2$;
- the inertial sublayer $C_1 \ln Re_\tau + C_2 \lesssim y^+ \lesssim 0.15 Re_\tau$;
- the wake region for $y/\delta \gtrsim 0.15$

The most significant difference seen between pipes and boundary layers was with respect to the start of the inertial sublayer, where constants C_1 and C_2 were found to be different ($C_1 \approx 47$ and $C_2 \approx -190$ for boundary layer and $C_1 \approx 78$ and $C_2 \approx -420$ for pipe). All these regions are indicated in Figure 8.1, together with some other characteristics indicative of each layer.

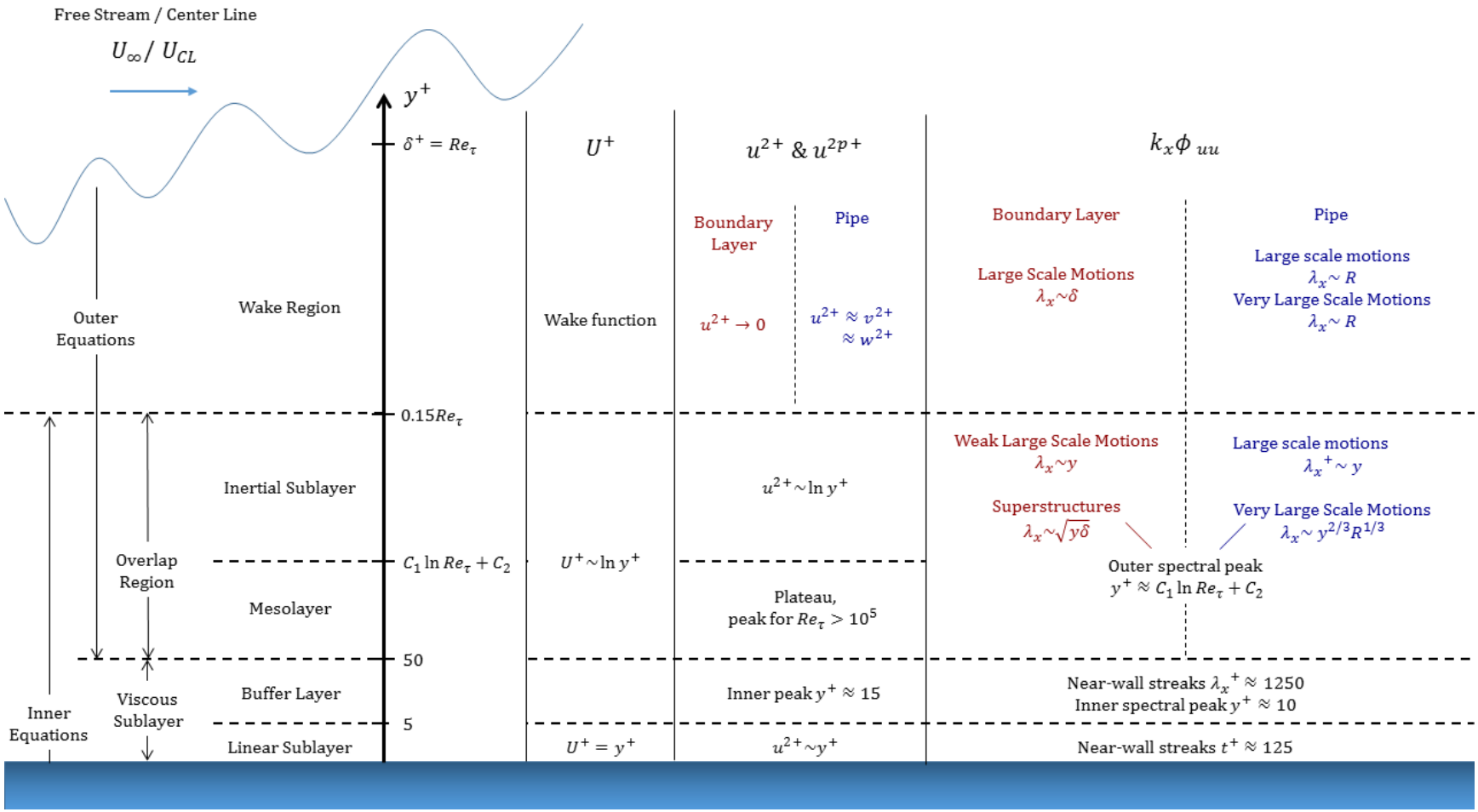

Figure 8.1: Schematic showing various regions in boundary layer and pipe flow. Behavior of mean velocity U, turbulent fluctuations u^+ and energy spectrum $k_x\Phi_{uu}$ are also indicated in corresponding regions. All regions apply for pipes and boundary layers, with exceptions indicated in color. Constants C_1 and C_2 are different ($C_1 \approx 47$ and $C_2 \approx -190$ for boundary layer and $C_1 \approx 78$ and $C_2 \approx -420$ for pipe).

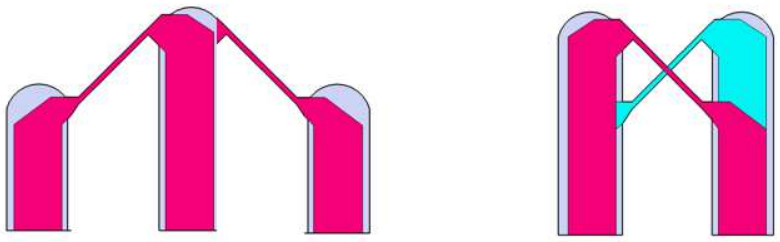

Figure 8.2: Schematic of possible designs of cross-NSTAP.

Our observations suggest that our experiments have finally reached a sufficiently high Reynolds numbers ($Re_\tau \approx 10,000$) where the scale separation between the energetic and dissipative scales is large enough for self-similar behavior of the flow.

8.1 Future Work

In order to check and confirm that the observations and trends seen here truly represent the limit of infinite Reynolds number, it may be necessary to study even higher Reynolds numbers. But perhaps much more important at this point in turbulence research is to concentrate on the precision of the data. Novel technologies evolve quickly and experimentalists should take advantages of these new emerging possibilities. Instead of measuring at larger Reynolds numbers, it is important to measure more precisely, and pay attention to small details, which can be of high importance in the overall picture. This includes more precise estimation of the wall shear stress, parameters influencing the estimation of the von Karman constant and overcoming limitations of end-conduction, spatial and temporal filtering, calibration precision and other parameters affecting the measurement of turbulent fluctuations, just to name a few.

Scaling the streamwise turbulence quantities is an important endeavor, but in order to fully describe turbulent wall-bounded flows and develop appropriate models,

understanding the behavior of the wall-normal and spanwise components of turbulence is also needed. The nano-scale sensor developed in this work is a sound basis for developing more complex sensors with multiple sensing elements that could resolve multiple velocity components instantaneously (a sketch of two possible designs are shown in Figure 8.2). With a two-sensor NSTAP, u and v or u and w instantaneous velocities could be measured, and so a full Reynolds stress tensor can be measured with relatively good spatial and temporal resolution.

Additionally, the small size and flexibility in design of these sensors makes them ideal for temperature and humidity measurements with good temporal and spatial resolution. By combining instantaneous velocity and scalar measurements, the turbulent temperature and humidity fluxes could be studied, in order to gain a better understanding of the transport of mass, momentum, and energy in wall-bounded flows. This is particularly important for atmospheric boundary layers, as well as for the entire convective heat transfer community.

Bibliography

J. J. Allen, M. A. Shockling, G. J. Kunkel, and A. J. Smits. Turbulent flow in smooth and rough pipes. Phil. Trans. R. Soc. Lond. A, 365:699–714, 2007.

E. L. Andreas, K. J. Claffey, R. E. Jordan, C. W. Fairall, P. S. Guest, P. O. G. Persson, and A. A. Grachev. Evaluations of the von Kármán constant in the atmospheric surface layer. J. Fluid Mech., 559:117–149, 2006.

A. Ashok, S. C. C. Bailey, M. Hultmark, and A. J. Smits. Hot-wire spatial resolution effects in measurements of grid-generated turbulence. Experiments in Fluids, 53 (6):1713–1722, September 2012.

S. Bailey, M. Hultmark, K. Meyer, J. Hill, C. Kunkel, G.and Arnold, and A. Smits. Nano-scale thermal anemometry probe. APS Meeting Abstracts, pages A5+, November 2008.

S. C. Bailey, M. Hultmark, J. Schumacher, V. Yakhot, and A. J. Smits. Measurements of the dissipation scales in turbulent pipe flow. Physical Review Letters, 103: 103.014502, 2009.

S. C. C. Bailey and A. J. Smits. Experimental investigation of the structure of large- and very large-scale motions in turbulent pipe flow. J. Fluid Mech., 651:339–356, 2010.

S. C. C Bailey, G. J. Kunkel, M. Hultmark, M. Vallikivi, J. P. Hill, K. A. Meyer,

C. Tsay, C. B. Arnold, and A. J. Smits. Turbulence measurements using a nanoscale thermal anemometry probe. J. Fluid Mech., 663:160–179, 2010.

S.C.C. Bailey, M. Hultmark, J.P. Monty, P.H. Alfredsson, M.S. Chong, R.D. Duncan, J. H. M. Fransson, Hutchins N., I. Marusic, B.J. McKeon, H.M. Nagib, R. Örlü, A. Segalini, A.J. Smits, and R. Vinuesa. Obtaining accurate mean velocity measurements in high Reynolds number turbulent boundary layers using Pitot tubes. J. Fluid Mech., 715:642–670, 2013.

S.C.C. Bailey, M. Vallikivi, and A.J. Smits. Estimating the value of von Kármán's constant in turbulent pipe flow. J. Fluid Mech., 2014. accepted.

B. J. Balakumar and R. J. Adrian. Large- and very-large-scale motions in channel and boundary-layer flows. Phil. Trans. R. Soc. A, 365:665–681, 2007.

R. Betchov. Linfluence de la conduction thermique sur les anemom'etres 'a fils chauds. Verh. K. Akad.Wet., 51:721730, 1948.

G.P. Bewley, H. Nobach, M. Sinhuber, H. Xu, and E. Bodenschatz. The Variable Density Turbulence Facility. arXiv:1401.4970, 2014.

P. Bradshaw. An introduction to turbulence and its measurement. Pergamon Press, 1971.

P. Bradshaw and G. P. Huang. The law of the wall in turbulent flow. Proc. R. Soc. Lond. A, 451:165–188, 1995.

H. H. Bruun. Hot-Wire Anemometry: principles and signal analysis. Oxford University Press, 1995.

M.H. Buschmann and M. Gad-el Hak. Recent developments in scaling of wall-bounded flows. Prog. Aerosp. Sci., 42:419–467, 2009.

B. J. Cantwell. Organized motion in turbulent flow. Annu. Rev. Fluid Mech., 13: 457–515, 1981.

J. Chen, Z. Fan, J. Zou, J. Engel, and C. Liu. Two-dimensional micromachined flow sensor array for fluid mechanics studies. J. Aerospace Eng., 16:85–97, 2003.

T.-K. A. Chou and K. Najafi. Fabrication of out-of-plane curved surfaces in Si by utilizing RIE lag. Proceedings of 15th IEEE International Conference on Micro Electro Mechanical Systems, pages 145–148, 2002.

C.-K. Chung. Geometrical pattern effect on silicon deep etching by an inductively coupled plasma system. J. Micromechanical Microengineerin, 14:656–662, 2004.

J. H. Citriniti and W. K. George. The reduction of spatial aliasing by long hot-wire anemometer probes. Expts. Fluids, 23:217–224, 1997.

F. H. Clauser. The turbulent boundary layer. Advances in Mechanics, 4:1–51, 1956.

D. E. Coles. The law of the wake in the turbulent boundary layer. J. Fluid Mech., 1: 191–226, 1956.

D. E. Coles and E. A. Hirst. The young person's guide to the data. In Proc. Computation of Turbulent Boundary Layers Vol. II AFOSR-IFP-Stanford Conference 1968., 1968.

D. B. DeGraaff and J. K. Eaton. Reynolds-number scaling of the flat-plate turbulent boundary layer. J. Fluid Mech., 422:319–346, 2000.

J. C. del Álamo, J. Jiménez, P. Zandonade, and R. D. Moser. Scaling of the energy spectra of turbulent channels. J. Fluid Mech., 500:135–144, 2004.

T. Ebefors, E. Kalvesten, and G. Stemme. Three dimensional silicon triple-hot-wire anemometer based on polyimide joints. Proceedings MEMS 98. IEEE., pages 93–98, 1998.

R. M. Fand. Heat transfer by forced convection from a cylinder to water in cross flow. Int. J. Heat Mass Transfer, 8:995–1010, 1965.

H. H. Fernholz and P. J. Finley. The incompressible zero-pressure-gradient turbulent boundary layer: an assessment of the data. Prog. Aerospace Sci., 32:245–311, 1996.

K. A. Flack, M. P. Schultz, and T. A. Shapiro. Experimental support for Townsend's Reynolds number similarity hypothesis on rough walls. Phys. Fluids, 17:035102, 2005.

B. Ganapathisubramani, E. K. Longmire, and I. Marusic. Characteristics of vortex packets in turbulent boundary layers. J. Fluid Mech., 478:35–46, 2003.

L. Gaudet and K. G. Winter. Measurements of the drag of some characteristic aircraft excrescences immersed in turbulent boundary layers. Technical report, Royal Aircraft Establishment Farnborough (UK), 1973.

W. K. George. Is there a universal log law for turbulent wall-bounded flows? Phil. Trans. R. Soc. Lond. A, 365:789–806, 2007.

W. K. George and L. Castillo. Zero-pressure-gradient turbulent boundary layer. Appl. Mech. Rev., 50:689–729, 1997.

M. Guala, S. E. Hommema, and R. J. Adrian. Large-scale and very-large-scale motions in turbulent pipe flow. J. Fluid Mech., 554:521–542, 2006.

F. R. Hama. Boundary layer characteristics for smooth and rough surfaces. Trans. Soc. Naval Archit. Mar. Engrs, 62:333–358, 1954.

J. P. Hill. NSTAP: Fabrication and testing of nanoscale thermalanemometry probes. Mechanical and Aerospace Engineering, Princeton University., Senior Thesis,2007.

U. Högström, J.C.R. Hunt, and Ann-Sofi Smedman. Theory and measurements for turbulence spectra and variances in the atmospheric neutral surface layer. Boundary-Layer Meteorology, 103(1):101–124, 2002.

S. Hoyas and J. Jiménez. Scaling of the velocity fluctuations in turbulent channels up to $Re_\tau = 2003$. Phys. Fluids, 18:011702, 2006.

G. D. Huffman and P. Bradshaw. A note on von Kármán's constant in low Reynolds number turbulent flows. J. Fluid Mech., 53:45–60, 1972.

S. G. Huisman, S. Scharnowski, C. Cierpka, C. J. Kähler, D. Lohse, and C. Sun. Logarithmic boundary layers in strong taylor-couette turbulence. Phys. Rev. Lett., 110:264501, 2013.

M. Hultmark. A theory for the streamwise turbulent fluctuations in high Reynolds number pipe flow. J. Fluid Mech., 707:575–584, 2012.

M. Hultmark and A. J. Smits. Temperature corrections for constant temperature and constant current hot-wire anemometers. Meas. Sci. Tech., 21:105404, 2010.

M. Hultmark, S. C. C. Bailey, and A. J. Smits. Scaling of near-wall turbulence in pipe flow. J. Fluid Mech., 649:103–113, 2010.

M. Hultmark, A. Ashok, and A. J. Smits. A new criterion for end conduction effects in hot wire anemometry. Expts. Fluids, 22:055401, 2011.

M. Hultmark, M. Vallikivi, S. C. C. Bailey, and A. J. Smits. Turbulent Pipe Flow at Extreme Reynolds Numbers. Physical Review Letters, 108(9):1–5, 2012.

M. Hultmark, M. Vallikivi, S. C. C. Bailey, and A. J. Smits. Logarithmic scaling of turbulence in smooth- and rough-wall pipe flow. Journal of Fluid Mechanics, 728: 376–395, 2013.

N. Hutchins and I. Marusic. Evidence of very long meandering streamwise structures in the logarithmic region of turbulent boundary layers. J. Fluid Mech., 579:1–28, 2007.

N. Hutchins, T. B. Nickels, I. Marusic, and M. S. Chong. Hot-wire spatial resolution issues in wall-bounded turbulence. J. Fluid Mech., 635:103–136, 2009.

Nick Hutchins and Kwing-So Choi. Accurate measurements of local skin friction coefficient using hot-wire anemometry. Progress in Aerospace Sciences, 38(45):421 – 446, 2002.

F. P. Incropera, A. S. Lavine, and D. P. DeWitt. Fundamentals of Heat and Mass Transfer, chapter 7.2, pages 436–443. Wiley & Sons, Inc., 7 edition, 2011.

H. Jansen, M. D. Boer, R. Wiegerink, N. Tas, E. Smulders, C. Neagu, and M. Elwenspoek. RIE lag in high aspect ratio trench etching of silicon. Microelectronic Engineering, 35:45–50, 1997.

F. Jiang, Y.-C. Tai, C.-M. Ho, and W. J. Li. A micromachined polysilicon hot-wire anemometer. In Solid-State Sensor and Actuator Workshop, Hilton Head, SC, pages 264–267. IEEE, 1994.

J. Jiménez. Turbulent flows over rough walls. Annu. Rev. Fluid Mech., 36:173–196, 2004.

J. Jiménez and S. Hoyas. Turbulent fluctuations above the buffer layer of wall-bounded flows. J. Fluid Mech., 611:215–236, 2008.

J. Jiménez and R. D. Moser. What are we learning from simulating wall turbulence? Phil. Trans. R. Soc. Lond. A, 365:715–732, 2007.

J. M. Jiménez, M. Hultmark, and A. J. Smits. The intermediate wake of a body of

revolution at high Reynolds numbers. Journal of Fluid Mechanics, 659:516–539, 2010.

Gabriel Katul and Chia-Ren Chu. A theoretical and experimental investigation of energy-containing scales in the dynamic sublayer of boundary-layer flows. Boundary-Layer Meteorology, 86(2):279–312, 1998.

K. C. Kim and R. J. Adrian. Very large-scale motion in the outer layer. Phys. Fluids, 11(2):417–422, 1999.

J. C. Klewicki and R. E. Falco. On accurately measuring statistics associated with small-scale structure in turbulent boundary layers using hot-wire probes. J. Fluid Mech., 219:119–142, 1990.

L. G. Kovasznay, V. Kibens, and R. F. Blackwelder. Large-scale motion in the intermittent region of a turbulent boundary layer. J. Fluid Mech., 41(2):283–325, 1970.

G. J. Kunkel, C. B. Arnold, and A. J. Smits. Development of NSTAP: a nanoscale thermal anemometry probe. AIAA Paper 2006-3718, 2006.

G. J. Kunkel, J. J. Allen, and A. J. Smits. Further support for Townsend's Reynolds number similarity hypothesis in high Reynolds number rough-wall pipe flow. Phys. of Fluids, 19(5):055109, 2007.

L. I. Langelandsvik, G. J. Kunkel, and A. J. Smits. Flow in a commercial steel pipe. J. Fluid Mech., 595(323-339):323–339, 2007.

M. Lesieur and O. Métais. New trends in large-eddy simulations of turbulence. Annu. Rev. Fluid Mech., 28:45–82, 1996.

P. M. Ligrani and P. Bradshaw. Spatial resolution and measurement of turbulence

in the viscous sublayer using subminiature hot-wire probes. Expts. Fluids, 5(6): 407–417, 1987a.

P. M. Ligrani and P. Bradshaw. Subminiature hot-wire sensors: development and use. J. Phys. E: Sci. Instrum., 20:323–332, 1987b.

L. Löfdahl, G. Stemme, and B. Johannson. Silicon based flow sensors for mean velocity and turbulence measurements. Expts. Fluids, 12:391–393, 1992.

R. R. Long and T.-C. Chen. Experimental evidence for the existence of the mesolayer in turbulent systems. J. Fluid Mech., 105:9–59, 1981.

F. A. MacMillan. Experiments on Pitot tubes in shear flow. Ministry of Supply, Aero. Res. Council, 3028, 1957.

I. Marusic and G. J. Kunkel. Streamwise turbulence intensity formulation for flat-plate boundary layers. Phys. Fluids, 15:2461–2464, 2003.

I. Marusic, M. Uddin, and A.E. Perry. Similarity law for the streamwise turbulence intensity in zero-pressure-gradient turbulent boundary layers. Phys. Fluids, 12: 3718–3726, 1997.

I. Marusic, R. Mathis, and N. Hutchins. High Reynolds number effects in wall turbulence. Int. J. Heat Fluid Flow, 31:418–428, 2010a.

I. Marusic, R. Mathis, and N. Hutchins. Predictive model for wall-bounded turbulent flow. Science, 329:193–196, 2010b.

I. Marusic, B. J. McKeon, P. A. Monkewitz, H. M. Nagib, A. J. Smits, and K. R. Sreenivasan. Wall-bounded turbulent flows: recent advances and key issues. Phys. Fluids, 22:065103, 2010c.

Ivan Marusic, Jason P. Monty, Marcus Hultmark, and Alexander J. Smits. On the logarithmic region in wall turbulence. Journal of Fluid Mechanics, 716, 1 2013.

R. Mathis, N. Hutchins, and I. Marusic. Large-scale amplitude modulation of the small-scale structures in turbulent boundary layers. J. Fluid Mech., 628:311–337, 2009.

B. J. McKeon. High Reynolds number turbulent pipe flow. PhD thesis, Princeton University, 2003.

B. J. McKeon and A. J. Smits. Static pressure correction in high Reynolds number fully developed turbulent pipe flow. Meas. Sci. Tech., 13:1608–1614, 2002.

B. J. McKeon, J. Li, W. Jiang, J. F. Morrison, and A. J. Smits. Pitot probe corrections in fully developed turbulent pipe flow. Meas. Sci. Tech., 14(8):1449–1458, 2003.

B. J. McKeon, J. Li, W. Jiang, J. F. Morrison, and A. J. Smits. Further observations on the mean velocity distribution in fully developed pipe flow. J. Fluid Mech., 501: 135–147, 2004a.

B. J. McKeon, C. J. Swanson, M. V. Zagarola, R. J. Donnelly, and A. J. Smits. Friction factors for smooth pipe flow. J. Fluid Mech., 511:41–44, 2004b.

G. L. Mellor and K. Herring. A survey of the mean turbulent field closure models. AIAA Journal, 11/5:590–599, 1973.

C. Meneveau and J. Katz. Scale invariance and turbulence models for large-eddy simulation. Annu. Rev. Fluid Mech, 32:132, 2000.

C. Meneveau and I. Marusic. Generalized logarithmic law for high-order moments in turbulent boundary layers. J. Fluid Mech., 719:R1, 2013.

M. Metzger, B. J. McKeon, and H. Holmes. The near-neutral atmospheric surface layer: turbulence and non-stationarity. Phil. Trans. R. Soc. Lond. A, 365(1852): 859–876, 2007.

K. Meyer. Fabrication and testing of nanoscale thermal anemometry probes (NSTAP). Mechanical and Aerospace Engineering, Princeton University., Senior Thesis,2008.

C. B. Millikan. A critical discussion of turbulent flows in channels and circular tubes. In Proceedings of the Fifth International Congress of Applied Mechanics, Cambridge, MA, 1938.

P. Moin and K. Mahesh. Direct numerical simulation: A tool in turbulence research. Annual Review of Fluid Mechanics, 30:539–578, 1998.

J. P. Monty. Developments in smooth wall turbulent duct flows. PhD thesis, University of Melbourne, 2005.

J. P. Monty, J. A. Stewart, R. C. Williams, and M. S. Chong. Large-scale features in turbulent pipe and channel flows. J. Fluid Mech., 589:147–156, 2007.

J. P. Monty, N. Hutchins, H. C. H. Ng, I. Marusic, and M. S. Chong. A comparison of turbulent pipe, channel and boundary layer flows. J. Fluid Mech., 632:431–442, 2009.

J. F. Morrison, B. J. McKeon, W. Jiang, and A. J. Smits. Scaling of the streamwise velocity component in turbulent pipe flow. J. Fluid Mech., 508:99–131, 2004.

H. M. Nagib and K. A. Chauhan. Variations of von Kármán coefficient in canonical flows. Phys. Fluids, 20:101518, 2008.

H. C. H. Ng, J. P. Monty, Hutchins N., M. S. Chong, and I. Marusic. Comparison of turbulent channel and pipe flows with varying Reynolds number. Exp. Fluids, 51 (5):1261–1281, 2011.

T. B. Nickels, I. Marusic, S. M. Hafez, and M. S. Chong. Evidence of the k^{-1} law in a high-Reynolds-number turbulent boundary layer. Phys. Rev. Letters, 95:074501, 2005.

R. Örlü, J. H. M. Fransson, and P. H. Alfredsson. On near wall measurements of wall bounded flows - The necessity of an accurate determination of the wall position. Prog. Aerosp. Sci., 46:353–387, 2010.

J. M. Österlund, A. V. Johansson, H. M. Nagib, and M. H. Hites. A note on the overlap region in turbulent boundary layers. Phys. Fluids, 12(1):1–4, 2000.

V. C. Patel. Calibration of the Preston tube and limitations on its use in pressure gradients. J. Fluid Mech., 23:185–208, 1965.

A. E. Perry and C. J. Abell. Scaling laws for pipe-flow turbulence. J. Fluid Mech., 67:257–271, 1975.

A. E. Perry and M. S. Chong. On the mechanism of wall turbulence. J. Fluid Mech., 119:173–217, 1982.

A. E. Perry and J. D. Li. Experimental support for the attached-eddy hypothesis in zero-pressure- gradient turbulent boundary layers. J. Fluid Mech., 218:405–438, 1990.

A. E. Perry and J. F. Morrison. A study of the constant-temperature hot-wire anemometer. Journal of Fluid Mechanics, 47(3):577–599, 1971.

A. E. Perry, A. J. Smits, and M. S. Chong. The effects of certain low frequency phenomena on the calibration of hot wires. Journal of Fluid Mechanics, 90:3:415–431, 1979.

A. E. Perry, S. M. Henbest, and M. S. Chong. A theoretical and experimental study of wall turbulence. J. Fluid Mech., 165:163–199, 1986.

A. E. Perry, S. Hafez, and M. S. Chong. A possible reinterpretation of the Princeton superpipe data. J. Fluid Mech., 439:395–401, 2001.

A.E. Perry and C.J. Abell. Asymptotic similarity of turbulence structures in smooth- and rough-walled pipes. J. Fluid Mech., 79:785–799, 1977.

U. Piomelli and E. Balaras. Wall-layer models for large-eddy simulations. Annu. Rev. Fluid Mech, 34:34974, 2002.

S. Pirozzoli and M. Bernardini. Probing high-reynolds-number effects in numerical boundary layers. Physics of Fluids, 25:021704, 2013.

S. B. Pope. Turbulent Flows. CUP, 2000.

L. Prandtl. Bericht ber untersuchungen zur ausgebildeten turbulenz. Z. Angew. Math. Mech, 5(2):136–139, 1925.

D. I. Pullin, M. Inoue, and N. Saito. On the asymptotic state of high reynolds number, smooth-wall turbulent flows. Physics of Fluids, 25(1):105116, 2013.

M. P. Rao, M. F. Aimi, and N. C. MacDonald. Single-mask, three-dimensional microfabrication of high-aspect-ratio structures in bulk silicon using reactive ion etching lag and sacrificial oxidation. App. Phys. Lett., 85-25:6281–6283, 2004.

M. R. Raupach, R. A. Antonia, and S. Rjagopalan. Rough-wall turbulent boundary layers. Appl. Mech. Rev., 44:1–25, 1991.

L. F. Richardson. Weather prediction by numerical process. Cambridge University Press, Cambridge, UK, 1922.

S. K. Robinson. Coherent motions in turbulent boundary layers. Annu. Rev. Fluid Mech., 23:601–639, 1991.

B. J. Rosenberg, M. Hultmark, M. Vallikivi, S. C. C. Bailey, and A. J. Smits. Turbulence spectra in smooth- and rough-wall pipe flow at extreme Reynolds numbers. Journal of Fluid Mechanics, 731:46–63, August 2013.

H. Schlichting and K. Gersten. Boundary Layer Theory. Springer-Verlag, New York, NY, 8th edition, 2000.

M. P. Schultz and K. A. Flack. Reynolds-number scaling of turbulent channel flow. Phys. Fluids, 25:025104, 2013.

M. A. Shockling, J. J. Allen, and A. J. Smits. Roughness effects in turbulent pipe flow. J. Fluid Mech., 564:267–285, 2006.

J. Sillero, J. Jiménez, R. D. Moser, and N. P. Malaya. Direct simulation of a zero-pressure-gradient turbulent boundary layer up to re_θ= 6650. Journal of Physics: Conference Series, 318:022023, 2011.

A. J. Smits and I. Marusic. Wall-bounded turbulence. Physics Today, pages 25–30, September 2013.

A. J. Smits, B. J. McKeon, and I. Marusic. High Reynolds number wall turbulence. Annu. Rev. Fluid Mech., 43:353–375, 2011a.

A. J. Smits, J. Monty, M. Hultmark, S. C. C. Bailey, M. Hutchins, and I. Marusic. Spatial resolution correction for turbulence measurements. J. Fluid Mech., 676: 41–53, 2011b.

C. J. Swanson, B. Julian, G. G. Ihas, and Donnelly R. J. Pipe flow measurements over a wide range of Reynolds numbers using liquid helium and various gases. J. Fluid Mech., 461:51–60, 2002.

S. Tavoularis. Measurement in Fluid Mechanics. Cambridge University Press, 2005.

G. I. Taylor. The spectrum of turbulence. Proc. R. Soc. Lond., 164(919):476–490, 1938.

H. Tennekes and J. L. Lumley. A First Course in Turbulence. The MIT Press, Cambridge, Massachusetts, 1972.

A. A. Townsend. The Structure of Turbulent Shear Flow. CUP, Cambridge, UK, 1976.

C. Tropea, A. Yarin, and J. Foss, editors. Springer Handbook of Experimental Fluid Mechanics. Springer, 2007.

Y. Tsuji, B. Lindgren, and A. V. Johansson. Self-similar profile of probability density functions in zero-pressure gradient turbulent boundary layers. Fluid Dyn. Res., 37: 293–316, 2005.

U.S. Energy Information Administration. Annual energy outlook 2014, early release. EIA, 2013.

M. Vallikivi. Turbulence measurements with a nano-scale thermal anemometry probe. Master's thesis, Chalmers University of Technology, Sweden, 2010.

M. Vallikivi and A. J. Smits. Fabrication and characterization of a novel nano-scale thermal anemometry probe. J. of MEMS, 2014. accepted.

M. Vallikivi, M. Hultmark, S. C. C. Bailey, and A. J. Smits. Turbulence measurements in pipe flow using a nano-scale thermal anemometry probe. EXPFL, 51:1521–1527, 2011.

T. von Kármán. Mechanische ähnlichkeit und turbulenz. In Proceedings of the 3rd International Congress on Applied Mechanics, 1930.

Yu-Hsiang Wang, Chia-Yen Lee, and Che-Ming Chiang. A MEMS-based Air Flow Sensor with a Free-standing Microcantilever Structure. Sensors, 7:2389–2401, 2007.

W. W. Willmarth and L. K. Sharma. Study of turbulent structure with hot wires smaller than the viscous length. Journal of Fluid Mechanics, 142:121–149, 1984.

M. Wosnik, L. Castillo, and W. K. George. A theory for turbulent pipe and channel flows. J. Fluid Mech., 421:115–145, 2000.

X. Wu, J. R. Baltzer, and R. J. Adrian. Direct numerical simulation of a 30r long turbulent pipe flow at $r^+ = 685$: large- and very large-scale motions. J. Fluid Mech., 698:235–281, 2012.

J. C. Wyngaard. Measurements of small scale turbulence structure with hot-wires. J. Sci. Instrum., 1:1105–1108, 1968.

X. Xiong, T. Dallas, S. Gangopadhyay, J. Berg, and T. Henryk. Design and Analysis of a Dual-Mode MEMS Micromirror. Micro and Nanosystems, 2(1):23–31, April 2010.

M. V. Zagarola. Mean-Flow Scaling of Turbulent Pipe Flow. PhD thesis, Princeton University, June 1996.

M. V. Zagarola and A. J. Smits. Mean-flow scaling of turbulent pipe flow. J. Fluid Mech., 373:33–79, 1998.

M. V. Zagarola, D. R. Williams, and A. J. Smits. Calibration of the preston probe for high Reynolds number flows. Meas. Sci. Technol., 12:495501, 2001.

E-S. Zanoun, F. Durst, and H. Nagib. Evaluating the law of the wall in two-dimensional fully developed turbulent channel flows. Phys. Fluids, 15(10):3079–3089, 2003.